OPTICAL SUPER-RESOLUTION AND PERIODICAL FOCUSING EFFECTS BY DIELECTRIC MICROSPHERES

by

Arash Darafsheh

A dissertation submitted to the faculty of
The University of North Carolina at Charlotte
in partial fulfillment of the requirements
for the degree of Doctor of Philosophy in
Optical Science and Engineering

Charlotte

2013

Approved by:

_____
Dr. Vasily N. Astratov

_____
Dr. Michael A. Fiddy

_____
Dr. Gregory J. Gbur

_____
Dr. Angela D. Davies

_____
Dr. Christopher J. Evans

ABSTRACT

ARASH DARAFSHEH. Optical super-resolution and periodical focusing effects by dielectric microspheres. (Under the direction of DR. VASILY N. ASTRATOV)

Optical microscopy is one of the oldest and most important imaging techniques; however, its far-field resolution is diffraction-limited. In this dissertation, we proposed and developed a novel method of optical microscopy with super-resolution by using high-index dielectric microspheres immersed in liquid and placed on the surface of the structures under study. We used barium titanate glass microspheres with diameters of D~2-220 μm and refractive indices n~1.9-2.1 to discern minimal feature sizes ~$\lambda/4$ (down to ~$\lambda/7$) of various photonic and plasmonic nanostructures, where λ is the illumination wavelength. We studied the magnification, field of view, and resolving power, in detail, as a function of sphere sizes.

We studied optical coupling, transport, focusing, and polarization properties of linear arrays of dielectric spheres. We showed that in arrays of spheres with refractive index $n=\sqrt{3}$, a special type of rays with transverse magnetic (TM) polarization incident on the spheres under the Brewster's angle form periodically focused modes with radial polarization and $2D$ period, where D is the diameter of the spheres. We showed that the formation of periodically focused modes in arrays of dielectric spheres gives a physical explanation for beam focusing and extraordinarily small attenuation of light in such chains. We showed that the light propagation in such arrays is strongly polarization-dependent, indicating that such arrays can be used as filters of beams with radial polarization. The effect of forming progressively smaller focused beams was experimentally observed in chains of sapphire spheres in agreement with the theory.

We expanded the concept of periodically focused modes to design a practical device for ultra-precise contact-mode laser tissue-surgery, with self-limiting ablation depth for potential application in retina surgery. By integrating arrays of dielectric spheres with infrared hollow waveguides and fibers, we fabricated prototypes of the designs and tested them with an Er:YAG laser. Furthermore, we proposed another design based on conical arrays of dielectric spheres to increase the coupling efficiency of the probe.

ACKNOWLEDGMENTS

I am very thankful to my advisor, Dr. Vasily N. Astratov, for his advice and support; for his constructive criticisms on my presentations, papers, and dissertation; and for the scientific discussions we had during my study at the University of North Carolina at Charlotte. Without his help, this dissertation work would have not been possible.

I thank members of my committee, Dr. Michael A. Fiddy, Dr. Gregory J. Gbur, Dr. Angela D. Davies, and Dr. Christopher J. Evans for accepting to serve in the committee and their time and comments.

I am grateful to Dr. Nathaniel M. Fried for his guidance in surgical applications of lasers and fruitful discussions, to Dr. Michael A. Fiddy for discussions which initiated the work on super-resolution imaging, and to Dr. Angela D. Davies for sharing high numerical-aperture microscope objectives.

During my graduate studies, I enjoyed discussing scientific issues with my fellow Mesophotonics Laboratory members, Dr. Oleksiy Svitelskiy, Kenneth W. Allen, S. Adam Burand, and Yangcheng Li. I am grateful for the opportunity to be involved in a number of collaborations with different groups with which Mesophotonics laboratory has collaborative works. I also would like to thank fellow graduate students Thomas C. Hutchens and Mona Mayeh for productive discussions.

I am thankful to Dr. Lou Deguzman, Scott Williams, Dr. Awad Gerges, and Dr. Robert Hudgins for showing me how to operate the equipment in the Optics center at the UNCC. I would like to thank the staff of the Physics department and the Optics center, Wendy Ramirez and Mark Clayton, for helping me with the administrative issues.

I was supported through a fellowship from TIAA-CREFF for Fall 2008 and Spring 2009 and by GASP award from Fall 2008 to Spring 2013. My graduate assistantship in Dr. Astratov's Mesophotonics Laboratory was supported through his grants from NSF, NIH, and ARO.

I am grateful to Dr. Faramarz Farahi and Dr. Mohammad A. Kazemi for their guidance and introducing the UNCC Optical Science and Engineering graduate program to me.

I deeply thank my family for their endless love and support which motivated me to pursue my academic education up to this level.

DEDICATION

To my parents, Dr. Rafat Rafiei and Dr. M. Reza Darafsheh,

for their endless love and support.

TABLE OF CONTENTS

LIST OF FIGURES

LIST OF ABBREVIATIONS

2-D	two dimension(al)
3-D	three dimension(al)
AFM	atomic force microscopy
ATR	attenuated total reflectance
BTG	barium titanate glass
BD	blu-ray® disk
CCD	charge-coupled device
CV	cylindrical vector
CW	continuous wave
CROW	coupled resonator optical waveguide
D	diameter
dB	decibel
Er:YAG	erbium: yttrium aluminium garnet
FCS	fluorescence correlation spectroscopy
FDTD	finite difference time domain
FFT	fast-Fourier transform
FOV	field of view
FWHM	full width at half-maximum
GMM	generalized multiparticle Mie
h-SIL	hemispherical solid immersion lens
HWG	hollow waveguide
ID	inner diameter

IPA	isopropyl alcohol
IR	infra-red
KTP	potassium titanyl phosphate
LASIK	laser-assisted in situ keratomileusis
M	magnification
NA	numerical aperture
NIM	nanojet-induced mode
NPD	nanoparticle dimer
NSOM	near-field scanning optical microscopy
OD	outer diameter
PDMS	polydimethylsiloxane
PDR	proliferative diabetic retinopathy
PFM	periodically focused mode
PMMA	poly(methyl methacrylate)
PNJ	photonic nanojet
PSF	point-spread function
PTFE	polytetrafluoroethylene
Q-factor	quality factors
SEM	scanning electron microscopy
SIL	solid immersion lens
SNOM	scanning near-field optical microscopy
SOP	state of polarization
s-SIL	super-spherical solid immersion lens

TE	transverse electric
TM	transverse magnetic
UV	ultraviolet
WF	weight factor
WGM	whispering gallery mode
YAG	yttrium aluminium garnet

CHAPTER 1: INTRODUCTION

1.1. Outline and Overview of the Dissertation

In this dissertation, we investigate the optical properties of individual dielectric microspheres and more complicated structures formed by multiple spheres. Individual spheres can confine light inside the cavities leading to strong resonant properties. They can also reflect and refract incident beams to focus light. These properties are diversified in microspherical arrays, leading to unusual imaging, focusing, and optical transport effects.

Chapter 1 is dedicated to the review of related literature. The plan of this introductory chapter directly corresponds to the order in which these dissertation chapters are presented, such that sub-sections 1.2-1.4 can be considered as introductions to corresponding Chapters 2-4. First, in sub-section 1.2, we consider spatial resolution limits [1-10] in optical microscopy and super-resolution imaging techniques [11-65]. Then, in sub-section 1.3, we consider resonant [66-84] and non-resonant [85-107] optical properties of dielectric microspheres. Finally, in sub-section 1.4 we discuss focusing microprobes for laser tissue-surgery applications. In the chapter summary, we present the motivation and goals of the present dissertation work.

In Chapter 2, we propose a novel super-resolution microscopy technique. We show, experimentally, that microspheres with diameters (D) in the range 2-220 μm and with high refractive indices (n~1.9-2.1) can be used for super-resolution imaging of liquid-

immersed nanostructures. Using micron-scale microspheres, we demonstrate the ability to discern the shape of a pattern with a minimum feature size of $\lambda/7$, where λ is the illumination wavelength. For spheres with $D>50$ μm, the discernible feature sizes were found to increase to $\lambda/4$. Detailed data on the resolution, magnification, and field-of-view are then presented in this chapter. This imaging technique can be used in biomedical microscopy, microfluidics, and nanophotonics applications.

In Chapter 3, we introduce the concept of periodically focused modes (PFMs) in chains of dielectric spheres. The results presented in this chapter lay foundations for our work on developing novel light focusing devices and optical scalpels, which operate based on the PFM formation principle. We also show that the PFM concept introduced in this dissertation, in the limit of geometrical optics, is inherently related to the concept of nanojet-induced modes (NIMs), introduced earlier for chains formed by wavelength-scale spheres [108-110]. We show, theoretically, that the Brewster's angle conditions for transverse magnetic (TM) polarized rays can be periodically reproduced in chains of spheres with refractive index $n=\sqrt{3}$ giving rise to PFMs with $2D$ period, where D is the diameter of the spheres. Using ray tracing, for a spherical emitter with the diameter D, we show that chains of spheres work as filters for PFMs at $1.72<n<1.85$. This leads to tapering of the focused beams combined with the reduction of their attenuation along the chain. Experimentally, we observe the "beam tapering" effect in chains of 300 μm sapphire spheres, with index $n\sim1.77$ in visible. Furthermore, we show that the light propagation in such chains is strongly polarization-dependent, indicating that such arrays can be used as radial polarizers.

In Chapter 4, we design, fabricate, and test a device capable of focusing multimodal beams in contact with tissue. We study the focusing of multimodal beams by chains of dielectric microspheres assembled directly inside the cores of hollow waveguides (HWGs). The device designs are optimized for laser surgery in a contact mode with strongly absorbing tissue. By analyzing a broad range of parameters, we demonstrate that chains formed by three or five spheres, with refractive index $1.65<n<1.75$, improve the spatial resolution by a factor of 2, compared with a single-sphere designs. By integrating arrays of dielectric spheres, with infrared hollow waveguides and fibers, we fabricate prototypes of the designs and test them with an Er:YAG laser. Furthermore, we propose another design based on conical arrays of dielectric spheres to increase the coupling efficiency of the probe. Potential applications include ultra-precise laser ablation or coagulation in the eye and brain, cellular surgery, and coupling of light into photonic microstructures.

Conclusions are drawn and future possible extensions of the work are proposed at the end of the dissertation.

1.2. Super-resolution Microscopy Techniques

The far-field spatial resolution of a lens-based optical imaging system, the smallest discernible features in the object, is limited by the wavelength of the incident light and by the numerical aperture (NA) of the objective lens system by almost half of the illuminating wavelength due to the diffraction of light waves [1].

The numerical aperture (NA) of an objective lens is defined by

$$\mathrm{NA} = n \sin \theta_{max}, \tag{1.1}$$

where n is the refractive index of the object-space medium, in which the lens is working, and θ_{max} is the half-angle of the maximum cone of light that can enter (exit) the lens, as illustrated in Fig. 1.1. For a circular face lens with aperture diameter D and focal length f working in air, NA is written approximately for the case $f>>D$ as:

$$\mathrm{NA} = D/(2f). \tag{1.2}$$

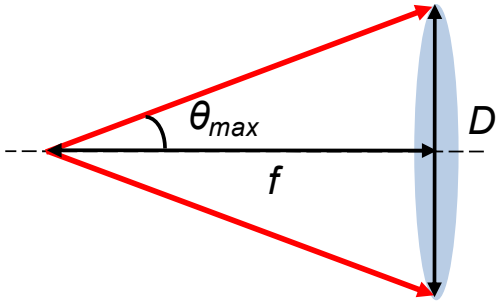

Figure 1.1: Numerical aperture (NA) of a lens.

Image resolution can be improved by using different techniques, such as liquid [18] or solid immersion lenses [19-37], near-field probes [39-43], super-oscillatory lenses [44-46], fluorescent [47-50], nonlinear, and negative refractive index materials [51-57], plasmon gratings [57, 58]. In this section, we briefly review basic principles of some of these imaging techniques with emphasis on a recently proposed microsphere nanoscope [63].

1.2.1. Diffraction Limit and Resolution Criteria

The far-field spatial resolution of any aplantic lens-based optical imaging instrument is fundamentally limited by the diffraction of light. The diffraction limit manifests itself due to the fact that the image of a point in the object plane is a finite-sized spot in the image plane, with a certain irradiance distribution known as the point-spread function

(PSF). The PSF is the Fourier transform of the transmittance function of the aperture [111].

The resolution of a microscope depends on the illumination characteristics, such as object-space wavelength, state of polarization [112], degree of coherence [113], condenser lens [114, 115]; and certain parameters of the aperture, such as shape, size, and apodization [8].

For a diffraction-limited optical system, an aberration-free system limited only by diffraction effects, various criteria such as Abbe [2], Rayleigh [3], Sparrow [4], and Houston [5] have been proposed to determine how close two object features, such as two point sources with equal intensities, can be to each other spatially to be discerned as two individual sources in the image plane. It is assumed that for shorter separations of the object points, it is not possible to unambiguously identify them as separate point sources. In this review, we consider incoherent image formation.

In a microscope system, the object features can be considered as a diffraction grating whose Fourier transform forms at the back focal plane of the objective lens. Superposition of theses spatial frequencies on the image plane forms the image. Since not all spatial frequencies pass through the lens, the resolution is limited. Therefore, in terms of spatial frequencies, a microscope operates as a low-pass filter; the transmission of the highest spatial frequency is a measure of the spatial resolution [9, 42].

According to the Abbe's microscope theory [2], incident light is diffracted by the object features. Object features separated by d are considered as a diffraction grating with period d. The diffracted orders can be collected totally or partially by the imaging system, as shown in Fig. 1.2.

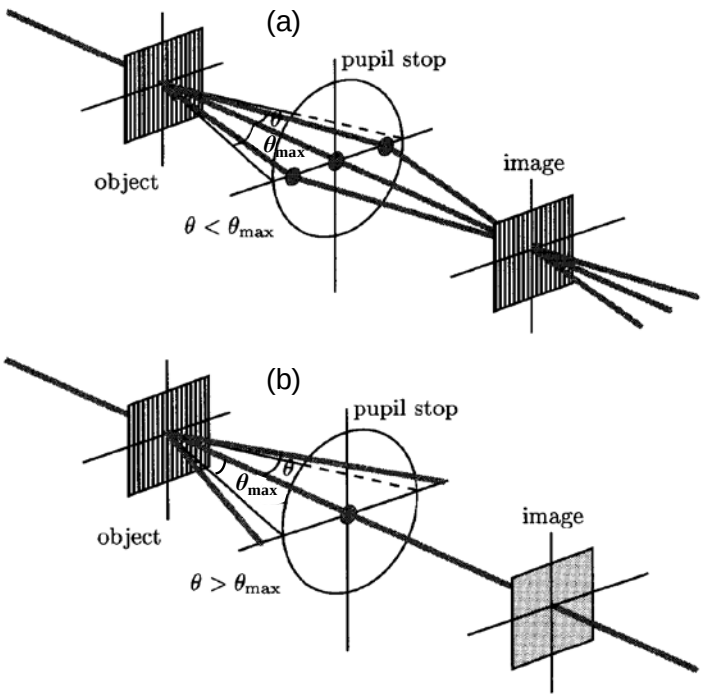

Figure 1.2: Illustration of the Abbe's theory where diffraction orders pass through (a) or stopped by (b) the lens pupil [42]. Reprinted with permission. © 2003 Imperial College Press.

The m^{th} diffraction maximum occurs at angle θ_m, which satisfies the following grating equation:

$$d \sin \theta_m = m\lambda, \tag{1.3}$$

where θ_m is the angle between the m^{th} diffraction order and the normal vector to the grating surface. From Eq. (1.3), it can be seen that the smaller the d (the smaller the details of an object) the larger the θ_m, for a given diffraction order. The zero-order and at least one of the first order diffracted rays need to be collected by the objective lens in order to resolve that period correctly [10]. The condition for passing one of the first order diffracted rays through the lens gives the Abbe diffraction limit:

$$d = \frac{0.5\lambda_0}{\mathrm{NA}}, \tag{1.4}$$

where λ_0 is the free-space wavelength of illumination. According to the Abbe limit, object features separated by less than $0.5\lambda_0$/NA cannot be resolved.

It can be seen from Eq. (1.4) that the resolution is improved by reducing the illumination wavelength (λ_0), increasing the refractive index of the object-space (n), and increasing the acceptance angle of the light collection objective (θ_{max}). The Abbe limit is ~200-250 nm for conventional white light microscopy systems. Improving the resolution beyond the Abbe limit, without reducing the wavelength or increasing the form factor of the instrument, has been labeled as super-resolution techniques in the literature [10]. The contribution of the near-field components of the scattered field of the object is a vital factor in super-resolution techniques, due to the fact that high spatial frequencies corresponding to sub-wavelength information of the object are carried by the evanescent components of the scattered field. Super-resolution without employing evanescent waves can be achieved by optical superoscillations [44-46]. Superoscillation refers to a phenomenon where a bandlimited function is able to locally oscillate arbitrarily faster than the highest Fourier component in its spectrum [44].

In the rest of this sub-section, we review a few other classical resolution criteria which are, in principle, related to the width of the main lobe of the PSF of the imaging aperture [8]. It should be pointed out that there is an essential distinction between the Abbe's resolution limit, which is based on a physical model, and the Rayleigh resolution criterion, which is rather a heuristic estimate of the resolution limit [3, 15].

The Rayleigh resolution limit states that two point sources with equal intensities are just resolved if the central maximum of the irradiance diffraction pattern produced by one point source coincides with the first zero of the irradiance diffraction pattern produced by

the second source. In this case, the composite irradiance distribution shows a saddle which has 81.1% or 73.6% of the maximum irradiance, respectively, for a square or circular shaped aperture, as shown in Fig. 1.3. For a square or circular shaped aperture, the PSF is of the form $Sinc^2$ or $Jinc^2$, respectively, where $Sinc(x)=sin(\pi x)/(\pi x)$ and $Jinc(x)=J_1(x)/x$, in which J_1 is the Bessel function of first kind of order 1. In the rest of this section, we consider circular apertures. For a circular aperture with diameter D, the PSF has an Airy disk [111] appearance:

$$I(r) = I_0 \left(\frac{2J_1(k_0 r \mathrm{NA})}{k_0 r \mathrm{NA}} \right)^2, \tag{1.5}$$

where $k_0=2\pi/\lambda_0$ is the free-space wave number of the illuminating light.

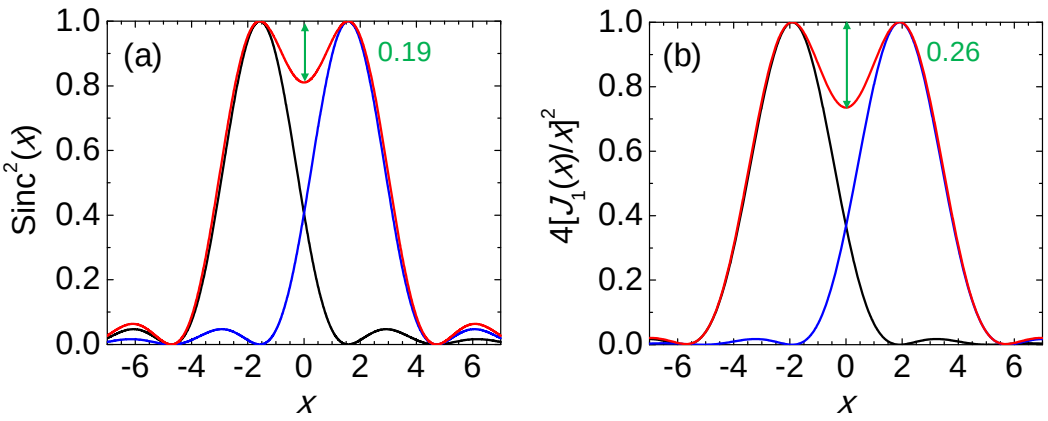

Figure 1.3: Rayleigh criterion for a (a) square and (b) circular aperture.

In order to satisfy the Rayleigh criterion, the distance between the two point sources should be equal to the radius of the Airy disk formed by an individual point source. Since the first zero of the $J_1(x)$ occurs at $x=1.22\pi$, the Rayleigh limit is calculated as:

$$\Delta_x = \frac{0.61\lambda_0}{\mathrm{NA}}. \tag{1.6}$$

In the context of spectroscopy, the Rayleigh criterion was generalized based on the ratio between the saddle irradiance and the maximum irradiance of either side [7]. Since for an irradiance pattern with sinc-like dependency, as shown in Fig. 1.3(a), the ratio between the saddle and the maximum of either side is 0.81, this number was generalized to other systems, such as Fabry-Perot interferometers, and stated that any two spectral lines are resolved if the ratio between the saddle and maximum is less than 0.81 [7]. However, the choice of this value is rather arbitrary [7]. Sparrow [4] has pointed out that the choice of this rather arbitrary value makes it subjective to compare the performance of two instruments and a fair comparison can be made only based on an "actual limit of resolution" [4, 7].

The Sparrow [4] resolution criterion states that two point sources, with equal intensities separated by a distance *d*, are just resolved if the second-order derivative of the composite irradiance distribution at the center just vanishes, i.e. $\frac{\partial^2 I}{\partial x^2} = 0$ at x=0. This condition was called "undulation condition" by Sparrow. In this case, the composite irradiance distribution shows no saddle at the middle because both central maxima, and the minimum in-between coincide [4]. The limit of resolution according to the Sparrow criterion is:

$$\Delta_x = \frac{0.473\lambda_0}{\mathrm{NA}}. \tag{1.7}$$

The Houston criterion states that two point sources with equal intensities are just resolved if the distance between the central maxima of the composite irradiance distribution is equal to the full-width at half maximum (FWHM) of the irradiance distribution of either point source [5]. The FWHM of the PSF for a circular aperture with diameter *D* is:

$$\Delta_x = \text{FWHM} = \frac{1.03\lambda f}{D} = \frac{0.515\lambda_0}{\text{NA}}. \quad (1.8)$$

Finally, it should be noted that if the PSF is exactly known, then a two-component model could be perfectly fitted to the data, regardless of the distance between the two point objects. In this case, there would be no limit to resolution. However, due to the presence of aberration or irregularity, precise knowledge of the PSF is not possible. In addition, the presence of measurement noise is also an issue. Therefore, the resolution fundamentally depends on the signal-to-noise ratio (SNR) [116].

1.2.2. Near-field Techniques

In near-field techniques, the role of evanescent waves which contain high spatial frequencies corresponding to sub-wavelength features of the sample is vital. In the near-field scanning optical microscopy (NSOM or SNOM) [38-40] technique, a near-field probe, which is usually a single mode optical fiber with a metal-coated tapered tip, is placed at a distance of a few nanometers from the sample and is raster-scanned across the sample area. Since the tip size of such a probe is much smaller than wavelength, only evanescent waves reach the tip. Due to the very short distance between the scanning tip and the sample, an accurate feedback system must be used to maintain the distance. Spatial resolution in NSOM is not limited by working wavelength and instead is limited by the size of the tip. Spatial resolution of the order of tens of nanometers can be achieved in SNOM using visible light. However, the throughput of NSOM (~10^{-6}-10^{-3}) [41] is significantly smaller than that of solid immersion techniques (~0.1-1) [27].

Another proposed technique for super-resolution imaging is based on using a material with a negative index of refraction. Metamaterials can be engineered to have negative refractive indices. Veselago [117], in his study of electrodynamics of materials

with simultaneously negative values of permittivity and permeability, showed that a planar lens with a negative refractive index can form an image. However, it was pointed out by Pendy [51] that such a material can cancel the decay of evanescent waves and can be used as a “perfect lens”. Such a “perfect lens” is “shortsighted” and fabrication of such a lens at visible regime involves engineering limitations and complexities. This limitation can be overcome in some metamaterial designs [52-55]; however, these structures have their own limitations; limited frequency ranges of operation, and absorption problems. All these structures are very challenging to fabricate.

1.2.3. Immersion Microscopy Techniques

For a dry microscope objective, i.e. working in air (n=1), the maximum achievable NA is limited by the maximum acceptance half-angle, $\theta_{max}=\pi/2$. This leads to a maximal theoretical NA=1 which in practice is typically limited by NA∼0.95. However, the NA can be increased by filling the object-space with a liquid, such as water or oil [18]. In this way, the resolution improvement depends of the refractive index of the immersion oil. In the liquid immersion microscopy technique, the objective lens is designed to work in a liquid environment. The refractive index of the imaging medium is also important in this technique to have a reasonable contrast with the refractive index of the immersion oil.

Implementation of a solid immersion lens (SIL) to improve spatial resolution of conventional microscopy was first reported in 1990 [19]. The similarity between the working principle of SIL microscopy and liquid immersion microscopy is that in the former the liquid is replaced by a hemispherical [19] or superspherical [20] solid dielectric with refractive index n, that is positioned directly on top of the object surface, as shown in Fig. 1.4. The high refractive index of the SIL shortens the effective

wavelength of the imaging illumination to λ_0/n, which improves the resolution. Furthermore, magnification and collection efficiency are improved by applying the SIL. The key distinction between the solid immersion and liquid immersion microscopy is that the former involves the near-field coupling. In order to achieve the coupling of near-field components of the scattered field into the SIL, the gap between the SIL and the object's surface should be smaller than the penetration depth of the evanescent field. This is achieved by pressing the SIL towards the object's surface or by filling the gap by using an index-matching liquid.

The SIL concept is related to a theory by Born and Wolf [1] which shows possession of two aplantic points (spherical aberration-free focal points) in a dielectric sphere [30]. Therefore, if a sphere placed on top of the sample surface is truncated by a plane parallel to the sample's surface and passes through either one of the aplantic points, a spherical aberration-free focused spot is achieved just on top of the sample. Based on this theory, morphologically, two types of conventional solid immersion lenses can be realized: i) hemispherical SIL (h-SIL) [19] and ii) super-spherical SIL (s-SIL) [20].

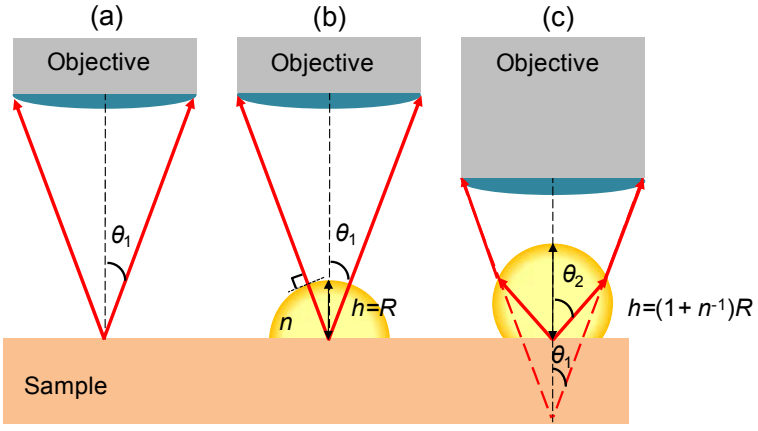

Figure 1.4: (a) An objective lens, (b) a hemispherical solid immersion lens (h-SIL), and (c) a super-spherical solid immersion lens (s-SIL).

An h-SIL [Fig. 1.4(b)] is a dielectric hemisphere [19], because one of the aplantic points is just at the center of the sphere. Magnification of an h-SIL, calculated by the geometrical optics formulae, is n.

An s-SIL [Fig. 1.4(c)], also known as Weierstrass SIL, is a truncated sphere with thickness $(1+1/n)R$, where R is the radius and n is the refractive index of the sphere [20]. This thickness is selected due to the fact that one of the aplantic points of the sphere is located at that distance from the vertex of the sphere. Magnification of an s-SIL, calculated by the geometrical optics assumptions, is n^2.

In 2010 [35], it was reported that a sub-hemispherical wavelength-scale SIL, illuminated with linearly polarized light focused by a high-NA objective lens, can focus light in its near field ~25% smaller than the FWHM of a conventional millimeter scale SIL (macro SIL) and hence improving the resolving power. The fact that the small wavelength-scale lenses or microlenses have better resolution than their enlarged counterparts plays an important, and not totally understood, role in different imaging and focusing techniques. We will address this property many times in different contexts in this dissertation.

1.2.4. Microsphere Nanoscope

Near-field microscopy using nanolenses [60], microdroplets [61], and especially, microspheres [62-64] emerged as a surprisingly simple way of achieving optical super-resolution. Recently, it was demonstrated [63] that silica spheres with a refractive index n~1.46 and with diameters in the range D~2-9 μm can convert high spatial frequencies of the evanescent field into propagating modes, that can be used for far field imaging of sub-diffraction-limited features by looking “through the microsphere” into a virtual

image produced by the microspheres below the surface of the structure, as illustrated in Fig. 1.5. This microsphere nanoscope system is capable of working in both reflection and transmission modes.

Super-resolution microscopy of different samples with sub-diffraction-limited features was achieved using silica microspheres in Ref. [63]. One particular sample was a commercial Blu-ray® disk (BD) which has 200-nm-wide stripes separated 100 nm apart. It was claimed that silica SILs failed to resolve 100 nm spaced line objects on the BD, as shown in Fig. 1.5(c) and 1.5(d), respectively, for 0.5 and 2.5 mm diameter h-SILs. Whereas, the D=4.74 μm microsphere was able to resolve 100 nm spaced line objects on the BD, as shown in Fig. 1.5(e). Similar results were reported for samples with feature sizes between 50 and 130 nm, and it was concluded that silica microspheres with $2<D<9$ μm overperform their h-SILs counterparts in terms of nanoimaging [63].

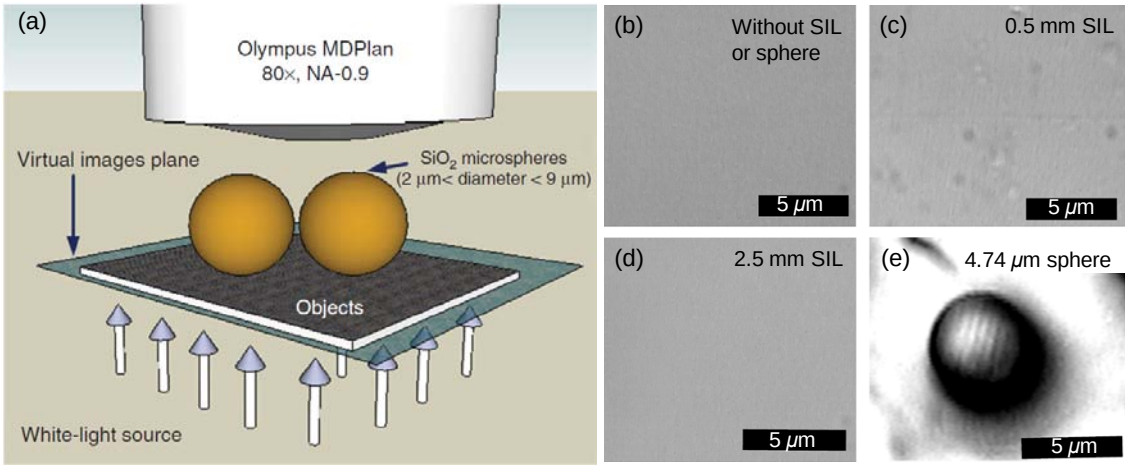

Figure 1.5: (a) Schematic of an optical nanoscope with microspheres placed on top of the sample. The spheres collect the near-field object information and form virtual images that are captured by the objective lens. (b) Optical microscopy of a Blu-ray® disk without SIL or sphere, (c) with a 0.5 mm SIL, (d) with a 2.5 mm SIL, and (e) with a 4.74 μm silica microsphere [63]. Reprinted with permission. © 2011 Macmillan Publishers Ltd: Nature Communications.

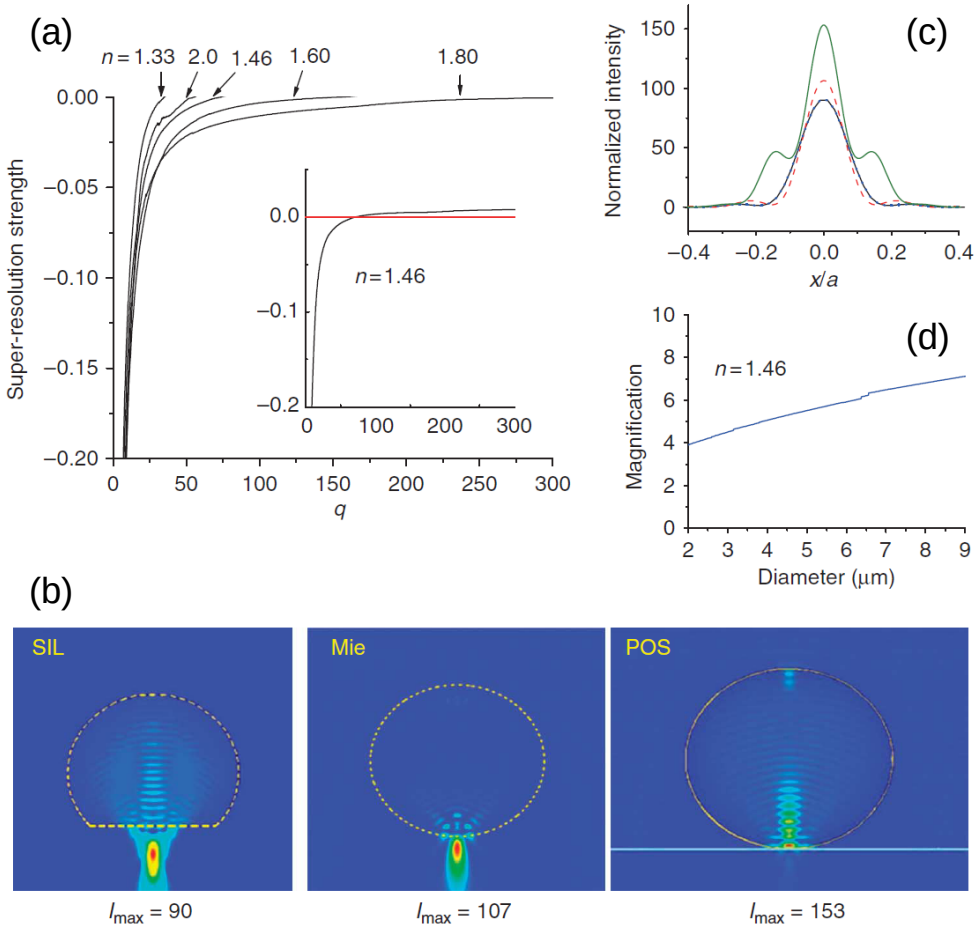

Figure 1.6: (a) Super-resolution strength vs. size parameter q. (b) Intensity distributions calculated for a freestanding s-SIL, a freestanding sphere, and a sphere on surface of a 40-nm-thick gold film (D=4.74 μm, n=1.46, and λ=600 nm). (c) FWHM of foci for s-SIL (blue), sphere (red), and sphere on substrate (green). (d) Virtual image magnification vs. sphere diameter D [63]. Reprinted with permission. © 2011 Macmillan Publishers Ltd: Nature Communications.

It was suggested that, on a fundamental level, a connection exists between the super-resolution imaging of micrometer-scale spheres and their ability to focus light down to sub-diffraction-limited dimensions [63]. Such tightly focused beams termed “photonic nanojets” are reviewed in more detail in Sections 1.3.2. Super-resolution strength of a micrometer-scale sphere was defined as: (focus spot size − Rayleigh limit) / (radius of the

sphere). As illustrated in Fig. 1.6(a), the calculations predicted maximal super-resolution strength for n=1.8. It has been argued that for n>1.8, the super-resolution strength should be reduced along a range of micrometer-scale sphere diameters where this effect can be expected [63]. It was shown by numerical modeling that the focus at the sphere-substrate contact region becomes sharper, as illustrated in Fig. 1.6 (b,c), and due to the optical reciprocity principle [118] the resolution can be improved.

Since a mathematical model for the near-field magnification has not yet been developed for the case of microspheres, it was proposed that the virtual image magnification (M) depends on the maximal field enhancement produced by the microspheres, similar to the geometrical optics case [63]. Virtual image magnifications calculated by geometrical optics approximations were fitted to a transcendental curve of the form $M \approx (I_{max}/I_0)^{\beta}$, where I_0 is the incident field upon the sphere and I_{max} is the maximum field enhancement produced by the sphere, already calculated in Ref. [119] as:

$$\frac{I_{max}}{I_0} = \frac{27n^4}{(4-n^2)^3}, \qquad n < \sqrt{2}. \tag{1.9}$$

$$\frac{I_{max}}{I_0} = \frac{27n^4}{(4-n^2)^3}\frac{n^2}{2n(n-\sqrt{2})+2}, \qquad n > \sqrt{2}. \tag{1.10}$$

It was found that β=0.34. Since the field enhancement effect increased for larger spheres, it was predicted that within the super-resolution window (size range where spheres with a given refractive index have super-resolution strength), magnification increases for larger spheres, as shown in Fig. 1.6(d) for microspheres with n=1.46 and 2<D<9 μm.

More recently, it has been shown that the super-resolution capability of this technique can be reinforced by semi-immersing the corresponding low-index

microspheres in a liquid micro-droplet, which produces a sharper contrast with a comparatively smaller magnification factor [64]. Although the imaging in the presence of the liquid is useful for biomedical applications, using semi-immersed spheres is technically complicated due to the dynamical droplet's evaporation process, which leads to gradually varying resolution and magnification of the optical setup. In some cases, this dynamical process can be used for quick evaluations of different structures and samples. However, many of the biomedical samples and cell cultures contain permanent fraction of water, and evaporation of water can be damaging for cells. In such cases, permanent presence of water is required. It has been argued, however, that the super-resolution effect cannot be expected [64] when the microsphere is absolutely submerged by the liquid layer.

1.3. Resonant and Non-resonant Optical Properties of Dielectric Spheres

In this section, we review the mechanisms of light interactions with microspheres. Microspheres can support internal resonances called whispering gallery modes (WGMs) [38]. One type of light interaction with microspheres involves excitation of WGMs, which can be achieved either evanescently or by using internal built-in sources of light [69]. Another type of interaction is based on refraction and reflection properties of microspheres, which does not require evanescent coupling and can be achieved by illuminating microspheres with plane waves from outside space. Plane wave illumination leads to a formation of tightly focused beams termed photonic nanojets (PNJs) [86].

1.3.1. Whispering Gallery Modes in Spherical Cavities

Electromagnetic waves can be strongly confined in cavities with circular symmetry, such as rings, cylinders, toroids, disks, and spheres, due to total internal reflection of light

[38, 68-71]. Such confined modes are called whispering gallery modes (WGMs) in analogy to acoustic whispering galleries. Due to minimal reflection losses, WGMs can reach very high quality (Q) factors. WGMs have many applications, such as biosensors [72-77] for single molecule or virus detection, or precisely size sorting [120, 121] of microspheres. In this work, WGMs in microspheres are considered.

Trapped waves inside a microsphere with radius R, propagate close to the surface of the sphere so that they traverse a distance of $\sim 2\pi R$ in a round trip. Under constructive interference condition, standing WGMs are formed in the cavity [122]. Constructive interference condition in a cavity with a circular symmetry can be approximated as $2\pi R \approx l(\lambda_0/n)$, where λ_0/n is the wavelength in the medium with refractive index n. This condition can be expressed in terms of the size parameter, $x = 2\pi R/\lambda_0 \approx l/n$.

The following approach for solving the electromagnetic field problem for a sphere with radius R and refractive index n was adopted from [70, 71]. Hansen's method [123] was used in which solutions of the vectorial Helmholtz equation have angular dependence described by the vectorial spherical harmonics [124], defined as:

$$\mathbf{X}_l^m = \boldsymbol{\nabla} Y_l^m \times \mathbf{r} / \sqrt{l(l+1)}, \tag{1.11}$$

$$\mathbf{Y}_l^m = r \boldsymbol{\nabla} Y_l^m / \sqrt{l(l+1)}, \tag{1.12}$$

$$\mathbf{Z}_l^m = Y_l^m \, \hat{\mathbf{r}}. \tag{1.13}$$

The angular mode number l indicates the order of the spherical harmonic Y_l^m that describes the angular field distribution. The index m is called the azimuthal mode number and can take $2l+1$ values from $-l$ to l.

The electromagnetic fields for both polarizations are represented by:

$$\mathbf{E}_{lm}^{\mathrm{TE}}(\mathbf{r}) = E_0 \frac{f_l(r)}{k_0 r}\mathbf{X}_l^m(\theta,\varphi), \tag{1.14}$$

$$\mathbf{B}_{lm}^{\mathrm{TE}}(\mathbf{r}) = \frac{E_0}{ic}\left(\frac{f_l'(r)}{k_0^2 r}\mathbf{Y}_l^m(\theta,\varphi) + \sqrt{l(l+1)}\frac{f_l(\mathbf{r})}{k_0^2 r^2}\mathbf{Z}_l^m(\theta,\varphi)\right), \tag{1.15}$$

$$\mathbf{E}_{lm}^{\mathrm{TM}}(\mathbf{r}) = \frac{E_0}{n^2}\left(\frac{f_l'(r)}{k_0^2 r}\mathbf{Y}_l^m(\theta,\varphi) + \sqrt{l(l+1)}\frac{f_l(\mathbf{r})}{k_0^2 r^2}\mathbf{Z}_l^m(\theta,\varphi)\right), \tag{1.16}$$

$$\mathbf{B}_{lm}^{\mathrm{TM}}(\mathbf{r}) = -\frac{iE_0}{c}\frac{f_l(r)}{k_0 r}\mathbf{X}_l^m(\theta,\varphi), \tag{1.17}$$

where

$$f_l(r) = \psi_l(nk_0 r) \qquad \text{for } r < R, \tag{1.18}$$

$$f_l(r) = \alpha\psi_l(k_0 r) + \beta\chi_l(k_0 r) \qquad \text{for } r > R \tag{1.19}$$

are solutions of Riccati-Bessel radial equation. $\psi_l(\rho) = \rho j_l(\rho)$ and $\chi_l(\rho) = \rho n_l(\rho)$, where j_l and n_l are spherical Bessel and Neumann functions, respectively.

Boundary condition for continuity of the tangential components of the fields was used to find the positions of resonances.

$$\psi_l(nk_0 R) = A\psi_l(k_0 R) + B\chi_l(k_0 R), \tag{1.20}$$

$$P\psi_l'(nk_0 R) = A\psi_l'(k_0 R) + B\chi_l'(k_0 R), \tag{1.21}$$

where $P=n$ for TE polarization, and $P=n^{-1}$ for TM polarization.

WGMs are modes of an open system in which a dissipation of energy occurs due to the leakage of the electromagnetic fields from the cavity. As an approximation it is assumed that the radiative part outside the sphere is negligible. So the resonance condition can be shown by the following characteristic equation, which determines the relation between wave number and radius of the sphere:

$$P\,\frac{J_{l+1/2}'(nk_0 R)}{J_{l+1/2}(nk_0 R)} = \frac{N_{l+1/2}'(k_0 R)}{N_{l+1/2}(k_0 R)}, \tag{1.22}$$

where J and N are Bessel and Neumann functions, respectively.

Various solutions of this equation determine an infinite set of wave vectors (eigenfrequencies) for a given *R*. In this case, introducing another index n_r (radial number) is necessary to indicate the correspondence between roots of Eq. (1.22) and eigenfrequencies. The characteristic equation is independent of the index *m*, which shows the degeneracy of these modes. Expanding Eq. (1.22) as an asymptotic series in powers of $\nu = (l + 1/2)^{-1/3}$ and Airy functions [66] gives:

$$nx_{l,n_r}^{P} = \nu + a_{1n_r}\nu^{1/3} + a_0\nu^0 + a_{-1n_r}\nu^{-1/3} + \cdots, \tag{1.23}$$

in which *x* is the size parameter and

$$a_{1n_r} = 2^{-1/3}\alpha_{n_r}, \tag{1.24}$$

$$a_0 = -\frac{P}{\sqrt{n^2-1}}, \tag{1.25}$$

$$a_{-1n_r} = \frac{3}{10}2^{-2/3}\alpha_{n_r}^2, \tag{1.26}$$

where α_{n_r} are roots of the Airy function *Ai*(-*z*) associated with the radial number n_r.

In summary, WGMs in microspheres are characterized [79, 80] by two polarizations (TE- and TM-modes) and three modal numbers: radial n_r, angular *l*, and azimuthal *m*.

i) The radial number, n_r, indicates the number of WGM intensity maxima along the radial direction.

ii) The angular number, *l*, represents the number of modal wavelengths that fit into the circumference of the equatorial plane of the sphere.

iii) The azimuthal number, *m*, for a freestanding sphere with a perfect shape is degenerate. The value for $l-m+1$ represents the number of WGM intensity maxima in the polar (perpendicular to the equatorial plane) direction.

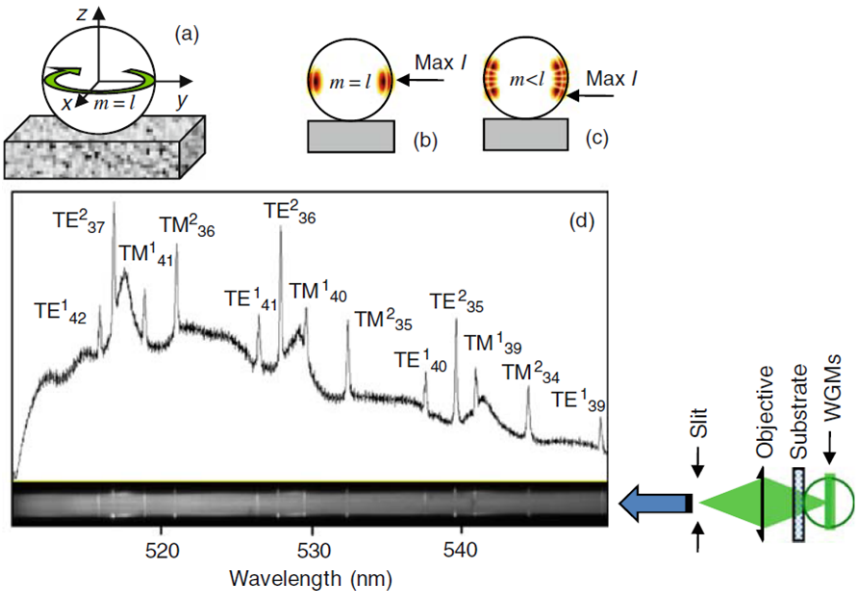

Figure 1.7: (a-c) Schematics of a single sphere on a substrate illustrating intensity maxima distributions for WGMs with different m. (d) Spectrum of a single green fluorescent sphere (D=5 μm) with TE_l^{nr} and TM_l^{nr} WGM peaks measured through a transparent substrate [69, 125]. Reprinted with permission. © 2009 SPIE.

In practice, the degeneracy of the azimuthal number, m, is removed by small deformations of the microspheres from the spherical shape [69] or by any perturbation at the surface of the sphere. A sphere on the substrate is rotationally invariant around the z-axis normal to the surface (playing the part of the polar axis), as shown in Fig. 1.7(a). The fundamental WGMs with $m=l$ are defined [69] in the equatorial plane of the sphere, parallel to the substrate. Such fundamental modes have the highest Q-factors, due to the fact they are separated from the substrate by the radius of the sphere. In contrast, the modes with $m<<l$ are damped, due to the fact that they have a spatial distribution with the maximum intensity approaching the substrate with a high refractive index, as illustrated in Figs. 1.7(b) and 1.7(c) for WGMs with n_r=2. A typical fluorescence spectrum of a single dye-doped D=5 μm polystyrene (n=1.59) sphere on a glass substrate

[125] is presented in Fig. 1.7(d). The WGM peaks with orthogonal polarizations are labeled $\mathrm{TE}_l^{n_r}$ and $\mathrm{TM}_l^{n_r}$, respectively.

The shape deformation, which breaks the symmetry around the z-axis, is very important factor since all spheres have a random distribution of this ellipticity on the level of at least 1%, in the same way as they have size disorder. WGM splitting caused by such ellipticity leads to the appearance of quasi-equidistant closely spaced peaks [67, 84] is very significant in a sense that it is comparable with the linewidths of individual modes depending on the sphere's size. This means that this ellipticity is likely to determine the real emission and coupling linewidths of WGMs.

The role of surface perturbation can be represented by a contact point with the substrate or contact with another sphere(s). A particle deposited on the surface of the sphere can also be considered as a surface perturbation. The strength of perturbation determines the amount of splitting between WGMs with different m numbers [69].

The shape deformation of a sphere can mix the modes with different m, giving rise to a broadening of all modes, due to tunneling to the substrate. These effects are likely responsible for the WGM linewidth broadening, observed in the experimental spectra of microspheres [69].

There are two ways of excitation of WGMs. WGMs can be "forced" due to evanescent coupling with tapered fibers [81] or stripe waveguides [126]. In this case, only few WGMs with different m numbers are excited because of their different overlap with the modes propagating in tapered fibers or stripe waveguides. Alternatively, WGMs can be excited using fluorescent properties of built-in light sources, such as dye-doped molecules. In this case, WGMs settle themselves depending on their life time, Q-factors,

and other conditions. For example, a sphere on a substrate have a fundamental mode in the equatorial plane parallel to the substrate.

1.3.2. Photonic Nanojets and Nanojet Induced Modes

In the previous section, we considered resonant properties of dielectric spheres. Non-resonant optical properties of dielectric spheres are not related to the coupling with WGMs. Microspheres can be used to focus light with a broad range of wavelengths. The focusing effects in sufficiently large ($r>>\lambda$) spheres follow the laws of geometrical optics [127]. Paraxial geometrical optics assumptions lead to the following relation for the back focal length (b.f.l.) of a sphere with radius R and refractive index n (Appendix D):

$$\text{b. f. l.} = \frac{R(2-n)}{2(n-1)}. \tag{1.27}$$

According to Eq. (1.27), based on paraxial geometrical optics approximations, collimated incident rays are focused inside or outside the sphere, if the refractive index of the sphere is greater or smaller than 2, respectively. For the case of n=2, the focal point is just at the shadow-side surface of the sphere, which is consistent with several studies on optical caustics [128-130].

By considering wave optics assumption, for an aberration-free converging thin lens with circular face (bi-convex or plano-convex), the incident plane wave is focused on the far-field with an Airy pattern irradiance distribution, with the FWHM~λ/2 according to Eq. (1.8). If we consider a dielectric sphere as a bi-convex converging lens, a focused spot size in excess of the diffraction limit is expected due to the presence of spherical aberration. However, it has been shown [85-87] that when the beam is focused just on or close to the shadow-side surface of the sphere, an interesting phenomenon occurs due to the near-field interactions of the sphere's boundary and the focused beam. In this case, a

highly localized electromagnetic beam at the shadow-side surface of the sphere is created, which is termed “photonic nanojet” (PNJ) or “photonic jet” (PJ) [85-87] (because its appearance is analogous to high-speed gradient that is characteristic of a jet in fluid mechanics). Photonic nanojets are defined as narrow intense electromagnetic beams propagating into the background medium from the shadow-side surface of a plane-wave illuminated lossless dielectric microcylinder [85] or microsphere [86] of diameter greater than the illuminating wavelength. The physical mechanism of the nanojet light confinement effect is a complicated scattering and interference problem. The interferences between the incident field and the scattered field by the microsphere lead to such a confinement [92, 106]. It was shown [107] that microspheres can have high NA and negligible small spherical aberration due to the compensation of the positive spherical aberration caused by the spherical surface, and the negative spherical aberration caused by the focal shift effects [131-133].

It was known that the electromagnetic field distributions inside and near the shadow-side surface of a plane wave-illuminated infinite dielectric cylinder have intense peaks along the incident axis, even for non-resonant conditions [134, 135]. However, by using finite-difference time-domain (FDTD) numerical solutions of Maxwell’s equations, the formation of localized intense nanoscale “photonic jets” in the vicinity of the shadow-side surface of plane wave-illuminated dielectric microcylinders was shown [85]. It was shown that such photonic nanojets have sub-diffraction limit lateral sizes and propagate over several wavelengths without significant divergence. The location and the intensity of photonic nanojets depended on the refractive index contrast between the particle and its surrounding medium, diameter of the particle (D), and the incident wavelength (λ).

Figs. 1.8(a-c) shows the computational results for a cylinder with D=5 μm and refractive index of n_1, surrounded by a medium with n_2=1, illuminated by a plane wave with λ_2=500 nm [85]. By decreasing the refractive index from n_1=3.5 to n_1=2.5, the internal field peak moved toward the shadow-side surface of the cylinder and emerged from the shadow-side surface of the cylinder for n_1=1.7 as a strong jet-like distribution with ~900 nm (1.8λ_2) length and ~200 nm (0.4λ_2) intensity FWHM, as illustrated in Fig. 1.8(c) [85].

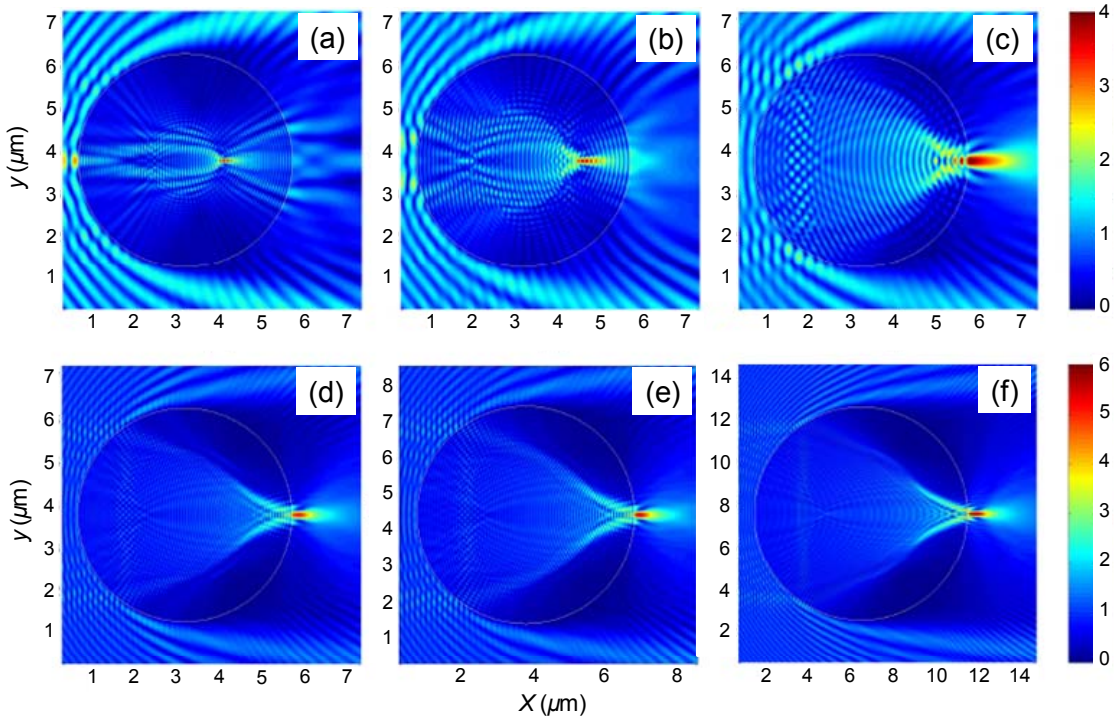

Figure 1.8: (a-c) Evolution of a photonic nanojet as the refractive index of the cylinder (D=5 μm) decreases. Refractive index of the background medium is n_2=1. Plane wave with λ_2=500 nm, propagating from left to right, impinges on the cylinder with refractive index of (a) n_1=3.5, (b) n_1=2.5, and (c) n_1=1.7. (d-f) Formation of photonic nanojets for different combinations of D, n_1, n_2, and λ_2. (d) D=5 μm, n_1=3.5, n_2=2.0, λ_2=250 nm, (e) D=6 μm, n_1=2.3275, n_2=1.33, λ_2=300 nm, and (f) D=10 μm, n_1= 2.3275, n_2=1.33, λ_2=300 nm [85]. Reprinted with permission.

It was shown [85] that photonic nanojets are generated for different combinations of D, n_1, n_2, and λ_2, provided that n_1/n_2 and D/λ_2 not significantly changes from the case of Fig. 1.8(c). The FWHMs of the intensity distributions in Figs. 1.8(d-f) are 120, 130, and 140 nm, respectively, which are smaller than half of the illumination wavelength.

The possibility of light focusing with sub-diffraction sizes by microspheres was mentioned in Ref. [62], without presenting explicit calculation detail about the focused beams' sizes. Formation of photonic nanojets in microspheres was studied in Ref. [86], based on rigorous separation-of-variables eigenfunction solution of Maxwell's equations in spherical coordinates. The incident plane wave of unity amplitude was expanded in spherical harmonics as [136]:

$$\mathbf{E}_i(\mathbf{r}) = \sum_{p=1}^{\infty} i^p\{(2p+1)/[p(p+1)]\}[\mathbf{M}_{o1p}^{(1)}(\mathbf{r}) - i\mathbf{N}_{e1p}^{(1)}(\mathbf{r})]. \quad (1.28)$$

The expansion of the scattered field was given by [136]:

$$\mathbf{E}_s(\mathbf{r}) = \sum_{p=1}^{\infty} i^p\{(2p+1)/[p(p+1)]\}[ia_p\mathbf{N}_{e1p}^{(3)}(\mathbf{r}) - b_p\mathbf{M}_{o1p}^{(3)}(\mathbf{r})], \quad (1.29)$$

where **M** and **N** are the vector spherical harmonics, with their superscript denotes the kind of the spherical Bessel function, a_p and b_p are the scattering Mie coefficients, and i= $\sqrt{-1}$.

The total external electric field induced by the plane wave was given by:

$$\mathbf{E}_i(\mathbf{r}) + \mathbf{E}_s(\mathbf{r}). \quad (1.30)$$

The coefficients a_p and b_p were calculated by an algorithm described in [137]. The computation results [Figs. 1.9(a-d)], showed nanojet formation at the shadow-side surface of a microsphere with n=1.59 and different diameters, illuminated by an x-polarized, z-propagating plane wave with λ=400 nm [86]. By increasing the sphere diameter, the nanojet moved away from the sphere, and its maximum intensity and FWHM increased.

It was shown that plane wave-illuminated dielectric microspheres create 3-D photonic nanojets with higher intensity compared with the intensity of 2-D nanojets formed by dielectric microcylinders.

Ref. [92] studied the spatial and spectral properties of 3-D nanojets by using rigorous Lorentz-Mie theory. The contribution of each spectral component to the nanojet was quantitatively studied, and it was found that such nanojets posses both evanescent and propagating components. It was found that the evanescent field components enhance and sharpen the nanojet field distribution. For example, when the evanescent field was removed from the nanojet formed by a D=2 μm sphere, the maximum field enhancement dropped by a factor of two, and the width of the nanojet increased by 10% [92].

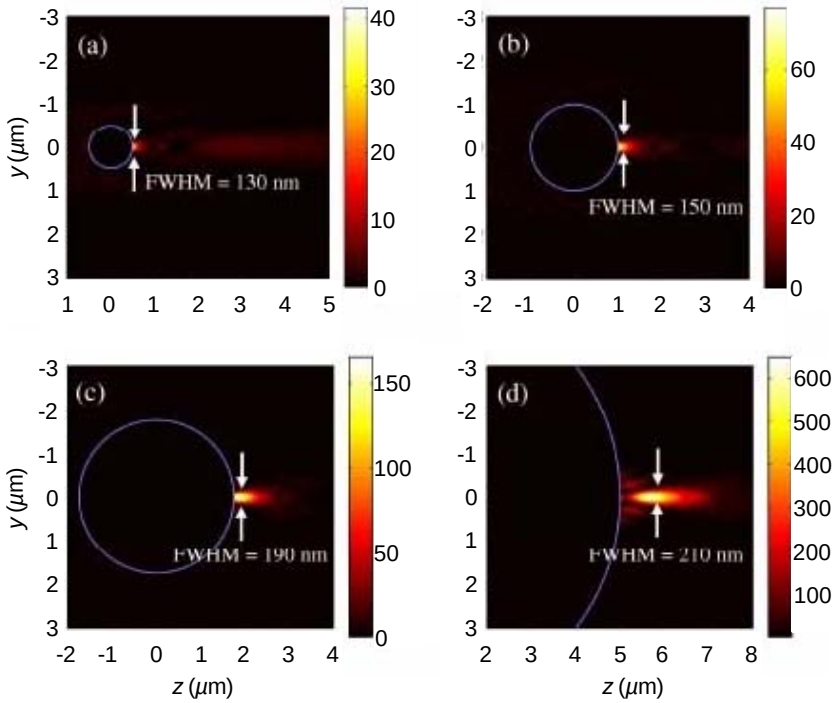

Figure 1.9: Photonic nanojets formed by a plane wave-illuminated (λ=400 nm) dielectric sphere (n=1.59) with diameter of (a) 1 μm, (b) 2 μm, (c) 3.5 μm, and (d) 8 μm [86]. Reprinted with permission. © 2005 Optical Society of America.

If a tightly focused (NA>0.8) Gaussian beam incident on a microsphere is considered, instead of a plane wave incident, a photonic nanojet with 3-D subwavelength dimensions with an effective volume of $0.6(\lambda/n)^3$ is formed [93]. The interferences between the scattered field by the microsphere and the incident Gaussian field with high angular components lead to such a confinement [93].

Quantitative parameters of a photonic nanojet are: FWHM, peak intensity, length, and radial shift, as schematically illustrated in Fig. 1.10 [89].

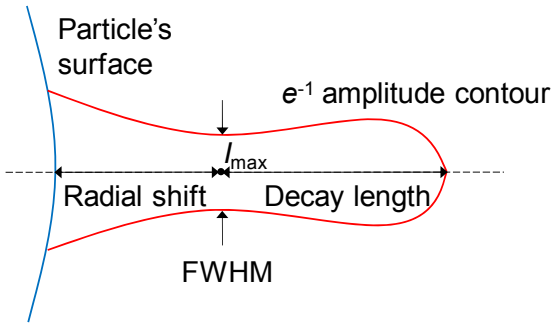

Figure 1.10: Schema of a photonic nanojet [89].

Specific properties of photonic nanojets are:

1) Narrow: The FWHM can be smaller than the diffraction limit [62, 85, 86].
2) Intense: Intensity can be enhanced up to 1000 times of the incident intensity [86, 87].
3) Elongated shape: A nanojet has a low divergence for few wavelength (~3λ) and can be engineered to have low divergence for more than 20λ [94, 95].
4) Non-resonant phenomenon: A nanojet can be created with small ($D\approx 2\lambda$, $n\sim 1.6$) and also with large ($D>40\lambda$, $n=2$) spheres [87, 88].
5) Possession of both propagating and evanescent components [92].

Tunable parameters for tailoring nanojets are:

1) Refractive index of the particle [85, 86] and refractive index distribution in the particle [94-96, 103].
2) Refractive index of the surrounding medium [85, 86].
3) Size of the particle [85, 86].
4) Wavelength of the illuminated light [85, 86].

   When the plane wave's wavelength matches the resonant wavelength of the sphere, nanojets formed at the shadow-side surface of the sphere become more intense and also narrower, compared with the case of off-resonant illumination. Narrowing effect, which can be a two-fold reduction of the FWHM of the nanojet, is due to the leakage of the whispering gallery modes from the sphere, which is more pronounce at the proximity of the surface due to its evanescent nature [138].
5) State of polarization of the incident light [99, 101].

   It is known that the irradiance distribution at the focal plane of a high NA lens, illuminated by a plane wave, is asymmetric due to polarization, i.e. the tightly focused beam is narrower in a direction perpendicular to the polarization [112]. This is also true for nanojets, when the sphere is incident by a linearly polarized plane wave [88]. The effect of incident polarization on the shape of nanojets was studied in Ref. [101] and it was shown that the irradiance profiles for linear and circular polarization incident beams are very similar with effective volume $\sim 8(\lambda/n)^3$. Whereas, an incident beam with azimuthal polarization creates a

doughnut beam, and incident beam with radial polarization forms a symmetric nanojet with effective volume ~$0.7(\lambda/n)^3$ [101].

6) Illumination condition, such as intensity [93] or phase [99] distribution of the incident light.

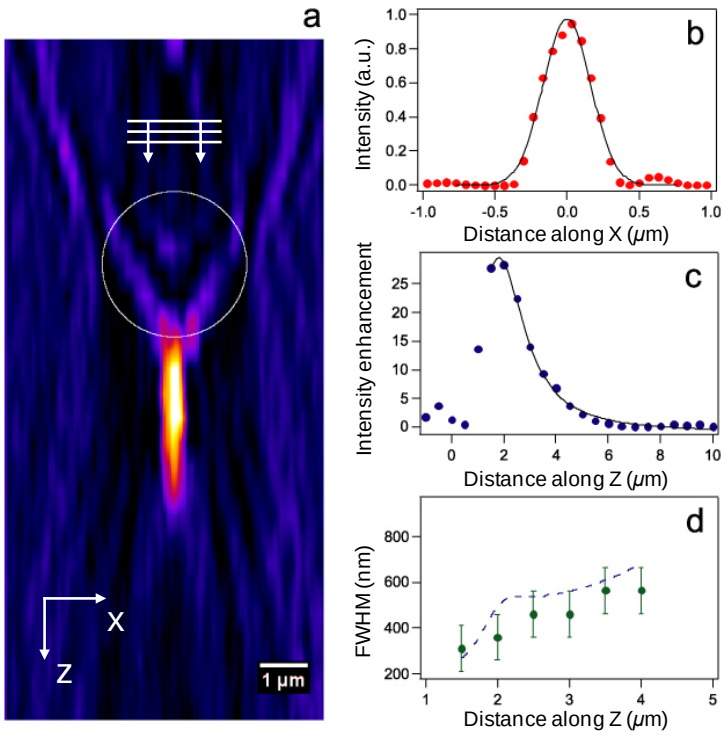

Figure 1.11: (a) Reconstruction of a photonic nanojet generated by a 3 μm latex microsphere (white circle). (b) Intensity profile along x-axis at the best focus point. Red dots are measured data, solid line is a Gaussian fit. (c) Intensity enhancement along z-axis at the center of the nanojet. Blue dots are measured data, solid line is a Lorentzian fit. (d) Measured FWHM of the nanojet (green dots). The dashed shows simulation results [91]. Reprinted with permission. © 2008 Optical Society of America.

Experimental observation of photonic nanojets formed by single latex (n=1.6) microspheres with D=1-5 μm illuminated by a plane wave (λ=520 nm) was reported in Ref. [91]. The imaging technique was based on fast scanning confocal microscopy in

detection mode. A diffraction-limited observation volume, scanned in three dimensions over the microsphere vicinity, was defined by the detection pinhole. 3-D nanojets were reconstructed from the collected stack of images, and nanojets with FWHMs of 300, 270, and 320 nm were observed for 1, 3, and 5 μm spheres, respectively. Fig. 1.11 illustrates the observation of a nanojet created by a 3 μm sphere with FWHM of 270 nm and beam propagation distance with subwavelength FWHM of more than 3λ.

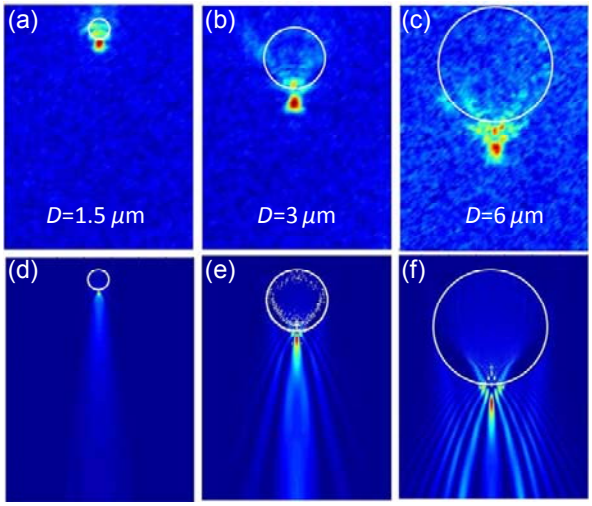

Figure 1.12: (a-c) Scattering distribution from microdisks in water (λ_{eff}=633/1.33=475 nm and refractive index contrast=1.5). (d-f) The calculated normalized intensity plots for a disk with diameter of (d) 1.5 μm, (e) 3 μm, and (f) 6 μm on a normalized linear scale [102]. Reprinted with permission. © 2012 Optical Society of America.

Experimental observation of nanojet formations from microdisks was reported in [102]. Nanojets were observed when Si_3N_4 microdisks with diameters 1-10 μm (400 nm height) were illuminated from the side. Scattered light from the disk-substrate system was observed by imaging from above, and subwavelength focusing was observed when the disks were in air. In water, the refractive index contrast was such that the nanojets were

formed (Fig. 1.12). The angular distribution of the intensity was in agreement with the analytical calculations for the case of an infinite cylinder [102]. It was also found that when the disks are illuminated with a focused Gaussian beam perpendicular to the substrate, extremely low divergence beams are formed (divergence angle ~10 times smaller than a focused Gaussian beam in free space with the same waist) [102].

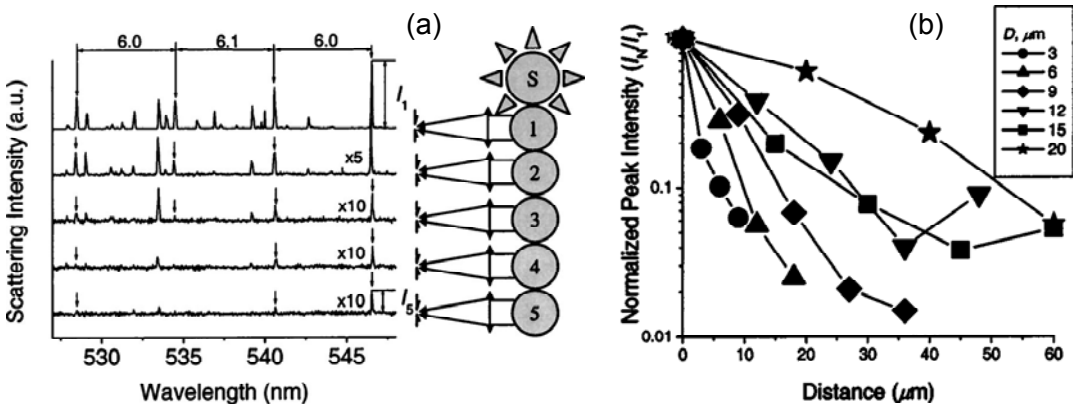

Figure 1.13: (a) Scattering spectra measured from a chain of D=9 μm polystyrene spheres coupled with a 10 μm dye-doped fluorescent sphere (S). The peaks originate from coupling of WGMs resonances of the S-sphere to other spheres. (b) Normalized scattering intensity peaks produced by different spheres along the chain as a function of the distance between the centers of the spheres [139]. Reprinted with permission. © 2004 American Institute of Physics.

Ref. [139] is one of the first experimental studies of optical coupling and transport phenomena in chains of dielectric microspheres using spatially resolved scattering spectroscopy. Linear chains of touching polystyrene (n=1.59) microspheres with mean diameters between 3-20 μm and size dispersion of ~1% were assembled by micromanipulation of dried microspheres on a flat substrate using a tapered optical fiber probe. Dye-doped spheres with fluorescence peaks due to whispering gallery modes

(WGMs) were attached to one end of the chains to couple light into the chains, as illustrated in Fig. 1.13(a). A pulsed source with high peak intensity was used to excite WGM lasing in the dye-doped source spheres. Since the spectrum of the excited fluorescent dye-doped spheres has strong lasing peaks at wavelengths corresponding to WGMs of the spheres, and has almost no emission intensity at other wavelengths, the coupling of the fluorescence emission into the chains was likely to be provided evanescently in this work. Due to evanescently coupling of the spheres, nanojet coupling was not expected in this work [139]. Lately, a different way of coupling light into the sphere-chains was realized by introducing a gap between the dye-doped source sphere and the first sphere in the chain in Ref. [110]. The experimental data showed attenuation of ~3-4 dB/Sphere for the modes with the best transport properties [Fig. 1.13(b)] [139]. Based on the evanescent mechanism of coupling light from the source sphere [139], the optical transport properties were interpreted in terms of coupling between WGM resonances with random detuning. In this case, the chain can be seen as a giant photonic molecule where individual resonators are detuned, and, as a result, are weakly coupled. The efficiency of coupling between size-mismatched microspheres with detuned WGM eigenstates was studied by numerical modeling and shown to be sufficiently high [140].

Ref. [108] studied optical coupling and transport phenomena in chains of dielectric microspheres using numerical calculations based on the generalized multiparticle Mie (GMM) theory. Light was coupled into the chains by plane waves launched from free space. It was shown that the nature of the electromagnetic field outside the microsphere is strongly dependent on its refractive index [108]. For example, for a plane wave-illuminated (λ=400 nm) sphere with D=3 μm and n=1.59, the focused beam possesses

not only evanescent fields, but also radiative-mode components [Fig. 1.14(a)]. In contrast, for n=1.8, the optical power within such a microsphere is totally internally reflected, and can tunnel out of the sphere through evanescent coupling [Fig. 1.14(b)]. Therefore, two distinct coupling mechanisms of optical transport in terms of the coupling efficiency between neighboring microspheres were identified:

i) Nanojet coupling (nonresonant micro-lensing), Figs. 1.14(c) and 1.14(e).

ii) Evanescent coupling (resonant WGM-based), Figs. 1.14(d) and 1.14(f).

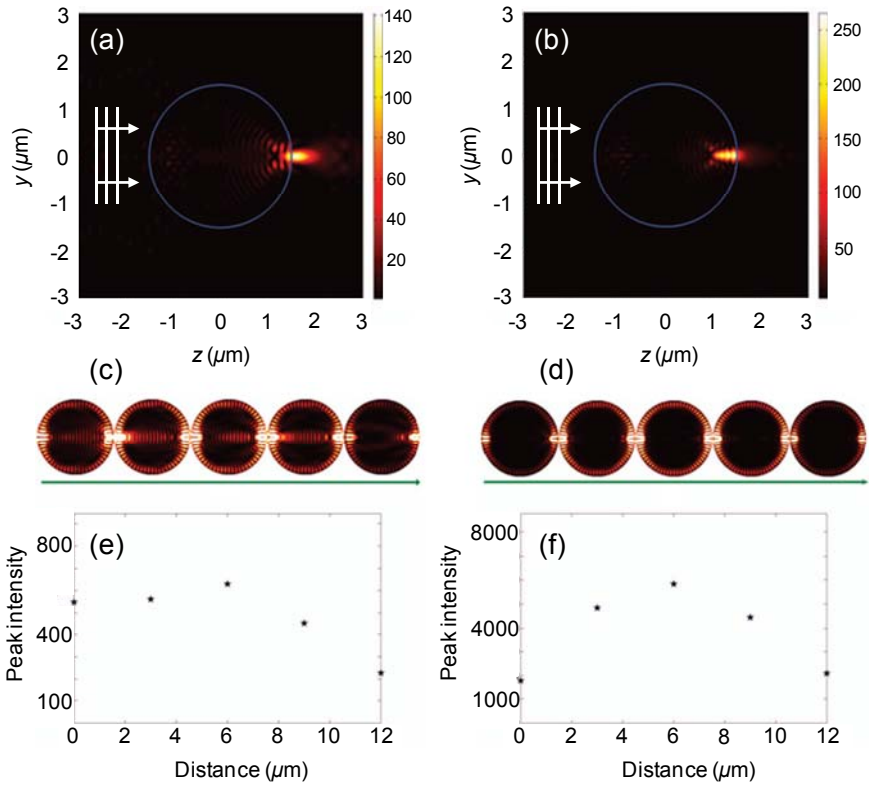

Figure 1.14: A PNJ formed at the shadow-side surface (circle) of a plane wave-illuminated (λ=400 nm) dielectric sphere (D=3 μm) with (a) n=1.59 and (b) n=1.8. Electric field intensity distributions of a chain of five spheres with (c) n=1.59 at λ=429.069 nm and (d) n=1.8 at λ=430.889 nm. (e,f) Peak intensity of each constituent sphere as a function of the distance between their centers corresponding to (c) and (d), respectively [108]. Reprinted with permission. © 2006 Optical Society of America.

Efficient WGM propagation through a chain of evanescently coupled microspheres can be achieved under resonant conditions using identical cavities [108]. However, optical coupling and transport through nanojet-inducing sphere-chains are less efficient due to the scattering losses caused by the radiative nature of photonic nanojets [108].

Ref. [109], experimentally, investigated the nanojet coupling and their attenuation properties in linear chains of touching polystyrene microspheres with diameters in the 2-10 μm range. Nanojet-coupling in such chains, leading to formation of nanojet-induced modes (NIMs), was observed. Locally excited sources of light, formed by several dye-doped fluorescent microspheres from the same chain of cavities, were used to couple light into NIMs, as shown in Figs. 1.15(a,b). The intensity of the CW photoexcitation was much smaller in this work, compared with the earlier work [139], indicating that the spheres were pumped well below the WGM lasing threshold. Under these conditions, most of the power of the source sphere was emitted into propagating modes. Although such a multimodal light source is far from the case of plane waves considered in [108], it still has some similarity with this case.

The formation and propagation of nanojet-induced modes were observed by means of scattering imaging technique. Fig. 1.15(b) shows efficient focusing in tiny volumes close to the touching points of adjacent spheres [109]. The light propagation along the chain was accompanied with a gradual narrowing of the focused spots [Figs. 1.15(b,c)]. Later, we termed the phenomenon of gradual decrease in sizes of the focused spots along the chain “beam tapering” effect. The so-called “beam tapering” effect was most pronounced in the first decade of spheres close to the source, where mode conversion into nanojet-induced modes, with corresponding mode conversion losses, occurs. Beyond the

first decade of spheres, the transverse sizes of these bright spots were saturated at the level of ~0.7 μm [Fig. 1.15(c)], which manifests the resolution limit of the imaging setup. This size represents only an upper limit for the spot sizes achieved in this work. In principle, focusing of plane waves by mesoscale spheres (n~1.6) can produce photonic nanojets with sizes smaller than the diffraction limit, as was stated earlier.

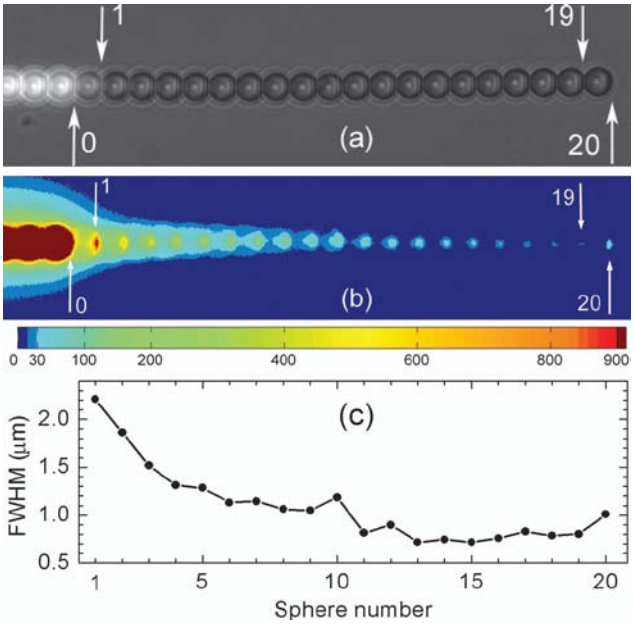

Figure 1.15: (a) A chain of polystyrene spheres (D=2.9 μm) coupled with fluorescent spheres as local light sources. (b) Scattering imaging shows the "beam tapering" effect manifested by progressive reduction in the focused spot sizes. (c) Cross-sectional FWHM of the spots [109]. Reprinted with permission. © 2007 Optical Society of America.

The following semi-empirical double-exponent fitting function was used to fit the experimental data:

$$I = I_1 10^{-0.1\beta_1 N} + I_2 10^{-0.1\beta_2 N}, \tag{1.31}$$

where I_1 and I_2 are intensities of two exponential components, β_1 and β_2 are their attenuation levels per individual sphere (in dB), and N is the propagation distance

expressed in number of spheres. The first and second exponents were associated with mode conversion losses occurring in the first several spheres, and propagation losses for nanojet-induced modes at longer distances from the source, respectively. It was found that for all studied chains, the strong initial light loss in the vicinity of the fluorescent source is characterized by the attenuation parameter β_1 which is of the order of several dB per sphere. Further propagation of the nanojet-induced modes was found to occur with significantly lower attenuation, $\beta_2 \leq 1$ dB per sphere. It was shown that the smaller the spheres the smaller the β_1 and β_2. For example, the nanojet-induced mode propagation loss of ~0.48 dB per sphere was measured for a chain of 1.9 μm spheres, which was also influenced by structural imperfections, such as slight deviations from the axial alignment of cavities. The reduction in attenuation in smaller spheres was explained by the increasing focusing strength in wave-length scale ($D \sim \lambda$) spheres compared with larger spheres. In the limit of geometrical optics ($D >> \lambda$), a sphere with $n=2$ provides a focused spot at the shadow-side surface of a sphere, while it has been demonstrated [86] that with a decrease of the diameter to a few λ, the required value of the refractive index drops to ~1.6, which is very close to the refractive index of polystyrene. Further work is necessary to reveal the intrinsic radiation loss of nanojet induced modes. The physical mechanism of the “beam tapering” effect remained unexplained.

Ref. [141] studied optical properties of colloidal waveguides fabricated by convective assisted capillary force assembly technique. Light transport in chains of 1 μm diameter polystyrene spheres was studied, and it was reported that no WGMs were detected in the transmitted light through such chains due to the small size of the particles and the damping into the surrounding medium. The attenuation of the nanojet induced

mode propagation was measured and compared to previous works. The results (Fig. 1.16) followed the same trend as previous results, especially in agreement with the observation in [109] that the smaller the spheres the smaller the attenuation per sphere.

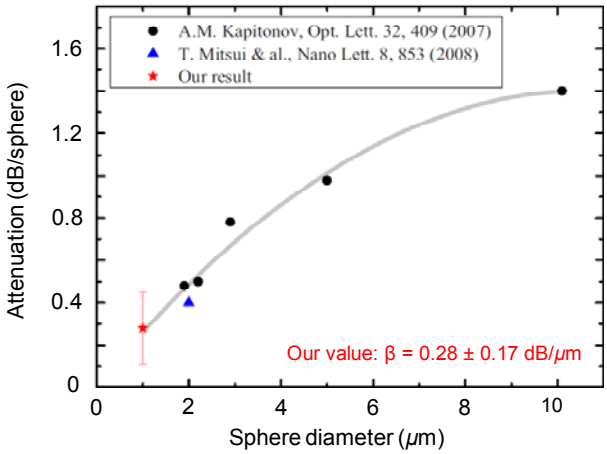

Figure 1.16: Evolution of attenuation in microsphere-chains as a function of the diameter [141]. Reprinted with permission. © 2010 American Vacuum Society.

Formation of "microjoints" (Fig. 1.17) with diameters ~300 nm between touching polystyrene microspheres in chains of self-assembled spheres (D=2 μm) was observed in Ref. [142]. This finding is important because the microjoint formation property is a general material property of polystyrene microspheres, and the influence of microjoints can be present in all studies of the optical transport properties of such chains performed by different groups [109, 110, 141]. Borosilicate glass microspheres, under the same assembly process, do not form such microjoints [Fig. 1.17(b)] due to the differences in chemical properties of glass and polystyrene. The microjoint formation mechanism was later described in Ref. [143]. The hydrophilic initiator residues at the terminals of polystyrene microspheres are exposed to water phase. As a result, the surface layer of the

microspheres is strongly hydrated and slightly swollen. When two microspheres are close enough, the neighbors have a large contact area due to surface tension. During the drying process, polystyrene spheres shrink slightly and the contact area is left as a microjoint [Figs. 1.17(c-f)].

The influence of micro-joints with diameters between 0-0.6 μm, formed between adjacent microspheres, on the optical transport properties in linear chains, composed of seven touching polystyrene microspheres (D=2 μm, λ=505.248 nm) was studied by FDTD simulations (FDTD Solutions System, Lumerical Solutions, Inc.) in Ref. [143]. The nanojet-induced mode coupling is increased due to micro-joints, while the WGM coupling is not influenced by the micro-joints, which suggests that NIM coupling can be controlled by changing the diameter of the micro-joint [143].

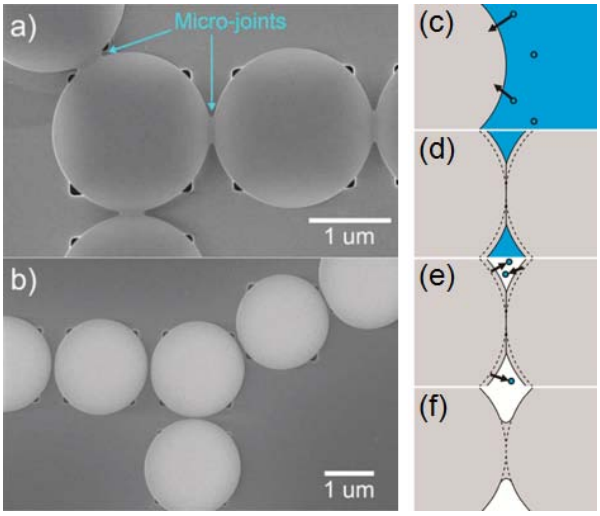

Figure 1.17: SEM image of (a) polystyrene spheres showing microjoints and (b) Borosilicate glass spheres where no micro-joints were found [142]. Reprinted with permission. © 2010 WILEY-VCH Verlag GmbH & Co. (c-f) Microjoint formation mechanism: (c) Water molecules are preserved at the vicinity of the surface. (d) Spheres are slightly swollen. (e) Dehydration by dewetting process. (f) Microspheres shrink slightly and the contact region is left as a microjoint [143]. Reprinted with permission. © 2011 Optical Society of America.

In Ref. [110], light propagation in straight chains of touching 5 μm polystyrene microspheres was studied by using spatially resolved spectroscopy. For non-collimated incident beams [Fig. 1.18, Case (i)] the maximum losses ~2-3 dB per sphere occured in the first few spheres, as shown in Fig. 1.18(c). Further along the chain, the losses became progressively smaller. Particularly, Fabry-Pérot fringes with propagation losses of ~0.08 dB per sphere in the maxima of transmission peaks were observed in long (>20 spheres) chains. For the case of quasi-plane wave incident [Fig. 1.18, Case (ii)], the periodical focusing of light in such chains was characterized with the periodicity of the nanojets corresponding to the size of two spheres (2*D*). It was concluded that nanojet-induced modes are the most favored propagating modes, which survive in long straight chains of coupled microspheres with disorder. The physical mechanism of the extraordinarily small attenuations of light observed in such long chains remained unexplained.

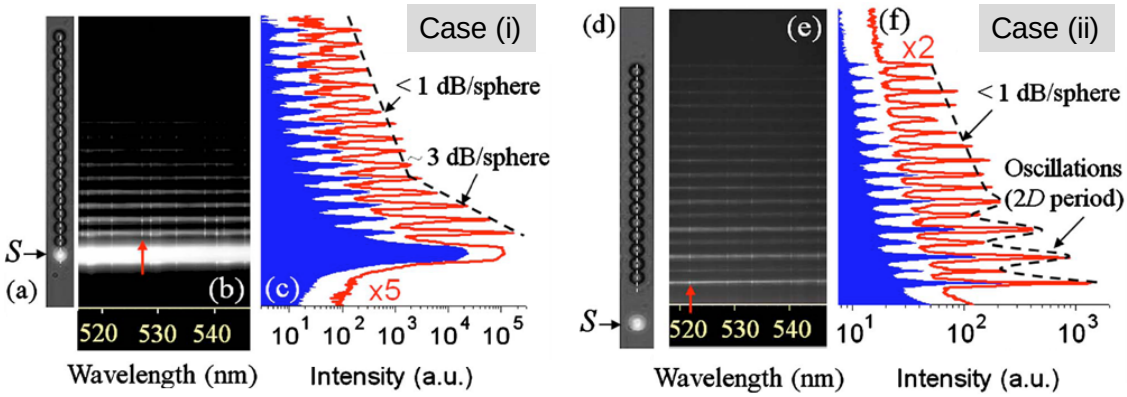

Figure 1.18: (a) Image of a chain of D=5 μm polystyrene spheres in contact with the dye-doped S-sphere. (b) Scattering spectral image at the central section in the spheres equatorial plane. (c) Intensity distribution measured at 527.3 nm TE_{41}^{1} WGM peak (red) and away from the WGM peaks at 525.0 nm (blue). The dashed lines are guides for eye. (d-f) Similar plots for the case of S-sphere located at a distance of 12 μm from the chain [110]. Reprinted with permission. © 2008 American Institute of Physics.

Nanojets and nanojet-induced modes have found several applications in various disciplines, such as nanoparticle detection and size sorting [90, 138, 144, 145], high-density optical data-storage disks [146-148], enhanced Raman scattering [149, 150], enhanced optical absorption in photovoltaics [151], nanostructuring and dry laser cleaning [152-160], nanoparticle trapping [161], optical nanoantenna [162], fluorescence correlation spectroscopy (FCS) [163-168], and Optical waveguides and focusing microprobes [109, 110, 141-143]. In the rest of this sub-section we describe application of nanojet-induced modes in the design of optical waveguiding and focusing microprobes. In Appendix B, a brief review of other applications of nanojets is given.

Optical waveguiding effects in photonic microstructures are achieved using different mechanisms, such as total internal reflection in layered structures [38], photonic bandgaps in photonic crystals [169], and weak coupling between high-quality (Q) cavities in coupled resonator optical waveguides (CROWs) [170].

As mentioned before, two distinct coupling mechanisms of optical transport have been identified in chains of touching dielectric microspheres: (i) whispering gallery mode coupling and (ii) nanojet-induced mode coupling [108-110, 139].

WGM coupling with random detuning, observed in slightly disordered chains of polystyrene microspheres [139], indicates the possibility of developing waveguides based on using high-Q resonators with size and positional disorder. In contrast to the resonant CROW structures formed by identical cavities, such waveguides have broad bandpass transmission characteristics for evanescently coupled signals. These waveguides are important for developing functional circuits integrated on a single chip, including optical buffers and delay lines, nonlinear elements, and sensors [139].

The NIM coupling observed in chains of polystyrene microspheres [109, 110] can be advantageous in some applications requiring broad band transmission combined with sharp beam focusing. Variations of microsphere diameters due to fabrication tolerances have little impact on waveguiding characteristics, in comparison with WGM coupling which is more sensitive to size disorder.

One interesting potential application of coupled microspheres is making use of the "beam tapering" effect. Since the "beam tapering" effect occurs in a broad range of wavelengths, it can be used in a variety of biomedical applications requiring a combination of tight focusing and high optical output.

1.4. Focusing Surgical Microprobes

Focusing of light is commonly utilized in optical microprobes, where a stable and well-confined electromagnetic beam is scanned or directed over a biological sample or photonic structure. Potential applications of such technologies are numerous; including ultra-precise laser tissue surgery [171], nanoscale patterning [157, 158], piercing of a cell [172], and biomedical optical spectroscopy [173]. Usually, a combination of high spatial resolution and high power transmission is desired; however, in a number of biomedical applications, where infrared (IR) beams are delivered by hollow waveguides (HWGs) or multimode fibers, sharp focusing of light is challenging due to the multimodal nature of the transmitted beams. In principle, this problem can be overcome by using single mode fibers; however, they are not readily available in the mid IR range. In addition, they have limited coupling efficiency with many practical radiation sources, and limited power transmission properties.

An important potential application of such microprobes is ultra-precise ophthalmic laser surgery [174]. Below we provide a brief description of the corresponding medical problem.

Nearly 4.1 million Americans have suffered some form of diabetic retinopathy since 2004, and that number has progressively increased annually [175]. Diabetic retinopathy is caused by damage to blood vessels of the retina and is the leading cause of blindness in working-age Americans [176]. Preventative surgeries must be performed to seal the leaking blood vessels on the retina. In order to do that, KTP (Potassium Titanyl Phosphate) laser radiation (λ=532 nm) delivered by a multimode fiber is utilized to make hundreds of therapeutic lesions by photocoagulation alongside a vitrectomy procedure to remove debris in the eye [177]. In some advanced cases, such as proliferative diabetic retinopathy (PDR), the debris inside the eye stays and forms encrusted layers, as well as exudate deposits on the retina. Vision becomes significantly impaired as the density of these deposits increases, particularly, if they form on the macular region. The existing surgical procedure for PDR involves using micro-hook needles, forceps, and other instruments to remove deposits off of the retina [178]. Incomplete removal of these deposits is the primary reason for retinal re-detachment and surgical failure rates. These techniques produce stress on the surgeon's steadiness and the patient's eye, allowing for errors like accidental puncture, tearing, and detachment. Therefore, the surgical procedure for PDR, advanced retinopathy of prematurity, and other similar intraocular surgeries could benefit from ultra-precise contact laser probes for ablation of ophthalmic tissues.

Over the past two decades, various optical elements including spheres [179], hemispheres, dome, cone, slanted shapes [180, 181], cylindrical gradient index (GRIN) lenses [174], and tapered fibers have been tested as tips for ophthalmic laser scalpels. These devices were usually designed to operate in a non-contact mode in air at a fixed working distance from tissue or in contact with tissue, creating relatively large spot diameters greater than 100 μm. Controlling the working distance is difficult during the surgery and may result in a variable laser spot size and intensity in tissue. These fibers and laser probes are not widely used in intraocular laser surgery, except for thermal coagulation, because they lose their ability to focus light in aqueous media.

The most developed laser surgical equipment and procedures are based on using lasers with the wavelengths from the region of relative transparency of tissue. One of the examples of such procedures is LASIK (Laser-assisted in situ keratomileusis) surgery [182], where the local surgical action is achieved due to the focusing of the laser beam deeply inside the tissue. However, the fibrotic membranes formed at the back of the eye have uneven relief and extremely small thickness. They are only one or two monolayers of cells thick, which correspond to 10-20 μm depth of treatment. The accuracy required for dissecting or removing these membranes go far beyond what is achievable by using existing laser surgery systems, such as LASIK. Inevitably, the retinal areas below the membranes would be destroyed in the case of application of such systems.

Our approach to this problem is based on application of erbium:YAG (Er:YAG, YAG=$Y_3Al_5O_2$) laser with λ=2.94 μm, which is strongly absorbed in tissue with extraordinarily shallow surgical action [183-189]. Er:YAG lasers were extensively tested in 1990's for intraocular surgeries. However, the problem of beam focusing inside the

eye was not solved. As a result, the spot sizes were fairly big; typically well above 100 μm. Under these conditions, laser-tissue interaction led to significant cavitation bubble process and the tissue cutting speed was found to be slow. The bubbles in tissue obstructed the surgical field-of-view, so that in some cases the surgery had to be interrupted.

In our work, we suggest to reduce these problems by using extremely compact beams produced by chains of spheres. In chapter 4, we aim to develop contact-mode microprobes, which ablate the tissue under touching conditions with the tip of the optical scalpel. Although contact surgery may allow for better surgical control and protection for adjacent healthy tissue, it has been used only in a limited number of studies [190]. Due to the refractive index of the tissue, conventional microprobes, designed to operate in air, lose their focusing capability when operated in contact with tissue [174, 179-181]. Our ray tracing in a conventional microprobe consisted of an optical fiber and a single focusing element, i.e. a sphere as a lens, shows that the focusing is not preserved when the probe is in contact condition with an aqueous medium (Fig. 1.19).

Ultra-precise contact surgery tools should provide compact beam sizes in tissue in both the depth and transverse dimensions. It is well known that the optical penetration depth in a medium is reduced by the strong absorption of the medium. Since Er:YAG laser radiation (λ=2.94 μm) closely matches a major water absorption peak in tissue and couples well into water and body fluids, it is useful for medicine and dentistry applications. Minimization of the transverse beam size in tissue, however, requires solving the problem of sharp focusing of multimodal beams of light which are delivered by hollow waveguides or multimodal fibers.

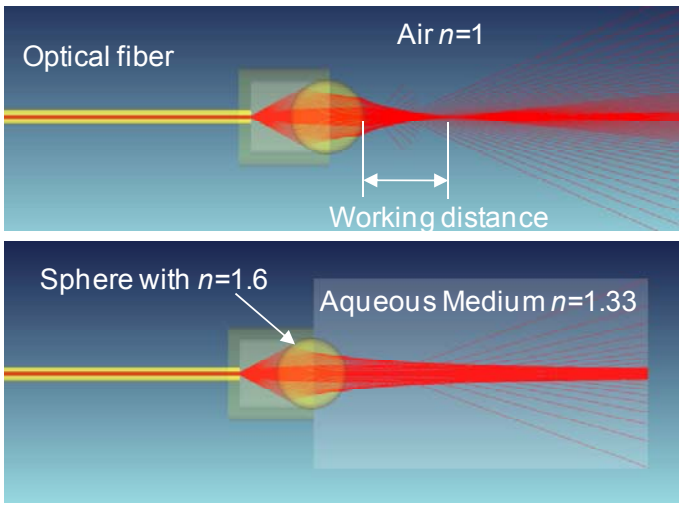

Figure 1.19: Microprobes designed to work at a certain working distance, lose their focusing in contact with tissue.

In the following sub-section, we briefly discuss some issues regarding the use of Er:YAG lasers for medical applications along with IR flexible delivery systems.

1.4.1. Erbium:YAG Laser for Medical Applications

The Er:YAG laser operates in the mid-infrared region of the electromagnetic spectrum at wavelength of 2.94 μm, which corresponds to an absorption peak of water, with absorption coefficient of $\sim 1.26\times10^4$ and penetration depth of ~ 1 μm [191]. The correspondence between the Er:YAG laser wavelength and maximal water absorption (Fig. 1.20) results in the sharpest containment of absorbed energy for any IR laser, which accounts for the minimal thermal damage observed in tissue interactions with the Er:YAG laser [184] compared with other IR lasers, including neodymium:YAG [192], holomium:YAG [193], and CO_2 lasers [194-197]. In addition to the mentioned advantageous wavelength properties, surgical cutting precision by means of laser technology is also dependent on control of pulse duration and spot size [184].

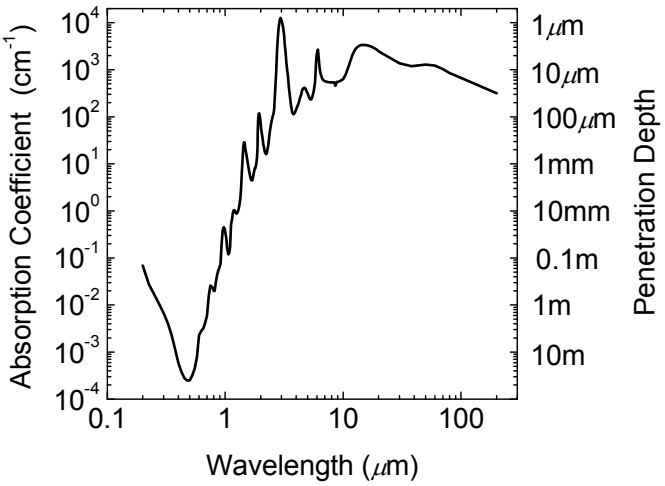

Figure 1.20: Water absorption coefficient and penetration depth as a function of wavelength [191].

The Er:YAG laser is presently used in the medical fields of ophthalmology [185, 198-203], dentistry [204, 205], and dermatology [206, 207]. The ablation threshold for soft tissue removal with the Er:YAG laser is ~1.6 J/cm^2 [208]. Thermal damage depths between 10-50 μm at the bottom of the ablation craters created in cornea tissue at high fluence have been reported [209]. For proliferative diabetic retinopathy (PDR) surgery, short optical penetration depth of the Er:YAG laser leads to ablating the exudate deposits, while minimizing thermal damage to the underlying retina, which is critical. In most current applications of the Er:YAG laser in dermatology and dentistry, where the tissue is readily accessible, a waveguide or fiber is not required to deliver the laser energy to the tissue. However, for endoscopic applications, like intraocular surgery, a dedicated fiber optic delivery system is required due to the fact that common silica based fibers do not transmit beyond ~2.5 μm. Different IR fibers and hollow waveguides have been developed to provide flexibility and high power transmission, which are reviewed in the following.

1.4.2. Infrared Waveguides

The necessity of using a flexible delivery system is dictated by the conditions of the surgery. The motions of the surgeon's hand should not be restricted during the surgery. This is a technically diverse area with several flexible delivery systems historically developed for the mid-IR spectral region. For this reason, in this subsection, we consider a general classification of such systems which play an important role in the design of surgical microprobes.

1.4.2.1. Classification of Infrared Fibers and Waveguides

Infrared fiber optics is defined as fibers that transmit radiation with wavelengths greater than ~2 μm. Such fibers are classified in three broad categories: glass, crystalline, and hollow waveguides (HWGs). These categories may be further subdivided according to the material or structure of the fiber [210]. In the following, a classification of IR fibers, with an example for each category, is provided [210, 211]:

1. Glass:
    1.1. Fluride: (example: ZBLAN.)
    1.2. Germanate: (example: GeO_2.)
    1.3. Chalcogenide: Sulfide, Selenide, and Telluride (example: AsGeTeSe.)
2. Crystalline:
    2.1. Single crystal: (example: Sapphire.)
    2.2. Polycrystalline: (example: AgBrCl.)
3. Hollow waveguide:
    3.1. Metal/dielectric film: (example: Ag/AgI films.)
        3.1.1. Metal-tube waveguides.

3.1.2. Plastic-tube waveguides.

3.1.3. Hollow glass waveguides (HGWs).

3.2. $n<1$: (example: Hollow sapphire at $\lambda=10.6$ μm.)

Except emerging heavy-metal fluoride glass fiber amplifiers, almost all IR fibers, currently available, are multimode with a step-index profile [210]. In comparison with silica fibers, IR fibers generally have higher loss, higher refractive index and dn/dT, lower melting or softening points, and greater thermal expansion [210]. Higher refractive index indicates more reflection or Fresnel loss for both fiber ends. The high dn/dT and low melting or softening point lead to thermal lensing and low laser induced damage thresholds for solid-core IR fibers [210]. IR fibers commonly used for the delivery of two popular IR lasers are:

1. Er:YAG lasers (~3 μm):
   1.1. HWG.
   1.2. Solid core:
      1.2.1. Sapphire.
      1.2.2. Fluoride glass, oxide glass.
2. CO_2 lasers (~10 μm):
   2.1. HWG.

Using HWGs is a suitable option for laser-power delivery at all IR laser wavelengths. In general, advantages of HWGs are high laser power threshold, low insertion loss, no end reflection, ruggedness, and small beam divergence. However, both optical and mechanical properties of HWGs remain inferior to silica fibers, and therefore

the use of HWGs is still limited to non-telecommunication, short-haul applications requiring only a few meters of waveguide [210].

1.4.2.2. Infrared Hollow Waveguides

Hollow-core waveguides may be grouped into two categories based on the materials of the core side-walls:

1. Leaky guides: inner wall material has $n>1$, and metallic and dielectric films are deposited on the inside of a metallic, plastic, or glass tube [Fig. 1.21 (a)].
2. Attenuated total reflectance (ATR) guides: inner wall material has $n<1$ in the wavelength region of interest, such as sapphire ($n=0.67$ at $\lambda=10.6$ μm) or some special $n<1$ oxide glasses. The ATR guides are fiber-like in that the index of the core ($n\approx1$) is greater than the index of the cladding [Fig. 1.21 (b)].

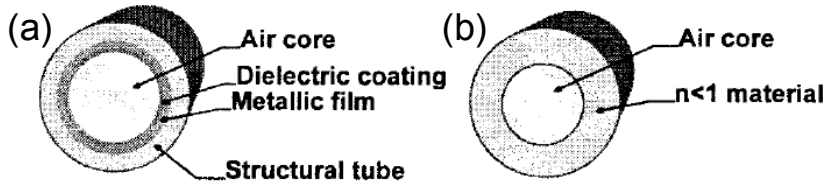

Figure 1.21: Structures of two types of HWGs: (a) leaky and (b) ATR guides [211]. Reprinted with permission. © 2000 Taylor & Francis.

The output beam profile of HWGs depends heavily on the bore size and on the quality and launch conditions of the input laser. In principle, HWGs are low-order mode guides because the higher-order modes are attenuated by the mode-dependant parameter $(u_{lm})^2$, where u_{lm} is the m^{th} root of the Bessel function J_{l-1}, see Eq. (1.36). In practice, however, mode distortion can occur even with a TEM_{00} input beam [210]. There are several ways in which higher-order modes may be generated in HWGs. The simplest

method is to launch a higher-order mode into the HWG with a low *f/#* launch, which is commonly encountered when using an Er:YAG laser, as these lasers are often multimode. Another method is to bend the HWG or apply a radial force to the outside of the guide. Other factors influencing the generation of higher-order modes are the surface roughness, the thickness of the glass wall, and the coupling efficiency [210].

There are two types of sources for loss in HWGs:

1. Propagation loss varies as $1/a^3$, where a is the bore radius [Fig. 1.22(a)].
2. Bending loss varies as $1/R$, where R is the bending radius [Fig. 1.22(b)].

Figure 1.22: Key parameters determining the losses in HWGs are (a) bore radius, a, and (b) bending radius, R [211]. Reprinted with permission. © 2000 Taylor & Francis.

1.4.2.3. Quantitative Parameters of Infrared Waveguides

The numerical aperture (NA) of a fiber is related to the critical angle in the fiber, and therefore to those rays which are propagated by only total internal reflection. The NA is related through Snell's law to the acceptance angle, θ_a. The acceptance angle defines a cone of angles within which all rays are guided in the fiber, as shown in Fig. 1.23.

$$n_0 \sin \theta_a = \text{NA}. \tag{1.32}$$

The NA of the fiber is, practically, defined by the Electronics Industry Association as the sine of the angle at which the power is fallen to 5% of the peak value [210].

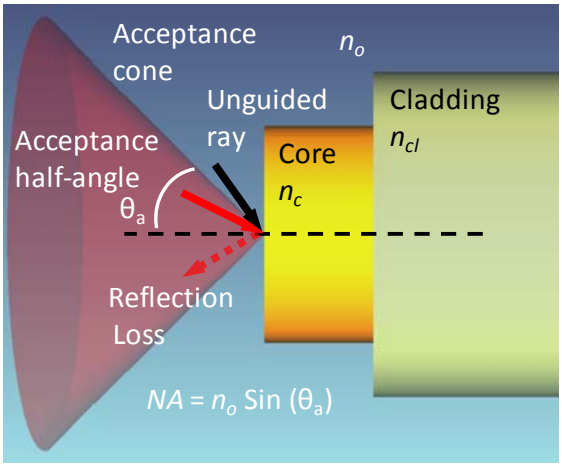

Figure 1.23: Schematic of a fiber optic showing guided and unguided rays, acceptance cone, and numerical aperture.

An important parameter related to the modal properties of a fiber is the fiber or V parameter. The V parameter governs the number of modes that can propagate, as well as certain aspects of the propagation of light in a fiber.

$$\mathrm{V} = \frac{2\pi a}{\lambda_0}\mathrm{NA} \cong \frac{2\pi a n_1\sqrt{2\Delta}}{\lambda_0}, \tag{1.33}$$

where λ_0 is the free space wavelength. The number of modes that can propagate in a multi-mode fiber is given by:

$$\mathrm{M} \approx \frac{4\mathrm{V}^2}{\pi^2}. \tag{1.34}$$

For example, for a multi-mode fiber with diameter $2a$=150 μm and NA=0.12 operating at 2.94 μm, there are ~150 propagating modes.

The dominating property that distinguishes IR fibers from conventional silica fibers is their higher loss. The loss for a fiber is specified in terms of the absorption coefficient, α. In general:

$$\alpha = \frac{10}{L}\log\frac{1}{T} = \frac{10}{L}\log\frac{\mathrm{P_{in}}}{\mathrm{P_{out}}}, \tag{1.35}$$

where L is the length of the fiber, T is the transmission, P_{in} and P_{out} are the input and output powers, respectively [210].

The extinction coefficient κ is related to the absorption coefficient α [cm^{-1}] in the material, specifically $\alpha = \frac{4\pi\kappa}{\lambda}$ [210].

The wave optics analysis of the modes in HWGs gives solutions of the electric and magnetic fields for the TE_{lm}, TM_{lm}, HE_{lm}, and EH_{lm} modes [210]. In cylindrical coordinate system, the l parameter is the number of periods in azimuthal direction and m parameter is the number of maxima and minima for each component in the radial direction. The attenuation coefficient for a straight waveguide with an innermost metallic layer with optical constants n and κ is given by:

$$\alpha_{lm} = \left(\frac{u_{lm}}{2\pi}\right)^2 \frac{\lambda^2}{a^3}\left(\frac{n}{n^2+\kappa^2}\right)_{metal} . F_{\text{film}}, \tag{1.36}$$

where u_{lm} is the m^{th} root of the Bessel function J_{l-1} and F_{film} is a term which accounts for the loss due to the dielectric film(s) [210]. The attenuation coefficient α_{lm} is the absorption coefficient determined from Maxwell's field equations, and since usually the power loss is measured, the corresponding power loss attenuation α, as given by Eq. (1.35), is α=2α_{lm}, due to the fact that the power is proportional to the square of the electric field [210].

1.5. Summary

The field of super-resolution imaging experienced a boost in the 1990's due to the invention of several novel techniques, such as near-field scanning optical microscopy (NSOM) and solid immersion lens (SIL) microscopy. Eventually, limitations of these techniques impeded their broad applications. The development of microfabrication

techniques made possible integrated microlenses in chip-scale structures, which showed improvement of the optical resolution over the macro-SILs [60]. New imaging technology through microspheres emerged as a potential solution to these problems, due to the simplicity and the broad band nature [63]. However, many issues regarding super-resolution imaging by microspheres remained open, at the time, when we started this dissertation. These issues include: i) the possibility of using total liquid-immersion of microspheres required in biomedical studies, ii) the possibility of using high index spheres, which generally should be helpful in achieving a better resolution, iii) the possible role and involvement of surface plasmons in achieving optical super-resolution, iv) the possible role of near-field effects in achieving super-resolution. These unresolved problems required urgent studies due to the multiple applications of super-resolution imaging. One direction of this dissertation was to study these problems.

In Chapter 2, we show the possibility of optical super-resolution imaging of structures totally immersed in a liquid. This has been achieved by using high-index spheres. Our obtained results generally point toward possible involvement of plasmons on metallic nanostructures. However, the results obtained from nonmetallic Blu-ray® disk showed that similar resolution can be also achieved using nonmetallic structures. Finally, we obtained detailed data on resolution, field-of-view, and magnification, which strongly support the involvement of near-fields in the formation of optical images in such structures. The minimal features sizes of $\sim\lambda/7$ were discerned by our technique, that cannot be explained by conventional far-field imaging mechanisms.

We reviewed a recent body of work regarding optical transport properties in chains of dielectric microspheres. Experimental [109, 110, 139] and theoretical [108, 140]

studies have shown that light transport in such chains is based on two distinct mechanisms: (i) evanescent WGM coupling and (ii) nanojet coupling. Both mechanisms have been observed in chains of polystyrene microspheres with a diameter, D, in 2-10 μm range [109, 110, 139]. These studies have revealed two effects which remained poorly understood, at the time, when we started this dissertation. Both effects were observed when such chains were optically coupled to multimodal sources of light such as dye-doped fluorescent microspheres. The first effect is an extraordinarily small attenuation of light, ~0.08 dB/sphere, observed [110] in such chains at long distances from the light source. The second effect is connected with a gradual decrease of the lateral width of the beams that are focused periodically along the chains ("beam tapering" effect) [109].

In Chapter 3, we study light propagation in chains of dielectric spheres in the limit of geometrical optics, which is a reasonable approximation for $D>>\lambda$, where λ is the wavelength of light. By introducing the concept of periodically focused modes (PFMs) in sphere-chains, we give a physical explanation for the extraordinarily small attenuation of light and the "beam tapering" effect in the limit of sufficiently large spheres, which should follow the laws of geometrical optics. Properties of PFMs, such as their focusing, attenuation, and polarization properties are studied in Chapter 3.

Focusing multimodal beams is a challenging task due to their multimodal nature. It becomes more challenging when the choice of a transparent lens material is limited. For example, in the mid-IR wavelength of λ~3 μm, single mode fibers are not readily available and the choice of lens materials with high optical transmission is limited. One particular motivation for mid-IR focusing microprobes is their application in laser surgery performed at strongly absorbing wavelength of Er:YAG laser. An example of

such surgeries is given by vitreoretinal surgery aimed at dissection or removal of fibrotic membranes, developed at the surface of retina in the course of proliferative vitreoretinopathy.

In the 1990's, the Er:YAG laser was identified as a promising candidate for precise surgery, due to the strong water absorption in soft tissues at its emission wavelength of λ=2.94 μm. However, Er:YAG laser did not gain widespread acceptance in the vitreoretinal surgery due to its relatively large size, slow rate of tissue cutting, and high price. In addition, the cutting rate was limited by vaporization bubbles that obstructed the surgeon's view, which made judgment more difficult. Another hurdle to overcome is represented by the limited focusing capability of current microprobes used in surgery. The mid-IR flexible delivery systems, such as fibers and hollow waveguides, are usually multimodal, which makes beam focusing very difficult. Over the past two decades various optical elements including spheres, hemispheres, domes, cones, slanted shapes, cylindrical gradient index lenses, and tapered fibers have been tested as ophthalmic laser probe tips. These devices are usually designed to operate in a non-contact mode in air, and lose their focusing capability in contact with tissue.

In Chapter 4, we design, fabricate, and test a device capable of focusing multimodal beams in contact with tissue. We consider mid-IR flexible delivery systems and design ultra-precise surgical microprobes formed by chains of dielectric spheres, assembled directly inside the cores of hollow waveguides, for laser surgery in a contact mode with a strongly absorbing tissue. The working principle of the designed devices is explained by the concept of periodically focused modes, which we developed in Chapter 3.

CHAPTER 2: SUPER-RESOLUTION IMAGING BY LIQUID-IMMERSED HIGH-INDEX MICROSPHERES

2.1. Introduction

In recent years, research into properties of artificial materials and structures has allowed for a remarkable increase in the optical resolution of imaging systems well beyond the classical diffraction limit. The ideal imaging device should be able to capture the sub-diffraction-limited detail of an object and project it into the far-field with some magnification. Although immersion techniques, such as liquid immersion [18] or solid immersion lenses [19-37], are used to enhance the resolution of imaging system as mentioned in Section 1.2.3, such techniques are diffraction-limited. Spatial resolution beyond the diffraction limit is attained by super-resolution imaging devices, which have been realized using different techniques such as near-field probes [40-43], fluorescent [47-50], nonlinear, and negative index materials [51-56], and plasmon gratings [57, 58], as mentioned in Section 1.2 of Chapter 1. However, the applications of these structures and devices have been impeded to some extent by their sophisticated engineering designs and various technical limitations. In the framework of near-field microscopy, utilizing nanolenses [60], microdroplets [61], and especially, microspheres [63, 64] emerged as a surprisingly simple way of achieving optical super-resolution. As reviewed in Section 1.2.4, a microsphere nanoscope [63] based on using silica microspheres with refractive index $n \sim 1.46$ and diameters (D) in the range 2-9 μm can convert high spatial frequencies of the evanescent field into propagating modes that can be used for far-field imaging of

sub-diffraction-limited features of a sample by looking “through the microsphere” into a virtual image produced by the microsphere below the surface of the structure. More recently, it has been shown that the super-resolution capability of this technique can be reinforced by semi-immersing the corresponding low-index microspheres in a liquid micro-droplet, producing a sharper contrast with a comparatively smaller magnification factor [64]. Although imaging in the presence of the liquid is useful for biomedical applications, using semi-immersed spheres is technically complicated due to the dynamical droplet’s evaporation process, which leads to gradually varying resolution and magnification of the optical setup. It has been argued, however, that the super-resolution effect cannot be expected [64] when the microsphere (n∼1.46) is absolutely submerged by the liquid layer.

As reviewed in Section 1.2.4, it has been suggested [63] that, on a fundamental level, due to optical reciprocity principle [118] a connection exists between the super-resolution ability of micrometer-scale spheres and their ability to create “photonic nanojets”, discussed in Sections 1.3.2. As reviewed in Section 1.2.4, the calculations predicted maximal super-resolution strength for n=1.8. It has been argued that for n>1.8, the super-resolution strength should be reduced along with a range of micrometer-scale sphere diameters, where this effect can be expected [63].

The main task of this chapter is to propose and develop a novel imaging technique with super-resolution capable of imaging in aqueous environments. We propose a novel microscopy technique based on using high-index microspheres immersed in liquids. We, experimentally, demonstrate that the super-resolution imaging by microspheres totally immersed in a liquid is possible if the refractive index of spheres is higher than 1.9. By

using micron-scale barium titanate glass (BTG) microspheres with refractive indices $n\sim1.9$-2.1 immersed in isopropyl alcohol (IPA) with $n\sim1.37$, we demonstrate the ability to discern features as small as $\sim\lambda/7$, where λ=550 nm is the peak illumination wavelength. For spheres with $50<D<200$ μm, the discernible feature sizes increase to $\sim\lambda/4$. The lateral field-of-view (FOV) linearly increases with D reaching extraordinary large values ($\sim$30 μm) for $\sim$200 μm spheres. The lateral magnifications of the virtual images are within 2.5-4.5 range for spheres with D in 2-220 μm range. We present more detailed data on the resolution, magnification, FOV, and polarization effects. Our proposed imaging technique can be used in biomedical microscopy, microfluidics, and nanophotonics applications.

In this Chapter, first we describe the samples investigated in our work in Section 2.2. After that, we describe the experimental setup and imaging technique utilized for super-resolution microscopy in Section 2.3. Then, we show how imaging characteristics such as spatial resolution (Section 2.4), lateral magnification, and field of view (Section 2.5.) depend on spheres' sizes. In Section 2.6, we show polarization dependency in the observed images. In Section 2.7, we discuss the role of the numerical aperture (NA) of the objective lens. In Sections 2.8 and 2.9, respectively, we compare our technique with established techniques of solid immersion lens (SIL) microscopy and confocal microscopy. Finally, we conclude in Section 2.10.

2.2. Samples

We studied four types of samples containing line and point objects in our work. The first sample with linear objects was obtained using commercially available Blu-ray® disks (BD) (Verbatim Americas, LLC, Charlotte, NC) with nominal track pitch sizes of 300

nm, consisting of 200 nm width stripes separated by 100 nm width grooves, as shown in Fig. 2.1. The 100-μm-thick transparent protection layer of the disk was peeled off prior to conducting the experiments.

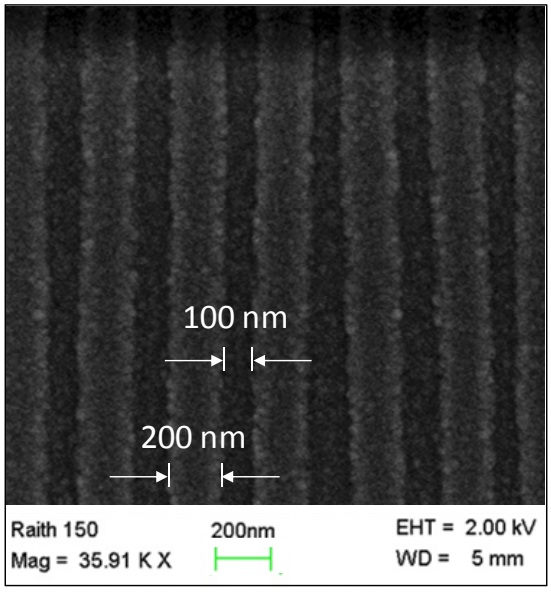

Figure 2.1: SEM image of a commercially available Blu-ray® disk with 200 nm width stripes separated by 100 nm width grooves.

The second type of samples with linear objects was represented by silver nanowires (PlasmaChem GmbH, Berlin, Germany) with nominal diameters ~100±20 nm self-assembled at the top of fused silica glass or GaAs substrates. Nanowire samples were assembled at the University of Sheffield, U.K., within a framework of a collaboration with the Low-Dimensional Structures and Devices group at the Department of Physics and Astronomy. Our scanning electron microscopy (SEM) measurements showed that many of the wires are wider than the nominal value, with diameters up to 300 nm. The SEM image of several wires is presented in Fig. 2.2.

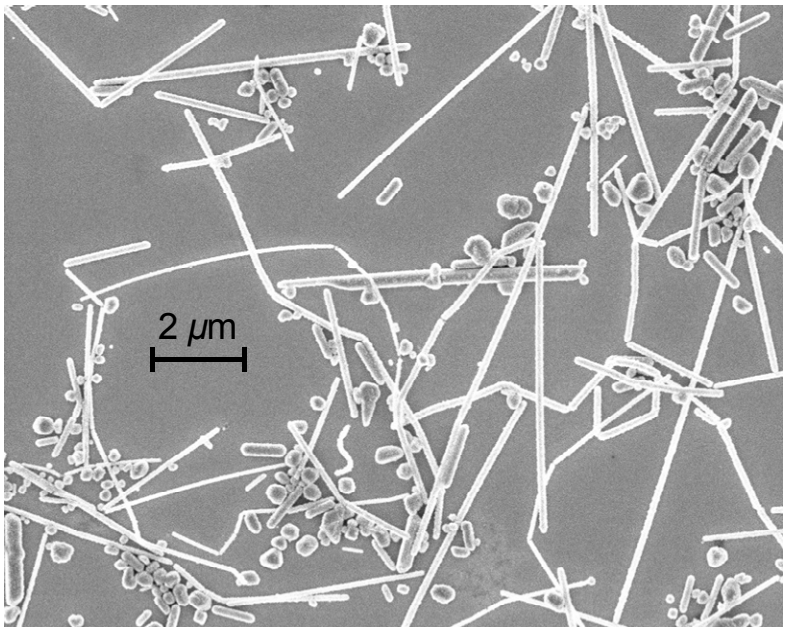

Figure 2.2: SEM image of silver nanowires with different diameters.

The third sample with point objects, Fig. 2.3, was represented by 2-D arrays of gold nanoparticle dimers (NPDs) with periods of 320 nm and 800 nm in *x* and *y* directions, respectively. The fabrication was performed by our collaborator, group of Dr. Luca Dal Negro from Boston University. The sample was passed to Dr. Astratov during his visit to Boston University in the summer of 2010 for joint studies of photonic nanojet-enhanced nanoplasmonic antenna effects. Eventually, we used this sample for super-resolution imaging studies. Each dimer consisted of two gold nanocylinders with 120 nm diameters and 30 nm height (2 nm Cr and 28 nm Au), which were fabricated on a fused silica substrate by electron beam lithography, metal evaporation, and lift-off process. The minimum edge-to-edge separations in dimers were 60, 120, and 150 nm in different arrays. The SEM images in Figs. 2.3(a) and 2.3(b) represent nanoparticle dimers with 150 nm and 120 nm separation (along *y* direction), respectively.

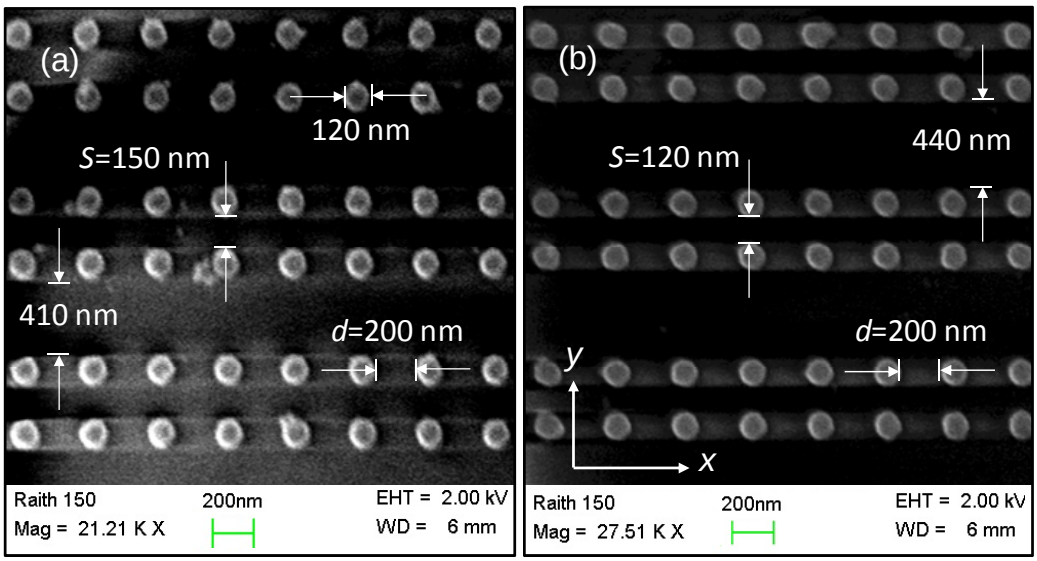

Figure 2.3: SEM image of arrays of gold dimers formed by 120 nm nanoparticles with (a) 150 nm and (b) 120 nm separations.

The fourth sample with point objects was fabricated at Air Force Research Laboratory (AFRL) by Dr. Nicholaos I. Limberopoulos and his group. This sample is represented by metallic nanoplasmonic 2-D arrays fabricated on a sapphire substrate using a bi-layer PMMA/ZEP520A e-beam photoresist lift-off mask exposed in a JEOL JBX-6300FS e-beam lithography system. The unit cell of the array was represented by four metallic cylinders with diameters D and distance d between their centers varying in different lattices. An example of such array is illustrated in Fig. 2.4(a) for D=100 nm and d=200 nm. Although one of the parameters of the design, d, was variable, the range of variation of the feature sizes, such as gaps between the cylinders, generally, demand too high resolution to be resolved optically. One feature of this design, namely the fact that the array of cylinders has a unitary cell formed by four cylinders in the corners of a rhomb instead of dimers, particularly complicates the task of resolving the images of individual cylinders. Such rhomb shapes represented in Fig. 2.4(a) can be considered as a

combination of two dimers in perpendicular directions. The problem, though, consists in superposition of the irradiance distribution produced by such perpendicular dimers. Actually, it makes it much more difficult to resolve the irradiance minimum at the center of the rhomb. We selected arrays with D=100 nm and d=150 nm where four cylinders were overlapped forming a "single atom" unit cell reminiscent of a rhombic shape, as illustrated in Fig. 2.4(b). The minimal edge-to-edge separation between the corners of such rhomb-like unit cells was S=250 nm. Although this pattern is not particularly challenging for imaging using visible light, it is convenient for our studies of the effects of finite NA of the microscope objective on the optical resolution described in Section 2.7.

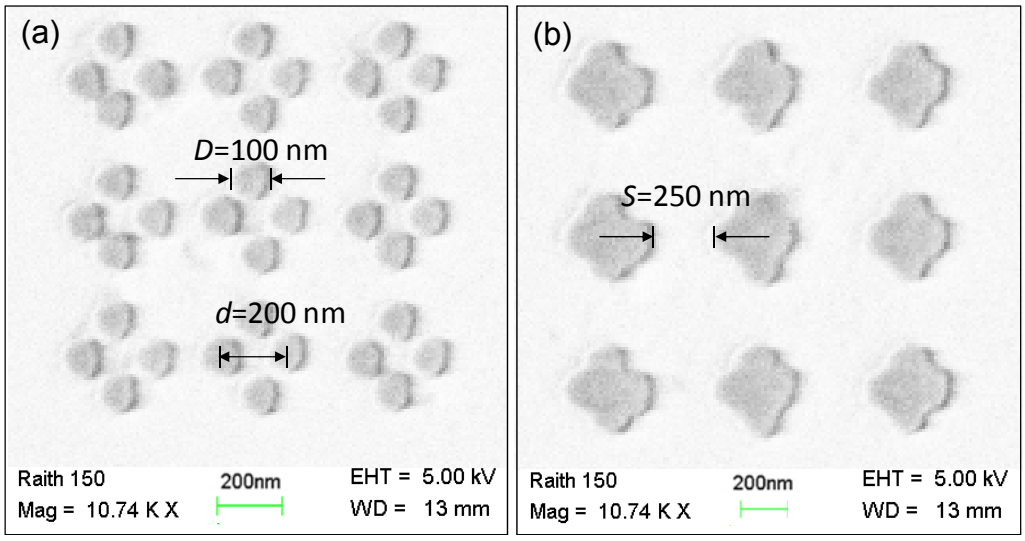

Figure 2.4: SEM images of two arrays with the comparable cylinder diameters D=100 nm and different separations between their centers, d=200 nm (a) and d=150 nm (b).

It should be mentioned that we initiated and developed the super-resolution imaging work and performed the optical characterizations at the UNCC.

2.3. Microscopy Technique

A schematic of our experimental setup and the virtual image formation are illustrated in Figs. 2.5(a) and 2.5(b), respectively. We used an FS70 Mitutoyo microscope equipped with a halogen lamp and a CCD camera (Edmund Optics, Barrington, NJ) in reflection illumination mode. The microscope was equipped with different Mitutoyo objectives: 100×(NA=0.9), 100×(NA=0.7), 100×(NA=0.5), and 20×(NA=0.4). Images had 1600×1200 pixels. The system spectral response was strongly peaked at 550 nm. Using additional filters we checked that all results are reproducible with narrow band (~20 nm bandwidth) illumination centered at 550 nm.

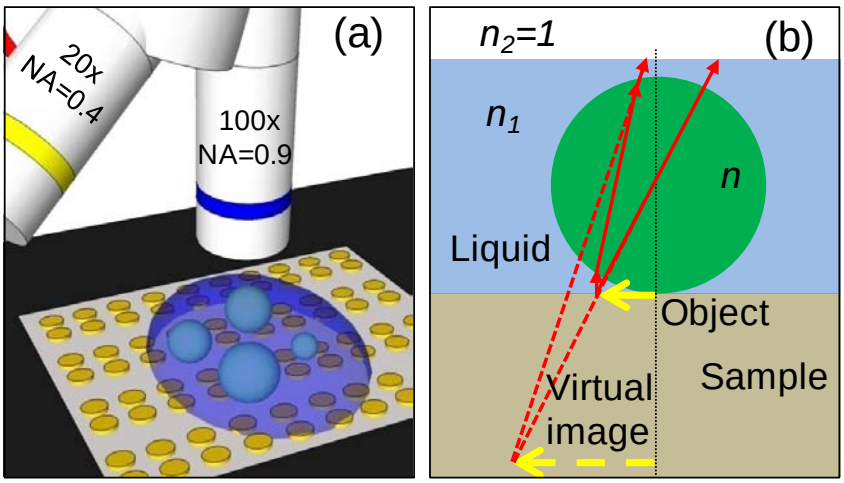

Figure 2.5: (a) Schematic of our novel microscopy method. (b) Virtual image formation by a liquid-immersed sphere.

Two modifications of barium titanate glass (BTG) microspheres (Mo-Sci Corporation, Rolla, MO) differing by their chemical composition, and as a result, by their refractive index (n~1.9 and ~2.1) were used. The microspheres were positioned on the specimen by using different techniques:

i) By micromanipulation of the spheres using a tapered-tip fiber optic or by a metallic micro-needle.

ii) By self-assembly where the liquid (IPA) suspension of microspheres was poured on the specimen by a micropipette.

IPA (or other liquids) was poured on the surface of the sample by a micro-syringe to totally cover the microspheres. Similar results were obtained using water or other liquids infiltration.

First, we present the experimental results obtained from the Blu-ray® disk (BD) and nanoparticle dimers (NPD) samples. The 100 nm features in the BD cannot be resolved by our microscope system. Conventional microscopy allows resolving only the largest 800 nm period of the NPD array along *y* direction [corresponding to the 410 nm distance in Fig. 2.3(a)] which is illustrated in Fig. 2.6(a) due to the stripe pattern outside the microsphere. Neither the 320 nm period, nor the 150 nm edge-to-edge separations in the NPDs are resolved in this image.

We observed that the super-resolution imaging of the BD sample without liquid can be achieved using microspheres with small-to-moderate refractive indices, such as borosilicate glass (n~1.47), soda lime glass (~1.51), polystyrene (~1.59), and sapphire (~1.77). However, all these microspheres were found to lose their imaging capability, if they are completely covered with a liquid such as IPA.

High index (n~1.9-2.1) barium titanate glass (BTG) spheres showed a different behavior in these experiments. Without liquid addition they did not produce any imaging. However, they provided super-resolution imaging in cases when they were totally covered with a liquid, as illustrated for nanoparticle dimers and Blu-ray® disk sample in

Figs. 2.6(b) and 2.6(d), respectively. The depth of focusing in these images is below the surface of the structure, as can be seen by comparison with conventional images of the same structures in Figs. 2.6(a) and 2.6(c), respectively.

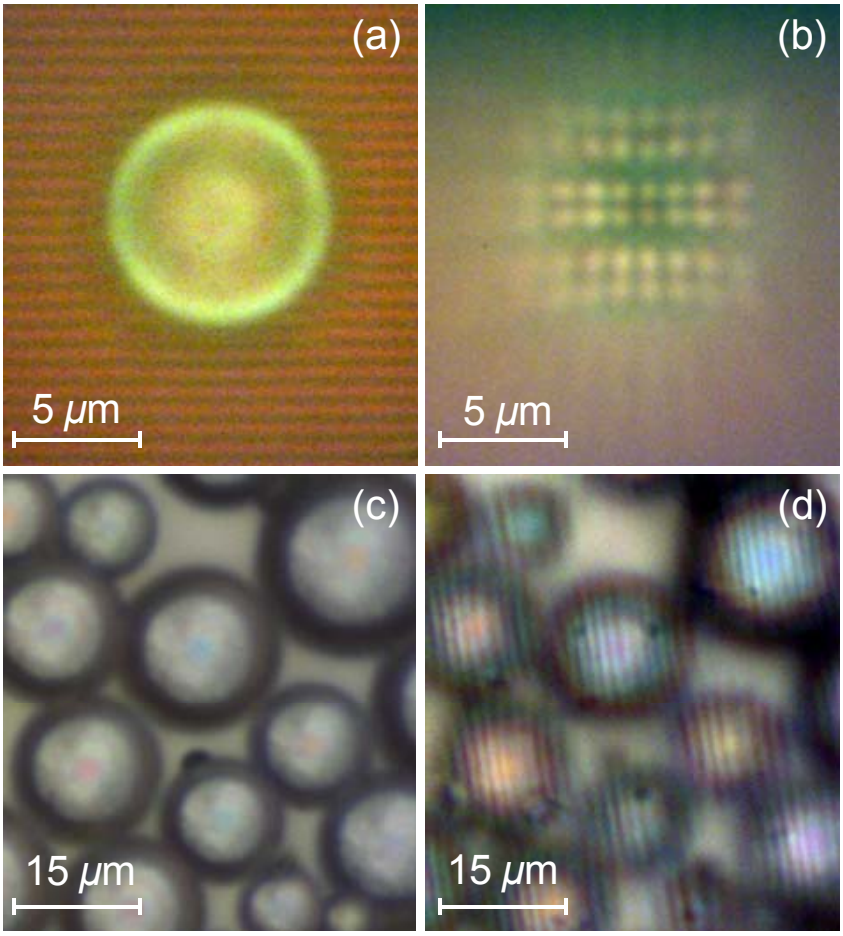

Figure 2.6: (a) A BTG sphere with n~1.9 immersed in IPA and (b) virtual imaging of the array through the microsphere at a different depth compared to (a) by a 100×(NA=0.9) objective. (c) BTG microspheres with diameters in the range ~5-20 μm fully immersed in IPA and (d) virtual imaging of the BD through the microspheres at a different depth compared to (c) by a 20×(NA=0.4) objective.

The far-field virtual images of individual gold nanoparticles with 150 nm separations are clearly resolved in Fig. 2.6(b). The gaps between the cylinders are selected as features

of interest. Similar resolution can be seen for a Blu-ray® disk, as illustrated in Fig. 2.6(d). These results show an ability to discern the shape of a pattern with minimum feature sizes $\sim\lambda/4$. This approach is somewhat different from classical resolution criteria mentioned in Section 1.2.1, where a resolution criterion is defined based on the ability to resolve the distance between two "point sources" with equal intensities. In our case, because of the finite sizes of the metallic cylinders the straightforward use of classical criteria of the optical resolution is complicated.

2.4. Spatial Resolution

In order to study the dependence of the resolution strength on the diameters of the spheres (D), we used the nanoparticle dimers (NPD) array with 120 nm minimal separation, illustrated in Fig. 2.7(a). We found that the resolution is generally deteriorated with increasing D, as illustrated in Figs. 2.7(b-d). The irradiance profiles were measured along the axis connecting two nanoparticles with the 120 nm separation, as illustrated in the insets to Figs. 2.7(b-d). Figs. 2.7(b-d) display double peak patterns which were fitted using two Gaussian peaks. The sums of the Gaussian peaks are represented by dashed (red) curves in Figs. 2.7(b-d).

As illustrated in Fig. 2.7(b) for the 4.2 μm sphere, the minimal discernible feature sizes ~75 nm ($\sim\lambda/7$) is estimated by assuming that two equally intense points are resolved when the saddle irradiance is 0.81 according to the generalized Rayleigh criterion, described in Section 1.2.1. This estimation is obtained by moving the two individual Gaussian fit functions towards each other in Fig. 2.7(b) until the irradiance of 0.81 is obtained. For D=53 μm spheres the same criterion leads to the minimal discernible feature sizes $\sim\lambda/4.5$.

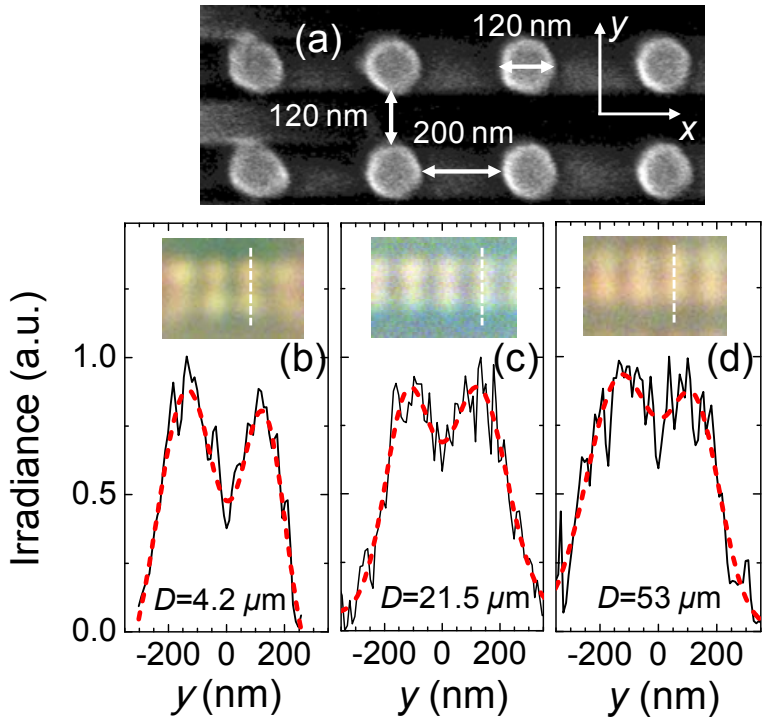

Figure 2.7: (a) SEM image of an array of gold NPDs formed by 120 nm nanoparticles with 120 nm separations. Resolving power of BTG microspheres with n~1.9 and different diameters D: (b) 4.2 μm, (c) 21.5 μm, and (d) 53 μm. Insets show optical microscope images obtained in (b-d) cases corresponding to the SEM image in (a).

The super-resolution strength of liquid-immersed high-index spheres stems from different factors:

i) For all sphere diameters, the resolution is improved due to increase of the effective NA of the system composed of microscope objective and liquid-immersed spheres, by reduction of the wavelength of light in a liquid in a same manner as in liquid immersion technique, and by the increase of the acceptance cone of the waves scattered by the surface pattern in a similar manner as in super-spherical solid immersion lenses (s-SILs). The latter factor is responsible

for the robustness of this technique to the variation of the NA of the microscope objective.

ii) For smaller values of the size parameter (q<100), the super-resolution strength can be additionally enhanced [63] due to "photonic nanojet" properties of mesoscale spheres. The evanescent field plays a significant role in the field distribution close to the surface of the sphere [92] for sufficiently large index contrasts; however, the role of near-field evanescent waves in the super-resolution imaging mechanisms requires more studies.

2.5. Lateral Magnification and Field-of-View

In order to study image magnification (M), we used microspheres with n∼1.9 and 2<D<220 μm, and the nanoparticle dimers (NPD) sample with 150 nm separations, as illustrated in Fig. 2.3(a).

The refraction law is determined by the refractive index contrast, n'=n/n_1∼1.39. For an object located at the sphere surface illustrated in Fig. 2.5(b), the virtual image lateral magnification can be calculated according to paraxial geometrical optics as:

$$|M| = |n'/(2-n')| \sim 2.3. \quad (2.1)$$

For spheres with D∼220 μm, where geometrical optics is expected to be a reasonable approximation, we measured M∼2.5. For smallest spheres, 2<D<6 μm, where the geometrical ray tracing is not applicable, we observed increasing M with the spheres' diameter similar to the previous studies of imaging by low-index spheres in air [63]. In the intermediate diameter range, 6<D<10 μm, we found that M reaches maximal values with significant variations from sphere to sphere in the 3.5-4.5 range, as illustrated in Fig. 2.8(a).

The measurements of magnification were complicated by difficulties in reproducing the same depth of focusing on the virtual images. In addition, the image magnification increases with the distance from the optical axis due to the pincushion distortion [212], which can be seen in Fig. 2.6(b) and in the inset to Fig. 2.8(b) due to the fact that the lines formed by nanoparticles that do not go through the center of the image are bowed inwards, towards the center of the image. To diminish the role of the pincushion effect we determined *M* in the central section of the images.

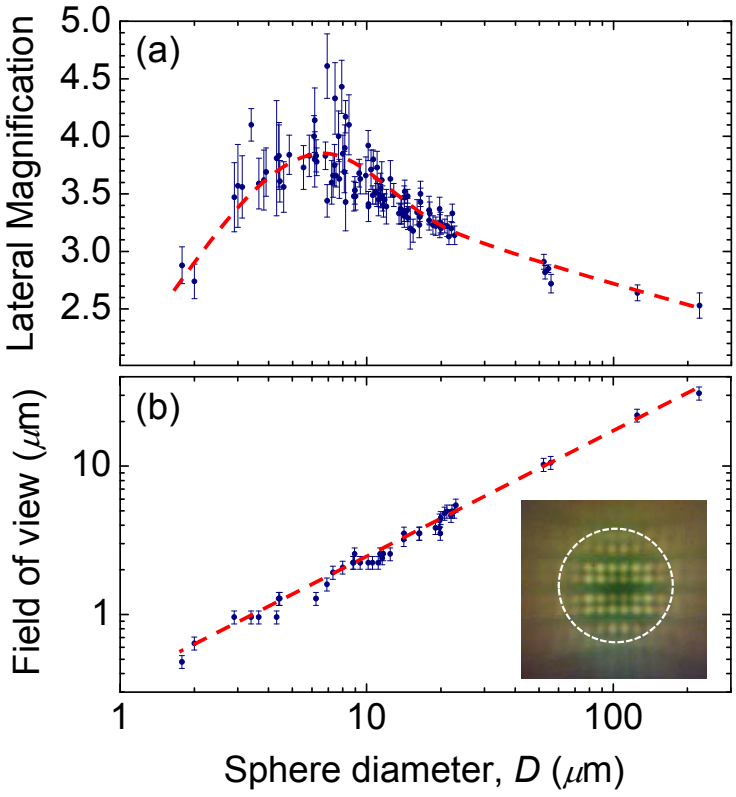

Figure 2.8: (a) Lateral magnification (*M*) and (b) FOV obtained by BTG microspheres with $n \sim 1.9$ as a function of *D*. The inset in (b) illustrates FOV for a sphere with $D=9$ μm. The measurements were performed using the NPD array. The dashed lines are guides for an eye.

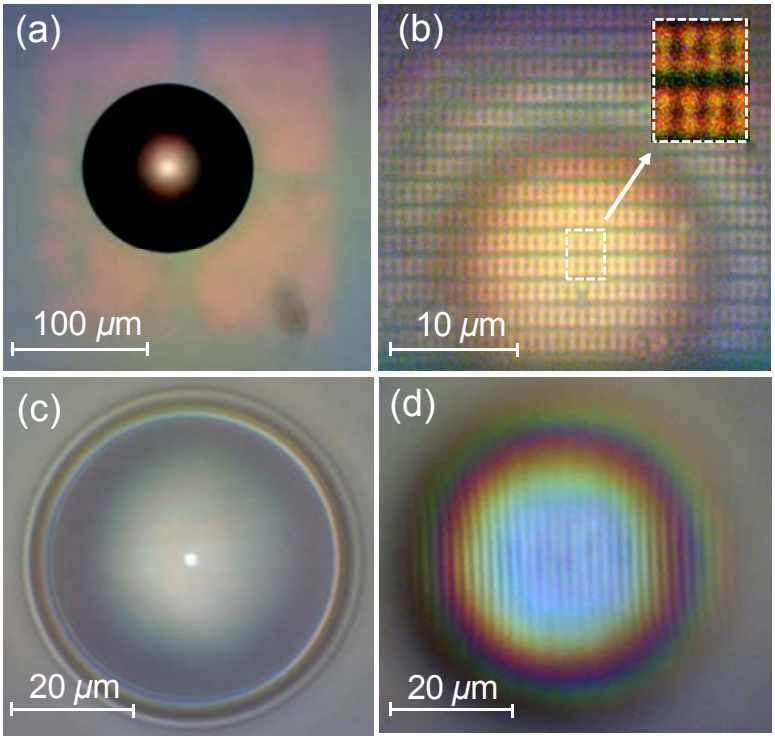

Figure 2.9: (a) A BTG microsphere with n~1.9 and D~125 μm fully immersed in IPA at the top of the NPD array with 150 nm separations, and (b) imaging through this microsphere by a 100×(NA=0.9) objective lens illustrating >20 μm super-resolution FOV. (c) BTG microsphere with n~2.1 and D~53 μm fully immersed in IPA at the top of a BD sample, and (d) imaging through this microsphere by a 20×(NA=0.4) objective lens illustrating the 100 nm grooves of the BD.

An important property for imaging applications is connected with the FOV, which was in previous studies limited to few microns due to small diameters of low-index spheres [63]. We found that high-index liquid-immersed spheres preserve their imaging capability at significantly larger diameters. As shown in Figs. 2.9(a) and 2.9(b) for a sphere with n~1.9 and D~125 μm, the 150 nm separations in the nanoparticle dimers array are resolved by this sphere over an extraordinary large (~22 μm) FOV. Similar results were obtained for the Blu-ray® disk sample using a sphere with n~2.1 and D~53 μm totally immersed in IPA, as illustrated in Figs. 2.9(c) and 2.9(d).

As illustrated in the inset to Fig. 2.8(b), FOV was defined as a diameter of a circle at the sample surface where we were able to discern the shape of the NPD array with 150 nm separations. A close to linear dependence of FOV on D was observed, as shown in Fig. 2.8(b).

2.6. Polarization Effects

The polarization effects were studied in the images of the silver wires, as illustrated in Fig. 2.10. In Fig. 2.10(b) a linearly polarized incident light was used to image the sample through a liquid-immersed BTG sphere with D~10 μm and n~1.91. Fig. 2.10(c) was obtained by transmitting the reflected beam from the sample through another linear polarizer (analyzer) whose axis is perpendicular to the incident polarization axis. Only is the region where the wire is perpendicular to the second polarizer (analyzer) vanished, as illustrated in Fig. 2.10(c), which shows that if the incident light is polarized parallel to the wire, the reflected light also has a pure state of polarization (linear), and it is also polarized parallel to the wire.

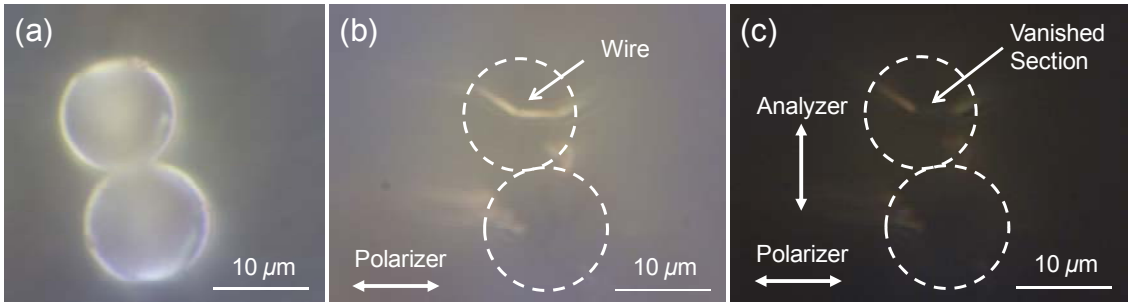

Figure 2.10: (a) BTG spheres placed on top of the sample. (b) Imaging through liquid-immersed spheres using linearly polarized incident light. (c) Placing an analyzer whose axis is perpendicular to the polarizer's axis after the reflected image leads to vanishing of the image of a wire which is perpendicular to the analyzer.

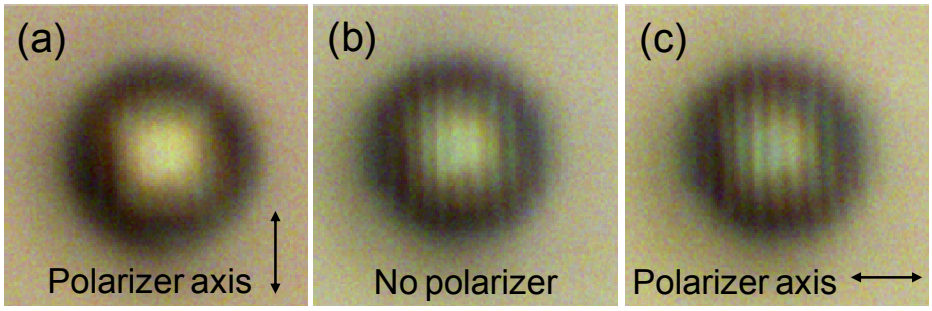

Figure 2.11: A BD sample imaged by a BTG microsphere with n~1.9 with polarizer's axis (a) parallel to the stripes, (b) no polarizer, and (c) perpendicular to the stripes.

The polarization effects were also studied in the images of the Blu-ray® disk (BD) samples by transmitting the reflected beam from the sample through a linear polarizer. If polarizer's axis is parallel to the BD stripes, the image has the worst contrast, as illustrated in Fig. 2.11(a). The maximal contrast of the image was achieved with a polarizer axis perpendicular to the BD stripes, as shown in Fig. 2.11(c). In comparison with a wire-grid polarizer [212], the BD sample is a complicated case which requires further studies.

2.7. Resolution Gain and Effect of the NA of the Objective Lens

In this section, we present the results obtained by using silver nanowires samples, described in Section 2.2. Due to their long length, the wires are seen by conventional microscopy technique, as shown in Fig. 2.12(a) by using a 100×(NA=0.9) objective.

The diffraction limit of our objective lens can be estimated as ~300 nm using the Abbe criterion. The FWHM of the irradiance distribution of a cross section of the wire in the image in Fig. 2.12(a) is ~390 nm. By using a BTG microsphere with D~9.6 μm immersed in IPA the image of the same wire is shown in Fig. 2.12(b). The size of this

image has been reduced by a magnification provided by the microsphere (M=3.6) in order to make this image directly comparable to conventional microscopy image in Fig. 2.12(a). The identical triangles in Figs. 2.12(a,b) connect the same features in these images to prove that both images represent the same optical magnification. The width of the wire in Fig. 2.12(b) is characterized with FWHM=230±30 nm, which shows ~1.7 times improvement in the spatial resolution. We believe that the actual size of the wire is ~200 nm based on SEM imaging of the wires.

In the previous section we showed that the use of smaller, micro-scale spheres can further increase the resolution. So, we believe that a better resolution can be realized by using liquid-immersed BTG spheres with 4-5 μm diameters.

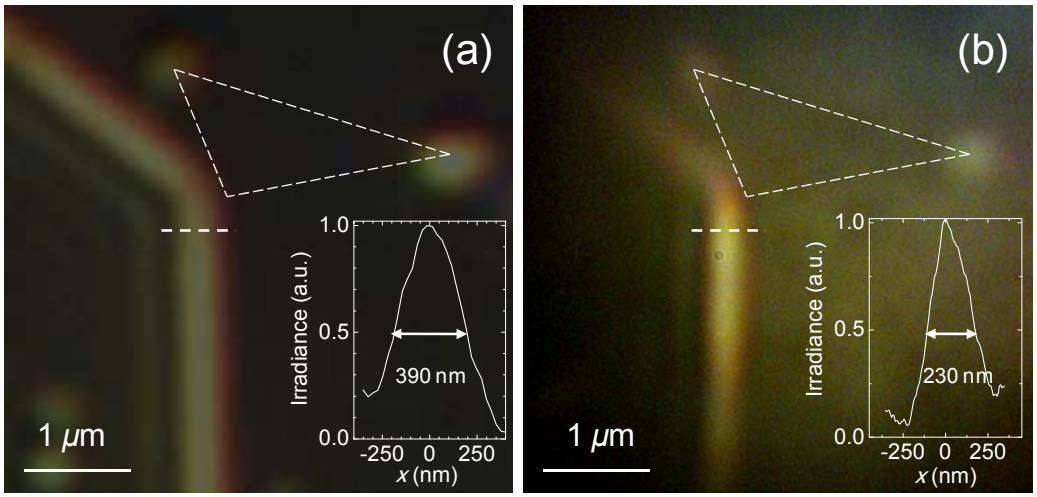

Figure 2.12: (a) Micrograph of a silver wire by 100×(NA=0.9) microscope objective shows a diffraction-limited size of ~390 nm. (b) Image of the same wire by the same objective through a 9.6 μm BTG sphere immersed in IPA shows ~230 nm size. Identical triangles connect the same features in these images to show that both images are presented in the same scale. The irradiance profiles were measured along dashed lines in these images.

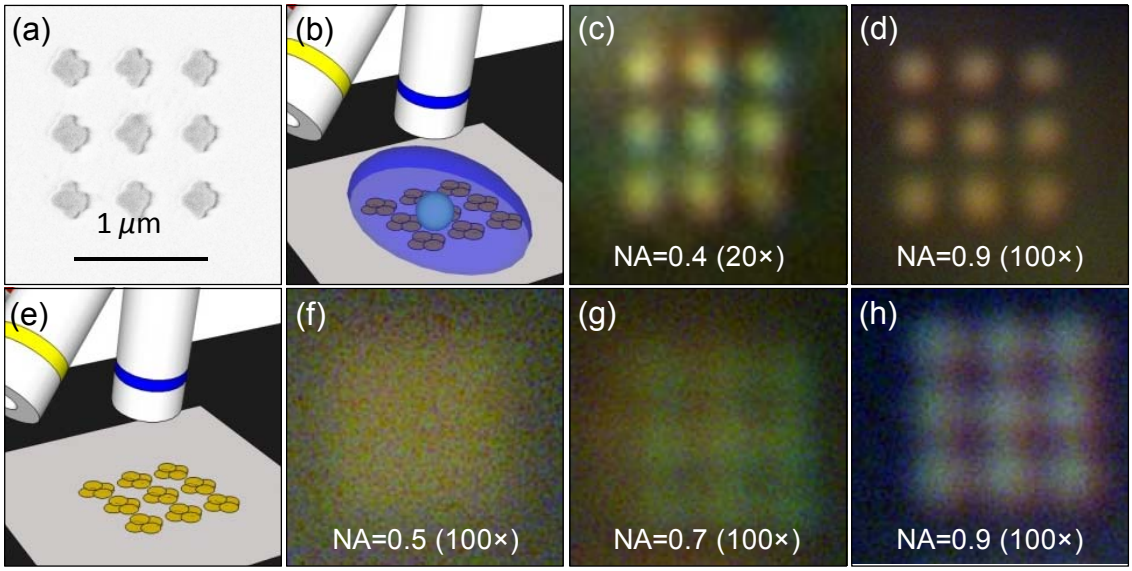

Figure 2.13: (a) SEM image of the sample. (b) Schematic of the experimental setup. (c,d) Optical micrographs of the sample through a liquid-immersed 21.7 μm BTG sphere by a 20×(NA=0.4) and 100×(NA=0.9) objective, respectively. (e) Schematic of conventional microscopy. (f-h) Conventional optical micrographs of the sample by 100×(NA=0.5), (NA=0.7), and (NA=0.9) objectives, respectively. Images (c, d, f-h) were normalized by their magnification factor.

We studied the effect of the NA of the microscope objective in more detail by using the sample shown in Fig. 2.13(a), which was described in Section 2.2. These arrays were visualized using liquid-immersed BTG microspheres, Figs. 2.13(b-d), and by conventional microscopy, Figs. 2.13(e-h). Figs. 2.13(c) and 2.13(d) were obtained through a 22 μm BTG sphere immersed in IPA by 20×(NA=0.4) and 100×(NA=0.9) objectives, respectively. Optical images of the sample obtained without using microspheres are presented in Figs. 2.13(f-h) for 100× microscope objectives with NA=0.5, 0.7, and 0.9, respectively.

As shown in Fig. 2.13(h), the minimal separations between the corners of the rhomb-like unit cells (~250 nm) are barely resolved by the high NA=0.9 objective. Just a small

decrease of NA from 0.9 to 0.7 leads to a very significant degradation of the quality of the optical image, as illustrated in Fig. 2.13(g). Instead, the images obtained using microspheres are found to be robust to the variations of the NA of the microscope objective. Comparison of the images in Figs. 2.13(c) and 2.13(d) reveals that the minimal separations between the rhombs are well resolved using the objective with NA=0.4.

2.8. Comparison with Solid Immersion Lens Microscopy

In this section, we utilized the solid immersion lens (SIL) microscopy technique to resolve features of some of the samples used in our previous work and to compare them with the results obtained by the liquid-immersed spheres. The experimental setup was the same as before, except that instead of the liquid-immersed spheres a dielectric hemisphere (h-SIL) was used, as schematically illustrated in Figs. 2.14(b) and 2.15(b).

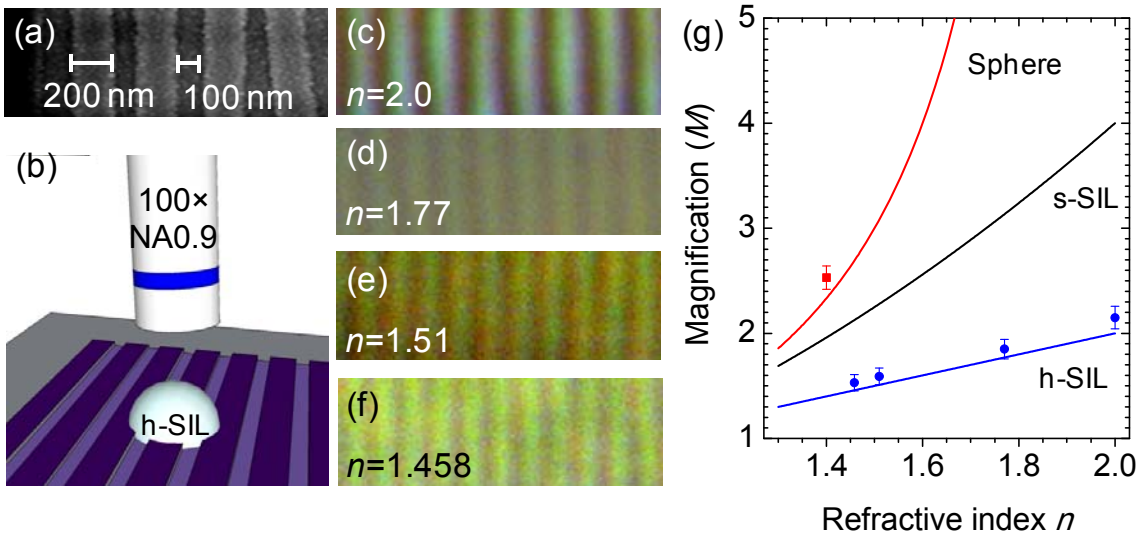

Figure 2.14: (a) SEM image of the BD sample. (b) Schematic of the microscopy setup with an h-SIL. (c-f) Images of the Blu-ray® disk by using an h-SIL with refractive index 2.0, 1.77, 1.51, and 1.458, respectively. (g) Experimental results and geometrical optics theoretical calculations of M vs. n.

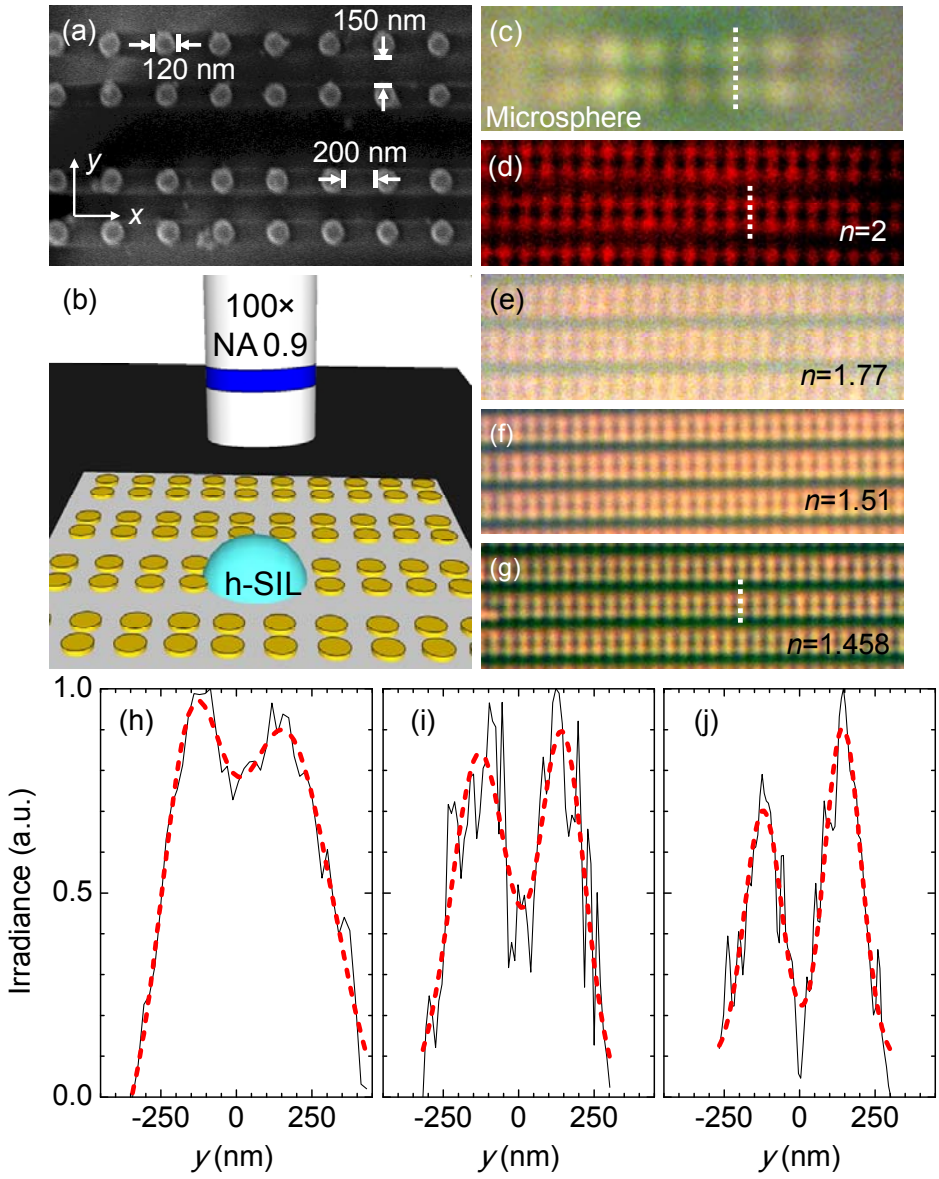

Figure 2.15: (a) SEM of the NPD sample. (b) Schematic of the experimental setup. (c) Optical micrograph of (a) by using a liquid-immersed BTG microsphere. (d-g) Optical micrographs of (a) by using h-SILs with n=2.0, 1.77, 1.51, and 1.458, respectively. (h-j) Irradiance profile along the axis of an NPD for (g), (d), and (c), respectively.

In order to perform imaging with SIL microscopy technique, we used dielectric hemispheres (Edmund Optics, Barrington, NJ) with 2 mm diameters made from fused silica (n~1.458), N-BK7 (n~1.51), sapphire (n~1.77), and S-LAH79 (n~2). The SILs

were placed on top of the samples and gently pressed against the samples to achieve as secure a contact condition as possible between the SIL and the sample. In some cases, a small amount of IPA was applied to fill the nano-gap between the SIL and the sample surface. In principle, a liquid with the same index as the SIL should have been used to function as an index matching liquid.

As shown in Fig. 2.14(c-f), all h-SILs managed to resolve the features on the Blu-ray® disk (BD), the SEM image of which is presented in Fig. 2.14(a). The same result was obtained for the gold nanoparticle dimers (NPD) sample, as illustrated in Fig 2.15(d-g). The reason that the quality in Figs 2.14(d) and 2.15(e) are poor is due to the fact that the material of the SIL was sapphire, which is a birefringent material and produces two images.

As we mentioned in Section 1.2.3, geometrical optics magnification (M), of h-SIL is equal to the refractive index of the SIL material, i.e. $M=n$. The lateral magnification factor of the experimental SIL microscopy results for each SIL material was measured and compared with the corresponding theoretical value. As can be seen in Fig. 2.14(g), there existed a good agreement between experimental and theoretical values of M for h-SILs. This was an expected result due to the fact that the millimeter-scale size of the the SILs fits well in the domain of geometrical optics.

In Fig. 2.14(g), the magnification values of a sphere, a super-spherical solid immersion lens (s-SIL), and a hemispherical solid immersion lens (h-SIL), calculated by geometrical optics laws, are compared. It shows that the spheres provide more magnification compared to the SILs with the same n in the frame work of geometrical optics. As we showed in detail in Fig. 2.8(a) in Section 2.5, we measured magnification

values in the range of 2.5-4.5 for liquid-immersed spheres (refractive index contrast n' =1.39) with $2<D<220$ μm. Since the experimental magnification values of spheres depend on the size of the sphere, i.e. $M \propto D$, and the magnification values of meso-scale spheres cannot be explained by geometrical optics laws, we showed only the magnification value of the largest sphere size used in our experiments in Fig. 2.14(g), i.e. M=2.53 for D=220 μm. By comparing the experimental results of magnification of the SIL microscopy technique with liquid-immersed spheres, it can be concluded that spheres provide more magnification compared with their SIL counterparts. It should be pointed out that although spheres provide dramatically more magnification in comparison with both s- and h-SILs, the magnification factor is not enough to enhance the resolution.

We used the nanoparticle dimers (NPD) sample to compare the resolution of the SIL microscopy technique with the resolution obtained using liquid-immersed spheres. The images obtained by the SIL technique are presented in Figs. 2.15(d-g) for different SIL materials. Fig. 2.15(c) was obtained by a liquid-immersed sphere. Qualitatively, by comparing Figs. 2.15(d-g) with Fig. 2.15(c), it can be directly seen that the microsphere provides better resolution as well as more magnification compared with SILs.

In order to quantitatively compare the resolution of the images obtained by the SILs with the resolution of the liquid-immersed spheres, we selected images obtained by the SILs with the lowest and highest refractive indices, i.e. n=1.458 and 2.0, as shown in Figs. 2.15(g) and 2.15(d), respectively. Furthermore, the image obtained by a ~9 μm liquid-immersed sphere, shown in Fig. 2.15(c), was selected. The irradiance profile along the nanoparticle dimer's axis, indicated by a dashed line in Figs. 2.15(g), 2.15(d), and 2.15(c) was plotted for each case, as illustrated in Figs. 2.15(h-j), respectively. Each

profile contains a background, which is a certain level of irradiance in the region located outside the image of the dimer. This background level was subtracted in Figs. 2.15(h-j). A double-peak Gaussian curve was used for fitting each irradiance profile. The irradiance level of the saddle in each plot can be used as an estimate for the image resolution. The saddle irradiance in Figs. 2.15(h-j) is ~0.8, 0.4, and 0.1, respectively, which shows superior spatial resolution of the images obtained through spheres. It should be noted that, although the refractive index contrast for the spheres-liquid case was only ~1.39 while for air-SILs were 1.458 and 2.0, the sphere provided a better resolution.

It should be pointed out that the role of mesoscale phenomena should be considered to obtain a fair comparison between the SIL microscopy technique and imaging by using liquid-immersed spheres, i.e. the performance of the microspheres should be compared with the performance of the micron-scale SILs. Nevertheless, advantages of microspheres over SILs can be summarized as the following:

i) Spheres provide more magnification factor comparing with SILs.

ii) Micron-scale spheres have superior resolution comparing with macro SILs used in this work.

iii) For spheres, resolution enhancement can be achieved even with lower NA microscope objectives in comparison with h-SILs.

iv) Microsphere manufacturing and handling is less complicated comparing with micron-scale SIL fabrication.

2.9. Comparison with Confocal Microscopy

In this section, we compared imaging resolution of our novel technique with the resolution of the established technique of confocal microscopy. In order to perform

confocal microscopy, we used an Olympus OLS4000 LEXT microscope equipped with a 100×(NA=0.95) objective lens in confocal mode. Illumination was provided at λ=405 nm. We used the gold nanoparticle dimers (NPDs) sample with 60 nm dimer's separation, shown in Fig. 2.16(a).

The result of the confocal microscopy of the sample is presented in Fig. 2.16(b). It shows that the 60 nm gaps in dimers are not resolved. However, by using a barium titanate glass microsphere with n~1.9 and D~10 μm immersed in isopropyl alcohol (IPA), the 60 nm gaps between the dimers are resolved, as illustrated in Figs. 2.16(c) and 2.16(d). Fig. 2.16(c) has been obtained by the same microscope (Olympus OLS4000 LEXT, λ=405 nm, 100×NA=0.95) operating in reflection mode (not in the confocal mode). Figs. 2.16(a-c) have been normalized by their magnification factors.

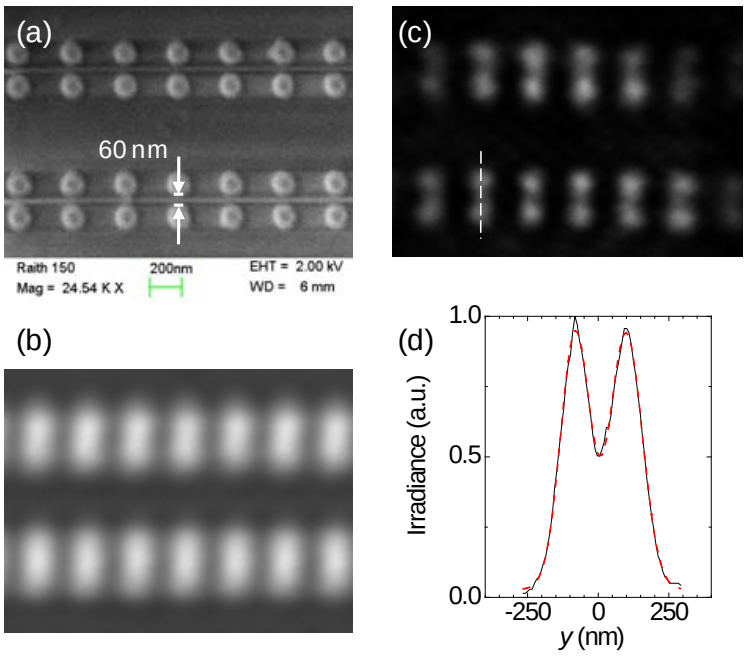

Figure 2.16: (a) SEM of the NPD sample with 60 nm dimer separation. Optical micrograph of the sample using (b) confocal microscopy and (c) a liquid-immersed microsphere. (d) Irradiance distribution along the dimer's axis shown with a dashed line in (c).

2.10. Conclusions

Projection imaging by microspheres [63] has emerged as a surprisingly simple way of achieving far-field super-resolution. Applications of microspheres in biomedical microscopy often require liquid immersion of the samples which greatly reduces the refractive index contrast of the imaging systems and diminishes their super-resolution capability. In this work, we solved this problem by proposing a novel imaging technique based on using high refractive index spheres in a liquid environment.

For liquid-immersed barium titanate glass (BTG) microspheres with refractive index $n\sim$1.9-2.1 and diameters (D) on the order of several microns, we demonstrated the ability to discern the shape of a pattern with the minimum feature sizes $\sim\lambda/7$. For larger microspheres with diameter size $50<D<220$ μm, the discernible feature sizes were found to increase to $\sim\lambda/4$. We observed that the field of view linearly increases with D reaching extraordinary large values (>30 μm) for $D>200$ μm. This property reduces the requirements to precise positioning of microspheres. The lateral magnification of the virtual images was found to be within 2.5-4.5 range for spheres with diameters in 2-220 μm range.

Possible involvement of surface plasmons in the image formation mechanism was studied by imaging silver nano-wires. Polarization-dependent imaging in reflection mode provided evidence about involvement of plasmonic resonances in silver nano-wires. However, this point requires further studies since the imaging of Blu-ray® disk showed that the similar resolution can be also achieved using non-metallic structures.

Comparison between images obtained using liquid-immersed microspheres and established techniques of solid immersion lens (SIL) and confocal microscopy showed

superior resolution and more image magnification of our technique. In addition, resolution enhancement can be achieved with lower NA microscope objectives compared with that for h-SIL. Furthermore, microsphere manufacturing and handling is less complicated compared to the [micron-scale] SIL fabrication.

The imaging method which we proposed in this chapter can be expanded to IR or UV wavelengths depending on application and can be realized using spheres made from various high-index materials such as titania or semiconductors. Depending on application, the structures can be infiltrated with water or with polymer materials. Due to its simplicity, the super-resolution imaging by high refractive index microspheres can find many applications in biomedical microscopy, microfluidic devices, and nanophotonics.

CHAPTER 3: OPTICAL CHARACTERISTICS OF LINEAR ARRAYS OF DIELECTRIC SPHERES

3.1. Introduction

A periodic sequence of lenses can relay light between two points [38], as schematically illustrated in Fig. 3.1. However, the optical losses in these types of periodically focusing waveguides are considered to be high due to the reflections at the lenses.

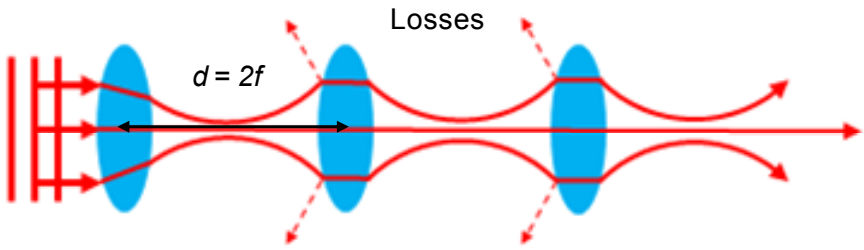

Figure 3.1: A sequence of identical lenses with focal length f and separation $d=2f$ to relay light between two points.

Integration of TE and TM polarized reflections of a linearly polarized incident plane wave on a sphere with n=1.58 immersed in water (n/n_b=1.19), allows estimating the total reflection loss ~0.27 dB/sphere [213]. This estimation is rather discouraging for developing any practical waveguiding structure based on multiple lenses (spheres) since the beam transmitted through a large number of lenses is attenuated dramatically. For example, the beam passing 100 lenses is expected to be attenuated by three orders of magnitude. Nevertheless, the successes in fabrication of well-ordered long chains of

dielectric microspheres by self-assembly or micromanipulation techniques have stimulated interest in their optical properties [125, 140-143, 214-221]. Initially, this interest was aimed at studying the light coupling between whispering gallery modes (WGMs) in chains of spherical resonators termed coupled resonator optical waveguides (CROWs), which show waveguiding with interesting dispersion characteristics [170]. The notable advance in this area has been the identification of two distinct mechanisms of optical transport in the sphere-chains [108, 139]:

i) Evanescent whispering gallery mode coupling and

ii) Nanojet coupling based on periodical focusing.

Both mechanisms have been observed in chains of polystyrene microspheres with diameters D~2-10 μm [109, 110, 139]. The optical transport properties of long sphere-chains are determined by nanojet-induced modes (NIMs) with their period equal to the diameter of two spheres ($2D$) [109, 110].

These studies have revealed two effects which remained poorly understood, at the time, when we started this dissertation. These two effects are extraordinary small attenuation of light ~0.08 dB/sphere observed in sphere-chains at long distances from the light source [110], and the gradual decrease of the lateral width of the beams that are focused periodically along the chain ("beam tapering" effect) [109]. Both effects are observed when sphere-chains are optically coupled with multimodal light sources, such as dye-doped fluorescent microspheres.

Taking into account that the experiments were performed with meso-scale spheres with $4<D/\lambda<20$, where λ is the wavelength of light, the full understanding of these effects requires an exact solution of Maxwell's equations for the entire range of variation of

spheres' diameters. In principle, such analysis can be performed by finite difference time domain (FDTD) or other techniques; however, this is a very computationally extensive problem, especially in three dimensional (3-D) cases.

In this dissertation, we state a somewhat limited, but still very important task of finding if the optical properties of chains of dielectric spheres can be explained in the limit of geometrical optics. This approach has limitations since it is only applicable to sufficiently large spheres with $D>>10\lambda$; however, this is one of the important limiting cases of the general theory, and understanding of this case is very useful for developing a more general theory. In addition, chains formed by enlarged spheres can be fabricated and tested experimentally to prove the validity of the developed theory.

The main task of this chapter is to study, experimentally and theoretically, the optical transport in linear arrays of touching identical dielectric spheres with $D>>10\lambda$. More specific questions include:

i) How much optical power is attenuated,

ii) How the beam size is changed, and

iii) How the state of polarization (SOP) is altered,

as a function of the refractive index (n) and number of spheres (N) consisting the chains.

We show that the optical properties of such chains are fundamentally determined by the periodically focused modes (PFMs), shown in Fig. 3.2. These modes have an unusual spatial configuration which significantly reduces the reflection losses compared with that of incident plane waves. We show, theoretically, that the Brewster's angle conditions for TM polarized incident rays are periodically reproduced in arrays of spheres with refractive index $n=\sqrt{3}=1.73205\ldots$ giving rise to lossless PFMs with $2D$ period and radial

(longitudinal when focused) polarization. This situation, sketched in Fig. 3.2, implies that the rays are incident on the sphere parallel to the axis of the chain and the off-axial offset (h) is fixed at a certain value to provide the Brewster's angle conditions for the TM polarization. One might think that in practice this condition can be met only for a single ray or for a circle of rays (with a right offset h) in 3-D case. In fact, we show that in order to achieve small losses, this condition is not required strictly and low-loss "quasi-PFMs" with $2D$ period exist in a range of structural parameters. More specifically, we show that along with a special case of PFMs that propagate without loss in chains of spheres with refractive index $n=\sqrt{3}$, similar periodic modes exist in a broad range of indices from $\sqrt{2}$ to 2. For each n, such quasi-PFMs have various radial extents in the regions between the neighboring spheres. We show that for 10-sphere long chains with $1.68<n<1.80$, the propagation losses for such modes are smaller than 1 dB.

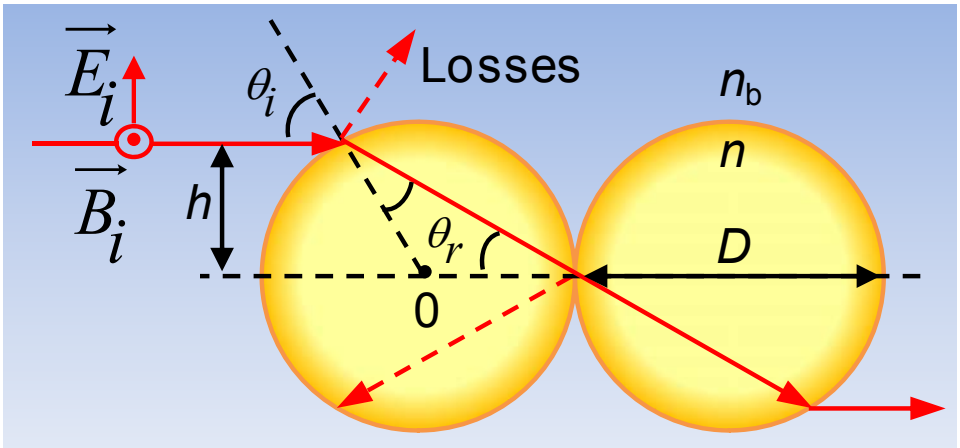

Figure 3.2: Ray picture of a PFM in a linear chain of spheres.

In many cases, we use a spherical emitter as a light source, with the same diameter D as the rest of the spheres in the chain. We show that such sphere-arrays work as quasi-

PFM filters in a broad range of indices; however the effect of PFM filtering becomes especially pronounced at $1.72<n<1.85$, which leads to a gradual "tapering" of the focused beams and a decrease of their optical power attenuation along the chain.

Taking into account the radial symmetry of the problem, TM polarization of the incident ray means that in 3-D case it corresponds to radial state of polarization of the incident beam. In addition to the spherical source of light, we also consider a collimated incident beam modeled in geometrical optics. In the latter case, degree of radial polarization in excess of 0.9 is calculated in the output of 10-sphere-long chains with $1.68<n<1.80$.

Experimentally, the "beam tapering" effect is studied in arrays of $D\sim300$ μm sapphire ($n\sim1.77$ in visible) and polystyrene ($n\sim1.59$) spheres optically coupled with a same size dye-doped fluorescent sphere as a local light source. We observed "beam tapering" effect in chains of sapphire spheres in good agreement with our modeling results.

PFM concept is very useful for developing novel focusing, wave-guiding, and polarizing components due to their extraordinary optical properties.

3.2. Periodically Focused Modes

In this section, we introduce periodically focused modes (PFMs) for linear chains of dielectric spheres in the limit of geometrical optics, which are essential for interpreting our modeling and experimental results. In the succeeding sections, we use the PFM mechanism to interpret our modeling and experimental results.

In order to find the conditions for a periodic propagation of rays in a linear chain of dielectric spheres with diameters D, we consider a ray parallel to the optical axis

impinging upon a chain, as illustrated in Fig. 3.2. The refraction of this ray depends on its angle of incident (θ_i), which depends on the lateral offset (h) of the ray with respect to the optical axis, as drawn in Fig. 3.2. Due to rotational symmetry, the refraction angles of all rays parallel to the optical axis with the same lateral offset h are equal in their respective incidence planes. Hence, each ray with a lateral offset h can be considered as a representative of a mode or family of rays with the same offset, whose locus is a ring with radius h. Such rays are periodically focused with a period of $2D$ and form PFMs when the refracted rays pass through the point where the neighboring spheres touch, leading to the following equation:

$$\theta_i = 2\cos^{-1}(n/2n_b), \tag{3.1}$$

or equivalently for the axial offset of the ray:

$$h/D = 0.5\sin(2\cos^{-1}(n/2n_b)), \tag{3.2}$$

where n_b is the refractive index of the background medium. Without loss of generality, it is considered that n_b=1 in this work. The derivation details of the equations used in this chapter are in Appendix C.

The conditions represented by Eqs. (3.1) and (3.2) describe rays, with fixed offset h, propagating parallel to the axis of the chain, which corresponds to an infinitely narrow circle of rays in a cross-sectional view. However, in any optical experimental situation, the illumination inevitably has rays with various offsets and certain range of angles, which brings about the question about how practically useful is the PFM concept. In other words, how the properties of small attenuation and periodical focusing are tolerable to the variations of the parameters of the chains, such as n. The first impression is that the variation of n would destroy the $2D$ periodicity of the PFMs. However, chains of spheres

offer another possibility, which allows preserving the 2*D* periodicity of the modes even for spheres' refractive indices different from $\sqrt{3}$. More specifically, the 2*D* periodicity can be preserved for a different axial offset of these modes. These modes will not be incident on the spherical surfaces at the Brewster's angles exactly, but their angle of incidence will still be close enough to the Brewster's angle to provide sufficiently small attenuation for some range of refractive indices.

In our further analysis, we assume that these modes play a dominant role in the transmission properties of such chains, simply due to the fact that their angles of incidence are periodically reproduced and are sufficiently close to the Brewster's angles. So, in our calculations we consider different *n*'s and calculate the amount of the axial offsets required for achieving 2*D* periodicity as a function of *n*. The result of the computation of the refractive index dependencies of the angle of incidence (θ_i) and normalized axial offset (*h*/*D*) for the modes with 2*D* periodicity is presented in Figs. 3.3(a) and 3.3(b), respectively. The defined quasi-PFMs exist in a broad range of indices ($\sqrt{2}<n<2$). The angle of incidence and axial offset of these modes decrease with the increase of the refractive index, as illustrated in Figs. 3.3(a) and 3.3(b), respectively.

The incident rays have two possible states of polarization with respect to their plane of incidence [212]:

i) TE (transverse-electric) or S (senkrecht, which means perpendicular in German), where the electric-field vector is orthogonal to the plane of incidence.

ii) TM (transverse-magnetic) or P (parallel), where the electric field vector lies within the plane of incidence.

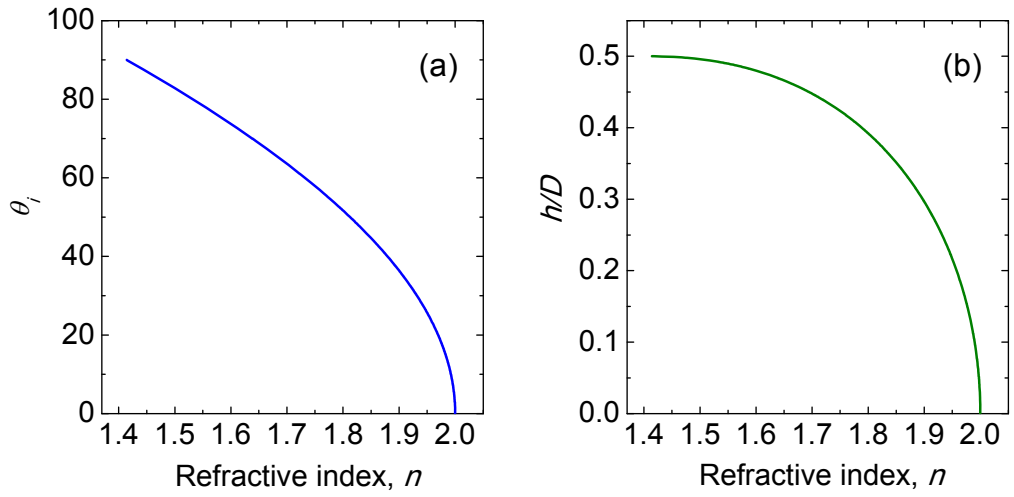

Figure 3.3: Refractive index dependences of the (a) angle of incidence and (b) normalized axial offset of the PFMs required for 2*D* periodicity.

Propagation losses for an incident ray, schematically illustrated in Fig. 3.2, is calculated by taking into account Fresnel reflection coefficients [212] at each spherical interface using the following equations for the TE and TM polarizations, respectively:

$$R_{TE} = \frac{\sin^2(\theta_i/2)}{\sin^2(3\theta_i/2)}, \tag{3.3}$$

$$R_{TM} = \frac{\tan^2(\theta_i/2)}{\tan^2(3\theta_i/2)}, \tag{3.4}$$

where θ_i is obtained from Eq. (3.1).

The modes with 2*D* periodicity tend to have smaller propagation losses due to the fact that their external (θ_i) and internal (θ_r) angles of incidence are periodically reproduced. Zero propagation loss for TM polarized rays occurs when both the external and internal angles of incidence are equal to the corresponding Brewster's angles. For a given ray incident on a sphere, if the external angle of incidence is equal to the Brewster's angle, i.e. $\theta_i = \tan^{-1}(n/n_b)$, then the internal angle of incidence is

consequently equal to the corresponding Brewster's angle, i.e. $\theta_r = \tan^{-1}(n_b/n)$, as shown in Appendix C.

The 2*D* periodicity and the Brewster's angle of incidence conditions for the rays shown in Fig. 3.2 lead to the following equation:

$$\tan^{-1}(n/n_b) = 2\tan^{-1}(n_b/n). \quad (3.5)$$

Therefore, the exact conditions for the Brewster's angle of incidence are satisfied at $n/n_b=\sqrt{3}$, $\theta=\pi/3$, and $h/D=\sqrt{3}/4$.

In physical optics, such rays correspond to PFMs with axial symmetry, 2*D* period along *z*-axis, and extremely small losses. The closest analog of such beams is cylindrical vector beams [222]. Similar to the modes in waveguides, PFMs should have properties determined by the phase; however, these properties are beyond the scope of this section. It should be noted that in the wave optics, the corresponding beams inevitably have a certain radial extent.

In our geometrical optics modeling, we allow a variation of *n* in a broad range; however, for each *n* we select the angle of incidence and axial offset of the rays in agreement with the dependences presented in Fig. 3.3. Therefore, for each *n*, the rays which form configurations with a 2*D* period inside the chain are considered. For non-absorbing spheres, the transmission losses are determined by the reflection coefficients given by Eqs. (3.3) and (3.4). For multiple spheres, these coefficients are multiplied to calculate the transmittance and corresponding reflection losses for rays with TE and TM polarization.

The transmittance and the reflection loss as a function of *n* in chains with *N*=1, 5, 10, and 20 spheres for rays with TE and TM polarizations are presented in Figs. 3.4(a) and

3.4(b). It is seen that the total transmission (zero loss) occurs at $n=\sqrt{3}$ for TM polarization which satisfies the Brewster's angle conditions. It is interesting, however, that the high transmission properties are preserved in a broad range of indices around $n=\sqrt{3}$ for the TM polarization. It is seen that for 10-sphere-long chains with $1.68<n<1.80$, where both the external and internal angles of incidence are close to the corresponding Brewster's angles, total propagation losses of TM polarized PFMs are smaller than 1 dB. For the TE polarization, PFM losses exceed 20 dB in the same range of indices, as illustrated in Fig. 3.4(b). This means that for a set of randomly polarized collimated incidence rays, the output has mainly rays with TM polarization component, as schematically illustrated in Fig. 3.5 for an incident ray parallel to the z-axis with an axial offset h. Since these rays are located around a circle with radius h represented by Eq. (3.2), the global states of polarization of the output beam tends to be radial.

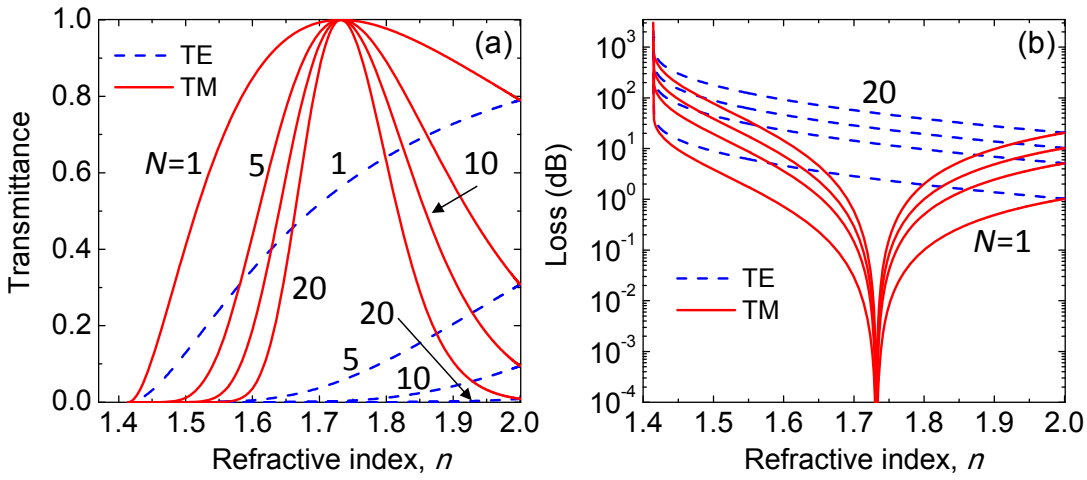

Figure 3.4: Transmittance (a) and loss (b) in chains of N=1, 5, 10 and 20 spheres as a function of n for TE and TM polarizations.

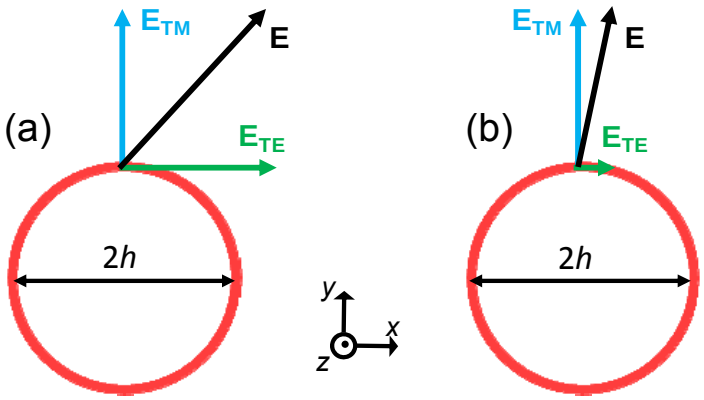

Figure 3.5: Illustration of evolution of the global SOP of transmitted beams through the sphere-chains. (a) The *z*-propagating incident ray has equal TE and TM components. (b) Upon transmission of the ray through several spheres, the TE component is attenuated dramatically, while the TM component is transmitted without loss (or with much smaller loss).

Light sources can contain not only collimated, but also non-collimated beams. The non-collimated rays are not coupled with the PFMs or quasi-PFMs, so the description of the polarization effects is expected to be more complicated in those cases. However, simple argument about the Brewster's angle conditions show that the PFMs are the best surviving type of modes in sufficiently long chains. Thus, although different light sources can be used, the state of polarization at the output of long chains can still be analyzed using the concept of quasi-PFMs. However, certainly, a more detailed modeling is required for each light source in order to quantitatively study the degree of polarization of the exiting beams. This is among the goals of the following sub-sections of this chapter.

3.3. Description of the Modeling Technique

Ray tracing is a widely applicable technique for modeling the light propagation in optical systems. The modeling of light propagation by ray tracing is commonly called geometrical optics [212]. In this work, numerical ray tracing is conducted by an optical

design software, ZEMAX-EE (Radiant Zemax LLC, Redmond, WA), in the non-sequential mode. It takes into account Fresnel reflections and refractions at the spherical interfaces, which leads both to a gradual attenuation of initial rays once they propagate through the structure and to the emergence of new rays. The rays are traced down to a weight factor (WF) of 10^{-3} which provides a good convergence of the numerical solutions.

A sphere with diameter *D* which emits rays with random polarization and direction throughout its entire volume is considered as the light source. Such a light source can be seen as a collection of point sources inside a spherical volume radiating uniformly in all directions. The source sphere (S) is placed in contact with the first sphere of a chain of spheres with the same size, as shown in Fig. 3.6.

Advantages of considering the S-sphere as a light source are:

i) A direct comparison of the modeling results to experiments performed using fluorescent dye-doped spheres can be made because the emission properties of the spherical ray emitter mimics the properties of fluorescent microspheres, in which the role of the point sources is played by dye molecules.

ii) All spatial dependencies scale with *D*, which permits use of dimensionless units: $X=x/D$, $Y=y/D$, and $z=Z/D$.

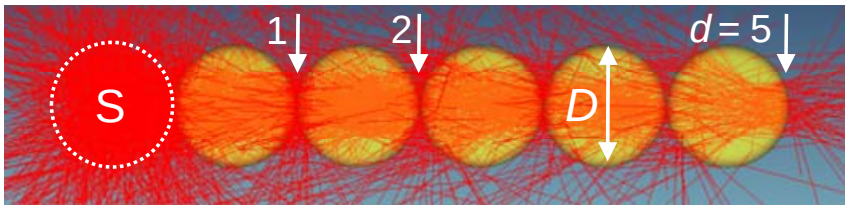

Figure 3.6: A spherical ray emitter (S-sphere) with diameter *D* is used to couple light into chains of spheres with the same diameter *D*.

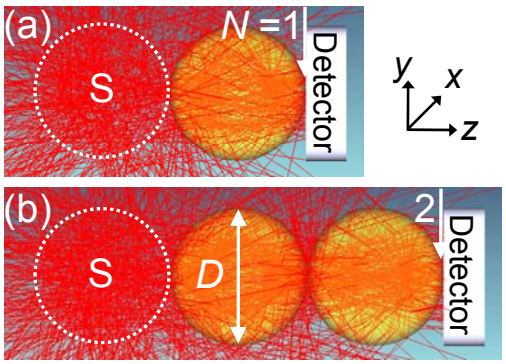

Figure. 3.7: Calculation of the transmitted power after (a) N=1 and (b) 2 identical spheres, optically coupled by a spherical ray emitter (S) with the same diameter size D.

The XY beam profiling is performed by positioning a squared-shape detector, with a unit dimensionless surface area, perpendicular to the axis in contact with the end-sphere in the chain (Fig. 3.7). It is placed at different distances, d=1, 2, …, N, measured in dimensionless normalized units from the right vertex of the S-sphere, for arrays of 1, 2, …, N spheres, respectively. The irradiance distributions (with units of $[W/m^2]$ in radiometric terminology) are calculated from the density of the rays at the detector plane with their weight factor taken into account.

The transmitted total optical power was calculated by using a disk-shaped detector, with the same diameter as the spheres in order to collect all of the transmitted power, but to avoid collection of stray light away from the structure. This detector was also placed perpendicular to the axis of the chain in contact to the end-sphere in a given chain.

The spheres are modeled by considering only the real part of their refractive index (i.e. imaginary part of the refractive index is 0 and the real part is constant) and therefore, material absorption, dispersion, and scattering are not considered. In general, a value for the wavelength should be assigned in the program, which is an important factor in cases

where material dispersion is considered, such as in calculation of chromatic aberrations in optical systems. In these cases, the materials are either directly selected from the glass catalogs of the ZEMAX or defined by considering their dispersion characteristics (Abbe number). Since our aim is to characterize optical properties of chains of spheres as a function of their refractive indices in a much broader range (which can be achieved by using different materials), we neglect the dispersion effects for a given refractive index of the spheres. Therefore, the results are independent of the wavelength in the domain of validity of geometrical optics assumptions. However, since the program needs an input wavelength, λ=550 nm is selected. This value of λ is symbolically selected because it is close to the peak emission of the dye-doped spheres used in our experiments. However, as stated before, this choice of λ is arbitrary and the results are independent of the wavelength because the spheres are considered lossless and modeled by constant refractive indices.

For each case, we study the effect of the refractive index (n) and number of the spheres (N) on the transmitted optical power and the beam size on the detector's plane in contact with the end-sphere. The transmitted power is studied over a wide range of refractive indices from n=1.4 to 3.0, and the beam size is studied for chains of up to N=100 spheres. The spheres in each chain are identical, i.e. they have the same refractive index and size.

3.4. Optical Characteristics

In the following section, we study three main characteristic features of the sphere-chains, i.e. power transmission, evolution of the transverse beam profile, and degree of radial polarization, using numerical ray tracing. The details of the numerical modeling

have been mentioned in the previous section. Here, first we begin with the study of the optical power transmission in the chains of up to 100 spheres and show that there is a range of refractive indices for which a local minimum occurs in the power attenuation plots. Then, we show that the minimum attenuation is accompanied by the "beam tapering" effect. Finally, we study the state of polarization and show that the output beams have a radial state of polarization, the degree of which increases with the number of spheres in the chain. We explain all these characteristic features based on the formation of periodically focused modes.

3.4.1. Optical Power Transport

In this section, we study the dependency of optical power on the refractive index (n) and the number of spheres (N) of the chains. First, the total power is calculated after each sphere in the sphere-chains. Then, the power attenuation is calculated in each section of the chains. Finally, the power transmission is analyzed in sections of the chains separated by different distances from the light source.

In order to study the optical power transport in chains of spheres, a sphere with a given index of refraction n is placed in contact with a same size source sphere (S) and a disk shaped plane detector with the same diameter as the spheres is placed perpendicular to the axis of the chain in contact with the end-sphere.

In the limit of geometrical optics, transmitted power is determined by the number of rays reaching the detector, with their weight factor taken into account. The total power on the detector in each case is denoted by $P_{n,N}$, where n stands for the refractive index and N represents the number of spheres in the chain. The source sphere does not contribute to the length of the chains.

In a similar manner, another identical sphere (i.e. with the same n and D) is added to the previous sphere to form an array of N=2 spheres, optically coupled from one end with the S-sphere, as illustrated in Fig. 3.7(b). By adding spheres successively to the chain and moving the detector along the z-axis of the chain, the values for $P_{n,1}$, $P_{n,2}$, up to $P_{n,100}$ are calculated. This procedure is performed in order to find the values for $P_{n,N}$ with $1.3 \leq n \leq 3$ and $1 \leq N \leq 100$. In each chain, values of $P_{n,N}$ are normalized by the value of $P_{n,1}$ in the corresponding chain. Therefore, the power after the first sphere is 1 in normalized units for all refractive indices, although their absolute powers are different due to different Fresnel losses. This approach is considered to provide a convenient way of comparing the calculated data to the experimental data, because usually the images of the dye-doped fluorescent microspheres are too bright and saturated.

The calculated relative transmitted powers in chains of N=20 spheres as a function of the number of spheres (N) for some refractive indices are presented in Fig. 3.8. The slope of each curve in each section of the chain is considered as an estimate of the optical power attenuation. The steeper slope in the first few spheres takes place due to the limited angular acceptance of the chain, which cannot be efficiently coupled to the spherical light source. The mode filtering is especially pronounced in the first few spheres, leading to increased losses (~1.2 dB/sphere) in this section of the chains. However, away from the source, the attenuation gradually decreases (the plot has less inclination) and at long distances from the source (N>10) the magnitude of attenuation is mainly determined by the refractive index (Fig. 3.8). The general trend is that the higher the refractive index the higher the attenuation. However, there exists a local minimum of attenuation in the region of $1.72<n<1.85$ due to the periodically focused modes, as will be explained later.

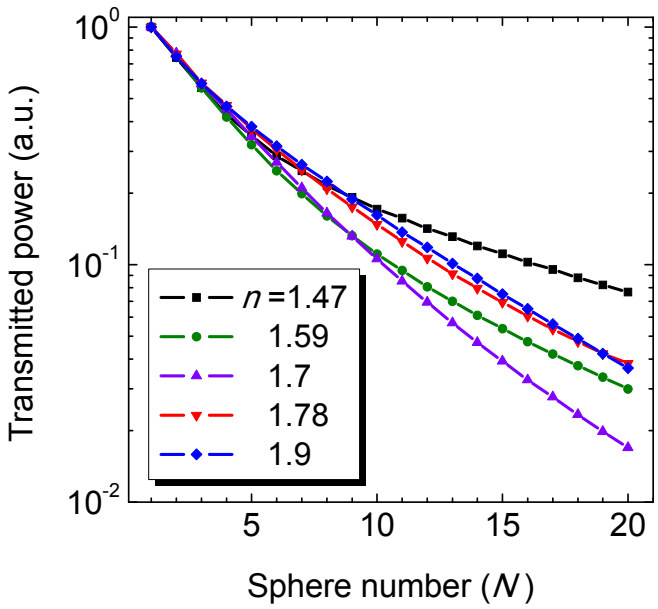

Figure 3.8. Transmitted power in chains of 20 spheres for some indices.

Although coupling is more efficient for collimated beams along the axis, this sub-optimal source (S-sphere) in terms of coupling to PFMs was selected due to the advantages mentioned in Section 3.3. Since main mode filtering processes take place in the vicinity of the source spheres, it can be suggested that the propagation effects deeper inside the chains are determined by the properties of the chains themselves rather than by the light source properties used in modeling.

The power transport characteristics are studied in more detail by calculating the power attenuation per sphere as a function of the refractive index for different sections of each chain, as presented in Fig. 3.9 for 16^{th}-20^{th}, 36^{th}-40^{th}, and 56^{th}-60^{th} sphere segments of each chain. Since partial reflections by the spheres are proportional to the refractive indices of the spheres, according to Fresnel's equations, higher attenuation for spheres with a higher refractive index is expected. However, the strong non-monotonic variations in the region of $1.72<n<1.85$ do not follow this trend. This behavior can be explained

due to the formation of PFMs. Some of the incident rays from the spherical source are reasonably close to the PFMs, or quasi-PFMs conditions, because they are close to collimated beams and have axial offsets close the optimal offset for PFMs. These rays are attenuated less, which is more pronounced as rays propagate further away from the S-sphere. In geometrical optics, the key property is the fact that although the illumination provided by the S-sphere contains a variety of meridional and skew rays, only the PFMs survive in long sphere-chains.

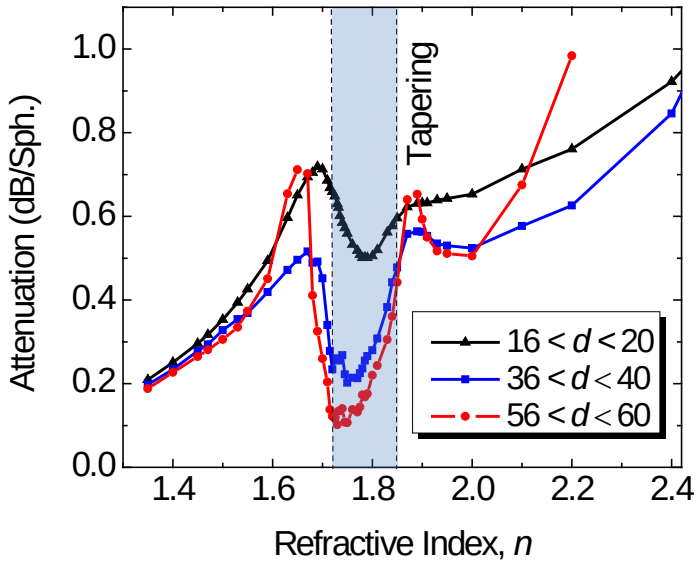

Figure 3.9: Attenuation per sphere as a function of the refractive index calculated for different segments of the chains.

3.4.2. Focusing

We study the focusing characteristics of the sphere-chains over a wide range of refractive indices ($1.3 \leq n \leq 3$). The beam reshaping that occurs as a function of the refractive index is illustrated in Fig. 3.10 for 20-sphere long chains. For n=1.5 and 1.67, the beam has an almost uniform radial irradiance distribution with the full width at half

maximum (FWHM) Y_{20}~0.4-0.5. However, for n=1.72, 1.785, and 1.85, the central section of the beam acquires a quasi-Gaussian shape with a much narrower FWHM. For n=1.785, this is indicated by Y_{20}~0.1. Further increase of n, leads to beam broadening, as illustrated for n=1.90.

The evolutions of the beam profiles at different distances (d) from the S-sphere for a chain with n=1.785 are illustrated in Figs. 3.11(a) and 3.11(c). After the first sphere (d=1), the beam has a quasi-Gaussian shape with FWHM Y_1~0.45, as shown in Fig. 3.11(c). After propagation through ten spheres, the beam profile displays a narrower central peak superimposed on a wide and flat background. After 100 spheres, the central peak becomes extraordinarily narrow and Y_{100}~0.04. In addition, an extremely narrow "ring" with diameter of ~0.8 and much weaker peak irradiance than the irradiance of the central peak is formed. The gradual tapering of the central beam, accompanied by the "ring" formation, is seen in the calculated irradiance patterns in Fig. 3.11(a).

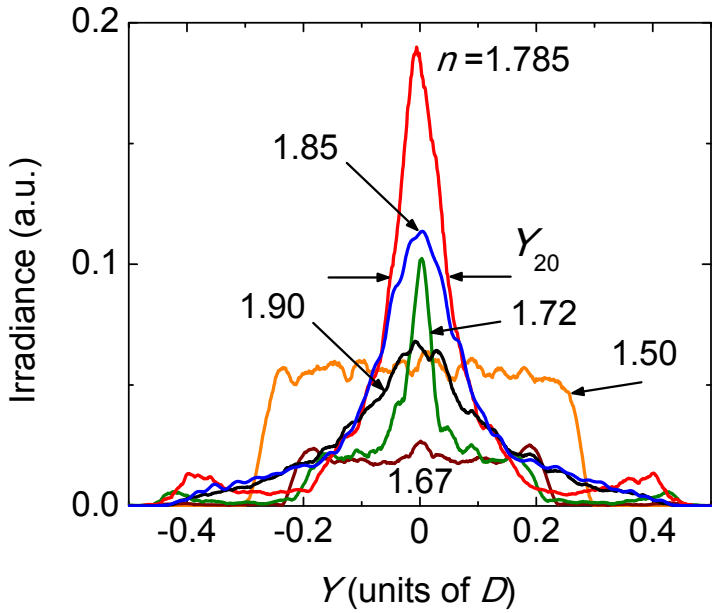

Figure. 3.10: Irradiance profiles after 20 spheres for some indices.

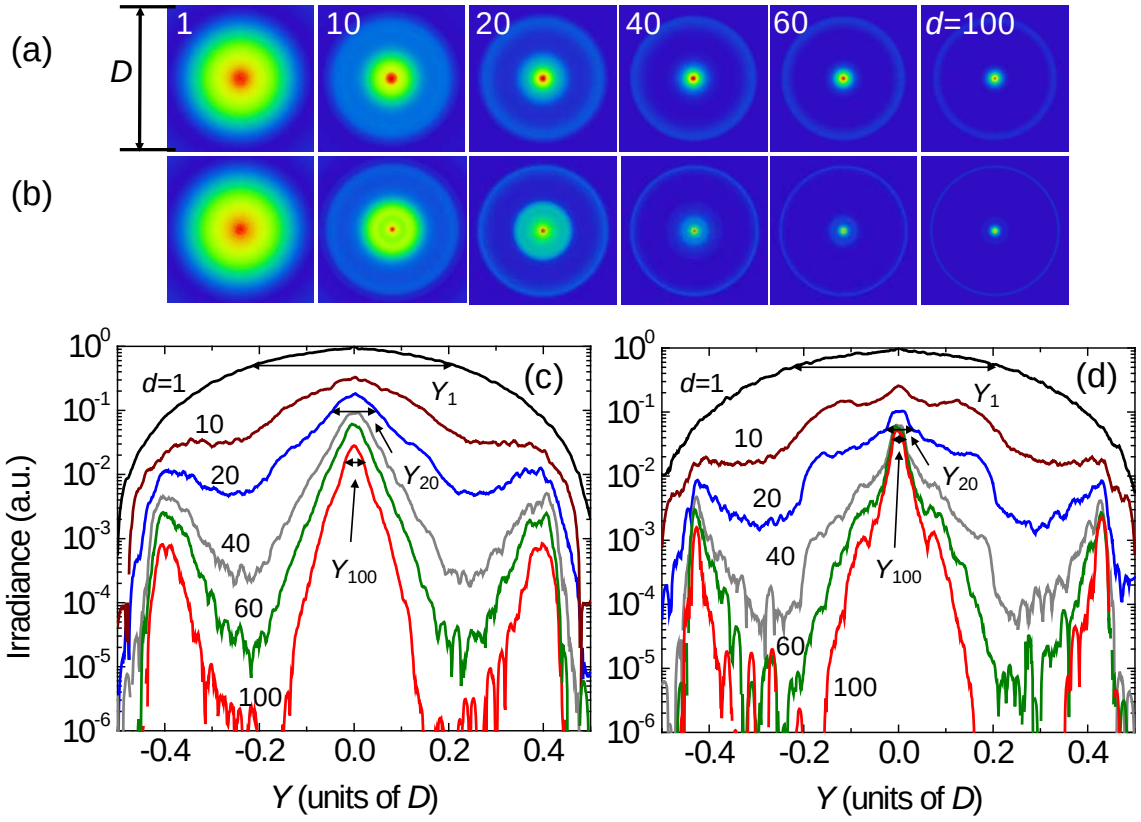

Figure. 3.11: (a,b) Irradiance patterns calculated at different distances from the S-sphere for n=1.785 and $n=\sqrt{3}$, respectively. (c,d) Normalized irradiance profiles of the calculated patterns shown in (a) and (b), respectively.

The choice of n=1.785 was because it shows local maximum irradiance in the 20-sphere-long chains, compared with other indices, as presented in Fig. 3.10. We also considered $n=\sqrt{3}$. In this case, after the first sphere, the beam has a FWHM Y_1~0.44, as illustrated in Figs. 3.11(d). After propagation through 100 spheres, the central peak becomes extraordinarily narrow and Y_{100}~0.028. In addition, an extremely narrow "ring" with a diameter of $\sim 0.84 \sim \sqrt{3}/2$ and much weaker peak irradiance than the irradiance of the central peak is formed. The gradual tapering of the central beam accompanied by a ring formation is seen in the calculated irradiance patterns in Fig. 3.11(b).

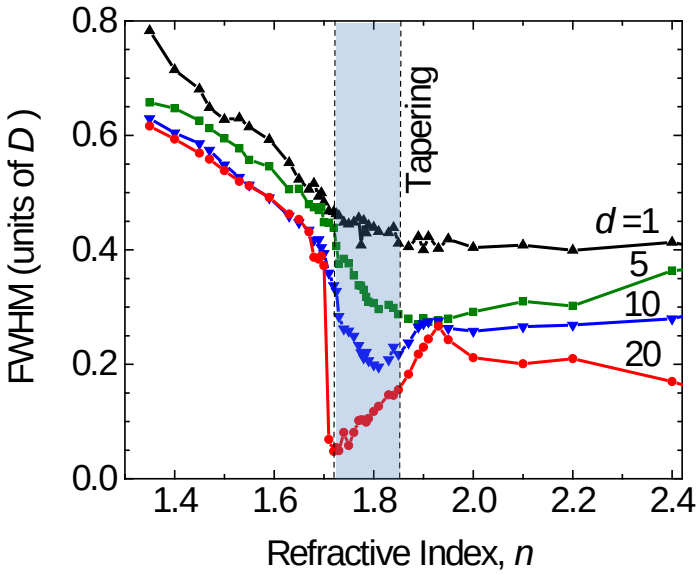

Figure 3.12: FWHMs of the central peaks calculated as a function of the refractive index at different distances in the chain.

We study the focusing characteristics in more detail by calculating the FWHMs of the irradiance profiles, as a function of the refractive index, for chains of N=1, 5, 10, and 20 spheres. The "tapering" of the central beam is clearly seen over the $1.72<n<1.85$ range at $d \geq 10$, as illustrated in Fig. 3.12. The reduction of the attenuation of the total transmitted power over this range is seen in Fig. 3.9, with a local minimum of attenuation ~0.1 dB/sphere attained at n=1.72-1.75, for a $56 \leq d \leq 60$ section of the chain.

We interpret these observed effects based on the formation and transmission of PFMs. Although the illumination provided by the S-sphere contains a variety of meridional and skew rays, only PFMs survive in the long chains. Since PFMs are sharply focused, the "beam tapering" effect is explained by the dominant contribution of PFMs in the output beams. The "ring" pattern appears due to the filtering of the second PFM shifted by D. The PFM filtering properties are actually preserved in a range of indices

from 1.72 to 1.85. For example, superposition of two fundamental PFMs shifted by D in a $16 \leq d \leq 20$ section of a chain with n=1.785 is shown in Fig. 3.13.

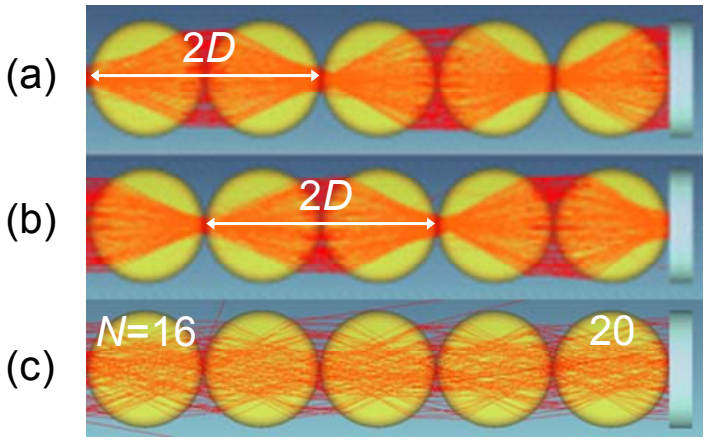

Figure 3.13: (a,b) Two PFMs shifted by D. (c) Ray tracing from 16th to 20th sphere for n=1.785 shows a superposition of two PFMs.

3.4.3. State of Polarization

State of polarization (SOP) of a light beam is a consequence of the vectorial nature of light. Spatially homogenous SOPs are linear, circular, and elliptical polarizations, where the SOP does not depend on the locus in the beam cross section [222]. However, spatially variant SOPs exist, such as radial and azimuthal polarizations, as schematically presented in Fig. 3.14.

Cylindrical vector (CV) beams, with axial symmetry in both amplitude and phase [222], are a class of beams with spatially variant SOP. They are vector-beam solutions to the full vector electromagnetic wave equation [223]. CV beams with radial and azimuthal polarizations have attracted recent attention because of their potential to create new effects mainly due to their unique focusing properties under high-numerical-aperture [222]. Various applications of radially polarized focused beams in high-resolution

microscopy, nanoparticle manipulation, remote sensing, and material processing can be found in the literature [222]. For example, it has been shown by numerical modeling and also experimentally confirmed that beams with radial polarization produce tighter focal spots with strong localized longitudinal field component [224, 225].

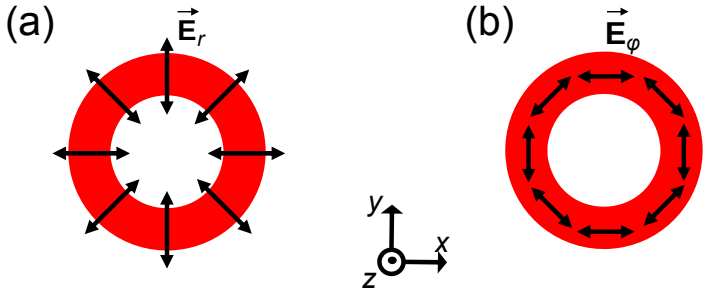

Figure 3.14: Schematic of *xy*-plane profiles of beams propagating in *z* direction with (a) radial and (b) azimuthal state of polarization.

Several active and passive methods [226-247] have been suggested to generate cylindrical vector (CV) beams with radial or azimuthal state of polarization. Active or passive methods of generating CV beams refer to methods of forming such beams inside or outside of the laser cavity, respectively. CV beams can be generated inside a laser cavity by placing a uniaxial crystal, whose axis is parallel to the optical axis of the cavity, in a telescope arrangement [226], placing a Brewster window [228] into a laser resonator with circular symmetry, linear superposition of orthogonally polarized TEM_{01} Guassian modes [230], image-rotating cavities [236], thermal bipolar lensing effect in solid-state lasers [237], a conical Brewster prism [240], and polarization-selective cavity mirrors with radial [229] or concentric [241] grooves. Generation of such beams outside a laser cavity can be utilized by interference of linearly polarized TEM_{01} and TEM_{10} Gaussian

modes [227], using subwavelength gratings [231-233], mode selection inside an optical fiber [235], propagation through a few-mode fiber excited by Lagurre-Gaussian beams [238], optical rotation by a liquid-crystal cell [239], a set of two conical reflectors and a cylindrical sheet of polarizing film [243], and using internal conical diffraction [245].

The facts that TM polarized periodically focused modes (PFMs) have extremely small losses, whereas TE polarized PFMs have extremely large losses, means that the chains of spheres can be used to generate radially polarized modes. In order to study the polarizing capability of such chains, a practical source of light, consisting of rays with random polarizations and all values of parameter h/D for $h<D/2$, is considered. Such rays are characterized with a broad range of angles of incidence θ_i. Only the TM polarized rays with parameters close to what presented in Fig. 3.3 should effectively contribute to the total transmission through sufficiently long chains.

In this section, we study the state of polarization for the output beams as a function of n and N, for sphere-chains coupled with one of the following light sources:

i) A collection of collimated rays, as shown in Fig. 3.15(a), to represent a plane wave incident in geometrical optics and

ii) The S-sphere to represent an ultimately multimodal incident beam.

The degree of polarization $P(\mathbf{r})$ of a quasi-monochromatic light beam at point $\mathbf{r}$ is generally defined as the ratio of the (averaged) irradiance of the polarized portion of the beam to its total (averaged) irradiance, both taken at the same point [212]. This rigorous and unambiguous definition of the degree of polarization is, however, sometimes difficult to use in practical cases. In such situations, various *ad hoc* definitions of the degree of polarization are frequently used in the form:

$$Q(\mathbf{r}) = \frac{|I_x(\mathbf{r}) - I_y(\mathbf{r})|}{I_x(\mathbf{r}) + I_y(\mathbf{r})}, \tag{3.6}$$

where I_x and I_y are the averaged irradiances in two mutually orthogonal directions, their choice being suggested by the geometry of the problem. Unlike the degree of polarization $P(\mathbf{r})$, the quantity $Q(\mathbf{r})$ depends on the choice of the x and y axes. It has been theoretically demonstrated [248], however, that the *ad hoc* definition in the form of Eq. (3.6) will correctly represent the degree of polarization $P(\mathbf{r})$, provided that I_x and I_y are taken to be true eigenvalues of the polarization matrix representing the symmetry of a given problem. For the cylindrical vector beams, the polarization eigenvalues are represented by the irradiances of the radially (I_r) and azimuthally (I_φ) polarized beams.

For the range of indices $1.7<n<1.8$, the output beams formed by the chains of even number of spheres, illuminated by collimated incident rays (case i), consist of:

a) A "ring" with radius h determined by Eq. (3.2),

b) A compact central beam formed by the paraxial rays, and

c) A weak background illumination.

Since the dominant contribution to the output optical power is due to the ring shape region with radius h, satisfying PFM or quasi-PFM conditions, we performe the calculations of the degree of polarization for this ring shape region.

In order to estimate I_r and I_φ, we use the fact that after an even number of spheres the irradiance distribution is radially expanded in the detector plane, as schematically illustrated in Fig. 3.14. We place a vertically oriented linear polarizer (along y) after the end-sphere in the chain, as illustrated in Fig. 3.15(c), and performe irradiance calculation in a narrow stripe region (extended along y) with dimensions $D/10 \times D/100$ placed after the polarizer, as schematically indicated by a stripe labeled I_r in Fig. 3.15(c).

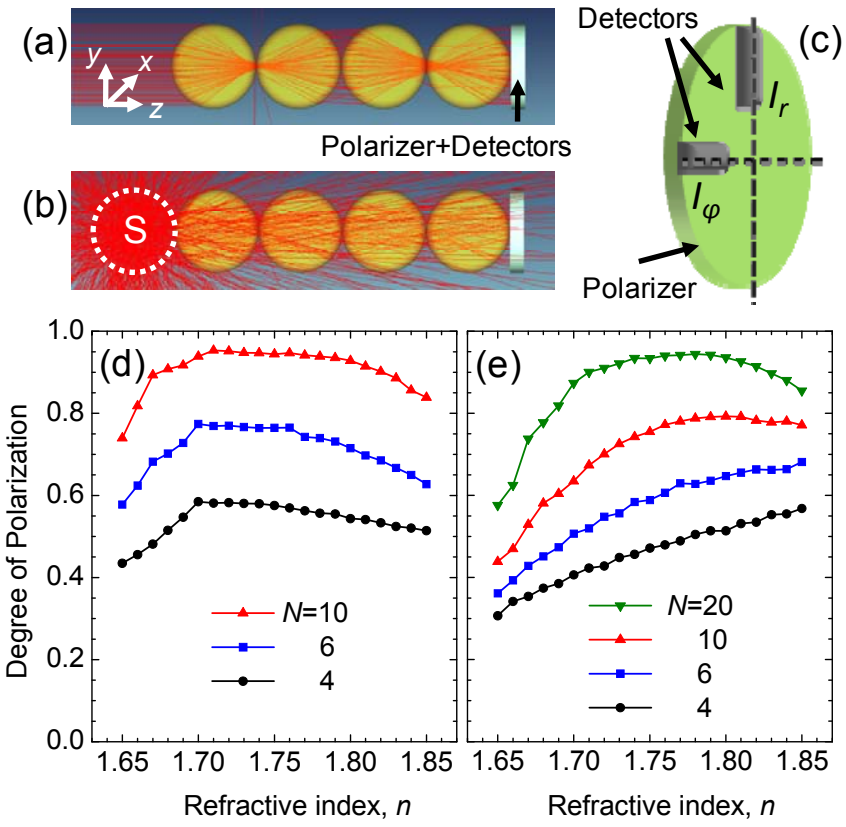

Figure 3.15: (a) Collimated rays and (b) S-sphere, used as a light source. (c) A linear polarizer, the axis of which is along y, is placed after the end-sphere before two small detectors to calculate I_r and I_φ. (d) Degree of radial polarization vs. n for N=4, 6, and 10 spheres corresponding to (a). (e) Degree of radial polarization vs. n for N=4, 6, 10, and 20 spheres corresponding to (b).

This stripe detector provides a local calculation of the irradiance of TM component of the incident rays, which can be taken as a measure of the irradiance of radially polarized beams. From the axial symmetry, it follows that an estimate of the irradiance of the azimuthally polarized beams can be obtained by using a 90° rotated stripe labeled I_φ in Fig. 3.15(c). By using relationships $I_x=I_r$ and $I_y=I_\varphi$ in Eq. (3.6), we calculate the degree of radial polarization as a function of n for chains with different lengths. The degree of radial polarization increases with the length of the chain, reaching a very high value of

~0.9 for a 10-sphere chain with any refractive index within the n=1.68-1.8 range, as shown in Fig. 3.15(d)

For case (ii), where we had S-sphere as the light source, as shown in Fig. 3.15(b), we use the same method and calculate the degree of radial polarization as a function of n for chains with different lengths. As presented in Fig. 3.15(e), the degree of radial polarization increases as the length of the chain increases, and reaches a high value of ~0.9 for a 20-sphere chain with any index of refraction within the n=1.7-1.8 range. Because of the extreme multimodal nature of the light source (S-sphere), it takes 20 spheres to reach degree of radial polarization ~0.9 in this case.

3.5. Disorder Effects

We considered so far that all spheres in the chains were in contact and identical, i.e. same size and same refractive index. Furthermore, no material dispersion and scattering were considered for the spheres. Any deviation from the ideal condition is a disorder. Disorders mainly break the symmetry in the chains; therefore, the ideal conditions for the propagation of periodically focused modes are not met. We can assume different types of disorders as will be mentioned in this section. In practice, a combination of different types of disorders can exist in a given chain.

In this section, we briefly mention different types of possible disorders and perform numerical modeling to study the effect of size variation in a perfectly linear chain of spheres. A perfectly linear chain is defined as a chain in which the centers of all spheres are placed on a single line, i.e. the optical axis.

3.5.1. Shape Disorder (Deviation from a Perfect Sphere)

For a given particle with volume V_p and surface area A_p, sphericity ψ is defined as the ratio of the surface area of a sphere with the same volume as the given particle, to the surface area of the particle according to Eq. (3.7) [249]:

$$\psi = \frac{\pi^{1/3}(6V_p)^{2/3}}{A_p}. \tag{3.7}$$

Eq. (3.7) gives ψ=1 for a perfect spherical object, and any departure from a perfect sphere gives ψ<1, according to the isoperimetric inequality [250].

Any deviation from a perfect spherical shape breaks the symmetry in the chain and so in the periodically focused modes. In Fig. 3.16, objects 1 and 4 are perfect spheres, whereas objects 2 and 3 are deviated from perfect spheres.

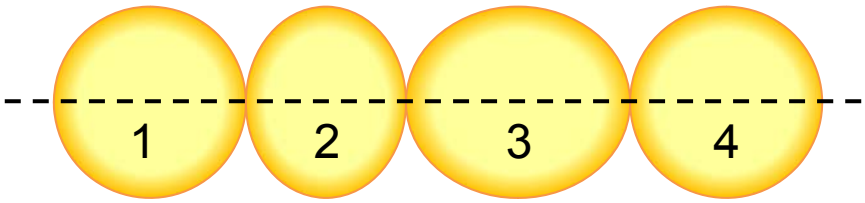

Figure 3.16: Deformation from spherical shape for objects 2 and 3.

The shape disorder can be overcome to some extent mainly during manufacturing or surface finishing process of the microspheres. Furthermore, prior to the assembling of these chains, the spheres can be visually investigated for their shape.

Experimentally, the magnitude of the elliptical deformation of spheres, which is related to the sphericity, can be estimated by measuring the splitting of the azimuthal whispering gallery modes (WGMs).

3.5.2. Spacing Disorder (Presence of Gap between Spheres)

We have considered so far that the spheres in a sphere-chain are touching each other. Introducing non symmetrical gaps between the spheres breaks the symmetry. In Fig. 3.17(a), the gaps between adjacent spheres are equal, whereas in Fig. 3.17(b) the gaps are not equal. In the case of the presence of symmetry in gaps pattern between the spheres, the structure is still periodic and the propagation of periodically focused modes might be possible at a different refractive index compared to the case of touching spheres.

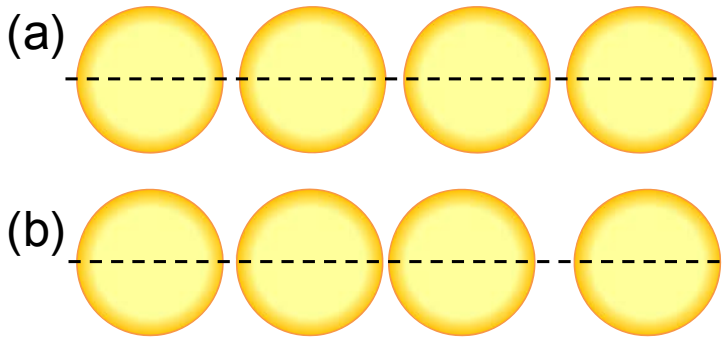

Figure 3.17: Sphere-chains with (a) symmetric and (b) non-symmetric gaps.

3.5.3. Scattering inside Spheres and from Their Surfaces

Any inhomogeneity in the spheres' material causes scattering. In order to study the effect of scattering on the periodically focused modes, in principle, local scattering points can be added to the spheres in our model.

During the fabrication process of the spheres, by purifying the material and avoiding bubble formations, the amount of scattering inside the spheres can be reduced. In order to reduce the surface scattering, the surface finishing of the spheres is a critical factor.

3.5.4. Size Disorder

Size disorder happens when the particles have [almost] perfect spherical shapes while possessing different diameters. The simplest case of size disorder in sphere-chains occurs when the centers of the spheres are placed on the same axis. We term this case of size disorder "axial size disorder". It is also possible that the centers of the spheres are not located on the same line; instead, they are located on a same plane. We term this case of size disorder a "meridional size disorder". A more general case of size disorder happens when the centers of spheres are not located on a same plane, as shown in Fig. 3.18 for a chain of barium titanate glass microspheres. We term this case of size disorder a "skew size disorder". The third sphere from the left in Fig. 3.18 looked sharper at a different depth of focus, indicating its center is placed at a different plane.

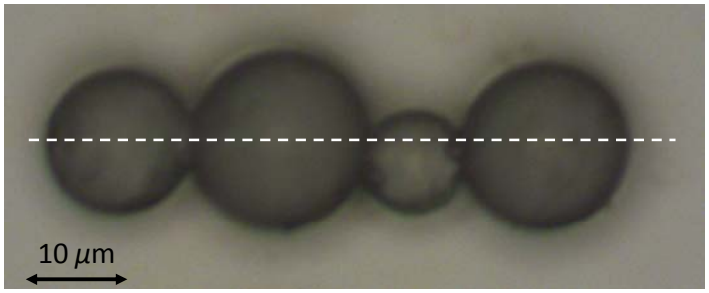

Figure 3.18: A chain of microspheres with "skew size disorder".

In this section, we perform numerical modeling to study the effect of size variation in a perfectly linear chain of spheres. The centers of the spheres are located on the same axis and the spheres are in contact. A $\pm\varepsilon$ % size uncertainty is added to their nominal diameters. If we consider ε percent of deviation in diameters from the nominal value, D_{nom}, then for the diameters of the sphere we can write:

$$D = D_{nom} \pm (\varepsilon\ \%). \tag{3.8}$$

This random distribution of diameters can be modeled using a generator of random numbers (x_i) in the range from 0 to 1 by means of the following formula:

$$D_i = \left(1 + \frac{\varepsilon}{100}(2x_i - 1)\right) D_{nom}. \tag{3.9}$$

We generate a set of 20 random numbers and by using Eq. (3.9) assign 5% size deviation to the diameters of the spheres. We model chains of 20-spheres long with the randomly disordered diameters, and calculate the FWHM after the 20th spheres and the optical power attenuation in the 16th-20th spheres regions.

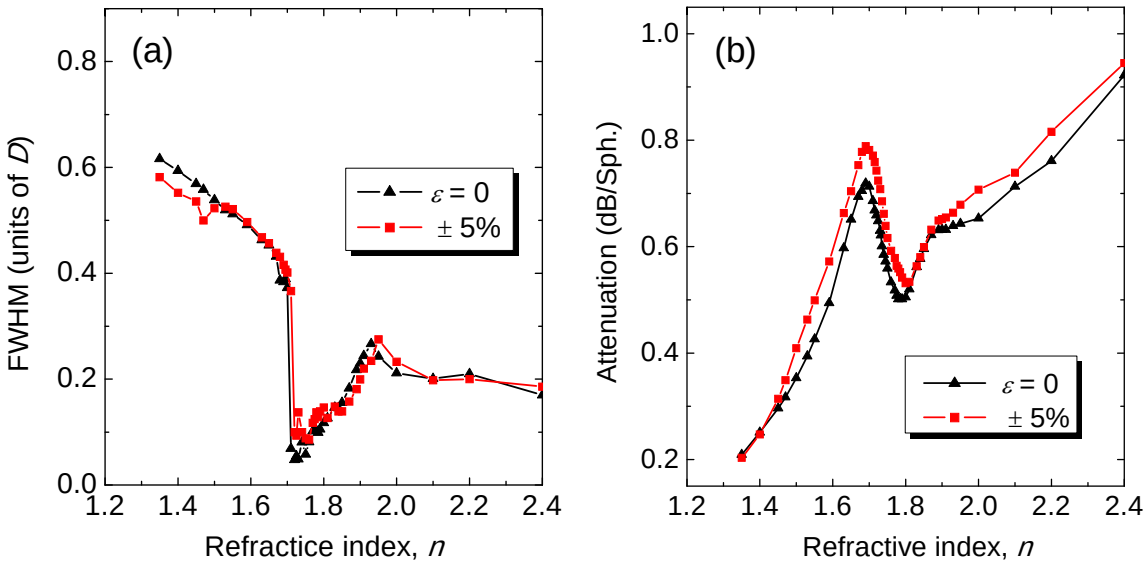

Figure 3.19: (a) Normalized spot sizes after N=20 spheres and (b) power attenuation in 16-20th section of the chains as a function of the refractive index for the ideal chains (black) and chain with ±5% size disorder (red).

As shown in Fig. 3.19(a), the "beam tapering" effect is not significantly perturbed by the disorder. The deviation from the ideal model varies based on the refractive index of

the spheres. For some indices, less sensitivity to the size disorder is seen. However, in the range $1.72<n<1.85$, the attenuation is more by ~8% compared to the perfect model. The spot sizes presented in Fig. 3.19(b) are on average larger by ~30% in the disordered structures. However, for some indices, spot sizes are smaller compared to the spot sizes in the perfect structures.

It should be noted that the results presented in Fig. 3.19 are for only one realization of the size disorder. In order to obtain a more rigorous result, we need to average the results over many realizations. By using this example, we just showed in a semi-quantitative way, that this type of size disorder (axial size disorder) does not significantly destroy the optical transport and focusing properties of the sphere-chains.

In our modeling, we modeled the spheres by a single value of the real part of the refractive index, i.e. no dispersion was considered. This assumption is reasonably valid when we have a laser source. In addition to dispersion, birefringency effect should also be considered for birefringent crystals.

One important material with good optical properties in visible and IR wavelengths is sapphire (or ruby), which is used in our experimental works at different wavelengths of illumination light. Room temperature dispersions for sapphire in the wavelength range λ=0.2-5.5 μm are obtained from refractive index of Al_2O_3, according to Eqs. (3.10) and (3.11) for ordinary and extraordinary rays, respectively [251]. This dependency is shown in Fig. 3.20.

$$n_o^2 - 1 = \frac{1.4313493\lambda^2}{\lambda^2-(0.0726631)^2} + \frac{0.65054713\lambda^2}{\lambda^2-(0.1193242)^2} + \frac{5.3414021\lambda^2}{\lambda^2-(18.028251)^2}, \tag{3.10}$$

$$n_e^2 - 1 = \frac{1.5039759\lambda^2}{\lambda^2-(0.0740288)^2} + \frac{0.55069141\lambda^2}{\lambda^2-(0.1216529)^2} + \frac{6.5927379\lambda^2}{\lambda^2-(20.072248)^2}. \tag{3.11}$$

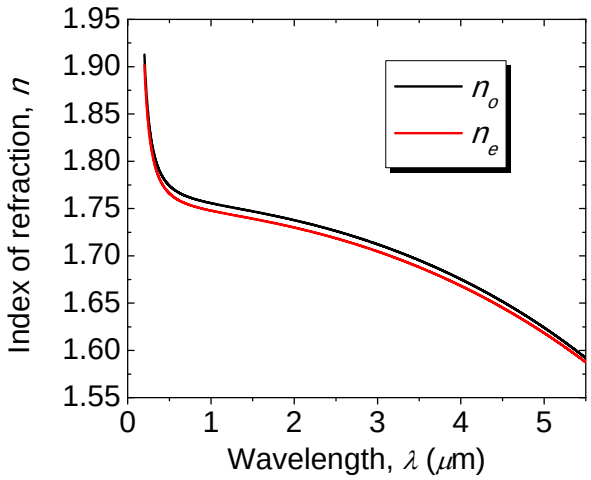

Figure 3.20: Dispersion relations for refractive indices of Al_2O_3.

3.6. Experimental Results

In the following sections, our experimental results are presented and compared to the modeling results. Fist, we describe our techniques for assembling linear chains of spheres. Consequently, the experimental results on focusing properties, optical power transport, and the phase properties of the chains of spheres are presented.

3.6.1. Assembly of Sphere-chains

We assembled the sphere-chains in two different ways:

1) Sphere-chains were assembled on glass substrates using a micro-needle, controlled by a hydraulic micromanipulator (Fig. 3.21).
2) Sphere-chains were assembled inside plastic micro-capillaries (Fig. 3.22).

The assembly of the sphere-chains by infiltration inside capillaries is generally an alternative approach compared to assembly or self-assembly on a substrate. It has an advantage that the positions of the spheres are fixed inside the capillaries and they can be carried to different experimental setups. However, the field of view is less in the case of imaging the scattered light from the sidewalls of capillaries. The motivation of using

micro-capillaries comes from an application of such focusing chains in tissue-surgery, where they should be assembled as self-supported “needles” of optical scalpels. In the next chapter, we use the same technology of assembling the spheres inside the capillaries to integrate sphere-chains with infrared hollow waveguides (HWGs) and fibers.

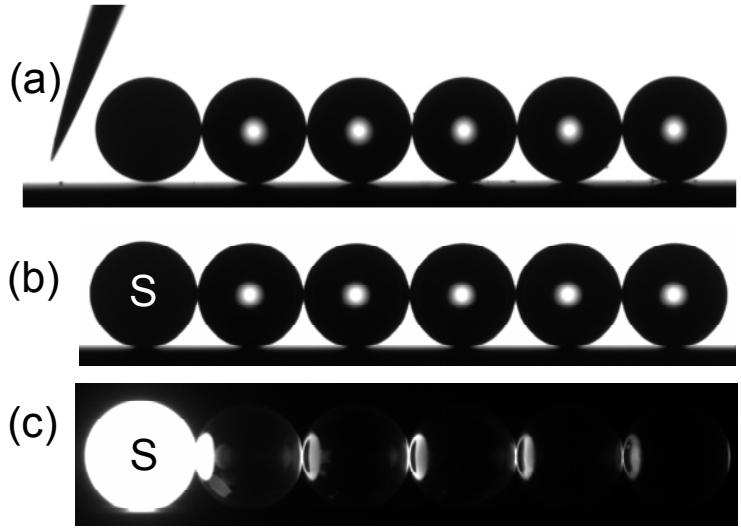

Figure 3.21: (a,b) A chain of N=5 sapphire spheres with D=300 μm, assembled on a glass substrate, using a micro needle controlled by a hydraulic micromanipulator. (c) Fluorescence emission of the S-sphere propagates in the chain.

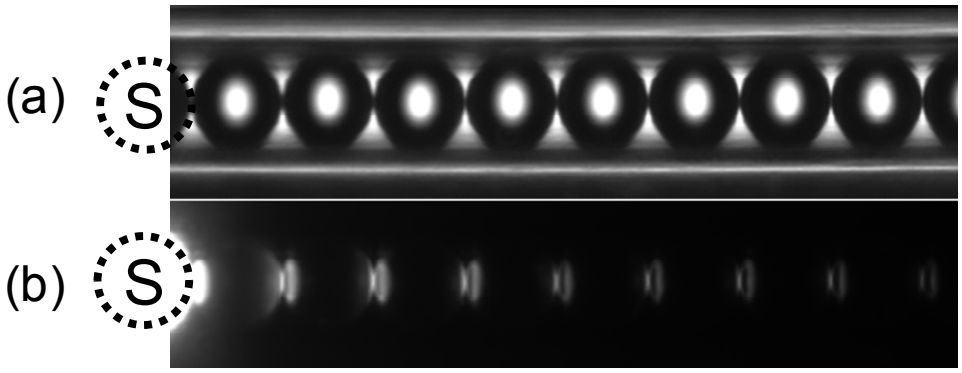

Figure 3.22: (a) A chain of sapphire spheres with D=300 μm assembled inside a PTFE tube with ID equal to the spheres diameters. (b) Fluorescence emission of the S-sphere propagates in the chain.

Infiltration was performed using micromanipulation and micro-pneumatic propelling of the spheres. In order to provide tight packing of the microspheres, while keeping the chains straight and symmetric along the axis of the cylindrical structure, the size of microspheres should match the bore size of the micro-capillary, as shown in Fig. 3.22 for 300 μm sapphire microspheres inside a polytetrafluoroethylene (PTFE) micro-capillary. Using similar technique, sphere-chains with 50 μm spheres (borosilicate glass, soda-lime glass, and barium titanate glass) were assembled inside micro-capillaries.

Since the 50 μm polystyrene microspheres, used in this work, were mixed in a liquid for preservation purposes, infiltration of 50 μm polystyrene microspheres was different from other spheres mentioned so far. A few droplets of polystyrene microspheres (D=49.7±0.7 μm) in water (Duke Scientific Corporation, Palo Alto, CA) were poured over a microscope slide (Gold Seal® Products, Portsmouth, NH). Once the polystyrene microspheres were dried, they were inserted in a PTFE tube. Then, the fluorescent dye-doped spheres were inserted to form a chain of polystyrene microspheres with local light sources [Fig. 3.27(a)]. Green fluorescent dye-doped polystyrene spheres with D=51±6 μm (Fluoro-Max™, Thermo Scientific, Fremont, CA) were used as local light sources. As a micro-capillary, a PTFE tube with 50 and 356 μm inner and outer diameters, respectively, and 150 μm wall thickness (Cole-Parmer, Vernon Hills, IL) was used.

3.6.2. Focusing Properties

Experimentally, the light focusing properties of linear arrays of dielectric spheres were studied for chains of sapphire (Swiss Jewel Company, n=1.77, D=300±3 μm) and polystyrene (Thermo Fisher Scientific, n=1.59, D=289±6 μm) microspheres assembled on a glass microscope slide. Schematic of our experimental setup is drawn in Fig. 3.23. In

order to couple light with the chains of spheres, we used a local light source (S-sphere) formed by one dye-doped fluorescent polyethylene sphere (Cospheric, Santa Barbara, CA) with the same diameter as the spheres forming the chain, placed at the begging of each chain, as shown in Figs. 3.21-3.24. The fluorescence excitation of the S-sphere was provided through a 40×NA=0.6 microscope objective at λ=340-370 nm by a mercury lamp (USH-103D, USHIO Inc., Japan) integrated with an inverted IX-71 Olympus microscope. The intensity of excitation was well below the threshold for lasing whispering gallery modes. A fraction of the total fluorescence from the S-sphere is coupled to the chain. The propagation of the fluorescence emission of the S-sphere in the chains was visible due to the light scattering away from the axis of the chain in a vertical direction toward the microscope objective, as shown in Figs. 3.24(a) and 3.24(b). The images were registered by a CCD video camera with variable exposure times and 12 bit dynamic range.

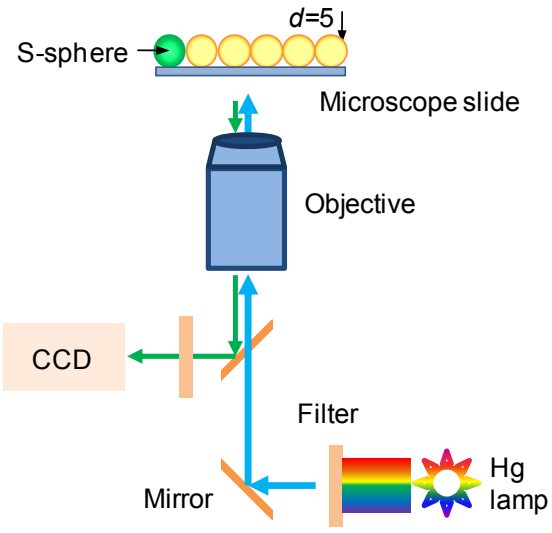

Figure 3.23: Schematic of the experimental setup for capturing the scattered light from the interfaces between the spheres.

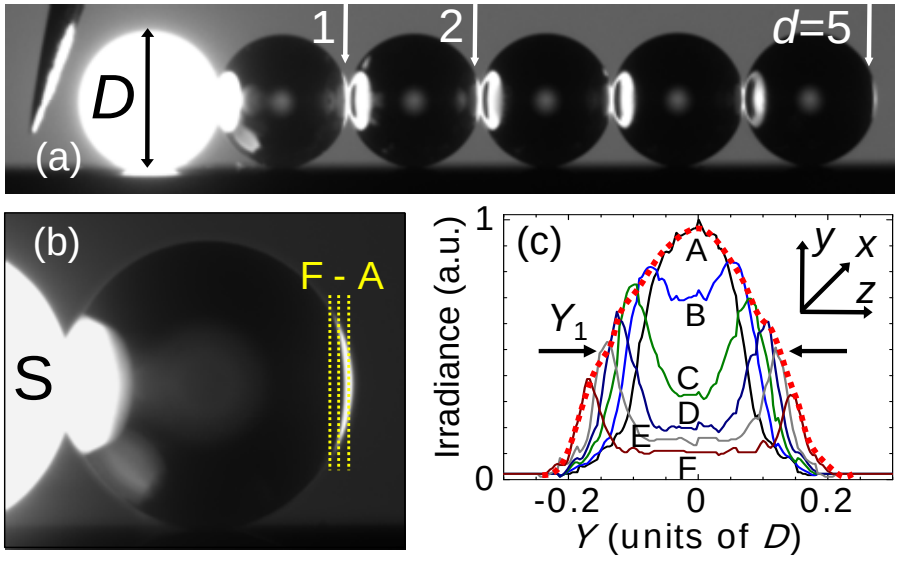

Figure 3.24: (a) A chain of D=300 μm sapphire microspheres in contact with a dye-doped S-sphere. (b) Expanded image of the scattered light at the shadow-side surface of the sapphire sphere. (c) Envelope (dashed) of the maxima of the A-F irradiance profiles with its FWHM shown as Y_1.

A digital image of the bright region at the shadow-side surface of a single sphere attached to the S-sphere was obtained with focusing at the equatorial plane of the sphere, as illustrated in Figs. 3.24(a) and 3.24(b). We assumed that due to the surface scattering, the brightness along the equator of the spheres is representative of the local intensity of the beam guided by the chain in the axial direction. This assumption allowed a simple estimation of the beam FWHM using the envelope of the maxima of the irradiance profiles measured along closely spaced lines A-F, as illustrated in Fig. 3.24(c).

A comparison between experimental and modeling results for a polystyrene and sapphire sphere is shown in Fig. 3.25. In Figs. 3.25(c) and 3.25(d), the envelopes (dashed red line) of the maxima of the irradiance profiles of experimental results for a polystyrene and a sapphire sphere, respectively, are presented. Figs 3.25(e) and 3.25(f) are corresponding modeling results, which should be compared to the envelope profiles

shown in Figs. 3.25(c) and 3.25(d), respectively. As seen in Fig. 3.25, a good agreement exists between the modeling and experimental results.

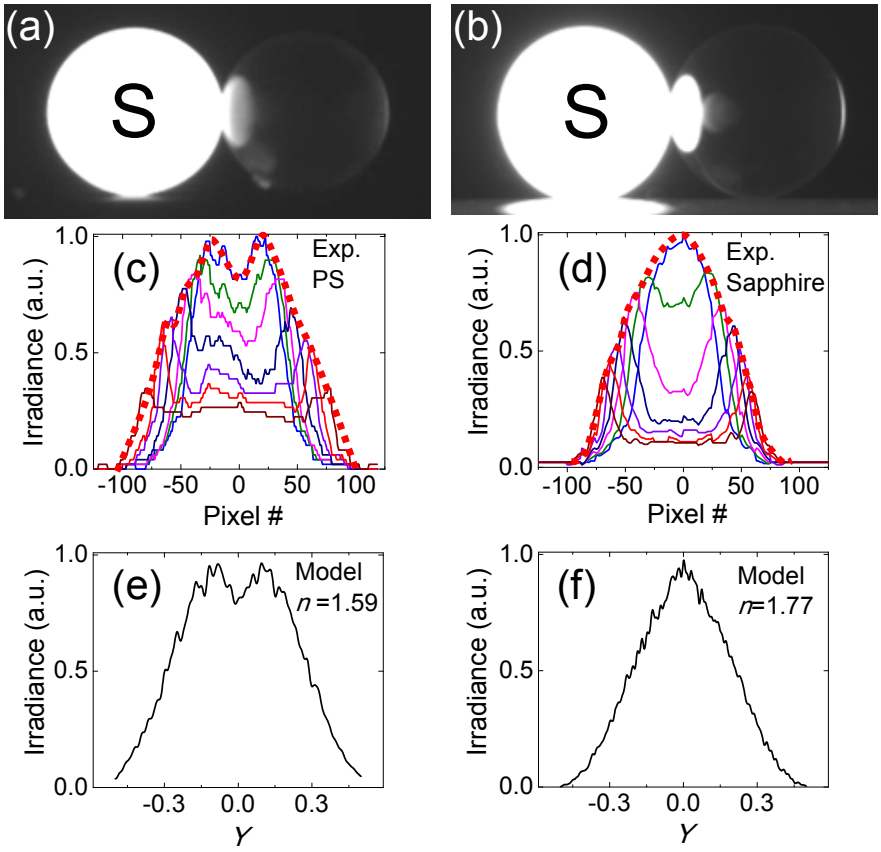

Figure 3.25: (a,b) A polystyrene and sapphire sphere, respectively, with D=300 μm coupled with a dye-doped fluorescent S-sphere. (c,d) Different irradiance cross sections at the distal surface of the spheres (a) and (b), respectively. The envelope of the maxima of the irradiance profiles is represented by the dashed curve. (e,f) Modeling results corresponding to (c) and (d), respectively.

We performed experiments for several chains of up to 12 polystyrene and sapphire spheres. The spheres were added one by one to each chain and images were recorded for each case. The spot sizes (Y_d), measured from the images, were normalized to the size of the first spot in the corresponding chain (Y_1), in order to compare them in a single plot.

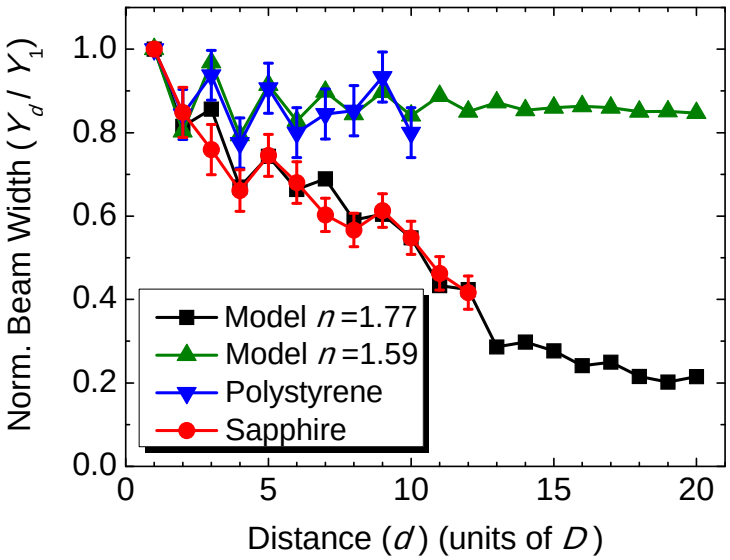

Figure 3.26: Normalized beam FWHM (Y_d /Y_1) measured for sapphire and polystyrene sphere-chains and comparison to the modeling for n=1.77 and 1.59, respectively.

Our measurements performed for chains of sapphire and polystyrene spheres with variable lengths, using the same procedure, showed the pronounced "beam tapering" effect in sapphire chains very well, and the absence of this effect in the polystyrene chains, as illustrated in Fig. 3.26. A very good agreement exists between the normalized beam FWHMs (Y_d /Y_1) and the corresponding modeling results in both cases, as demonstrated in Fig. 3.26.

Since experimental observations from chains of sapphire microspheres (n=1.77 and D=300 μm) shows progressive beam size reduction in agreement with the modeling results, and furthermore, experimental results for polystyrene (n=1.59) spheres are also in an agreement with the geometrical optics modeling results, which shows that the "beam tapering" effect is absent for polystyrene spheres, therefore, we presume that the "beam tapering" effect, which was observed previously by Dr. Astratov's group in chains of

mesoscale polystyrene microspheres (n=1.59 and D=2-5 μm) [109], is due to the mesoscale optical properties, when the ratio of the sphere diameter and the wavelength of light is less than 10. Another potentially important factor can be connected with a possible role of microjoints [142, 143] formed between adjacent spheres, as introduced in Section 1.3.2 of Chapter 1. Fundamental understanding of the role of mesoscale phenomena, such as interference and diffraction, and microjoints developed between the microspheres is needed to explain the "beam tapering" effect for wavelength-scale polystyrene microspheres.

3.6.3. Optical Power Transport

Since the main aim of this chapter was to understand the optical properties of chains of spheres in the limit of geometrical optics, we performed detailed measurements of the optical power attenuation in structures formed by sufficiently large spheres with 50 μm diameters ($D\sim100\lambda$). We studied sphere-chains made from borosilicate glass (n=1.47), soda-lime glass (n=1.50), polystyrene (n=1.59), and barium titanate glass (n=1.9) spheres.

The assembly of the sphere-chains was performed differently in this section compared with Section 3.6.2. We used infiltration inside capillaries, as described in Section 3.6.1, and found that the field-of-view was sufficient for developing light attenuation studies in this section.

The light optical power attenuation properties of chains of microspheres inside micro-capillaries were investigated by imaging through the sidewalls by collecting the scattered light, as mentioned in previous section. Fig. 3.27(a) illustrates a chain of 50 μm polystyrene spheres assembled inside a plastic micro-capillary. In order to couple light

with the sphere-chains, we used local light sources formed by a few fluorescent polystyrene spheres (Thermo Scientific, Fremont, CA) with the same diameter as the spheres forming the chain, placed at the begging of each chain. Several spheres as light sources behave somewhat different from a single S-sphere. The difference is that periodically focused modes (PFMs) can settle in the source spheres before entering the un-doped spheres. Actually, this difference was experimentally observed in Ref. [109] due to different attenuation properties away from such sources.

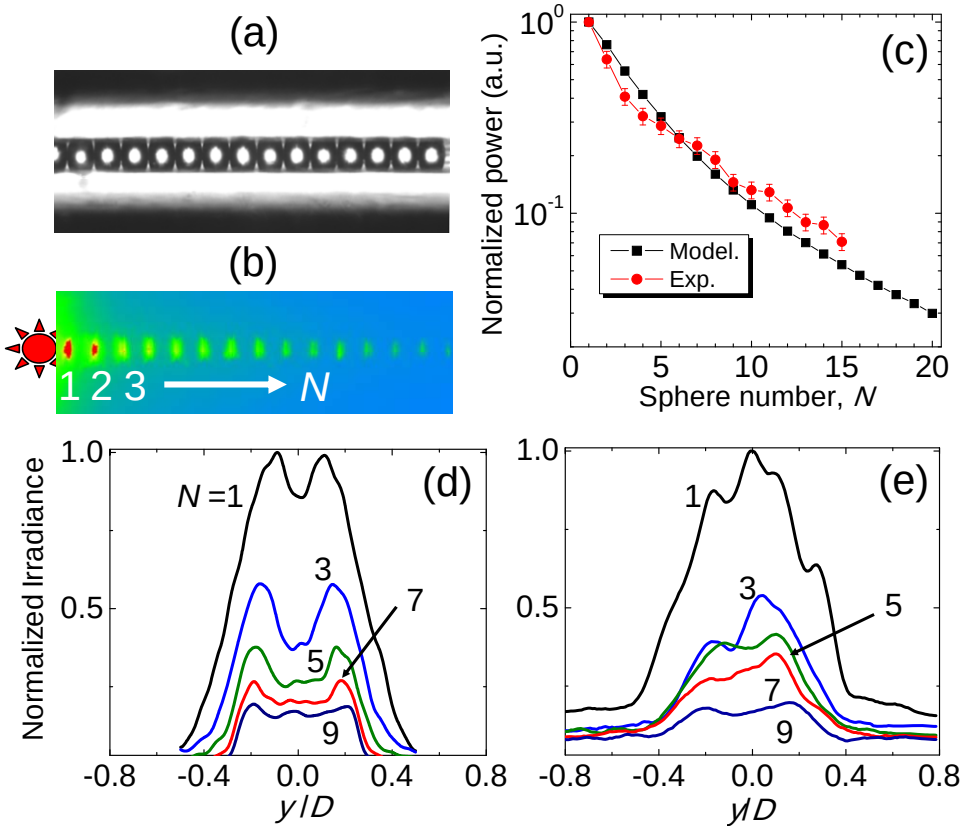

Figure 3.27: (a) An array of 50 μm polystyrene spheres assembled in a plastic tube. (b) Light propagation in (a) when exited by UV. (c) Measured (experiment) and calculated (modeling) total transported power in (b). (d) Ray tracing results of irradiance profiles for chains of polystyrene spheres to be compared to the experimental results (e).

The imaging through the transparent cylindrical sidewalls was performed in the same experimental setup as described in Sections 3.6.2, except that the fluorescence excitation was provided at λ=460-500 nm to match the excitation spectra of the dye-doped fluorescent polystyrene spheres used in the experiments of this section. In order to eliminate any possibility of detecting excitation at 460-500 nm, the images were obtained through a spectral filter at λ>510 nm.

Light propagation in a chain composed of 50 μm polystyrene spheres is presented in Fig. 3.27(b). Since the condition of collection of scattered light is the same along the chain, one can assume that the summation of pixel grey level values contained in each bright spot should be proportional to the optical power propagating after each sphere inside the chain. The total power contained in each bright region is estimated by integrating the pixel grey level values within certain area in each bright spot. It is important to notice that this is an integrated irradiance (i.e. total optical power) after each sphere. Similar to the calculated optical power distributions in Fig. 3.8, the experimental data are also normalized on the power level determined after the first sphere in the chain, i.e. the position indicated by 1 in Fig. 3.27(b). The experimental results obtained by the technique described above are represented by red dots in Fig. 3.27(c), which is in reasonable agreement with the results of numerical ray tracing, presented at the same plot. A slight difference between the results of measurements and modeling can be explained by the role of partially reflecting walls of the micro-capillary, which is not taken into account in our calculations. Similar results are obtained for chains formed by the borosilicate and soda-lime glass spheres. For chains formed by high-index (n=1.9) barium titanate glass spheres, the experimentally measured transmission are less than the

theoretical values due to the absorption of light by the material of microspheres at 510-570 nm.

Modeling results of irradiance distribution for chains with odd number of spheres (n=1.59) are presented in Fig. 3.27(d), and the corresponding experimental irradiance profiles are presented in Fig. 3.27(e). By comparing Fig. 3.27(d) to Fig. 3.27(e), it is seen that an agreement exist between the modeling results performed for free-standing polystyrene spheres, and experimental results performed for spheres assembled inside capillaries. As predicted by the modeling [Fig. 3.27(d)], "beam tapering" effect is not observed experimentally [Fig. 3.27(e)] for chains of polystyrene spheres with $D>>\lambda$.

3.6.4. Phase Properties

The experimental study of phase properties of periodically focused modes (PFMs) was performed in a collaborative work with Dr. Anatole Lupu from CNRS (Centre National de la Recherche Scientifique), France. In summer of 2011, Dr. Astratov was awarded a travel grant of a French Program, Triangle de la Physique, which attracts internationally recognized scientists to French laboratories. The broader goal of this program is to seed the international and national collaborations based on the proposals of international visitors. One of these laboratories was Institute for Fundamental Electronics (IEF) affiliated with University of Paris, where Dr. Astratov established collaboration with Dr. Lupu. The experiment design and interpretation of the results of this section were done jointly. The experiments were performed during Dr. Astratov's visit at IEF and they were later continued by Dr. Lupu. The samples were fabricated at UNCC.

The idea of the collaborative experimental project was to combine the fabrication capabilities and basic optical characterization as well as the developed theory at UNCC

with more advanced ultrahigh resolution spectral transmission measurements available at IEF. These measurements allow studying the PFM phase properties. A simple way to take into account the phase properties in PFMs is to assume that quasi-plane waves are traveling within the chain, approximately along the trajectory of the optical rays. This approach permits us to maintain the simplicity of ray optics but at the same time retain the phase associated with the wave, so that the self-consistency condition (similar to that in waveguides) or the condition for constructive interference of the waves can be used. Using the analogy with the waveguides, we can assume that this approach is applicable only to sufficiently large spheres $D>>10\lambda$.

The experimental study of phase properties of the PFMs is based on launching multiple modes into a chain of spheres and studying the spectral oscillations of the irradiance of the beam transmitted through the chain, as illustrated in Fig. 3.28. Different modes experience back and forth reflections in such structures that can be understood due to the presence of multiple low-Q Fabry-Perot resonators with different effective lengths (l_i, where i=1, 2, … is the modal number) depending on the geometrical configuration of these modes. By performing a fast Fourier transform (FFT) of the transmission spectra, we are able to find the optical path lengths (L_i) of these resonators. Using the model of a parallel plane Fabry-Pérot cavity, this path length can be represented as $L_\mathrm{i} = l_\mathrm{i}\, n_\mathrm{i,eff}$, where $n_\mathrm{i,eff}$ is the effective refractive index experienced by a given mode. Thus, the path length positions of the peaks in FFT spectra, in principle, allow identification of the modes responsible for the optical transport in a given structure.

The experimental setup used in this work is illustrated in Fig. 3.28(a). The chains of high quality ruby spheres (Swiss Jewel Company, n~1.74 at λ~1.2 μm) with D=300±3

μm were assembled inside transparent flexible Tygon® tubing (Cole-Parmer Instrument Company, Vernon Hills, IL) with internal diameter ID=250 μm. The fact that ID<D provided a tight packing of spheres with their precise axial alignment inside the tube, as shown in Fig. 3.28(b). Using pneumatic and hydraulic micromanipulators the spheres were assembled in a contact position inside the tube. The end sphere was slightly extended from the tube to provide good optical access to the last focused beam in the chain.

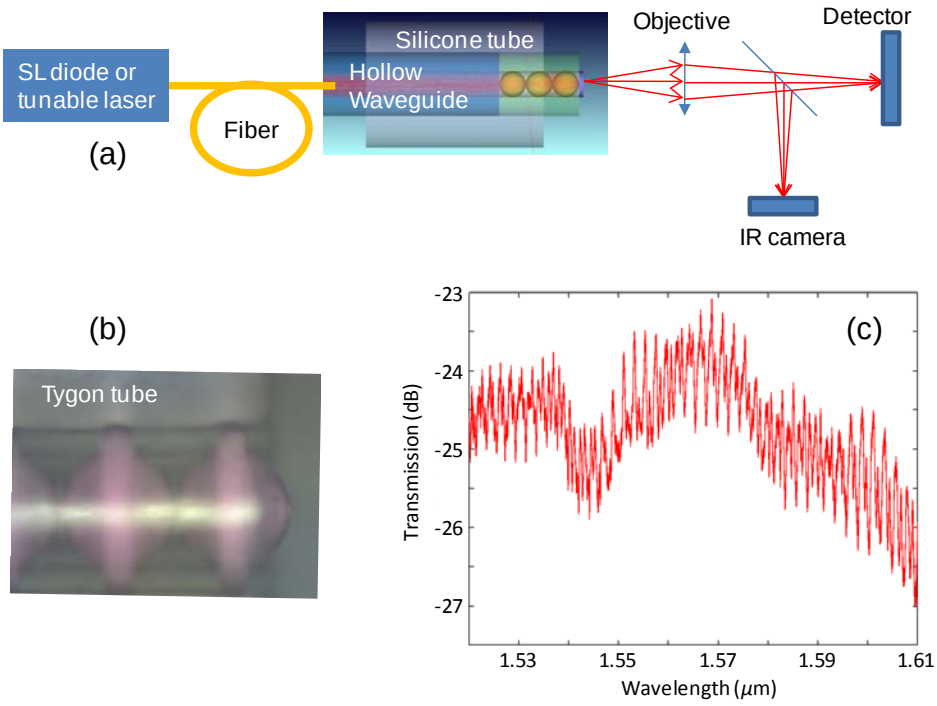

Figure 3.28: (a) Experimental setup. (b) Tight packing of D=300 μm ruby spheres inside plastic tube. (c) Typical high resolution transmission spectrum for a three-sphere chain illustrating a complex pattern of oscillations.

As a source of light we used either a super luminescent OptoSpeed diode with ~50 nm spectral half-width centered at λ~1.2 μm or a tunable YENISTA system which

covers a wide range of wavelengths from 1250 to 1650 nm. The YENISTA system provided mode-hop-free sweeping operation through the entire range of tenability, with a ~1 pm wavelength resolution. The light was coupled into a standard telecommunication fiber, which was inserted into a 30 mm piece of hollow waveguide (HWG) (Polymicro, Phoenix, AZ) with ID=300±20 μm. The chain of microspheres was integrated with the HWG using a silicone tube, as illustrated in Fig. 3.28(a). Although the HWG was not designed to operate at λ~1.2-1.6 μm, we estimated that the total propagation losses in the HWG were limited to a few dB in our experiments.

The purpose of this setup was to provide illumination with multiple meridional and skew rays with an ~10-15º range of propagation directions. The focused beam produced by the end sphere was imaged at the Hamamatsu InGaAs camera and at the same time at the detector of the YENISTA system, as shown in Fig. 3.28(a). A typical transmission spectrum with ~1dB oscillations is illustrated for a three sphere chain in Fig. 3.28(c).

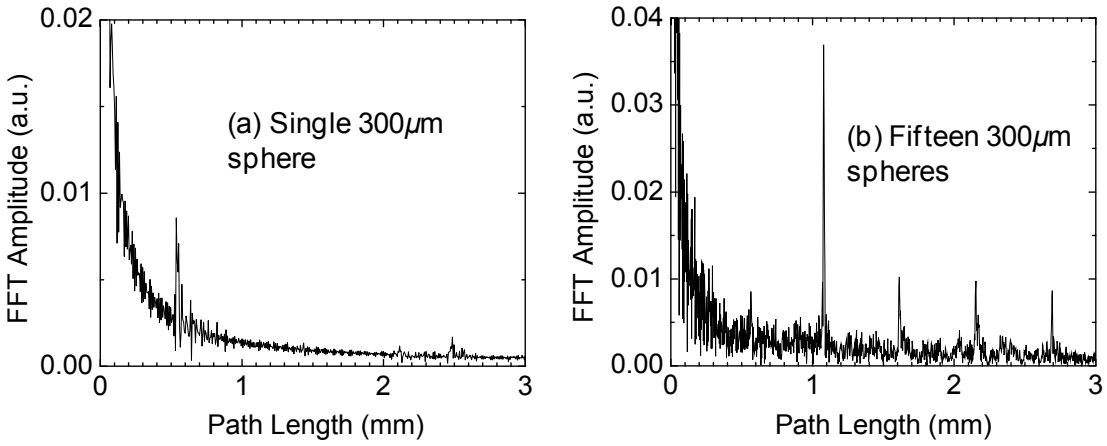

Figure 3.29: (a,b) FFT amplitudes found in transmission spectra of single spheres and 15-sphere long chains with D=300 μm, respectively.

The fast Fourier transform (FFT) amplitudes measured for a single sphere and for a 15-sphere chain are presented in Figs. 3.29(a) and 3.29(b), respectively. The peaks represent modes with different spatial periodicity in the structure. The single sphere gives rise to a dominant peak with the path length L_1=536 μm, which was found to be very close to the product $Dn_{1,\text{eff}}$, where $n_{1,\text{eff}}$ =1.75 is the refractive index of ruby at λ~1.2 μm. This allows us to interpret this peak due to the internal reflections of the rays passing through the center of the sphere. In contrast, the 15-sphere chain shows a series of peaks with the positions which are the multiple integers of L_1, as shown in Fig. 3.29(b). The dominant peak with a path length L_2=1079 μm can be associated with a periodically focused mode (PFM). It can be shown that despite the complicated PFM configuration, the effective cavity length is close to $2L_1$ in this case, in very good agreement with the position of the dominant FFT peak. Thus, these results provide strong evidence that the PFMs are the best surviving modes in long chains of spheres.

3.7. Conclusions

In this chapter, we introduced the concept of periodically focused modes (PFMs) in linear arrays of dielectric spheres in the limit of geometrical optics considerations, which is a reasonable approximation for $D>>10\lambda$, where D is the diameter of the spheres and λ is the illuminating wavelength. We showed that PFMs are a key concept for understanding light focusing and transport properties of coupled microspheres with sufficiently large diameters. We, theoretically, demonstrated that PFMs are responsible for small light attenuation (<0.1 dB/Sphere) in long chains, and efficient transmission of PFMs leads to gradual tapering of the periodically focused beams.

We showed, theoretically, that when $n=\sqrt{3}=1.73\ldots$ a special type of TM polarized incident rays propagate through the chain without attenuation under the Brewster's angle conditions. These rays give rise to PFMs with the period $2D$, which can be considered as a geometrical optics analog of nanojet induced modes (NIMs) observed in earlier works using micron-scale polystyrene microspheres [109, 110]. Via numerical ray tracing, by considering a spherical emitter, we showed that chains of spheres are natural PFM filters that lead to "beam tapering" effects and dramatic reductions of optical power attenuation for $1.72<n<1.85$.

We observed the "beam tapering" effect in chains of sapphire ($n\sim1.77$) microspheres with $D=300$ μm and showed very good agreement between the experimental results and the theory. The results scale with the diameter of the spheres and can be used for developing novel light focusing devices, which can be coupled with multimodal fibers or waveguides to operate in contact with a medium such as tissue. Examples of such applications include ultra-precise laser procedures in the eye and brain [171, 174] or piercing a cell [172], as well as for coupling light into photonic microstructures. Another interesting possibility is based on using microspheres made from optically nonlinear and/or active materials, where a combination of sharp focusing with periodicity should result in efficient optical parametric and lasing processes.

Furthermore, using geometrical optics approximation, we showed that along with the PFMs in sphere-chains with refractive index $n=\sqrt{3}$, which propagate without loss, similar modes should exist in a broad range of indices from $\sqrt{2}$ to 2, giving rise to quasi-PFMs which have the same $2D$ period, but different amount of lateral extent depending on the refractive index of the spheres. These modes have very small propagation losses for TM

polarization and extremely high losses for TE polarization that allows developing efficient filters of radial polarization. Due to symmetry considerations, such chains can be considered as filters of radial polarization. We showed that for 10-sphere long chains with $1.68<n<1.80$, such modes have total propagation losses smaller than 1 dB. Our approach is applicable to sufficiently large spheres with $D\geq 10\lambda$. Using a collection of collimated rays with random polarization as a model for the collimated incident beams, we demonstrated high degree of radial polarization (~ 0.9) of the beams formed by the 10-sphere long chains. These properties make chains of microspheres very interesting subject for developing novel focusing elements with polarizing capability.

Finally, in this chapter, we studied the phase properties of PFMs using a novel method based on a combination of ultrahigh resolution spectroscopy with Fourier analysis of the transmission spectra of chains of ruby spheres. We demonstrated that PFMs are the best surviving modes in long chains of spheres. Transition to physical optical properties with interference and diffraction effects is expected in the case of smaller spheres ($D\leq 10\lambda$) which can lead to novel applications of such structures.

CHAPTER 4: DESIGN, FABRICATION, AND TESTING OF FOCUSING MULTIMODAL MICROPROBES

4.1. Introduction

Focusing microprobes provide a stable and well-confined electromagnetic beam, which can be scanned or directed over a photonic structure or biological sample, with potential applications in laser surgery [171], piercing of a cell [172], optical endoscopy and spectroscopy [173], high-density optical data storage [146, 148], photo-induced pattering of thin films [154, 157, 158], and more. If a tight focusing of the optical beams is required in combination with their flexible delivery, the solution is provided by single-mode optical fibers. However, in a number of biomedical applications, where infrared electromagnetic beams are delivered by hollow waveguides (HWGs) or multimode fibers, providing sharp focusing of light is a complicated task due to the multimodal nature of the transmitted beams.

In this chapter, we aim to develop ultra-precise contact-mode microprobes, which ablate tissue under touching conditions with the tip of the optical scalpel. A potential application of our work for treatment of proliferative diabetic retinopathy (PDR) has been discussed in Section 1.4 of Chapter 1.

As reviewed in Section 1.4.2 of Chapter 1, mid-IR flexible delivery systems, such as fibers and HWGs, are usually multimodal, that makes the beam focusing very difficult. Over the past two decades, various optical elements including spheres [179], hemispheres, domes, cones, slanted shapes [180, 181], cylindrical gradient index (GRIN)

lenses [174], and tapered fibers have been tested as ophthalmic laser probe tips. These devices are usually designed to operate in a non-contact mode in air, and lose their focusing capability in contact with tissue, as illustrated in Figs. 4.1(a) and 4.1(b). In addition, in the non-contact mode, it is difficult to control the working distance during the surgery, that may result in large (>100 μm) and variable beam sizes in tissue. It is interesting to note that by using high refractive index spheres, the focusing can be formed just at the tip of the device, thus making the position of the maximal irradiance in the beam less sensitive to the presence of the external medium, as illustrated in Figs. 4.1(c) and 4.1(d). Therefore, designing such a focusing device is desirable for the contact-mode operation.

As reviewed in Section 1.3.2 of Chapter 1, a wavelength-scale microsphere with refractive index $n\sim1.6$ produces a narrow focused beam termed a "photonic nanojet" on the shadow-side surface of the sphere [86, 87]. Such a nanojet propagates with little divergence for several wavelengths into the surrounding medium, while maintaining a subwavelength transverse beam width. Since the losses are limited by the Fresnel reflections, this concept is attractive for designing focusing devices with high optical transmission properties. However, the photonic nanojets from single spheres require strictly plane-wave [86] or conical [93] beams for illumination, such beams are not readily available in many applications.

Our approach to solve this problem, i.e. focusing a multimodal electromagnetic beam just on the back surface of a lens, is based on using the concept of periodically focused modes (PFMs), which we developed in Chapter 3 for linear chains of dielectric spheres. Such chains are capable of filtering PFMs whit $2D$ period, where D is the spheres'

diameter. Since the PFMs are focused just on the back surface of the spheres, such chains are ideal candidates for solving the mentioned problem. The transmission of the system can be quite high since the optical losses are determined by the Fresnel reflections. The key result for developing applications is the observation of the "beam tapering" effect, i.e. a decrease in the transverse beam size along the chain, as studied in Chapter 3. We propose that the chains of microspheres can be used in a contact-mode surgery, because the transmitted PFM appearing in close proximity to the surface of the end-sphere is not strongly affected by the external medium, due to the fact that the focusing is accomplished primarily inside the chain. Additional advantages of these structures are their simple integration with HWGs, currently used as flexible delivery systems in laser-tissue surgery applications, and their ability to focus multimodal input beams.

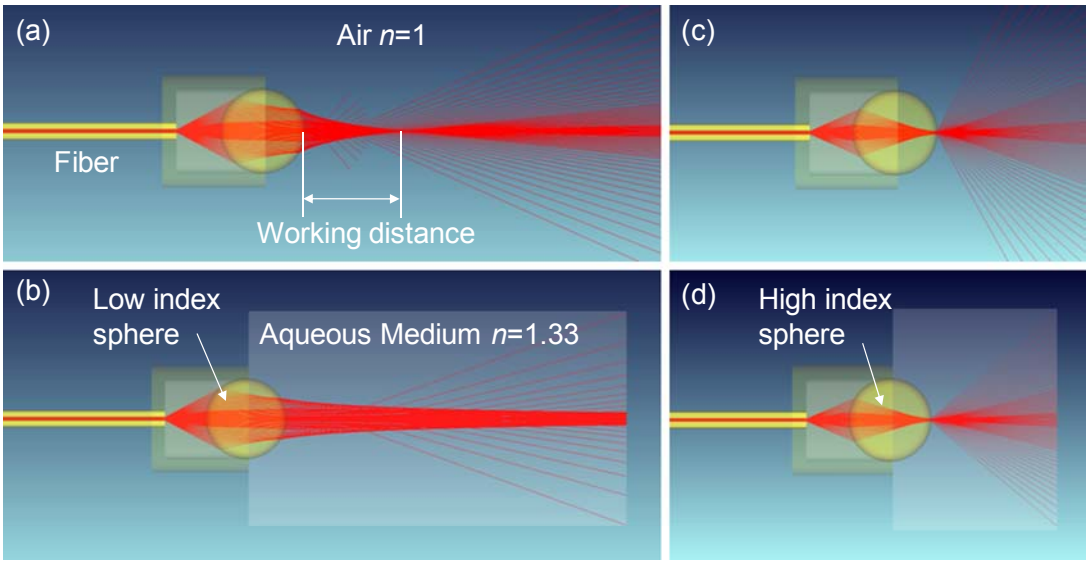

Figure 4.1: (a) A microprobe made by a low-index (n=1.6) sphere with a certain working distance in air. (b) The focusing is lost in tissue. (c) High-index sphere provides focusing at the tip. (d) The focusing is preserved in tissue.

In this chapter, we develop guidelines for designing high resolution contact-mode focusing multimodal microprobes. By analyzing a broad range of parameters, we show that chains of identical dielectric spheres with 300 μm diameter and refractive index n~1.65-1.75 provide two times better spatial resolution compared with a single-sphere design. Furthermore, we show that the conical chains of spheres provide more power coupling efficiency and peak irradiance in comparison with the chains of same-sized spheres. One particular potential advantage of the conical structures is the absence of background illuminations, which contribute to the lateral thermal damage zone in tissue, in their output beams.

4.2. Fiber-integrated Microprobes Formed by Uniform Sphere-arrays

The aim of our modeling is to create a generic design based on standard available optical components. Generally, a combination of desirable optical properties, good thermal and mechanical properties, and cost and ease of manufacturing dictates the number of readily available materials for any application.

4.2.1. Modeling Technique

As illustrated in Fig. 4.2, we assume that a multimode fiber (similar to a germanium oxide fiber) with core diameter of $2a$=150 μm is inserted into a hollow waveguide (similar to a hollow glass waveguide) with an internal diameter of $2a$=300 μm. These dimensions are typical for mid-IR waveguides [210]. The wavelength λ=2.94 μm is [symbolically] selected to match the emission line of the Er:YAG laser. As stated in Section 3.3 of Chapter 3, the choice of the wavelength does not influence our modeling results which are based on geometrical ray tracing. Smaller hollow waveguide (HWG) diameters would allow more compact focusing of the beams, however, diameters smaller

than $2a$=300 μm are rarely used in practice because of the strongly increasing propagation losses $\alpha \propto 1/a^3$, where α is the attenuation coefficient [210]. Previously, HWGs tapered to $2a$=200 μm have been used for achieving compact output beams [252]; however, such tapers have significant insertion losses and are challenging to fabricate.

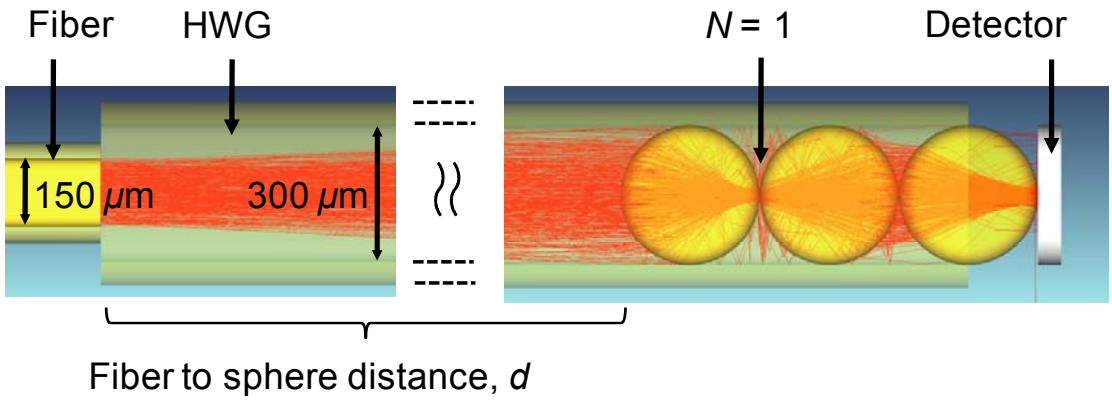

Figure 4.2: A focusing microprobe design based on a linear array of spheres placed inside a HWG.

Linear chains of N identical touching microspheres with diameter D=300 μm and refractive indices in the range 1.4- 2.0 are placed close to the HWG edge in a configuration in which half of the end sphere is extended from the HWG, as depicted in Fig. 4.2 for a 3-sphere chain.

The absorption of light by the HWG sidewalls are neglected, which is a good approximation for d<1 m [210]. The absorption of light and material dispersion in microspheres are not considered in our modeling.

The sub-millimeter dimensions of structures considered in our work make it difficult to find the exact solutions of Maxwell's equations based on numerical or analytical techniques, such as an integral formulation [253]. On the other hand, application of

geometrical optics is well justified in the case of $D>>10\lambda$ [179]. In order to perform our modeling, we use ZEMAX-EE, which has many advanced capabilities for designing similar structures.

The mid-IR multimode fibers used in laser surgery can support a few hundreds of modes and have approximately Gaussian radiant irradiance distributions with typical divergence angles of $2\beta=12°$. In order to model a multimode fiber in ray optics, a random distribution of point sources of light at the front surface of the fiber core is assumed, as shown in Fig. 4.3. Random distribution of such point sources leads to generation of both meridional and skew rays.

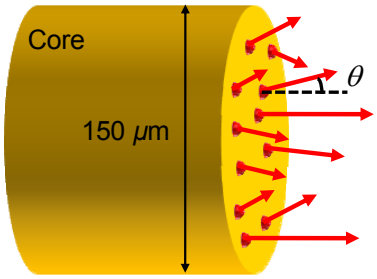

Figure 4.3: Schematic of the surface of the fiber with rays emitting from the core surface.

A total of 2×10^6 rays are traced in each calculation. In order to approximate a Gaussian distribution in the far-field, the following weight factor (WF) is introduced for each ray, depending on its starting polar angle θ:

$$\mathrm{WF}(\theta) = \exp\left(-2\theta^2/\beta^2\right), \tag{4.1}$$

where $\beta=6°$ [179]. The calculated average weight factor is applied in ten equally spaced angular steps from 0 to 6° along the cone of directions centered with the normal to the fiber surface.

Inside the device, the ray tracing takes into account the mirror reflections by the sidewalls of the HWG and the Fresnel reflections and refractions at the spherical interfaces, which leads to a gradual attenuation of initial rays once they propagate through the structure and to the emergence of new rays. We trace the rays down to a level of WF=10^{-4}, which provide good convergence of the numerical solutions. The irradiance distribution created by a device is calculated from the density of the rays at the detector plane with their weight factor taken into account. All calculations are performed with a random polarization of light.

In order to take into account the short penetration depth of light in tissue at λ=2.94 μm, we placed a totally absorbing detector in contact with the end-sphere in the *xy*-plane, as shown in Fig. 4.2. The square detector with 5000×5000 pixels has 300×300 μm size.

The use of a flat detector in our modeling is an approximation to the realistic surgical conditions due to a variable gap between the surface of the end-sphere and the detector, introduced by the curvature of the sphere. In practical surgery, the laser scalpel can be slightly pressed against the tissue surface providing close contact with the tissue along the surface of the end-sphere.

We proved numerically that the gap between the surface of the sphere and the detector was too narrow to allow for significant divergence of the rays sideways. We increased the refractive index of the medium in this gap region up to 1.33 and observed changes of the calculated irradiance profiles at the detector plane on the level of a few percent for reasonably well focused beams with widths below 20 μm. Thus, we concluded that the use of a flat detector in contact with the end sphere provides a good estimate of the transverse dimensions of the beam in strongly absorbing tissue.

It should be noted that, previously we reported focusing properties of sphere-chains in the presence of a non-absorbing tissue with a refractive index of 1.33, where the index of the external medium may affect the focusing ability of the spheres. In the designs presented in this chapter, however, this influence is minimized due to the fact that the focusing is provided primarily inside the device, so that the last focused beam is produced at the surface of the end-sphere. This is the key difference between the contact-mode devices developed in our work and non-contact focusing devices.

Finally, we should point out that the assumptions made in our modeling are simplistic and in practical surgery there will be many different factors. One of the most important factors is connected with vaporization of tissue by a focused laser beam. This factor can influence the depth of surgery, since the attenuation of the laser beam in a vapor is much smaller than in a liquid (tissue). The role of this factor is considered in greater detail in Section 4.2.2.3. Another factor is connected with the collateral damage which can propagate in tissue away from the focused beam due to the emission of shock waves and cavitation bubble formation [174]. These processes, however, are beyond the scope of the present work, where we determine the minimal dimensions of the light beams.

4.2.2. Optical Properties

4.2.2.1. Fiber-to-microsphere Separation

We start with the focusing properties of a multimode fiber in contact with a single sphere (d=0), as illustrated in Fig. 4.4. In principle, a tighter focusing can be achieved by using smaller spheres. The diameters of spheres, however, should be larger than the diameter of the core of the multimode mid-IR fiber (150 μm) to preserve high optical

throughput. Our numerical ray tracing result is illustrated for single spheres with diameters 300 μm and 150 μm in Figs. 4.4(a) and 4.4(b), respectively (HWG is not shown since the reflections by the HWG sidewalls are not important in such designs). Using a Gaussian approximation for the output beam irradiance profile, the full width at half maximum (FWHM) ~17 μm and ~10 μm is estimated for a high-index (n~2) sphere with 300 μm and 150 μm diameter, respectively, as seen in Fig. 4.4(c).

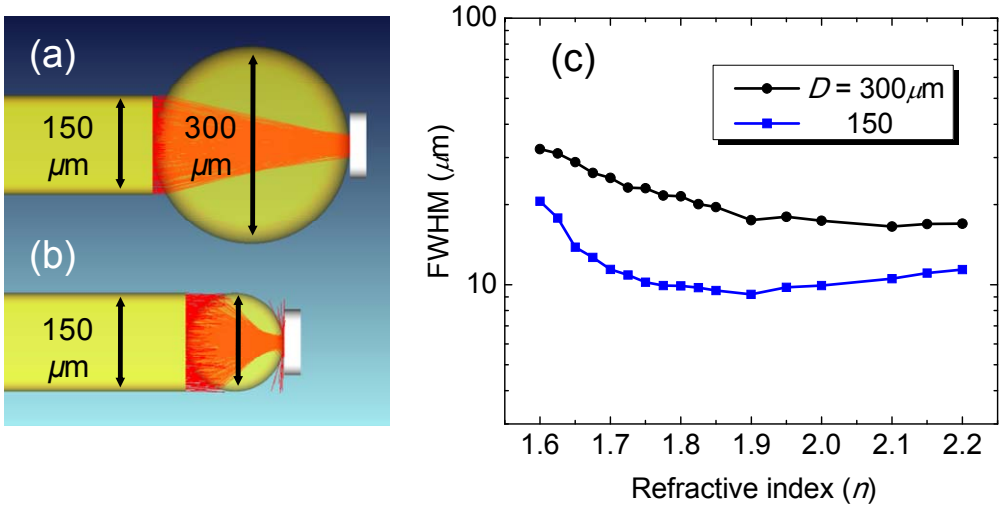

Figure 4.4: Ray tracing for a single (a) 300 μm and (b) 150 μm sphere with n=1.9 in contact with the core of the multimode fiber. (c) Calculated FWHM of the central irradiance peaks as a function of n for two structures shown in (a) and (b), respectively.

Fixing the microspheres at a precise and stable position centered with the axis of the fiber core can be a rather difficult problem in such structures, especially in surgical applications where the tip of the end sphere is in contact with the tissue. It is interesting that in the case of bundles of single mode fibers, the positions of much more compact 2 μm polystyrene spheres have been defined due to the selective wet-chemical etching of a micro-well array [164]. A similar approach can, in principle, be used for fixing larger

spheres at the edge of a multimode fiber; however, the refraction properties of light in such micro-wells and the robustness of such structures require further studies.

Next, we consider a typical example illustrating how the transverse irradiance profiles depend on the fiber-to-sphere distance d for the HWG structure with a single D=300 μm sphere with n=1.7, as illustrated in Fig. 4.5. For a small separation of 1 mm, the irradiance distribution in the detector plane has a complicated shape with a large width of ~40 μm. For d<1.5 mm, the rays do not hit the sidewalls of the HWG. The single sphere works as a thick lens with back focal length of 32 μm (Appendix D). The detector plane intercepts the rays before they converge in the imaging plane, resulting in broad irradiance distributions.

In contrast, for d>5 mm, the irradiance distribution is more similar to a Gaussian shape with a much narrower FWHM of ~13 μm. The shape of the irradiance profile is found to be not strongly dependent on d for d>20 mm, as illustrated in Fig. 4.5. This result can be understood based on a mirror effect produced by multiple reflections at the HWG sidewalls that lead to a formation of multiple virtual sources of light. Due to a larger d, the images of these sources are better focused at the plane of the detector, where they are overlapped. Generally, this leads to formation of an averaged envelope irradiance profile, which is not strongly dependent on d. For this reason, in our further analysis, we fix d=20 mm in order to focus on studies of other essential parameters of the system such as n and N. An additional advantage of this approach is that our results are independent of the way multimode beams are coupled into the HWG. For example, similar input beams can be produced by direct coupling of the multimode laser beam into the HWG without using the multimode fiber.

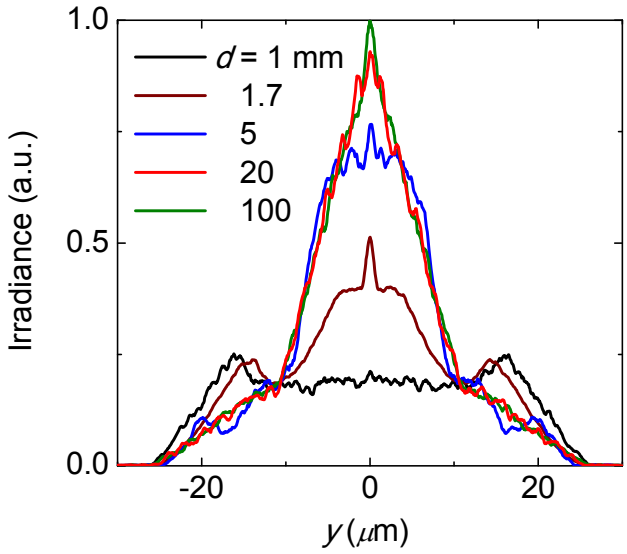

Figure 4.5: Irradiance profiles calculated for a single sphere with n=1.7 as a function of the fiber-to-sphere distance (d) inside a HWG.

4.2.2.2. Optical Focusing and Power Transport

In terms of the energy conservation, the optical microprobes considered in this work create three types of fluxes:

1) First, they produce a focused beam with the total power P_f and peak irradiance I_f along the optical axis.
2) Second, in some cases they produce a broad background illumination in the forward direction with the total power P_b and irradiance I_b.
3) Finally, a part of the incident power P_i is reflected by the spheres in a backward direction inside the HWG.

In the absence of absorption, $P_i=P_f+P_b+P_r$, where P_r is the reflected power.

We start with a single sphere case. The calculated irradiance distributions have approximately Gaussian shapes with FWHMs presented in Fig. 4.6(a). Producing small spots at the detector plane requires a sharp focusing of light at the tip of the end-sphere. It

can be achieved at n=2 in the paraxial regime. Due to the propagation of non-paraxial rays in the HWG, the role of the spherical aberration is significant, which results in smaller indices 1.8<n<1.9 required for the minimization of the spot sizes.

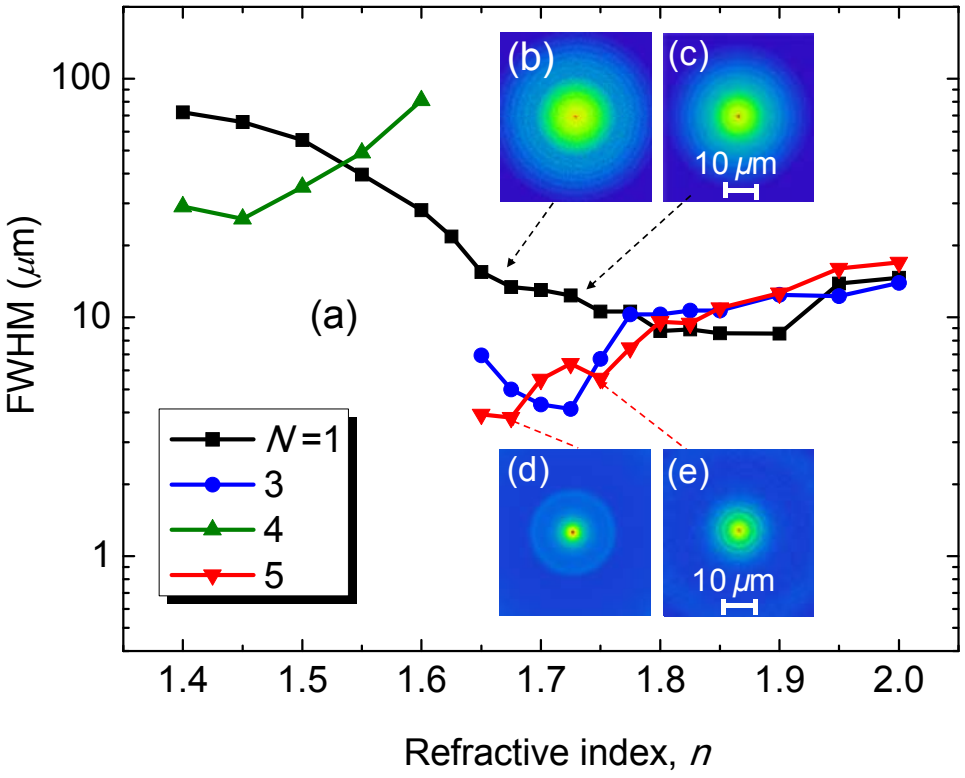

Figure 4.6: (a) Calculated FWHMs of the central irradiance peaks as a function of n. Irradiance distributions in a single sphere device for (b) n=1.675 and (c) 1.75. (d) Irradiance distributions in a five-sphere device for (d) n=1.675 and (e) 1.75.

Power coupling efficiency ($\eta=P_f/P_i$) to the central focused beam formed by each design is estimated by using a small circular detector, whose radius is equal to the FWHM of the focused beam, as illustrated in Fig. 4.7. According to this procedure, first, we calculate the entire irradiance profile over a broad area using a square detector, and then, we use the small circular detector to determine P_f.

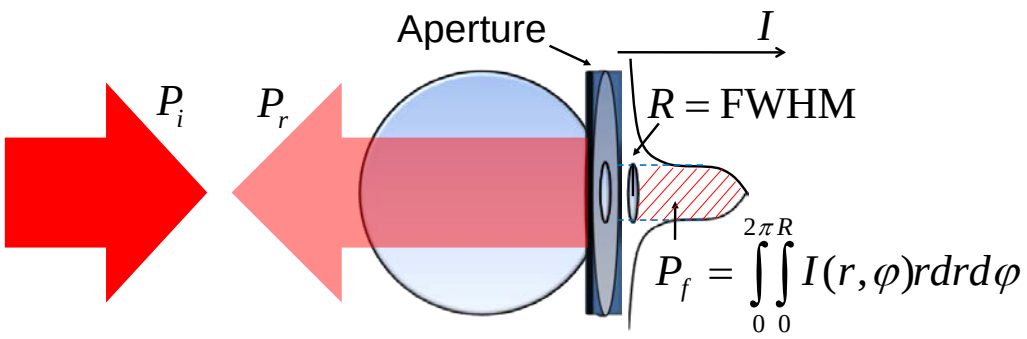

Figure 4.7: Integrating the beam irradiance on a circular region, whose radius is equal to the FWHM of the focused beam, gives P_f.

The calculated dependency of η on n is presented in Fig. 4.8(a). The single-sphere cases provide relatively high values for η~0.35, in combination with FWHMs~9 μm in the range of refractive indices $1.8<n<1.9$. Although this combination of parameters is reasonable for ultra-precise surgery, the choice of the materials which can be used for fabricating microspheres with such high refractive indices and good optical properties at λ~3 μm is extremely limited.

The focusing properties of the designed microprobes are found to be dramatically altered for chains of spheres, as illustrated for a five-sphere chain in Figs. 4.6(a). For $n<1.65$, both three- and five-sphere chains produce relatively broad irradiance profiles, with non-Gaussian distributions in the detector plane. Large spot sizes are also produced by two- and four-sphere chains, as shown in Fig. 4.6(a) for a four-sphere chain at $n<1.6$.

Most importantly, three- and five-sphere chains in the range $1.65<n<1.75$ are found to produce irradiance distributions with a very narrow central peak superimposed on a much broader and weaker background (I_f/I_b~10), as illustrated in Fig. 4.6. The Gaussian fit to the central peak shows that the FWHM of the focused beam can be as small as 3-6 μm for the range of $1.65<n<1.75$, which shows more than two times better spatial

resolution over single-sphere cases. The wavelength-scale dimensions of the focused beams indicate that we are approaching the limitations of the geometrical optics assumptions in these designs.

This greatly improved spatial resolution comes at the cost of the total optical power coupled to the focused beam. As shown in Fig. 4.8(a), the power coupling efficiency on a level of a few percent can be obtained. The peak irradiance (I_f) is attenuated in these structures by a factor of 0.2-0.4 compared with a single-sphere design with the same refractive index, as shown in Fig. 4.8(b).

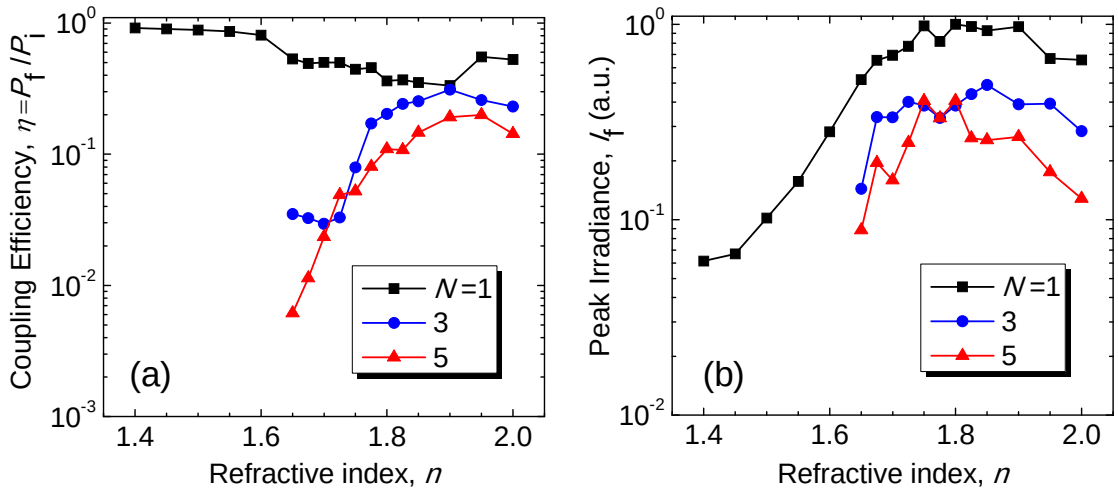

Figure 4.8: Comparison of (a) efficiency of coupling (η) of the incident power to the central focused beam and (b) peak irradiance (I_f) of the focused beam for microprobes formed by a 1, 3, or 5-sphere designs.

Interpretation of the observed effects is based on the fact that chains of spheres with refractive indices in the range $1.65<n<1.75$ effectively transmit the periodically focused modes (PFMs), the rays which are focused in such structures with a period equal to the size of two spheres ($2D$). These rays have a sharper focus and smaller propagation losses

that result in a structural resonance in the optical properties with gradual decrease of the focused spot sizes. The reason that in previous chapter we observed the “beam tapering” effect at $1.72<n<1.85$ is connected with the much broader directionality of the spherical light source (S-sphere) used in previous chapter.

The role of absorption in such structures was estimated for silver sidewalls in the HWGs in combination with a weakly absorbing sphere material, such as sapphire, in the mid-IR range. Only a minimal power loss of a few percent was observed due to the absorption.

4.2.2.3. Self-limiting Mechanism

One particular material whose refractive index lies in that range $1.65<n<1.75$, where chains of spheres shows advantage over a single sphere, is sapphire (or ruby) with $n\sim1.71$ at $\lambda=2.94$ μm. Sapphire is biocompatible and has excellent mid-IR transmission, thermal, and mechanical properties. Furthermore, inexpensive sapphire microspheres with excellent optical properties are commercially available. Ruby (Cr^{3+}:Al_2O_3) is composed primarily of sapphire (Al_2O_3) where a small fraction of the Al^{3+} ions ($\sim$0.05%) are replaced by Cr^{3+} ions [38].

The simulated irradiance distributions for chains of three, five, and seven spheres with $n=1.71$ are presented in Fig. 4.9. The irradiance profile for each case has been normalized, so the spot sizes can be compared on a single graph. As illustrated in Fig. 4.9, the FWHM is reduced from $\sim$12 μm for a single sphere to $\sim$6 μm for chains of spheres. Furthermore, the peak irradiance drops by a factor of 3.25, 5, and 6.5 for chains of three, five, and seven spheres, respectively.

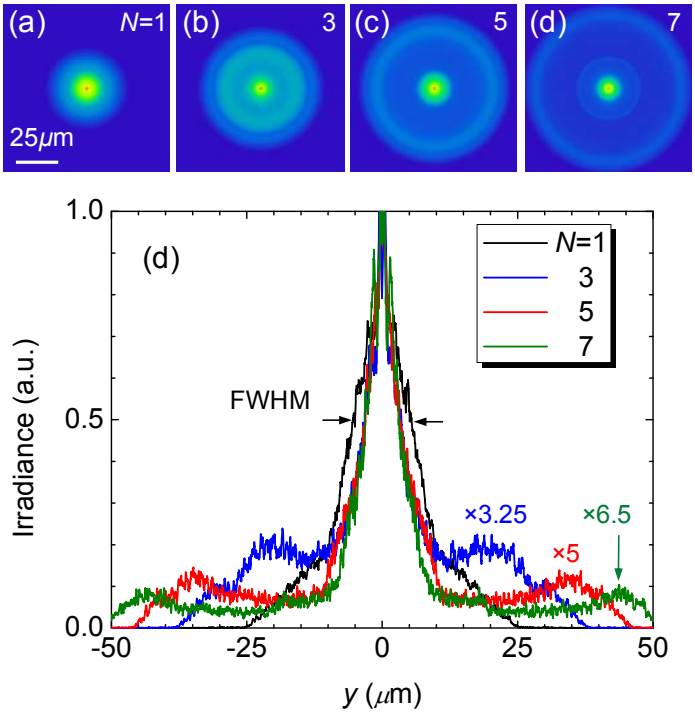

Figure 4.9: Irradiance distribution on the detector surface in contact with the end-sphere in microprobes with N=1, 3, and 5 spheres with n=1.71.

In order to model the operation of the device in the presence of cavitations bubbles, we place the detector at different distances from the tip of the device in a medium with n=1 and calculate the beam profiles at different distances from the tip of the device, as illustrated in Figs. 4.10(c-f) for devices with N=1, 3, 5 and 7 spheres (n=1.71), respectively. In a real surgical environment, the vaporized tissue would create a bubble just at the tip of the end-sphere, and the light would propagate through this bubble. In our modeling, we neglect the light absorption inside the bubble and assume that the vapor's refractive index is close to n=1. The irradiance profiles in Fig. 4.10 effectively represent the irradiance distribution at the distant bubble sidewall. The green dashed lines are used as a guide to represent how the irradiance peak of the beam reaching the opposite sidewall of the bubble depends on the bubble diameter.

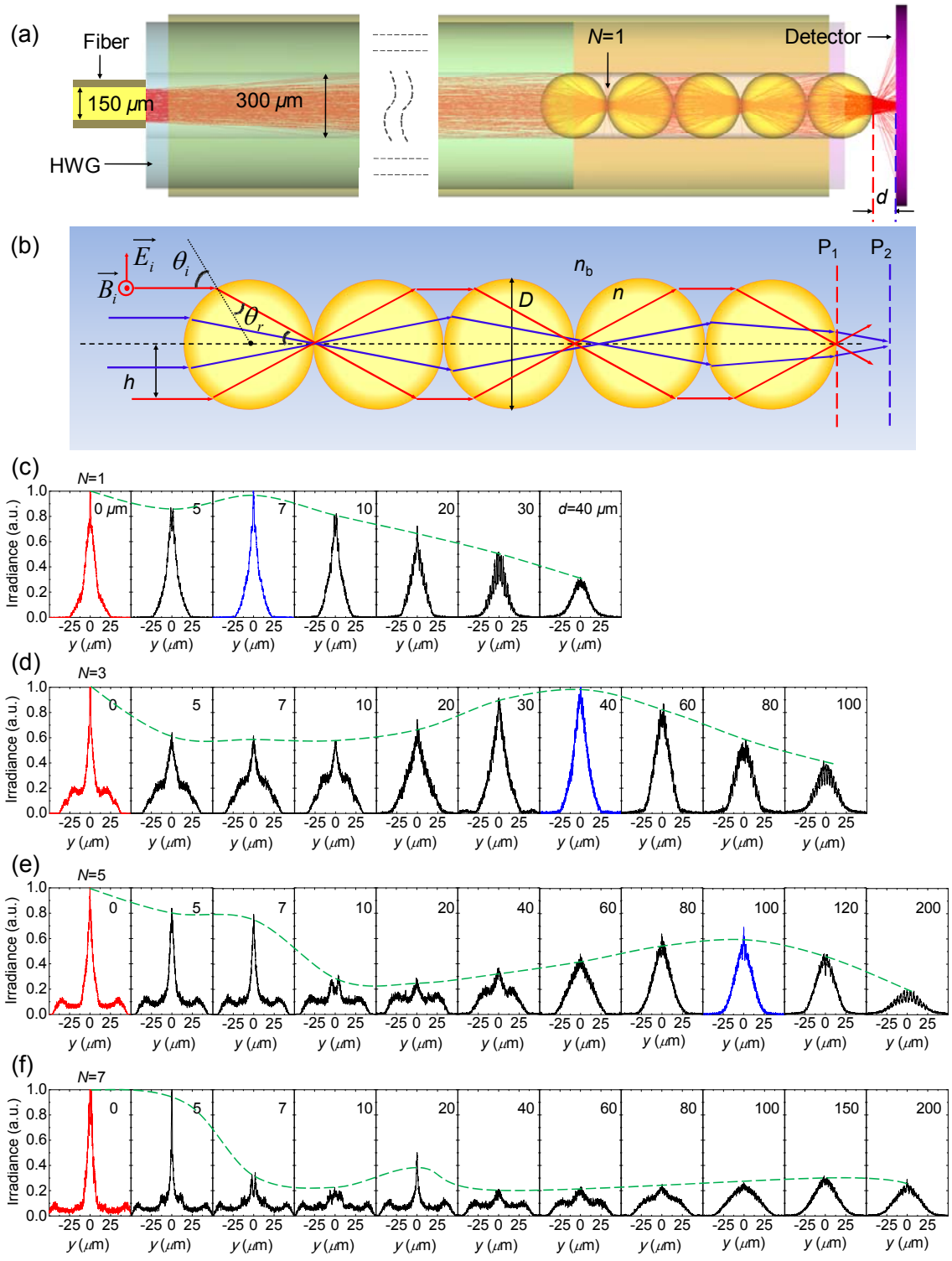

Figure 4.10: (a) Schematic of a microprobe with 5 spheres. (b) Red rays correspond to PFMs which provide sharp focusing at the surface of every odd number of spheres. Blue rays correspond to almost paraxial rays. (c-f) Irradiance distributions at different distances from the tip of a microprobe composed of 1, 3, 5, and 7 spheres (n=1.71), respectively.

For the single-sphere and the three-sphere chain, the irradiance peak experiences slow variations as the bubble grows. The irradiance peak for the five- and seven-sphere chains shows a peculiar behavior that can be very useful for controlling the depth of surgery. Once the bubble reaches ~10 μm size, the irradiance peak drops by a factor of four or more and stays at this low level for bubble sizes up to 20-30 μm, which indicates a possibility that the depth of the ablation craters in tissue would saturate at the 10-20 μm level in a practical surgery.

The mechanism of light focusing by such structures is based on properties of periodically focused modes (PFMs), schematically illustrated in Fig. 4.10(b) using red color. Making a transition from the ray picture to the physical optics, corresponding modes would have a cylindrical symmetry in radial direction and a period equal to the size of two spheres along the axis of the chain. Unusually high transmission properties of the PFMs can be understood due to the fact that corresponding rays intersect the spherical interfaces under the Brewster's angle condition for TM polarization, and as a result, they are not reflected. In Chapter 3, we showed that these modes play dominant role in the optical transmission properties of such chains for n~1.70-1.75. Although the rays with different off-axial offsets and angles of incidence are coupled into such chains from the source, only the PFMs survive in sufficiently long chains. The fact that the PFMs have $2D$ period for spheres with moderate indices of refraction (n<2) can be understood due to the significant spherical aberrations introduced by the large lateral offset of these modes. This is especially clear when compared with the case of propagation of paraxial and almost paraxial rays, shown in Fig. 4.10 using blue color. Paraxial rays have a period longer than $2D$ that is expected for n<2 (n=1.71), due to the absence of spherical

aberrations. As a result, the paraxial modes cannot be used for light focusing at the tip of the end-sphere. In addition, they attenuated much stronger compared with the PFMs in such structures, due to the fact that they intersect spheres at variable angles, which are, generally, different from the Brewster's angle.

The sharp focusing of light at the tip of the-end sphere for a 5-sphere chain, illustrated in Fig. 4.10(e), is explained by the PFM transmission effects. These chains are sufficiently long to suppress paraxial and other modes, except the PFMs. So, due to the $2D$ periodicity, the PFMs are focused at the tip of the end-sphere with extremely small focusing depth <10 μm. The reduction of the irradiance at longer distances is explained by the strongly divergent nature of the PFMs, which can act as a factor limiting the depth of surgery. When the probe is in contact with the tissue, it provides sharp focusing at the tip and locally ablates the tissue, creating a vapor bubble. A gap between the tip and the underlying tissue is created and the irradiance peak drops away from the tip due to the short focusing depth (fast divergence) of the PFMs, which slows down the tissue ablation.

4.2.2.4. Polarization Properties

As mentioned in Section 3.4.3 of Chapter 3, the global state of polarization of the PFMs is radial due to the facts that TM polarized PFMs have extremely small losses, whereas the TE polarized PFMs have extremely large losses.

In order to study the degree of radial polarization in the designed microprobes in this chapter, we consider chains of N=4, 6, and 10 spheres, optically coupled in the same way as discussed in section 4.2.1. By placing a linear polarizer and two local detectors, as schematically shown in Fig. 4.11(b), and following the procedure explained in Section

3.4.3 of Chapter 3, the degree of radial polarization is calculated for the output beams [Fig. 4.11(c)].

The degree of radial polarization increases with the length of the chain, reaching a very high value ~0.9 for a 10-sphere chain with any refractive index within n=1.70-1.80 range, as illustrated in Fig. 4.11(c). The altering of the state of polarization from random polarization to radial state is due to the filtering of the PFMs.

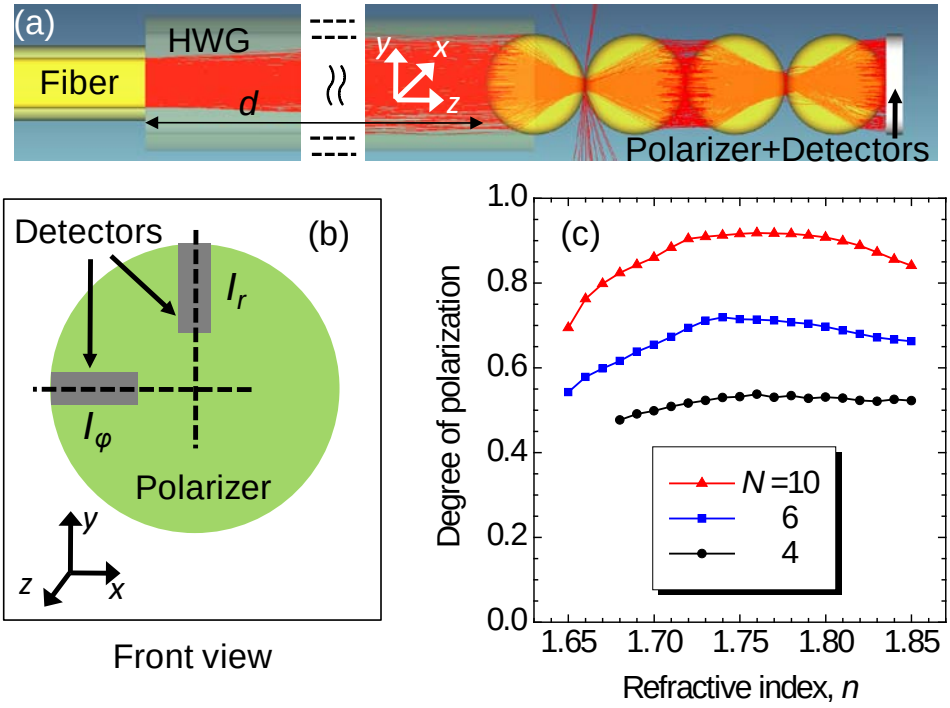

Figure 4.11: (a) A linear polarizer along y-axis is placed after the end-sphere in the chain before two local detectors. (b) Front view of the polarizer and detectors. (c) Degree of radial polarization as a function of n for N=4, 6, and 10.

The light source considered in this section, i.e. a multimode fiber coupled with a HWG, can be seen as a somewhat intermediate case between the light sources considered in Section 3.4.3, i.e. collimated incident rays and the S-sphere. Although it has a strong

preferential direction of rays, the rays are not parallel like in the case of collimated rays considered in Section 3.4.3. This leads to a polarization conversion efficiency which is expected to be much more than the S-sphere case, but less than the case of the collimated rays, which is consistent with the modeling results for different light sources presented in Figs. 3.15(d) and 3.15(e).

4.2.3. Fabrication and Testing

In this section, we present our experimental results for microprobes composed of chains of sapphire or ruby spheres, and compare them to the results of our numerical modeling.

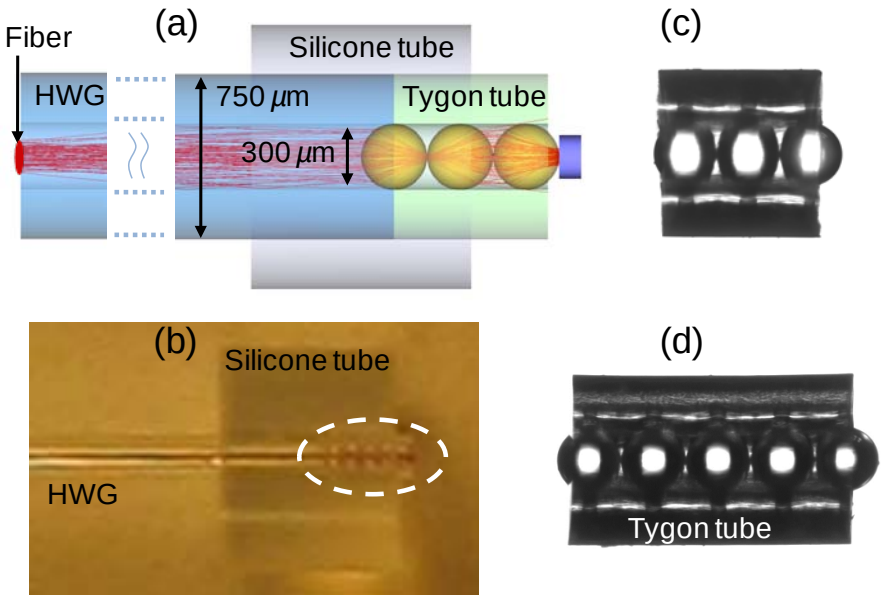

Figure 4.12: (a) Schematic of a microprobe with a three-sphere chain. (b) Image of a five-sphere microprobe. (c,d) chains of N=3 and 5 spheres with D=300 μm packed inside Tygon® tubes, respectively.

Schematic of the device is shown in Fig. 4.12(a). We assembled linear arrays of touching high quality sapphire and ruby spheres (Swiss Jewel Company, Philadelphia,

PA) with mean diameters D=300±2.5 μm inside transparent flexible Tygon® S-54-HL composition tubes (Cole-Parmer Instrument Company, Vernon Hills, IL) with ID=0.25 and OD=0.76 mm by using a hydraulic micromanipulator in a manner that the gap between the spheres is controllable by visual inspection through the sidewalls. The samples were made with no gap between the spheres. Tygon® tube is non-toxic, non-pyrogenic, hydrophobic, and biocompatible, which can be sterilized by ethylene oxide, steam, radiation, or chemical methods. The fact that ID<D provided a tight packing of the spheres with their precise axial alignment inside the tubes, as shown in Figs. 4.12(c) and 4.12(d) for a chain of 3- and 5-spheres, respectively. The end sphere was slightly extended from the tube to provide a good optical access to the last focused beam in the chain. We used a 5 mm piece of silicone tube with ID~700 μm to connect the 30±2 mm piece of HWG (Polymicro Technologies, Phoenix, AZ), with ID=300±20 μm and OD=750±25 μm, to the chain of spheres, in a way that the chain of spheres and the HWG are axially aligned, as shown schematically in Figs. 4.12(a,b).

In order to characterize the fabricated microprobes, we performed two types of experiments:

1) Optical characterization by a lens and an IR beam profiler.
2) Characterization by comparing their burn patterns in a heat sensitive paper.

The experimental setups used for imaging and burn patterns are illustrated in Figs. 4.13(a) and 4.13(b), respectively.

We used a piece of 1 m multimode germanium oxide trunk fiber (Infrared Fiber Systems, Silver Spring, MD) to transport light from the Er:YAG diode laser (MIR-Pac, Sheaumann Laser Inc., Marlborough, MA), with quasi-continuous operation at λ=2.94

μm, to the HWG (HWEA300750, Polymicro Technologies, Phoenix, AR). In principle, another piece of a flexible plastic tube, with an ID equal to the diameter of the fiber and OD~300 μm, could be used to fix and align the fiber inside the HWG.

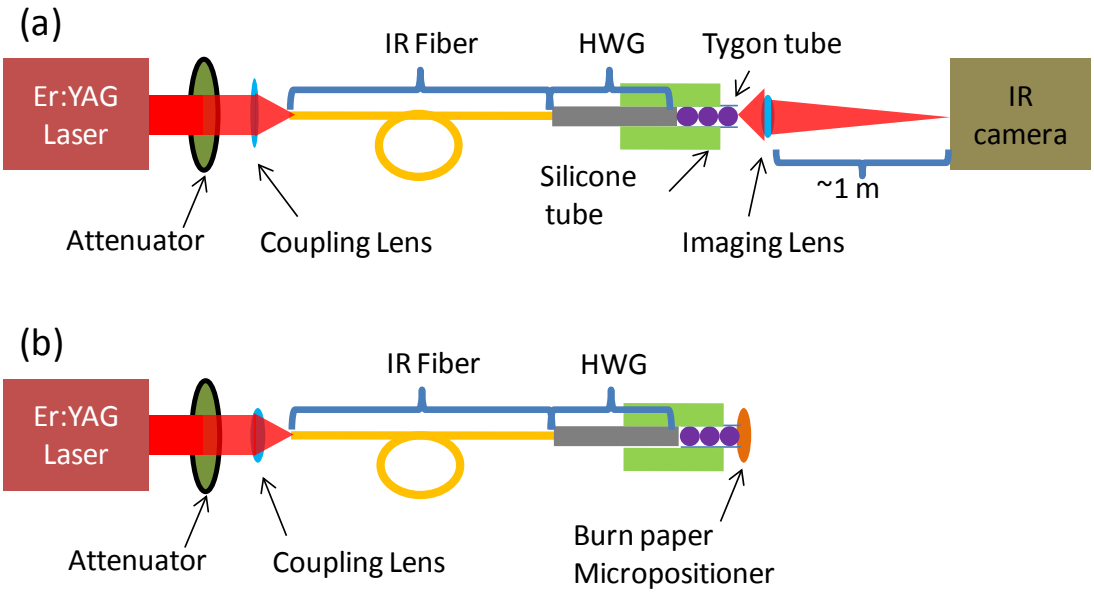

Figure 4.13: Schematic of the experimental setup for (a) imaging the output beams and (b) creating burn pattern by the microprobes.

We used a 12.7-mm-focal-length CaF_2 lens to couple erbium laser radiation into the germanium oxide trunk fiber. Another lens was placed after the chains for imaging, as shown in Fig. 4.13(a). Direct measurement of the output irradiance profile was done by using a 124×124 matrix pyroelectric IR beam analyzer (Pyrocam III, Ophir-Spiricon LLC., North Logan, UT) in chopped mode. The size of each element was 85×85 μm^2.

In order to study the resolution of the prototype device, we compared the dimensions of the beams produced by a bare HWG, a single sapphire or ruby sphere (D=300 μm), and sphere-chains. Initially, we directly imaged the beams at the pyroelectric IR beam

analyzer, placed at a distance ~1 m from the CaF_2 lens, shown in Fig. 4.13(a). In addition, to mimic surgical conditions typically encountered in the clinic, the fiber was manually manipulated and twisted through a broad range of configurations during the experiments. This resulted in a variation of the modal structure of the output beam with a corresponding broadening of the focused spot.

The imaging results, presented in Figs. 4.14(e-h), showed smaller spot sizes for three- and five-sphere chains compared with a single-sphere case. However, more direct comparison of these results with the calculated irradiance distributions at the surface of the end-sphere, shown in Figs. 4.14(a-d), was complicated due to the fact that the quality of the imaging of the focused beams was suffered from an incomplete collection of light by the lens with NA=0.5, as illustrated in Fig. 4.15(b). For this reason, this method could only be used for semi-quantitative characterization of the output beams.

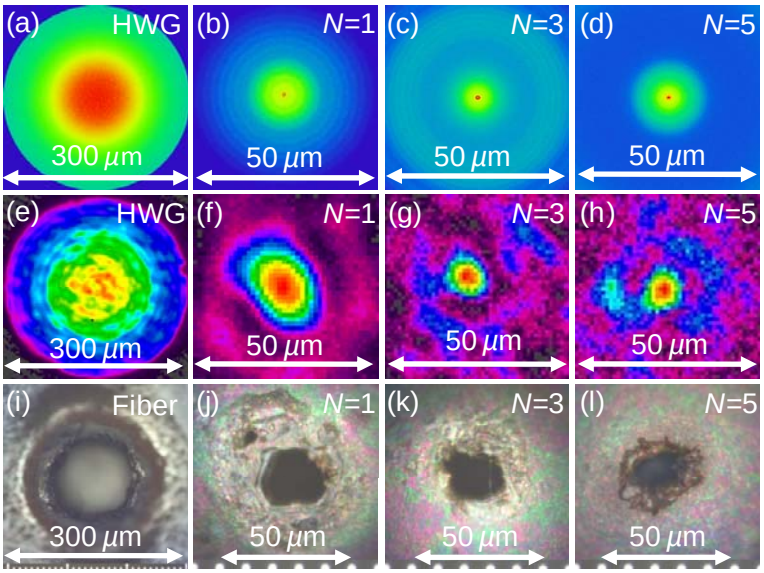

Figure 4.14: Simulation results for (a) HWG, (b) single-sphere, (c) 3-sphere chain, and (d) 5-sphere chain. IR images of the beams created by (e) bare HWG, (f) single sphere, (g) 3-sphere, and (h) 5-sphere chains. (i-l) Holes in the burn paper produced by the same structures as in (e-h).

The irradiance distributions were directly characterized by using laser alignment papers (Zap-It Corp., Salisbury, NH) in contact with the tip of the end-sphere, as illustrated in Figs. 4.14(i-l). Such burn patterns experienced the total angular distribution of rays produced by the device. This characterization showed a good qualitative agreement with the results of the optical beam profiling, which can be seen by comparing the burn patterns in Figs. 4.14(i-l) with the corresponding images in Figs. 4.14(e-h) and Figs. 4.14(a-d).

Figure 4.15: Beam characterization of the microprobes using a lens with NA=0.5. (a) A bare HWG and (b) A HWG with a single sphere showing rays beyond the NA of the lens are not captured by the lens.

Our ray tracing simulation ignores the modal properties of physical beams guided by the fiber and HWG. For example, Fig. 4.14(h) shows probably several different modes which are characterized by certain “patterns”. In addition, we observed a switching between the different “patterns” when the fiber was bent. This effect cannot be properly explained by the ray tracing. However, by shaking the fiber during the experiments, we tried to mix as many modes as possible to make the beam at the output of the HWG, Fig. 4.14(e), more similar to the ray tracing result presented in Figs. 4.14(a). Furthermore,

pixel dimensions of the IR beam analyzer, slight deviation of the fiber from central position in the HWG, surface roughness of the metallic layer in the HWG, the discontinuity of the modes distribution, and misalignment and size mismatch in the chains of spheres are other parameters affecting the experimental results.

We measured the total output power obtained from each structure by an IR power meter (PowerMax, Coherent Inc., Santa Clara, CA). We normalized the output power (P_{out}) of each structure by dividing it by the output power of the bare HWG (P_0). For the cases of N=1, 3, and 5, we measured P_{out}/P_0=0.75, 0.52, and 0.44, respectively, in agreement with the corresponding modeling results of 0.87, 0.63, and 0.5. The losses are mainly due to the back reflections of light from the spheres surfaces. Our experimental measurements did not show pronounceable difference in the optical properties of ruby and sapphire at λ=2.94 μm. This result can be explained by the fact that Cr^{3+} ions do not contribute to absorption of light at this wavelength.

The microprobes, which we designed, fabricated and tested in this section, were given to the Biomedical Optics Laboratory for *ex vivo* tests on porcine corneal tissues.

4.3. A Sub-optimal Microprobe Design for Preliminary *ex vivo* Testing

In this section, we present our modeling results of sub-optimal microprobe designs. The choice of this sub-optimal design was determined by easiness of its practical realization at that time.

In the sub-optimal designs, instead of using identical D=300 μm spheres, a 350 μm sphere is used as the end-sphere. The reason for using this enlarged sphere is a necessity to fix it at the end of the HWG by using an adhesive. The rest of the spheres are inserted inside the HWG as schematically shown in Fig. 4.16.

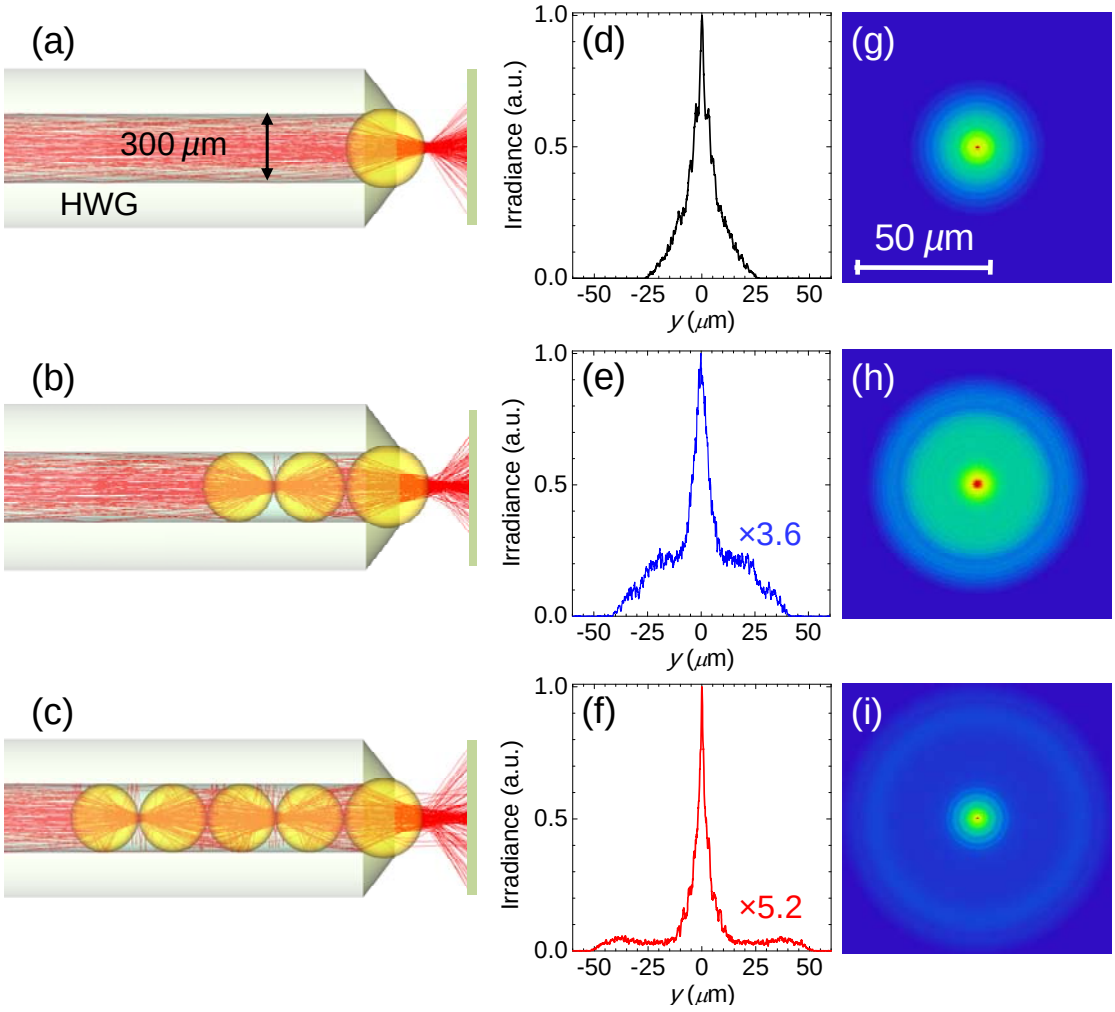

Figure 4.16: (a) A microprobe design with a 350 μm sphere at the end of a HWG. (b,c) A three- and five-sphere chains consisting of 300 μm spheres placed inside a HWG and a 350 μm sphere at the end of the HWG. (d,g), (e,h), and (f,i) Normalized irradiance profiles at 8.5, 10, and 9 μm distance from the tip of the end-sphere for designs shown in (a), (b), and (c), respectively.

Our numerical modeling is conducted using the same light source, as mentioned in Section 4.2.1, and a 30-mm-HWG. The simulation results are presented in Fig. 4.16(d-i). In these sub-optimal designs, the focusing is formed at an ~10 μm distance from the tip. The five-sphere chain produces two-fold smaller spot compared with the single-sphere case. The enlarged end-sphere experiences relatively smaller positive spherical

aberrations because its size is larger than the beam diameter that results in the focusing of the beam slightly in front of the tip of the end-sphere.

Experimental *ex vivo* results of these microprobes on porcine corneal tissues were in agreement with our modeling results. It showed that smaller ablation craters with shorter penetration depths were achieved by using sphere-chains compared with a single-sphere case. However, such chains created wider lateral thermal damage zones due to the interactions of the non-PFMs with tissue. In principle, this issue could be solved by reducing the irradiance level of the incident laser beam closer to the ablation threshold.

It should be noted that in this dissertation, we developed an approach to assemble tightly packed spheres inside plastic tubes that allows us to obtain sphere-chains formed by the same size spheres. Our approach has been described in Section 3.6.1 of Chapter 3 and Section 4.2.3 of this chapter.

In the next section, we propose an alternate design, which creates a more compact central beam and suppresses the background illumination associated with the non-PFMs.

4.4. Microprobe Designs Using Conical Arrays of Spheres

In previous sections, we showed that spheres-chains are capable of focusing multi-modal incident beams due to the transmission of the periodically focused modes (PFMs). In addition, we designed focusing multimodal microprobes that operate based on the formation of PFMs in such arrays to be used for an ultra-precise laser-tissue surgery application. Sphere-chains showed improvement of the spatial resolution over single-sphere designs with the same diameter and refractive index. However, this improvement in spatial resolution came at the cost of the total power coupled to the focused beam. The power coupling efficiency on the order of a few percent and the peak irradiance

attenuated by a factor of 0.2-0.4 were calculated for such optimized chains. Furthermore, experimental *ex vivo* results of testing microsphere-chains on corneal tissues showed that smaller ablation craters with shorter penetration depths can be achieved compared with those of a single-sphere device. However, such chains created wider lateral thermal damage zones due to the contribution of the interactions of non-PFMs with the tissue.

In this section, we aim to improve the power coupling efficiency and peak irradiance of the focused beams produced by the microprobes, by designing chains of microspheres with progressively smaller diameters. We show that these chains produce spot sizes comparable to the previously optimized cases for arrays of identical spheres, but with 3-4 times more coupling efficiency and 2 times more peak irradiance. In addition, the output irradiance profiles from the conical designs show quasi-Gaussian distributions with no background illuminations, contributing to the lateral thermal zone, for almost the entire range of indices ($1.65<n<2.2$) considered in this work.

4.4.1. Modeling Technique

Similar to the other two designs mentioned in previous sections of this chapter, we assume that the Er:YAG laser is coupled with a multimode fiber in order to provide maximal flexibility required in surgery. Next, we assume that the fiber is inserted in a piece of hollow waveguide (HWG) used as an actual microprobe. In order to design a focusing microprobe capable of focusing multimodal beams in contact with an absorbing medium with extremely short penetration depth, a focusing conical chain of spheres is assembled at the end of the HWG, as illustrated in Fig. 4.17. The conical chain is formed by three axially aligned spheres with progressively smaller diameters, which are calculated in a way that the spheres can be embedded in a truncated cone (Fig. 4.17).

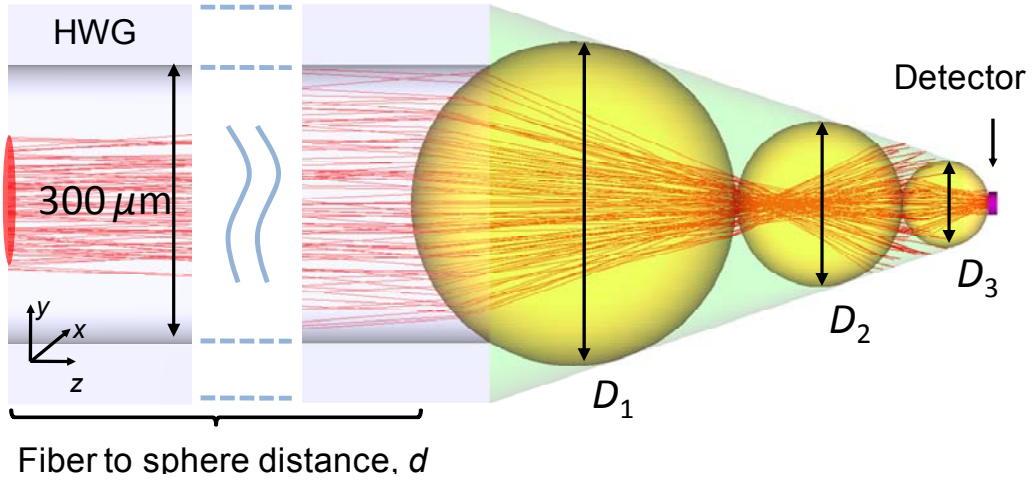

Figure 4.17: Schematic of a conical array of spheres assembled at the end of a HWG.

The core diameter of the multimode fiber and the bore diameter of the HWG are considered 150 and 300 μm, respectively. These dimensions are typical for mid-IR waveguides [210]. The size of the first sphere is considered fixed, D_1=350 μm, so that the sphere can be fixed by gluing to the edge of the HWG, as mentioned in Section 4.3.

The diameter of the second sphere, D_2, depends on the size of the third sphere. D_2=132 μm and D_2=94 μm are calculated for the cases of D_3=50 μm and D_3=25 μm, respectively (Appendix E). The spheres' sizes well correspond to the limit of geometrical optics, maybe with the exception of a single case of D_3=25 μm (D_3~9λ) which needs to be considered more carefully since D/λ~9. In principle, it can be done by using finite-difference time-domain (FDTD) numerical modeling; however such analysis goes beyond this work. It should be noted that the description based on geometrical optics should be asymptotically valid in the limit of short wavelengths.

As showed in Section 4.2.2.1, the distance between the fiber and the first sphere (d) is not critically important in the limit of sufficiently large separations (d>20 mm). For

this reason, we considered d=30 mm in order to study other parameters of the system, such as refractive indices (n) and diameters (D) of the spheres.

Three main parameters studied in our designs are:

i) The focused spot size defined as the FWHM of the irradiance distribution on the xy-plane in contact with the tip of the end-sphere,

ii) Peak irradiance of the focused beam, and

iii) Power coupling efficiency, $\eta=P_f/P_i$, defined in section 4.2.2.2.

4.4.2. Optical Properties

The irradiance distribution obtained from each design at the detector plane is fitted by a Gaussian distribution and the corresponding FWHM is calculated as an estimate of the spot size. The FWHMs, peak irradiances, and power coupling efficiencies are calculated for conical arrays with D_3=50 and D_3=25 μm, as a function of the refractive index for the range of $1.65 \leq n \leq 2.2$, presented in Fig. 4.18. The corresponding values of FWHM, peak irradiance, and power coupling efficiency for the cases of a single-sphere and chains of three identical spheres with D=300 μm, calculated in Section 4.2.2.2, are added to the plots in Fig. 4.18 to make direct comparison easier.

As presented in Fig. 4.18(a), the conical arrays with third sphere sizes D_3=50 and D_3=25 μm show progressively smaller beam sizes compared with the corresponding single-sphere cases indicated by N=1. In the case of D_3=25 μm, beam sizes ~4-7 μm is achieved over the entire range ($1.7<n<2.2$) of indices considered in this work. In contrast, chains formed by three identical spheres, indicated by N=3 in Fig. 4.18(a), provide a compact beam with a comparable size only in a narrow range ($1.675<n<1.725$) of indices.

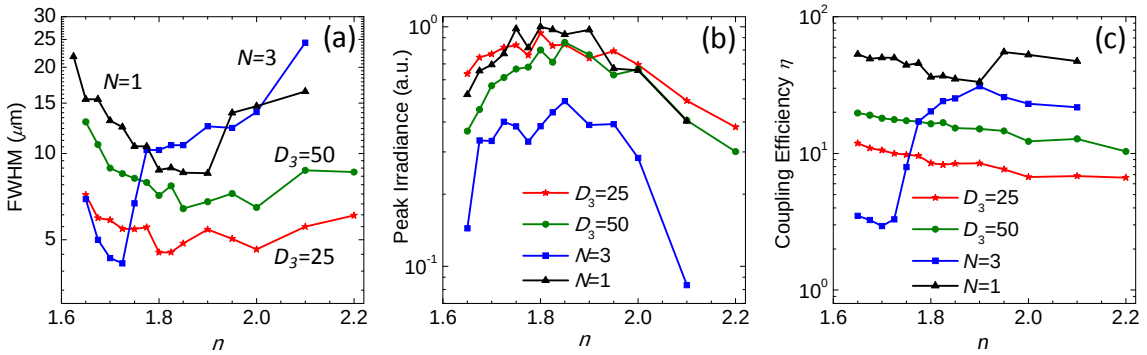

Figure 4.18: (a) FWHM, (b) Peak irradiance, and (c) Power coupling efficiency as a function of the refractive index for different designs.

Although the focused beams obtained from the optimum cases in both conical and identical sphere arrays have comparable sizes, the advantage of the conical arrays over the identical sphere-arrays comes from their greater peak irradiance and power coupling efficiency. As shown in Figs. 4.18(b) and 4.18(c), for arrays of identical spheres with optimum refractive indices $1.675<n<1.725$, the peak irradiance (I_f) is attenuated by a factor of 0.2-0.4 and the power coupling efficiency is on the level of a few percent. However, in the conical arrays peak irradiance is attenuated only by a factor of 0.6-0.8, which shows improvement by a factor of 2 compared with arrays of three identical spheres. Furthermore, coupling efficiencies of about ten percent are calculated for the conical structures, which are 3-4 times more than the coupling efficiencies of the arrays of identical spheres. Increased coupling efficiency of the conical structures compared with that of the arrays of identical spheres, which produce comparable beam sizes to those of the conical arrays, is due to the higher peak irradiances produced by the conical structures.

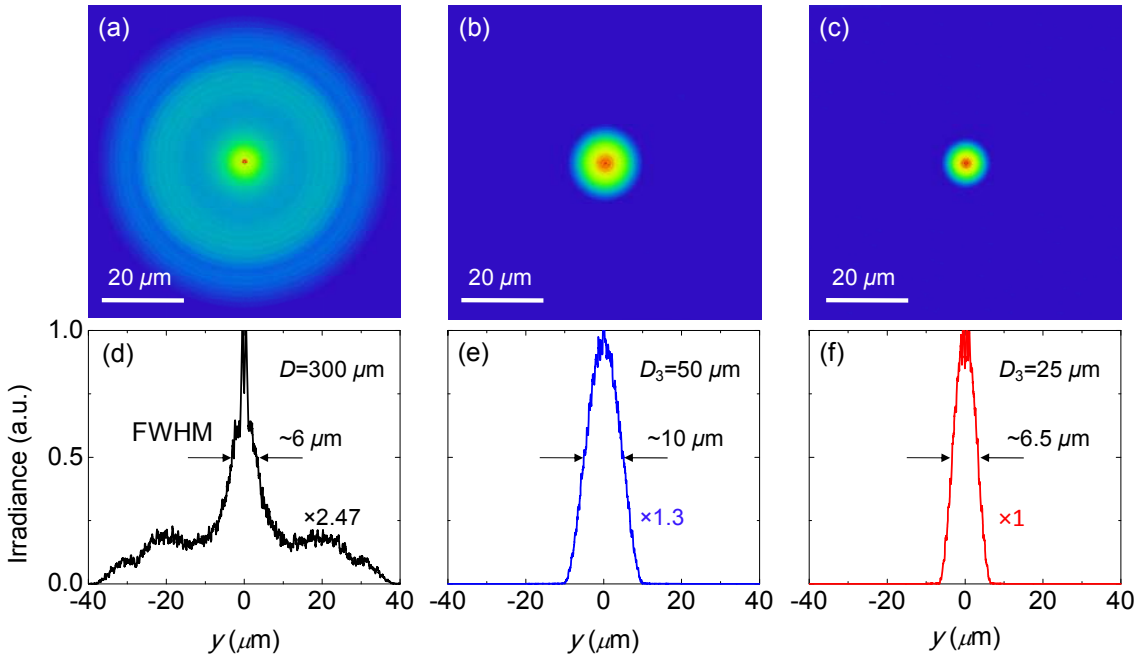

Figure 4.19: Irradiance profiles of (a) chains of three identical spheres with D=300 μm, (b) a conical structure with n=1.71 and D_3=50 μm, (c) a conical structure with n=1.71 and D_3=25 μm. (d-f) normalized irradiance distributions corresponding to (a-c), respectively.

A particular advantage of the conical arrays over the arrays of identical spheres is connected with the fact that the background illumination surrounding the central focused beam in the latter is practically absent in the former, as illustrated in Fig. 4.19. Irradiance distribution of the output beam of a chain of three identical D=300 μm spheres with $1.675<n<1.725$, where they are advantageous in terms of spot sizes, has a central peak with a FWHM~3-6 μm superimposed on a broader and weaker background with the total power P_b and irradiance I_b due to the contribution of non-PFMs, as shown in Figs. 4.19(a) and 4.19(d) for n=1.71. However, the output irradiance profile of a conical structure shows a quasi-Gaussian shape with almost no such a background illumination for the entire range of indices ($1.65<n<2.2$) considered in this work, as illustrated in Figs. 4.19(e) and 4.19(f) for D_3=50 and 25 μm, respectively. We consider n=1.71 because it is

the refractive index of sapphire (or ruby) at ~3 μm wavelength, and also it is in the range where arrays of identical spheres are advantageous over single-sphere microprobe. As mentioned earlier, conical arrays provide more peak irradiance compared with the chains of identical spheres, which is seen directly by comparing Fig. 4.19(f) with Fig. 4.19(d) that shows 2.47 times more peak irradiance in Fig. 4.19(f).

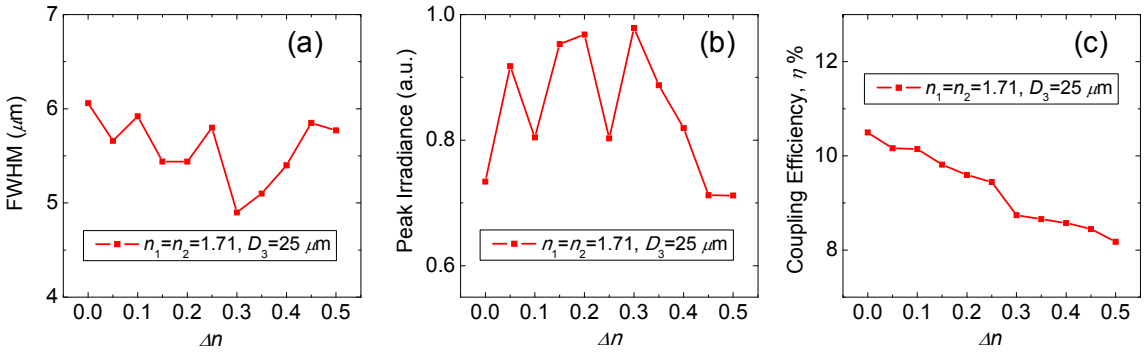

Figure 4.20: Calculated (a) FWHM, (b) Peak irradiance, and (c) Power coupling efficiency for D_3=25 μm, n_1=n_2=1.71, and n_3=1.71+Δn.

In the remaining part of this section, we present the modeling results of conical arrays of spheres with different refractive indices. We consider a conical array of spheres with refractive indices n_1, n_2, n_3, where n_3 is the refractive index of the end-sphere with D_3=25 μm. It is considered that n_1=n_2=1.71 since the sapphire spheres with excellent optical qualities and properties at λ~3 μm can be obtained. We change the index of the end-sphere from 1.71 to 2.21 in Δn=0.05 steps and perform the calculations for each case. The calculated FWHMs, peak irradiances, and coupling efficiencies, as a function of Δn, are presented in Figs. 4.20(a-c), respectively.

As seen in Fig. 4.20(a), for all calculated cases starting from Δn=0, i.e. n_1=n_2=n_3=1.71, to Δn=0.5, i.e. n_1=n_2=1.71, n_3=2.21, the FWHMs are still between 5-6

μm, indicating that this conical structure produces a compact focusing for different high-index spheres. Furthermore, the peak irradiances and power coupling efficiencies are still at least twice as what can be obtained from arrays of three identical D=300 μm spheres with optimum refractive index. However, the coupling efficiency tends to reduce with Δn, indicating that the case of spheres with the same index n=1.71 provides the optimal combination of parameters.

4.5. Conclusions

In this chapter, we studied the focusing properties of multimodal microprobes capable of operating in contact conditions with strongly absorbing media. We designed, fabricated, and tested a device capable of focusing multimodal beams in contact with a tissue.

The designs were optimized for the wavelength of the Er:YAG laser (λ=2.94 μm), which is strongly absorbed in tissue. Our designs showed improvement of the spatial resolution of multi-sphere microprobes by a factor of more than two compared with single-sphere devices. It was demonstrated that the transverse beam sizes of 3-6 μm are possible in three- and five-sphere structures with optimized index of refraction, $1.65<n<1.75$. The peak irradiance and power coupling in these structures were determined as well. An additional advantage of multiple-sphere optical microprobes is connected with the availability of inexpensive microspheres, with excellent optical and mechanical quality and minimal mid-IR absorption, such as sapphire or ruby spheres with n=1.71at $\lambda \sim 3$ μm.

We fabricated the designed microprobes by integrating microsphere-chains with infrared hollow waveguides (HWGs) and fibers. Our integration technique was based on

placing the spheres inside a flexible tube to provide a tightly packed straight array of spheres. Then, the sphere-array was connected to an infrared HWG, optically coupled with an infrared multi-mode fiber. Microprobes were characterized by i) IR imaging and ii) their burn patterns on heat-sensitive papers. The proposed concept of light focusing, developed by the numerical modeling, was experimentally realized.

Furthermore, we proposed focusing microprobes based on using conical arrays of dielectric spheres. A thorough comparison of the results showed the advantage of conical arrays with various diameters of the end-sphere, D_3=25 μm or D_3=50 μm, over other structures. Compared with a single 300 μm sphere, the conical designs provided focused beams with much smaller FWHM. In comparison with chains of three identical 300 μm spheres, the conical structures: i) have 3-4 times more coupling efficiency, ii) provide at least 2 times more peak irradiance, iii) are capable of operating in a much wider range of sphere indices, and iv) do not produce background illumination. The last property might be especially important for developing applications of these structures in ultra-compact surgery because of the potentially reduced thermal damage area on the tissue.

Potential applications of these microprobes include ultra-precise laser procedures in the eye and brain, piercing a cell, and coupling of multimodal beams into photonic microstructures.

CHAPTER 5: CONCLUSIONS AND FUTURE DIRECTIONS

In the first part of this dissertation, we investigated super-resolution imaging ability of high-index dielectric microspheres in liquid environments. We proposed a super-resolution microscopy technique based on liquid immersion of high-index microspheres. By using barium titanate glass microspheres with n~1.9-2.1 immersed in isopropyl alcohol or other liquids, we showed that minimal feature sizes ~$\lambda/7$ can be discerned by an ~5 μm diameter sphere. Based on our experience, we predict that this technique can have broad applications with various structures for imaging and with various sphere materials. The prospect of using biological samples, such as cells, needs further study of a possible plasmons involvement with metallic surfaces. However, such biomedical applications would be of major importance for developing applications of this technique.

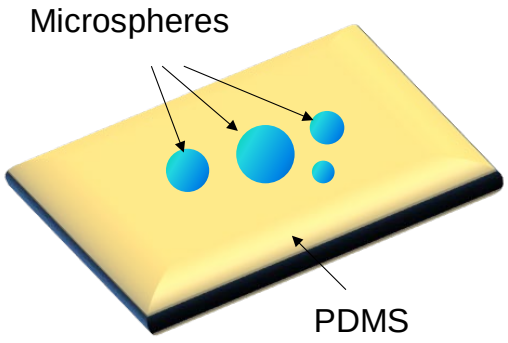

Figure 5.1: Schematic illustrating high-index microspheres embedded in a material with an ability to solidify such as PDMS forming a thin film which can be transferred and attached to the top of the structure under study. The microspheres are embedded in this thin film.

The future direction of this research is connected with using spheres made from various high index materials such as titania or semiconductors. Depending on the application, the spheres can be immersed in a liquid or in polymer materials, as schematically illustrated in Fig. 5.1. Due to its simplicity, the super-resolution imaging by high-index microspheres can find many applications in biomedical microscopy, micro-fluidic devices, and nanophotonics.

Furthermore, the following can be investigated:

1. Imaging by using a radially polarized incident light on the microspheres, as it is known that radial polarization leads to sharper focusing of light [225]. This direction can be studied by using low-index ($1.45<n<1.6$) microspheres in air or high-index ($n>1.9$) spheres in liquids.
2. The possible contribution of the whispering gallery modes (WGMs), inside the microspheres, to the improvement of image resolution.
3. The role of plasmon excitation can be studied in detail by using samples made from different metals on glass or semiconductor substrates and different illumination filters.
4. Develop a near-field imaging theory for the liquid-immersed microspheres to explain the two different magnification regimes, which we observed experimentally in Chapter 2.
5. Use dielectric cylinders to resolve sub-diffraction-limited features since it is known that dielectric cylinders [85] can also produce photonic nanojets, as reviewed in Section 1.3.2 of Chapter 1. For example an etched fiber down to its core which gives a cylinder with <8 μm diameter can be placed on top of the

samples, as schematically illustrated in Fig. 5.2(a). In our initial studies, we placed an etched silica fiber (n~1.46) with diameter ~7 μm semi-immersed in isopropyl alcohol (IPA) on the gold nanoparticle dimmers (NPD) sample described in Section 2.2 of Chapter 2. The 150 nm separations between dimers were clearly resolved using this method, as presented in Figs. 5.2(c) and 5.2(d). By comparing Fig. 5.2(d) with Fig. 2.15(h), it can be seen that imaging through the dielectric cylinder has better resolution compared with imaging by the dielectric hemisphere (h-SIL). The 200 nm gaps in x direction were not resolved due to one dimensional nature of the photonic nanojets created by the cylinder.

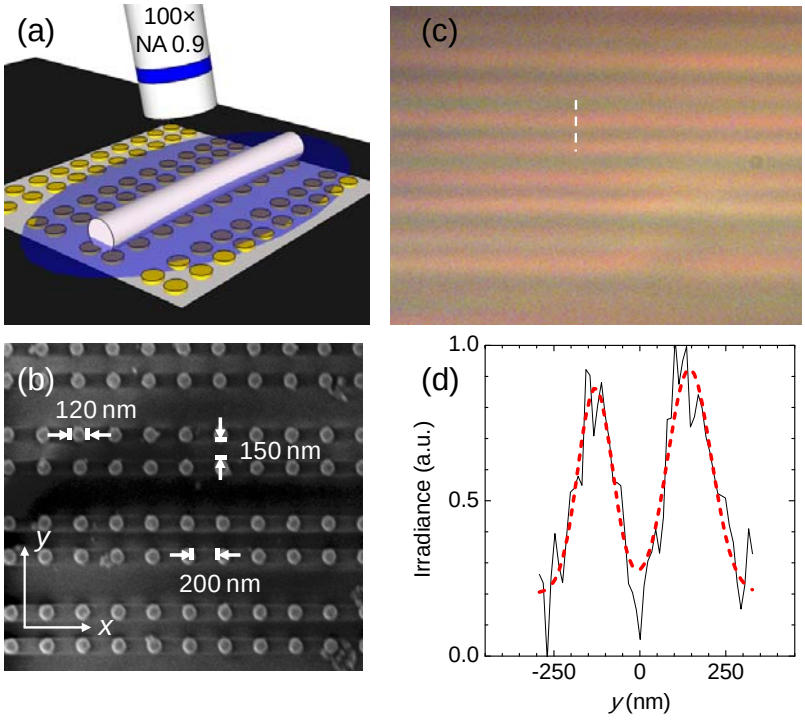

Figure 5.2: (a) Schematic of the imaging method with an etched optical fiber semi-immersed in IPA. (b) SEM of the NPD sample. (c) Micrograph of the sample. (d) Irradiance profile along the dashed line shown in (c).

In the second part of this dissertation, we studied light transport and periodical focusing properties of linear chains of touching dielectric spheres. We described a new waveguiding mechanism in such chains based on the concept of periodically focused modes (PFMs). PFMs are formed if a collimated incident ray satisfies the Brewster's angle condition and crosses the optical axis on the shadow-side surface of the sphere. These rays periodically propagate along the chain without loss. In real physical chains, these aspects of light propagation and focusing should be studied based on the concepts of waves. The formation of optical modes in such structures is novel and interesting. The theoretical understanding of these effects requires modeling tools capable of solving Maxwell's equations in complex geometries. We anticipate that the modal propagation losses will not be zero in physical optics, however, they can still be quite small, an interesting area of future studies. The PFM concept gives a physical explanation for an extraordinarily small attenuation of light in such chains, together with a successive focused spots' size reduction. The results of our work, which scale with spheres' sizes in the limit of geometrical optics assumptions, can be used for developing light focusing devices, coupled with multimodal light sources. Examples of such applications include ultra-precise laser procedures in the eye and brain or piercing a cell, as well as for coupling light into photonic microstructures. Directions for future works are the following:

1. Using microspheres made from optically nonlinear and/or active materials, such as ruby, where a combination of sharp focusing and periodicity should lead to efficient optical parametric and lasing processes.

2. Study the role of the observed microjoints [142, 143] formed between polystyrene sphere-chains in light transport in such chains. For example, a natural question to ask is the following: if chains of glass microspheres, which do not show microjoint formation between the spheres, with the same refractive index as polystyrene (n=1.59) are assembled, how do their optical transport properties differ from their polystyrene counterparts?
3. Experimentally study the polarization properties of such chains for both mesoscale and larger spheres.
4. Study "beam tapering" effect, optical power transport, and polarization properties by means of finite-difference time-domain (FDTD) or finite element method (FEM) modeling for the case of smaller spheres $D<10\lambda$.

In the third part of this dissertation, by using the concept of PFM in chains of dielectric spheres, we designed, fabricated, and tested microprobes for laser-tissue surgery capable of focusing the input laser beams in contact with tissue. The proposed design composed of two main components: i) Er:YAG laser delivery and ii) focusing section. Infrared laser is delivered by a multimode fiber and coupled to a hollow waveguide. As a focusing section, a chain of sapphire (or ruby) spheres was used to provide very compact focusing just at the tip of the probe. In this way, the focusing is not perturbed by the tissue. Furthermore, due to the sharp focusing, the beam is very diverging just away from the tip, which provides a shallow depth of surgery. The final goal of these studies was to commercially manufacture that device for retina surgery, where the role of the probe is to provide very fine cuts through the fibrotic membranes formed at the retina surface.

One interesting direction, which is related to this work, is that by engineering a cylindrical vectors beam [222] with radial polarization or a “doughnut beam” incident on the sphere, sharp focusing can be achieved by using just one sphere. If such a beam is formed at the output of the fiber, then the fiber should be placed in very proximity of the sphere and there is no need to use the hollow waveguide (HWG). This approach may increase the power coupling efficiency of the microprobe.

In principle, the work on developing focusing microprobes can be developed towards using single mode fibers and single-mode delivery systems. The advantage of such systems is connected with better focusing capability, which in many cases does not require multiple sphere chains for achieving tightly focused spots. The problem of development of these systems though is connected with their poor coupling efficiencies. Some advances in this area have been obtained in visible and near-IR regimes [254, 255]. However application of such systems in mid-IR regime would require single-mode laser sources and flexible delivery systems. This is a highly promising area of applications which is under development in the Mesophotonics Laboratory.

REFERENCES

[1] M. Born and E. Wolf, [Principles of Optics, 7th Edition] Cambridge University Press, Cambridge, UK (2003).

[2] E. Abbe, "Beiträge zur theorie des mikroskops und der mikroskopischen wahrnehmung," Archiv für Mikroskopische Anatomie, 9(1), 413-418 (1873).

[3] Lord Rayleigh, "Investigations in optics, with special reference to the spectroscope," Philosophical Magazine, 8(49), 261-274 (1879).

[4] C. M. Sparrow, "On spectroscopic resolving power," Astrophysical Journal, 44(2), 76-86 (1916).

[5] W. V. Houston, "A compound interferometer for fine structure work," Physical Review, 29(3), 478-484 (1927).

[6] A. Buxton, "Note on optical resolution," Philosophical Magazine, 23(154), 440-442 (1937).

[7] B. P. Ramsay, E. L. Cleveland, and O. T. Koppius, "Criteria and the intensity-epoch slope," Journal of the Optical Society of America, 31(1), 26-33 (1941).

[8] A. J. den Dekker and A. van den Bos, "Resolution: a survey," Journal of the Optical Society of America A, 14(3), 547-557 (1997).

[9] D. E. Wolf, "The optics of microscope image formation," Methods in Cell Biology, 81, 11-42 (2007).

[10] A. Lipson, S. G. Lipson, and H. Lipson, [Optical Physics, 4th Edition] Cambridge University Press, Cambridge, UK (2010).

[11] G. T. d. Francia, "Super-gain antennas and optical resolving power," Il Nuovo Cimento, 9(3), 426-438 (1952).

[12] W. Lukosz, "Optical systems with resolving powers exceeding the classical limit," Journal of the Optical Society of America, 56(11), 1463-1472 (1966).

[13] T. R. M. Sales and G. M. Morris, "Fundamental limits of optical superresolution," Optics Letters, 22(9), 582-584 (1997).

[14] S. W. Hell, "Microscopy and its focal switch," Nature Methods, 6(1), 24-32 (2009).

[15] M. E. Testorf and M. A. Fiddy, "Superresolution imaging-revisited," Advances in Imaging and Electron Physics, 163, 165-218 (2010).

[16] A. Neice, "Methods and limitations of subwavelength imaging," Advances in Imaging and Electron Physics, 163, 117-140 (2010).

[17] J. Lindberg, "Mathematical concepts of optical superresolution," Journal of Optics, 14(8), 083001(23 pp) (2012).

[18] R. Hooke, [Lectures and Collections. Cometa & Microscopium] John Martyn, Printer to the Royal Society, London (1678).

[19] S. M. Mansfield and G. S. Kino, "Solid immersion microscope," Applied Physics Letters, 57(24), 2615-2616 (1990).

[20] B. D. Terris, H. J. Mamin, D. Rugar, W. R. Studenmund, and G. S. Kino, "Near-field optical data storage using a solid immersion lens," Applied Physics Letters, 65(4), 388-390 (1994).

[21] B. D. Terris, H. J. Mamin, and D. Rugar, "Near-field optical data storage," Applied Physics Letters, 68(2), 141-143 (1996).

[22] G. S. Kino, "The solid immersion lens," Proceedings of SPIE, 3740, 2-5 (1999).

[23] Q. Wu, G. D. Feke, R. D. Grober, and L. P. Ghislain, "Realization of numerical aperture 2.0 using a gallium phosphide solid immersion lens," Applied Physics Letters, 75(26), 4064-4066 (1999).

[24] T. D. Milster, "Near-field optical data storage: avenues for improved performance," Optical Engineering, 40(10), 2255-2260 (2001).

[25] T. D. Milster, F. Akhavan, M. Bailey, J. K. Erwin, D. M. Felix, K. Hirota, S. Koester, K. Shimura, and Y. Zhang, "Super-resolution by combination of a solid immersion lens and an aperture," Japanese Journal of Applied Physics, 40(3B), 1778-1782 (2001).

[26] K. Karrai, X. Lorenz, and L. Novotny, "Enhanced reflectivity contrast in confocal solid immersion lens microscopy," Applied Physics Letters, 77(21), 3459-3461 (2000).

[27] Q. Wu, L. P. Ghislain, and V. B. Elings, "Imaging with solid immersion lenses, spatial resolution, and applications," Proceedings of the IEEE, 88(9), 1491-1498 (2000).

[28] Y. Zhang, "Design of high-performance supersphere solid immersion lenses," Applied Optics, 45(19), 4540-4546 (2006).

[29] A. N. Vamivakas, R. D. Younger, B. B. Goldberg, A. K. Swan, M. S. Ünlü, E. R. Behringer, and S. B. Ippolito, "A case study for optics: The solid immersion microscope," American Journal of Physics, 76(8), 758-768 (2008).

[30] K. A. Serrels, E. Ramsay, P. A. Dalgarno, B. D. Gerardot, J. A. O'Conner, R. H. Hadfield, R. J. Warburton, and D. T. Reid, "Solid immersion lens applications for nanophotonic devices," Journal of Nanophotonics,, 2(1), 021854(29pp) (2008).

[31] K. A. Serrels, E. Ramsay, R. J. Warburton, and D. T. Reid, "Nanoscale optical microscopy in the vectorial focusing regime," Nature Photonics, 2(5), 311-314 (2008).

[32] R. Chen, K. Agarwal, Y. Zhong, C. J. R. Sheppard, J. C. H. Phang, and X. Chen, "Complete modeling of subsurface microscopy system based on aplanatic solid immersion lens," Journal of the Optical Society of America A, 29(11), 2350-2359 (2012).

[33] S. Moehl, H. Zhao, B. Dal Don, S. Wachter, and H. Kalt, "Solid immersion lens-enhanced nano-photoluminescence: Principle and applications," Journal of Applied Physics, 93(10), 6265-6272 (2003).

[34] R. Chen, K. Agarwal, C. J. R. Sheppard, J. C. H. Phang, and X. Chen, "Resolution of aplantic solid immersion lens based microscopy," Journal of the Optical Society of America A, 29(6), 1059-1070 (2012).

[35] D. R. Mason, M. V. Jouravlev, and K. S. Kim, "Enhanced resolution beyond the Abbe diffraction limit with wavelength-scale solid immersion lenses," Optics Letters, 35(12), 2007-2009 (2010).

[36] M.-S. Kim, T. Scharf, M. T. Hag, W. Nakagawa, and H. P. Herzig, "Subwavelength-size solid immersion lens," Optics Letters, 36(19), 3930-3932 (2011).

[37] A. Vlad, I. Huynen, and S. Melinte, "Wavelength-scale lens microscopy via thermal reshaping of colloidal particles," Nanotechnology, 23(28), 285708(9pp) (2012).

[38] B. E. A. Saleh and M. C. Teich, [Fundamentals of Photonics, 2nd Edition] John Wiely & Sons, Hoboken, NJ (2007).

[39] D. W. Pohl, W. Denk, and M. Lanz, "Optical stethoscopy: Image recording with resolution $\lambda/20$," Applied Physics Letters, 44(7), 651-653 (1984).

[40] B. Hecht, B. Sick, U. P. Wild, V. Deckert, R. Zenobi, O. J. F. Martin, and D. W. Pohl, "Scanning near-field optical microscopy with aperture probes: Fundamentals and applications," Journal of Chemical Physics, 112(18), 7761-7774 (2000).

[41] S. J. Bukofsky and R. D. Grober, "Video rate near-field scanning optical microscopy," Applied Physics Letters, 71(19), 2749-2751 (1997).

[42] D. Courjon, [Near-field microscopy and near-field optics] Imperial College Press, London, UK (2007).

[43] L. Novotny, "The history of near-field optics," Progress in Optics, 50, 137-184 (2007).

[44] M. V. Berry and S. Popescu, "Evolution of quantum superoscillations and optical superresolution without evanescent waves," Journal of Physics A: Mathematical and General, 39(22), 6965-6977 (2006).

[45] N. I. Zheludev, "What diffraction limit?" Nature Materials, 7(6), 420-422 (2008).

[46] E. T. F. Rogers, J. Lindberg, T. Roy, S. Savo, J. E. Chad, M. R. Dennis, and N. I. Zheludev, "A super-oscillatory lens optical microscope for subwavelength imaging," Nature Materials, 11(5), 432-435 (2012).

[47] R. Heintzmann and G. Ficz, "Breaking the resolution limit in light microscopy," Briefings in Functional Genomics and Proteomics, 5(4), 289-301 (2006).

[48] J. M. Kasuboski, Y. J. Sigal, M. S. Joens, B. F. Lillemeier, and J. A. J. Fitzpatrick, "Super-resolution microscopy: A comparative treatment," Current Protocols in Cytometry, 62, 2.17.1-2.17.24 (2012).

[49] T. J. Gould, S. T. Hess, and J. Bewersdorf, "Optical nanoscopy: From acquisition to analysis," Annual Review of Biomedical Engineering, 14, 231-254 (2012).

[50] S. W. Hell, "Far-field optical nanoscopy," Science, 316(5828), 1153-1158 (2007).

[51] J. B. Pendry, "Negative refraction makes a perfect lens," Physical Review Letters, 85(18), 3966-3969 (2000).

[52] N. Fang, H. Lee, C. Sun, and X. Zhang, "Sub-diffraction-limited optical imaging with a silver superlens," Science, 308(5721), 534-537 (2005).

[53] T. Taubner, D. Korobkin, Y. Urzhumov, G. Shvets, and R. Hillenbrand, "Near-field microscopy through a SiC superlens," Science, 313(5793), 1595 (2006).

[54] Z. Liu, H. Lee, Y. Xiong, C. Sun, and X. Zhang, "Far-field optical hyperlens magnifying sub-diffraction-limited objects," Science, 315(5819), 1686 (2007).

[55] X. Zhang and Z. Liu, "Superlenses to overcome the diffraction limit," Nature Materials, 7(6), 435-441 (2008).

[56] Z. Jacob, L. V. Alekseyev, and E. Narimanov, "Optical hyperlens: Far-field imaging beyond the diffraction limit," Optics Express, 14(18), 8247-8256 (2006).

[57] I. I. Smolyaninov, Y.-J. Hung, and C. C. Davis, "Magnifying Superlens in the Visible Frequency Range," Science, 315(5819), 1699-1701 (2007).

[58] Q. Wang, J. Bu, P. S. Tan, G. H. Yuan, J. H. Teng, H. Wang, and X.-C. Yuan, "Subwavelength-sized plasmonic structures for wide-field optical microscopic imaging with super-resolution," Plasmonics, 7(3), 427-433 (2012).

[59] L. Alekseyev, E. Narimanov, and J. Khurgin, "Super-resolution imaging via spatiotemporal frequency shifting and coherent detection," Optics Express, 19(22), 22350-22357 (2011).

[60] J. Y. Lee, B. H. Hong, W. Y. Kim, S. K. Min, Y. Kim, M. V. Jouravlev, R. Bose, K. S. Kim, I.-C. Hwang, L. J. Kaufman, C. W. Wong, P. Kim, and K. S. Kim, "Near-field focusing and magnification through self-assembled nanoscale spherical lenses," Nature, 460(7254), 498-501 (2009).

[61] V. N. Smolyaninova, I. I. Smolyaninov, A. V. Kildishev, and V. M. Shalaev, "Maxwell fish-eye and Eaton lenses emulated by microdroplets," Optics Letters, 35(20), 3396-3398 (2010).

[62] V. V. Yakovlev and B. Luk'yanchuk, "Multiplexed nanoscopic imaging," Laser Physics, 14(8), 1065-1071 (2004).

[63] Z. Wang, W. Guo, L. Li, B. Luk'yanchuk, A. Khan, Z. Liu, Z. Chen, and M. Hong, "Optical virtual imaging at 50 nm lateral resolution with a white-light nanoscope," Nature Communications, 2, Article no. 218(6 pp) (2011).

[64] X. Hao, C. Kuang, X. Liu, H. Zhang, and Y. Li, "Microsphere based microscope with optical super-resolution capability," Applied Physics Letters, 99(20), 203102(3pp) (2011).

[65] Y. Ben-Aryeh, "Superresolution observed from evanescent waves transmitted through nano-corrugated metallic films," Applied Physics B, 109(1), 165-170 (2012).

[66] C. C. Lam, P. T. Leung, and K. Young, "Explicit asymptotic formulas for the positions, widths, and strengths of resonances in Mie scattering," Journal of the Optical Society of America B, 9(9), 1585-1592 (1992).

[67] V. S. Ilchenko, P. S. Volikov, V. L. Velichansky, F. Treussart, V. Lefèvre-Seguin, J.-M. Raimond, and S. Haroche, "Strain-tunable high-Q optical microsphere resonator," Optics Communications, 145(1-6), 86-90 (1998).

[68] A. N. Oraevsky, "Whispering-gallery waves," Quantum Electronics, 32(5), 377-400 (2002).

[69] V. N. Astratov, "Fundamentals and applications of microsphere resonator circuits," in [Photonic microresonator research and applications], I. Chremmos, O. Schwelb, and N. Uzunoglu Eds., Springer Series in Optical Sciences 156, 423-457, New York, NY (2010).

[70] A. Chiasera, Y. Dumeige, P. Féron, M. Ferrari, Y. Jestin, G. Nunzi Conti, S. Pelli, S. Soria, and G. C. Righini, "Spherical whispering-gallery-mode microresonators," Laser & Photonics Reviews, 4(3), 457-482 (2010).

[71] G. C. Righini, Y. Dumeige, P. Féron, M. Ferrari, G. Nunzi Conti, D. Ristic, and S. Soria, "Whispering gallery mode microresonators: Fundamentals and applications," Rivista Del Nuovo Cimento, 34(7), 435-488 (2011).

[72] S. Arnold, M. Khoshsima, I. Teraoka, S. Holler, and F. Vollmer, "Shift of whispering-gallery modes in microspheres by protein adsorption," Optics Letters, 28(4), 272-274 (2003).

[73] K. J. Vahala, "Optical microcavities," Nature, 424(6950), 839-846 (2003).

[74] K. R. Hiremath and V. N. Astratov, "Perturbation of whispering gallery modes by nanoparticles embedded in microcavities," Optics Express, 16(8), 5421-5426 (2008).

[75] F. Vollmer and S. Arnold, "Whispering-gallery-mode biosensing: label-free detection down to single molecules," Nature Methods, 5(7), 591-596 (2008).

[76] J. Ward and O. Benson, "WGM microresonators: sensing, lasing and fundamental optics with microspheres," Laser & Photonics Reviews, 5(4), 553-570 (2011).

[77] S. Arnold, S. I. Shopova, and S. Holler, "Whispering gallery mode bio-sensor for label-free detection of single molecules: thermo-optic vs. reactive mechanism," Optics Express, 18(1), 281-287 (2010).

[78] A. B. Matsko, A. A. Savchenkov, D. Strekalov, V. S. Ilchenko, and L. Maleki, "Review of applications of whispering-gallery mode resonators in photonics and nonlinear optics," IPN Progress Report, 42-162 (2005).

[79] A. B. Matsko and V. S. Ilchenko, "Optical resonators with whispering-gallery modes-Part I: Basics," IEEE journal of selected topics in Quantum Electronics, 12(1), 3-14 (2006).

[80] V. S. Ilchenko and A. B. Matsko, "Optical resonators with whispering-gallery modes-Part II: Applications," IEEE journal of selected topics in Quantum Electronics, 12(1), 15-32 (2006).

[81] O. Svitelskiy, D. Sun, A. Darafsheh, M. Sumetsky, A. Lupu, M. Tchernycheva, and V. N. Astratov, "Characterization of high index microsphere resonators in fiber-integrated microfluidic platforms," Proceedings of SPIE, 7913, 791314(7pp) (2011).

[82] O. Svitelskiy, Y. Li, A. Darafsheh, M. Sumetsky, D. Carnegie, E. Rafailov, and V. N. Astratov, "Fiber coupling to $BaTiO_3$ glass microspheres in aqueous environment," Optics Letters, 36(15), 2862-2864 (2011).

[83] T. Lu, H. Lee, T. Chen, S. Herchak, J.-H. Kim, S. E. Fraser, R. C. Flagan, and K. Vahala, "High sensitivity nanoparticle detection using optical microcavities," Proceeding of the National Academy of Sciences of the United States of America, 108(5), 5976-5979 (2011).

[84] M. Gerlach, Y. P. Rakovich, and J. F. Donegan, "Radiation-pressure-induced mode splitting in a spherical microcavity with an elastic shell," Optics Express, 15(6), 3597-3606 (2007).

[85] Z. Chen, A. Taflove, and V. Backman, "Photonic nanojet enhancement of backscattering of light by nanoparticles: a potential novel visible-light ultramicroscopy technique," Optics Express, 12(7), 1214-1220 (2004).

[86] X. Li, Z. Chen, A. Taflove, and V. Backman, "Optical analysis of nanoparticles via enhanced backscattering facilitated by 3-D photonic nanojets," Optics Express, 13(2), 526-533 (2005).

[87] A. Heifetz, S.-C. Kong, A. V. Sahakian, A. Taflove, and V. Backman, "Photonic nanojets," Journal of Computational and Theoretical Nanoscience, 6(9), 1979-1992 (2009).

[88] S. Lecler, Y. Takakura, and P. Meyrueis, "Properties of a three-dimensional photonic jet," Optics Letters, 30(19), 2641-2643 (2005).

[89] A. V. Itagi and W. A. Challener, "Optics of photonic nanojets," Journal of the Optical Society of America A, 22(12), 2847-2858 (2005).

[90] Z. Chen, A. Taflove, X. Li, and V. Backman, "Superenhanced backscattering of light by nanoparticles," Optics Letters, 31(2), 196-198 (2006).

[91] P. Ferrand, J. Wenger, A. Devilez, M. Pianta, B. Stout, N. Bonod, E. Popov, and H. Rigneault, "Direct imaging of photonic nanojets," Optics Express, 16(10), 6930-6940 (2008).

[92] A. Devilez, B. Stout, N. Bonod, and E. Popov, "Spectral analysis of three-dimensional photonic jets," Optics Express, 16(18), 14200-14212 (2008).

[93] A. Devilez, N. Bonod, J. Wenger, D. Gérard, B. Stout, H. Rigneault, and E. Popov, "Three-dimensional subwavelength confinement of light with dielectric microspheres," Optics Express, 17(4), 2089-2094 (2009).

[94] S.-C. Kong, A. Taflove, and V. Backman, "Quasi one-dimensional light beam generated by a graded-index microsphere," Optics Express, 17(5), 3722-3731 (2009).

[95] S.-C. Kong, A. Taflove, and V. Backman, "Quasi one-dimensional light beam generated by a graded-index microsphere: errata," Optics Express, 18(4), 3973 (2010).

[96] Y. E. Geints, A. A. Zemlyanov, and E. K. Panina, "Controlling the parameters of photon nanojets of composite microspheres," Optics and Spectroscopy, 109(4), 590-595 (2010).

[97] Y. E. Geints, E. K. Panina, and A. A. Zemlyanov, "Control over parameters of photonic nanojets of dielectric microspheres," Optics Communications, 283(23), 4775-4781 (2010).

[98] H. Ding, L. Dai, and C. Yan, "Properties of the 3D photonic nanojet based on the refractive index of surroundings," Chinese Optics Letters, 8(7), 706-708 (2010).

[99] M.-S. Kim, T. Scharf, S. Mühlig, C. Rockstuhl, and H. P. Herzig, "Engineering photonic nanojets," Optics Express, 19(11), 10206-10220 (2011).

[100] M.-S. Kim, T. Scharf, S. Mühlig, C. Rockstuhl, and H. P. Herzig, "Gouy phase anomaly in photonic nanojets," Applied Physics Letters, 98(19), 191114(3pp) (2011).

[101] Y. Liu, B. Wang, and Z. Ding, "Influence of incident light polarization on photonic nanojet," Chinese Optics Letters, 9(7), 072901(3pp) (2011).

[102] D. McCloskey, J. J. Wang, and J. F. Donegan, "Low divergence photonic nanojets from Si3N4 microdisks," Optics Express, 20(1), 128-140 (2012).

[103] Y. E. Geints, A. A. Zemlyanov, and E. K. Panina, "Photonic nanojet calculations in layered radially inhomogeneous micrometer-sized spherical particles," Journal of the Optical Society of America B, 28(8), 1825-1830 (2011).

[104] Y. E. Geints, A. A. Zemlyanov, and E. K. Panina, "Photonic nanojet effect in multilayer micrometer-sized spherical particles," Quantum Electronics, 41(6), 520-525 (2011).

[105] P. Bon, B. Rolly, N. Bonod, J. Wenger, B. Stout, S. Monneret, and H. Rigneault, "Imaging the Gouy phase shift in photonic jets with a wavefront sensor," Optics Letters, 37(17), 3531-3533 (2012).

[106] Y. E. Geints, A. A. Zemlyanov, and E. K. Panina, "Photonic jets from resonantly excited transparent dielectric microspheres," Journal of the Optical Society of America B, 29(4), 758-762 (2012).

[107] H. Guo, Y. Han, X. Weng, Y. Zhao, G. Sui, Y. Wang, and S. Zhuang, "Near-field focusing of the dielectric microsphere with wavelength scale radius," Optics Express, 21(2), 2434-2443 (2013).

[108] Z. Chen, A. Taflove, and V. Backman, "Highly efficient optical coupling and transport phenomena in chains of dielectric microspheres," Optics Letters, 31(3), 389-391 (2006).

[109] A. M. Kapitonov and V. N. Astratov, "Observation of nanojet-induced modes with small propagation losses in chains of coupled spherical cavities," Optics Letters, 32(4), 409-411 (2007).

[110] S. Yang and V. N. Astratov, "Photonic nanojet-induced modes in chains of size-disordered microspheres with an attenuation of only 0.08 dB per sphere," Applied Physics Letters, 92(26), 261111(3pp) (2008).

[111] J. W. Goodman, [Introduction to Fourier Optics, 3rd Edition] Roberts and Company Publishers, Greenwood, CO (2005).

[112] B. Richards and E. Wolf, "Electromagnetic diffraction in optical systems II, structure of the image field in an aplantic system," Proceedings of the Royal Society of London A, 253(1274), 358-379 (1959).

[113] D. N. Grimes and B. J. Thompson, "Two-point resolution with partially coherent light," Journal of the Optical Society of America, 57(11), 1330-1334 (1967).

[114] H. H. Hopkins and P. M. Barham, "The influence of the condenser on microscopic resolution," Proceedings of the Physical Society B, 63(10), 737-744 (1950).

[115] T. S. McKechnie, "The effect of condenser obstruction on the two-point resolution of a microscope," Optica Acta, 19(9), 729-737 (1972).

[116] J. W. Goodman, [Statistical Optics] Wiley, New York, NY (1985).

[117] V. G. Veselago, "The electrodynamics of substances with simultaneously negative values of ε and μ," Soviet Physics Uspekhi, 10(4), 509-514 (1968).

[118] R. J. Potton, "Reciprocity in optics," Reports on Progress in Physics, 67(5), 717-754 (2004).

[119] N. Arnold, "Theoretical description of dry laser cleaning," Applied Surface Science, 208-209, 15-22 (2003).

[120] J. Ng and C. T. Chan, "Size-selective optical forces for microspheres using evanescent wave excitation of whispering gallery modes," Applied Physics Letters, 92(25), 251109(3pp) (2008).

[121] J. J. Xiao, J. Ng, Z. F. Lin, and C. T. Chan, "Whispering gallery mode enhanced optical force with resonant tunneling excitation in the Kretschmann geometry," Applied Physics Letters, 94(1), 011102(3pp) (2009).

[122] R. K. Chang and A. J. Campillo Eds., [Optical Processes in Microcavities], Advanced Series in Applied Physics, Vol. 3, World Scientific, Singapore (1996).

[123] J. Stratton, [Electromagnétisme] Masson, Paris, France (1960).

[124] J. Jackson, [Classical Electrodynamics, 3rd Edition] John Wiley & Sons, New York, NY (1999).

[125] S. Yang and V. N. Astratov, "Spectroscopy of photonic molecular states in supermonodispersive bispheres," Proceedings of SPIE, 7194, 719411(9pp) (2009).

[126] G. S. Murugan, Y. Panitchob, E. J. Tull, P. N. Bartlett, D. W. Hewak, M. N. Zervas, and J. S. Wilkinson, "Position-dependent coupling between a channel waveguide and a distorted microsphere resonator," Journal of Applied Physics, 107(5), 053105(9pp) (2010).

[127] H. C. van de Hulst, [Light scattering by small particles] Dover Publications, Inc., New York, NY (1981).

[128] C. L. Adler, J. A. Lock, B. R. Stone, and C. J. Garcia, "High-order interior caustics produced in scattering of a diagonally incident plane wave by a circular cylinder," Journal of the Optical Society of America A, 14(6), 1305-1315 (1997).

[129] J. A. Lock, C. L. Adler, and E. A. Hovenac, "Exterior caustics produced in scattering of a diagonally incident plane wave by a circular cylinder: semiclassical scattering theory analysis," Journal of the Optical Society of America A, 17(10), 1846-1856 (2000).

[130] J. Kofler and N. Arnold, "Axially symmetric focusing as a cupsoid diffraction catastrophe: Scalar and vector cases and comparison with the theory of Mie," Physical Review B, 73(23), 235401(16 pp) (2006).

[131] C. J. R. Sheppard and P. Török, "Focal shift and the axial optical coordinate for high-aperture systems of finite Fresnel number," Journal of the Optical Society of America A, 20(11), 2156-2162 (2003).

[132] Y. Li, "Focal shifts in diffracted converging electromagnetic waves. I. Kirchhoff theory," Journal of the Optical Society of America A, 22(1), 68-76 (2005).

[133] S. Guo, H. Guo, and S. Zhuang, "Analysis of imaging properties of a microlens based on the method for a dyadic Green's function," Applied Optics, 48(2), 321-327 (2009).

[134] J. F. Owen, R. K. Chang, and P. W. Barber, "Internal electric field distributions of a dielectric cylinder at resonance wavelengths," Optics Letters, 6(11), 540-542 (1981).

[135] D. S. Benincasa, P. W. Barber, J.-Z. Zhang, W.-F. Hsieh, and R. K. Chang, "Spatial distribution of the internal and near-field intensities of large cylindrical and spherical scatters," Applied Optics, 26(7), 1348-1356 (1987).

[136] C. F. Bohren and D. R. Huffman, [Absorption and scattering of light by small particles] Wiley, New York, NY (1983).

[137] R. T. Wang and H. C. van de Hulst, "Rainbows: Mie computations and the Airy approximation," Applied Optics, 30(1), 106-117 (1991).

[138] A. Heifetz, J. J. Simpson, S.-C. Kong, A. Taflove, and V. Backman, "Subdiffraction optical resolution of a gold nanosphere located within the nanojet of a Mie-resonant dielectric microsphere," Optics Express, 15(25), 17334-17342 (2007).

[139] V. N. Astratov, J. P. Franchak, and S. P. Ashili, "Optical coupling and transport phenomena in chains of spherical dielectric microresonators with size disorder," Applied Physics Letters, 85(23), 5508-5510 (2004).

[140] A. V. Kanaev, V. N. Astratov, and W. Cai, "Optical coupling at a distance between detuned spherical cavities," Applied Physics Letters, 88(11), 111111(3pp) (2006).

[141] O. Lecarme, T. Pinedo Rivera, L. Arbez, T. Honeggar, K. Berton, and D. Peyrade, "Colloidal optical waveguides with integrated local light sources built by capillary force assembly," Journal of Vacuum Science & Technology B, 28(6), C6O11-C6O15 (2010).

[142] T. Mitsui, Y. Wakayama, T. Onodera, T. Hayashi, N. Ikeda, Y. Sugimoto, T. Takamasu, and H. Oikawa, "Micro-demultiplexer of coupled resonator optical waveguides fabricated by microspheres," Advanced Materials, 22(28), 3022-3026 (2010).

[143] T. Mitsui, T. Onodera, Y. Wakayama, T. Hayashi, N. Ikeda, Y. Sugimoto, T. Takamasu, and H. Oikawa, "Influence of micro-joints formed between spheres in coupled-resonator optical waveguide," Optics Express, 19(22), 22258- 22267 (2011).

[144] A. Heifetz, K. Huang, A. V. Sahakian, X. Li, A. Taflove, and V. Backman, "Experimental confirmation of backscattering enhancement induced by a photonic jet," Applied Physics Letters, 89(22), 221118(3 pp) (2006).

[145] S. Yang, A. Taflove, and V. Backman, "Experimental confirmation at visible light wavelengths of the backscattering enhancement phenomenon of the photonic nanojet," Optics Express, 19(8), 7084-7093 (2011).

[146] S.-C. Kong, A. Sahakian, A. Taflove, and V. Backman, "Photonic nanojet-enabled optical data storage," Optics Express, 16(18), 13713-13719 (2008).

[147] S.-C. Kong, A. Sahakian, A. Taflove, and V. Backman, "High-density optical data storage enabled by the photonic nanojet from a dielectric microsphere," Japanese Journal of Applied Physics, 48(3), 03A008(3 pp) (2009).

[148] S.-C. Kong, A. V. Sahakian, A. Heifetz, A. Taflove, and V. Backman, "Robust detection of deeply subwavelength pits in simulated optical data-storage disks using photonic jets," Applied Physics Letters, 92(21), 211102(3pp) (2008).

[149] K. J. Yi, H. Wang, Y. F. Lu, and Z. Y. Yang, "Enhanced Raman scattering by self-assembled silica spherical microparticles," Journal of Applied Physics, 101(6), 063528(5 pp) (2007).

[150] C. L. Du, J. Kasim, Y. M. You, D. N. Shi, and Z. X. Shen, "Enhancement of Raman scattering by individual dielectric microspheres," Journal of Raman Spectroscopy, 42(2), 145-148 (2011).

[151] M. J. Mendes, I. Tobías, A. Martí, and A. Luque, "Light concentration in the near-field of dielectric spheroidal particles with mesoscopic sizes," Optics Express, 19(17), 16207-16222 (2011).

[152] M. Mosbacher, H.-J. Münzer, J. Zimmermann, J. Solis, J. Boneberg, and P. Leiderer, "Optical field enhancement effects in laser-assisted particle removal," Applied Physics A, 72(1), 41-44 (2001).

[153] Y. F. Lu, L. Zhang, W. D. Song, Y. W. Zheng, and B. S. Luk'yanchuk, "Laser writing of a subwavelength structure on silicon (100) surfaces with particle-enhanced optical irradiation," Journal of Experimental and Theoretical Physics Letters, 72(9), 457-459 (2000).

[154] H.-J. Münzer, M. Mosbacher, M. Bertsch, J. Zimmermann, P. Leiderer, and J. Boneberg, "Local field enhancement effects for nanostructuring of surface," Journal of Microscopy, 202(1), 129-135 (2001).

[155] H.-J. Münzer, M. Mosbacher, M. Bertsch, O. Dubbers, F. Burmeister, A. Pack, R. Wannemacher, B.-U. Runge, D. Bäuerle, J. Boneberg, and P. Leiderer, "Optical near-field effects in surface nanostructuring and laser cleaning," Proceedings of SPIE, 4426, 180-183 (2002).

[156] W. Wu, A. Katsnelson, O. G. Memis, and H. Mohseni, "A deep sub-wavelength process for the formation of highly uniform arrays of nanoholes and nanopillars," Nanotechnology, 18(48), 485302(4pp) (2007).

[157] E. McLeod and C. B. Arnold, "Subwavelength direct-write nanopatterning using optically trapped microspheres," Nature Nanotechnology, 3(7), 413-417 (2008).

[158] R. Fardel, E. McLeod, Y.-C. Tsai, and C. B. Arnold, "Nanoscale ablation through optically trapped microspheres," Applied Physics A, 101(1), 41-46 (2010).

[159] L. Yue, Z. Wang, W. Guo, and L. Li, "Axial laser beam cleaning of tiny particles on narrow slot sidewalls," Journal of Physics D: Applied Physics, 45(36), 365106(8pp) (2012).

[160] L. Yue, Z. Wang, and L. Li, “Multiphysics modelling and simulation of dry laser cleaning of micro-slots with particle contaminants,” Journal of Physics D: Applied Physics, 45(13), 135401(8pp) (2012).

[161] X. Cui, D. Erni, and C. Hafner, “Optical forces on metallic nanoparticles induced by a photonic nanojet,” Optics Express, 16(18), 13560-13568 (2008).

[162] A. Devilez, B. Stout, and N. Bonod, “Compact metallo-dielectric optical antenna for ultra directional and enhanced radiative emission,” ACS Nano, 4(6), 3390-3396 (2010).

[163] S. Lecler, S. Haacke, N. Lecong, O. Crégut, J.-L. Rehspringer, and C. Hirlimann, “Photonic jet driven non-linear optics: example of two-photon fluorescence enhancement by dielectric microspheres,” Optics Express, 15(8), 4935-4942 (2007).

[164] H. Aouani, F. Deiss, J. Wenger, P. Ferrand, N. Sojic, and H. Rigneault, “Optical-fiber-microsphere for remote fluorescence correlation spectroscopy,” Optics Express, 17(21), 19085-19092 (2009).

[165] D. Gérard, A. Devilez, H. Aouani, B. Stout, N. Bonod, J. Wenger, E. Popov, and H. Rigneault, “Efficient excitation and collection of single-molecule fluorescence close to a dielectric microsphere,” Journal of the Optical Society of America B, 26(7), 1473-1478 (2009).

[166] D. Gérard, J. Wenger, A. Devilez, D. Gachet, B. Stout, N. Bonod, E. Popov, and H. Rigneault, “Strong electromagnetic confinement near dielectric microspheres to enhance single-molecule fluorescence,” Optics Express, 16(19), 15297-15303 (2009).

[167] H. Aouani, P. Schön, S. Brasselet, H. Rigneault, and J. Wenger, “Two-photon fluorescence correlation spectroscopy with high count rates and low background using dielectric microspheres,” Biomedical Optics Express, 1(4), 1075-1083 (2010).

[168] C. Kuang, Y. Liu, X. Hao, D. Luo, and X. Liu, “Creating attoliter detection volume by microsphere photonic nanojet and fluorescence depletion,” Optics Communications, 285(4), 402-406 (2012).

[169] E. Yablonovitch, “Inhibited spontaneous emission in solid-state physics and electronics,” Physical Review Letters, 58(20), 2059-2062 (1987).

[170] A. Yariv, Y. Xu, R. K. Lee, and A. Scherer, “Coupled-resonator optical waveguide: a proposal and analysis,” Optics Letters, 24(11), 711-713 (1999).

[171] P. Rol, P. Niederer, and F. Fankhauser, “High-power laser transmission through optical fibers: Applications to ophthalmology,” in [Laser applications in medicine and biology], M. L. Wolbarsht Ed., Plenum Press, 141-198, New York (1991).

[172] T.-H. Wu, T. Teslaa, M. A. Teitell, and P.-Y. Chiou, "Photothermal nanoblade for patterned cell membrane cutting," Optics Express, 18(22), 23153-23160 (2010).

[173] U. Utzinger and R. R. Richards-Kortum, "Fiber optic probes for biomedical optical spectroscopy," Journal of Biomedical Optics, 8(1), 121-147 (2003).

[174] D. X. Hammer, G. D. Noojin, R. J. Thomas, C. E. Clary, B. A. Rockwell, C. A. Toth, and W. P. Roach, "Intraocular laser surgical probe for membrane disruption by laser-induced breakdown," Applied Optics, 36(7), 1684-1693 (1997).

[175] The Eye Diseases Prevalence Research Group, "The prevalence of diabetic retinopathy among adults in the United States," Archives of Ophthalmology, 122(4), 552-563 (2004).

[176] T. A. Ciulla, A. G. Amador, and B. Zinman, "Diabetic retinopathy and diabetic macular edema," Diabetes Care, 26(9), 2653-2664 (2003).

[177] J. M. Krauss and C. A. Puliafito, "Lasers in ophthalmology," Lasers in Surgery and Medicine, 17(2), 102-159 (1995).

[178] G. L. Spaeth, H. Danesh-Meyer, I. Goldberg, and A. Kampik, [Ophthalmic Surgery: Principles and Practice, 4th Edition] Saunders, Philadelphia, PA (2011).

[179] R. M. Verdaasdonk and C. Borst, "Ray tracing of optically modified fiber tips, 1: spherical probes," Applied Optics, 30(16), 2159-2171 (1991).

[180] K. Iwai, Y.-W. Shi, M. Endo, K. Ito, Y. Matsuura, M. Miyagi, and H. Jelinkova, "Penetration of high-intensity Er:YAG laser light emitted by IR hollow optical fibers with sealing caps in water," Applied Optics, 43(12), 2568-2571 (2004).

[181] T. Watanabe and Y. Matsuura, "Side-firing sealing caps for hollow optical fibers," Lasers in Surgery and Medicine, 38(8), 792-797 (2006).

[182] G. A. Peyman, "Method for modifying corneal curvature," US Patent US4840175 A (1989).

[183] D. J. D'Amico, M. S. Blumenkranz, M. J. Lavin, H. Quiroz-Mercado, I. G. Pallikaris, G. R. Marcellino, and G. E. Brooks, "Multicenter clinical experience using an erbium:YAG laser for vitreoretinal surgery," Ophthalmology, 103(10), 1575-1585 (1996).

[184] D. J. D'Amico, P. D. Brazitikos, G. R. Marcellino, S. M. Finn, and J. L. Hobart, "Initial clinical experience with an erbium:YAG laser for vitreoretinal surgery," American Journal of Ophthalmology, 121(4), 414-425 (1996).

[185] P. D. Brazitikos, D. J. D'Amico, T. W. Bochow, M. Hmelar, G. R. Marcellino, and N. T. Stangos, "Experimental ocular surgery with a high-repetition-rate

erbium:YAG laser," Investigative Ophthalmology & Visual Science, 39(9), 1667-1675 (1998).

[186] H. Hoerauf, A. Brix, C. Scholz, J. Winkler, G. Dröge, R. Birngruber, A. Vogel, and H. Laqua, "Retinal photoablation with the Erbium:YAG laser. initial experimental results for traction-free removal of tissue," Ophthalmologe, 100(2), 115-121 (2003).

[187] M. H. Krause and D. J. D'Amico, "Ablation of vitreous tissue with a high repetition rate erbium:YAG laser," European Journal of Ophthalmology, 13(5), 424-432 (2003).

[188] D. P. Joseph, P. Allen, D. Negus, and J. Hobart, "A new and improved vitreoretinal erbium:YAG laser scalpel: long-term morphologic characteristics of retinal-choroidal injury," Ophthalmic Surgery, Lasers and Imaging, 35(4), 304-315 (2004).

[189] H. Hoerauf, A. Brix, J. Winkler, G. Droege, C. Winter, R. Birngruber, H. Laqua, and A. Vogel, "Photoablation of inner limiting membrane and inner retinal layers using the Erbium:YAG laser: an in vitro study," Lasers in Surgery and Medicine, 38(1), 52-61 (2006).

[190] D. Palanker, I. Hemo, I. Turovets, H. Zauberman, G. Fish, and A. Lewis, "Vitreoretinal ablation with the 193-nm excimer laser in fluid media," Investigative Ophthalmology & Visual Science, 35(11), 3835-3840 (1994).

[191] G. M. Hale and M. R. Querry, "Optical constants of water in the 200 nm to 200 μm wavelength region," Applied Optics, 12(3), 555-563 (1973).

[192] C. A. Puliafito, P. J. Wasson, R. F. Steinert, and E. S. Gragoudas, "Neodymium-YAG laser surgery on experimental vitreous membranes," Archives of Ophthalmology, 102(6), 843-847 (1984).

[193] S. Borirakchanyavat, C. A. Puliafito, G. H. Kliman, T. I. Margolis, and E. L. Galler, "Holmium-YAG laser surgery on experimental vitreous membranes," Archives of Ophthalmology, 109(11), 1605-1609 (1991).

[194] J. B. Miller, M. R. Smith, F. Pincus, and M. Stockert, "Intraocular carbon dioxide laser photocautery. I. Animal experimentation," Archives of Ophthalmology, 97(11), 2157-2162 (1979).

[195] J. B. Miller, M. R. Smith, and D. S. Boyer, "Intraocular carbon dioxide laser photocautery," Ophthalmology, 87(11), 1112-1120 (1980).

[196] S. M. Meyers, R. F. Bonner, M. M. Rodrigues, and E. J. Ballintine, "Phototransection of vitreal membranes with the carbon dioxide laser in rabbits," Ophthalmology, 90(5), 563-568 (1983).

[197] D. Karlin, F. Jakobiec, W. Harrison, T. Bridges, C. K. Patel, A. R. Strnad, and O. Wood, "Endophotocoagulation in vitrectomy with a carbon dioxide laser," American Journal of Ophthalmology, 101(4), 445-450 (1986).

[198] R. A. Hill, G. Baerveldt, S. A. Ozler, M. Pickford, G. A. Profeta, and M. W. Berns, "Laser trabecular ablation (LTA)," Lasers in Surgery and Medicine, 11(4), 341-346 (1991).

[199] S. A. Ozler, R. A. Hill, J. J. Andrews, G. Baerveldt, and M. W. Berns, "Infrared laser sclerostomies," Investigative Ophthalmology & Visual Science, 32(9), 2498-2503 (1991).

[200] M. L. McHam, D. L. Eisenberg, J. S. Schuman, and N. Wang, "Erbium: YAG laser trabecular ablation with a sapphire optical fiber," Experimental Eye Research, 65(2), 151-155 (1997).

[201] G. Stevens, Jr., B. Long, J. M. Hamann, and R. C. Allen, "Erbium:YAG laser-assisted cataract surgery," Ophthalmic Surgery and Lasers, 29(3), 185-189 (1998).

[202] C. C. Neubaur and G. Stevens, Jr., "Erbium:YAG laser cataract removal: role of fiber-optic delivery system," Journal of Cataract & Refractive Surgery, 25(4), 514-520 (1999).

[203] T. Wesendahl, P. Janknecht, B. Ott, and M. Frenz, "Erbium: YAG laser ablation of retinal tissue under perfluorodecaline: determination of laser-tissue interaction in pig eyes," Investigative Ophthalmology & Visual Science, 41(2), 505-512 (2000).

[204] P. Rechmann, D. S. Glodin, and T. Hennig, "Er:YAG lasers in dentistry: an overview," Proceedings of SPIE, 3248, 2-13 (1998).

[205] D. M. Clarkson, "A review of technology and safety aspects of erbium lasers in dentistry," Dental Update, 28(6), 298-302 (2001).

[206] T. S. Alster and J. R. Lupton, "Er:YAG cutaneous laser resurfacing," Dermatologic Clinics, 19(3), 453-466 (2001).

[207] R. Kaufmann, "Role of Erbium:YAG laser in the treatment of aged skin," Clinical and Experimental Dermatology, 26(7), 631-636 (2001).

[208] U. Hohenleutner, S. Hohenleutner, W. Bäumler, and M. Landthaler, "Fast and effective skin ablation with an Er:YAG laser: determination of ablation rates and thermal damage zones," Lasers in Surgery and Medicine, 20(3), 242-247 (1997).

[209] J. T. Walsh, Jr., T. J. Flotte, and T. F. Deutsch, "Er:YAG laser ablation of tissue: effect of pulse duration and tissue type on thermal damage," Lasers in Surgery and Medicine, 9(4), 314-326 (1989).

[210] J. A. Harrington, [Infrared Fibers and Their Applications] SPIE Press, Bellingham, WA (2004).

[211] J. A. Harrington, "A review of IR transmitting, hollow waveguides," Fiber and Integrated Optics, 19(3), 211-227 (2000).

[212] E. Hecht, [Optics, 4th Edition] Addison Wesley, San Francisco, CA (2002).

[213] A. Ashkin, "Acceleration and trapping of particles by radiation pressure," Physical Review Letters, 24(4), 156-159 (1970).

[214] T. Mukaiyama, K. Takeda, H. Miyazaki, Y. Jimba, and M. Kuwata-Gonokami, "Tight-binding photonic molecule modes of resonant bispheres," Physical Review Letters, 82(23), 4623-4626 (1999).

[215] B. M. Möller, U. Woggon, M. V. Artemyev, and R. Wannemacher, "Photonic molecules doped with semiconductor nanocrystals," Physical Review B, 70(11), 115323(5pp) (2004).

[216] Y. P. Rakovich, J. F. Donegan, M. Gerlach, A. L. Bradley, T. M. Connolly, J. J. Boland, N. Gaponik, and A. Rogach, "Fine structure of coupled optical modes in photonic molecules," Physical Review A, 70(5), 051801(R)(4pp) (2004).

[217] Y. Hara, T. Mukaiyama, K. Takeda, and M. Kuwata-Gonokami, "Heavy photon states in photonic chains of resonantly coupled cavities with supermonodispersive microspheres," Physical Review Letters, 94(20), 203905(4pp) (2005).

[218] S. P. Ashili, V. N. Astratov, and E. C. H. Sykes, "The effects of inter-cavity separation on optical coupling in dielectric bispheres," Optics Express, 14(20), 9460-9466 (2006).

[219] V. N. Astratov and S. P. Ashili, "Percolation of light through whispering gallery modes in 3D lattices of coupled microspheres," Optics Express, 15(25), 17351-17361 (2007).

[220] T. Mitsui, Y. Wakayama, T. Onodera, Y. Takaya, and H. Oikawa, "Observation of light propagation across a 90° corner in chains of microspheres on a patterned substrate," Optics Letters, 33(11), 1189-1191 (2008).

[221] C.-S. Deng, H. Xu, and L. Deych, "Effect of size disorder on the optical transport in chains of coupled microspherical resonators," Optics Express, 19(7), 6923-6937 (2011).

[222] Q. Zhan, "Cylindrical vector beams: from mathematical concepts to applications," Advances in Optics and Photonics, 1(1), 1-57 (2009).

[223] D. G. Hall, "Vector-beam solutions of Maxwell's wave equation," Optics Letters, 21(1), 9-11 (1996).

[224] S. Quabis, M. Eberler, O. Glöckl, and G. Leuchs, "Focusing light to a tighter spot," Optics Communications, 179(1-6), 1-7 (2000).

[225] R. Dorn, S. Quabis, and G. Leuchs, "Sharper focus for a radially polarized light beam," Physical Review Letters, 91(23), 233901(4pp) (2003).

[226] D. Pohl, "Operation of a ruby laser in the purely transverse electric mode TE_{01}," Applied Physics Letters, 20(7), 266-267 (1972).

[227] S. C. Tidwell, D. H. Ford, and W. D. Kimura, "Generating radially polarized beams interferometrically," Applied Optics, 29(15), 2234-2239 (1990).

[228] A. A. Tovar, "Production and propagation of cylindrically polarized Laguerre-Gaussian laser beams," Journal of the Optical Society of America A, 15(10), 2705-2711 (1998).

[229] A. V. Nesterov, V. G. Niziev, and V. P. Yakunin, "Generation of high-power radially polarized beam," Journal of Physics D: Applied Physics, 32(22), 2871-2875 (1999).

[230] R. Oron, S. Blit, N. Davidson, A. A. Friesem, Z. Bomzon, and E. Hasman, "The formation of laser beams with pure azimuthal or radial polarization," Applied Physics Letters, 77(21), 3322-3324 (2000).

[231] Z. Bomzon, V. Kleiner, and E. Hasman, "Formation of radially and azimuthally polarized light using space-variant subwavelength metal stripe gratings," Applied Physics Letters, 79(11), 1587-1589 (2001).

[232] Z. Bomzon, G. Biener, V. Kleiner, and E. Hasman, "Radially and azimuthally polarized beams generated by space-variant dielectric subwavelength gratings," Optics Letters, 27(5), 285-287 (2002).

[233] M. Berensa, M. Gecevičius, P. G. Kazansky, and T. Gertus, "Radially polarized optical vortex converter created by femtosecond laser nanostructuring of glass," Applied Physics Letters, 98(20), 201101(4pp) (2011).

[234] G. Biener, A. Niv, V. Kleiner, and E. Hasman, "Formation of helical beams by use of Pancharatnam-Berry phase optical elements," Optics Letters, 27(21), 1875-1877 (2002).

[235] T. Grosjean, D. Courjon, and M. Spajer, "An all-fiber device for generating radially and other polarized light beams," Optics Communications, 203(1-2), 1-5 (2002).

[236] D. J. Armstrong, M. C. Phillips, and A. V. Smith, "Generation of radially polarized beams with an image-rotating resonator," Applied Optics, 42(18), 3550-3554 (2003).

[237] I. Moshe, S. Jackel, and A. Meir, "Production of radially or azimuthally polarized beams in solid-state lasers and the elimination of thermally induced birefringence effects," Optics Letters, 28(10), 807-809 (2003).

[238] G. Volpe and D. Petrov, "Generation of cylindrical vector beams with few-mode fibers excited by Laguerre–Gaussian beams," Optics Communications, 237(1-3), 89-95 (2004).

[239] G. Miyaji, N. Miyanaga, K. Tsubakimoto, K. Sueda, and K. Ohbayashi, "Intense longitudinal electric fields generated from transverse electromagnetic waves," Applied Physics Letters, 84(19), 3855-3857 (2004).

[240] Y. Kozawa and S. Sato, "Generation of a radially polarized laser beam by use of a conical Brewster prism," Optics Letters, 30(22), 3063-3065 (2005).

[241] T. Moser, H. Glur, V. Romano, F. Pigeon, O. Parriaux, M. A. Ahmed, and T. Graf, "Polarization-selective grating mirrors used in the generation of radial polarization," Applied Physics B, 80(6), 707-713 (2005).

[242] J.-L. Li, K.-I. Ueda, M. Musha, A. Shirakawa, and L.-X. Zhong, "Generation of radially polarized mode in Yb fiber laser by using a dual conical prism," Optics Letters, 31(20), 2969-2971 (2006).

[243] A. Shoham, R. Vander, and S. G. Lipson, "Production of radially and azimuthally polarized polychromatic beams," Optics Letters, 31(23), 3405-3407 (2006).

[244] K. Yonezawa, Y. Kozawa, and S. Sato, "Generation of a radially polarized laser beam by use of the birefringence of a c-cut Nd:YVO4 crystal," Optics Letters, 31(14), 2151-2153 (2006).

[245] C. F. Phelan, J. F. Donegan, and J. G. Lunney, "Generation of a radially polarized light beam using internal conical diffraction," Optics Express, 19(22), 21793-21802 (2011).

[246] I. Moreno, J. Alberto, J. A. Davis, D. M. Cottrell, and J. B. Cushing, "Polarization manipulation of radially polarized beams," Optical Engineering, 51(12), 128003(7pp) (2012).

[247] F. Wang, Y. Cai, Y. Dong, and O. Korotkova, "Experimental generation of a radially polarized beam with controllable spatial coherence," Applied Physics Letters, 100(5), 051108(4pp) (2012).

[248] A. Al-Qasimi, O. Korotkova, D. James, and E. Wolf, "Definitions of the degree of polarization of a light beam," Optics Letters, 32(9), 1015-1016 (2007).

[249] H. Waddel, "Volume, shape and roundness of quartz particles," Journal of Geology, 43(3), 250-280 (1935).

[250] J. Steiner, "Einfache Beweis der isoperimetrischen Hauptsätze," Journal für die reine und angewandte Mathematik, 1838(18), 281-296 (1838).

[251] W. J. Tropf, M. E. Thomas, and E. W. Rogala, "Properties of crystals and glasses," in [Handbook of Optics (Volume IV), 3rd Edition], M. Bass, C. DeCusatis, J. M. Enoch, V. Lakshminarayanan, G. Li, C. MacDonald, V. N. Mahajan, and E. Van Stryland Eds., McGraw-Hill, Inc., New York, NY (2010).

[252] S. Narita, Y. Matsuura, and M. Miyagi, "Tapered hollow waveguide for focusing infrared laser beams," Optics Letters, 32(8), 930-932 (2007).

[253] I. D. Chremmos and N. K. Uzunoglu, "Analysis of scattering by a linear chain of spherical inclusions in an optical fiber," Journal of the Optical Society of America A, 23(12), 3054-3062 (2006).

[254] P. Ghenuche, H. Rigneault, and J. Wenger, "Hollow-core photonic crystal fiber probe for remote fluorescence sensing with single molecule sensitivity," Optics Express, 20(27), 28379-28387 (2012).

[255] P. Ghenuche, H. Rigneault, and J. Wenger, "Photonic nanojet focusing for hollow-core photonic crystal fiber probes," Applied Optics, 51(36), 8637-8640 (2012).

[256] J. A. Veerman, A. J. Wachters, A. M. van der Lee, and H. P. Urbach, "Rigorous 3D calculation of effects of pit structure in TwoDOS systems," Optics Express, 15(5), 2075-2097 (2007).

[257] J. Grandidier, D. M. Callahan, J. N. Munday, and H. A. Atwater, "Light absorption enhancement in thin-film solar cells using whispering gallery modes in dielectric nanospheres," Advanced Materials, 23(10), 1272-1276 (2011).

[258] C. Hägglund and B. Kasemo, "Nanoparticle plasmonics for 2D-photovoltaics: mechanisms, optimization, and limits," Optics Express, 17(14), 11944-11957 (2009).

[259] B. S. Luk'yanchuk, [Laser Cleaning] World Scientific, Singapore (2002).

[260] D. B. Chrisey, "Materials processing - The power of direct writing," Science, 289(5481), 879-881 (2000).

[261] P. Bharadwaj, B. Deutsch, and L. Novotny, "Optical antennas," Advances in Optics and Photonics, 1(3), 438-483 (2009).

[262] C.-L. Chen, [Elements of Optoelectronics & Fiber Optics] Richard D. Irwin, Inc. company, Chicago, IL (1996).

APPENDIX A: LIST OF PUBLICATIONS

Patent Application:

1. V. N. Astratov and **A. Darafsheh**, "Methods of super-resolution imaging by high-index microspheres," submitted to USPTO, Appl# 61/656,710 (2012).

Journal Articles:

1. **A. Darafsheh**, G. F. Walsh, L. Dal Negro, and V. N. Astratov, "Optical super-resolution by high-index liquid-immersed microspheres," Applied Physics Letters, 101(14), 141128(4pp) (2012).

2. **A. Darafsheh** and V. N. Astratov, "Periodically focused modes in chains of dielectric spheres," Applied Physics Letters, 100(6), 061123(4pp) (2012).

3. T. C. Hutchens, **A. Darafsheh**, A. Fardad, A. N. Antoszyk, H. S. Ying, V. N. Astratov, and N. M. Fried, "Characterization of novel microsphere chain fiber optic tips for potential use in ophthalmic laser surgery," Journal of Biomedical Optics, 17(6), 068004(7pp) (2012).

4. O. Svitelskiy, Y. Li, **A. Darafsheh**, M. Sumetsky, D. Carnegie, E. Rafailov and V. N. Astratov, "Fiber coupling to $BaTiO_3$ glass microspheres in aqueous environment," Optics Letters, 36(15), 2862-2864 (2011).

5. **A. Darafsheh**, A. Fardad, N. M. Fried, A. N. Antoszyk, H. S. Ying, and V. N. Astratov, "Contact focusing multimodal microprobes for ultraprecise laser tissue surgery," Optics Express, 19(4), 3440-3448 (2011). Selected by the Editors for publication in the Virtual Journal for Biomedical Optics (VJBO).

Submitted Journal Articles:

6. **A. Darafsheh**, N. Mojaverian, N. I. Limberopoulos, K. W. Allen, A. Lupu, and V. N. Astratov, "Formation of polarized beams in chains of dielectric spheres and cylinders," submitted.

7. **A. Darafsheh**, N. I. Limberopoulos, J. S. Derov, D. E. Walker Jr., and V. N. Astratov, "Comparison between microsphere-assisted, solid immersion lens, and confocal microscopies," to be submitted.

8. **A. Darafsheh** and V. N. Astratov, "Conical arrays of dielectric spheres as contact focusing microprobes," to be submitted.

9. **A. Darafsheh** *et al.*, "Optical super-resolution by dielectric microcylinders," to be submitted.

10. **A. Darafsheh**, T. C. Hutchens, A. Fardad, A. N. Antoszyk, H. S. Ying, N. M. Fried, and V. N. Astratov, "Contact focusing multimodal probes for potential use in ophthalmic surgery with the Erbium:YAG laser," to be submitted.

11. K. Allen, **A. Darafsheh** *et al.*, "Optical transport and focusing properties of chains of mesoscale spheres," to be submitted.

News Highlight:

1. V. N. Astratov, **A. Darafsheh**, M. D. Kerr, K. W. Allen, N. M. Fried, A. N. Antoszyk, and H. S. Ying, "Photonic nanojets for laser surgery," SPIE Newsroom, 12 March 2010.

Refereed Conference Proceedings:

1. **A. Darafsheh**, Y. Li, and V. N. Astratov, "Super-resolution microscopy by dielectric microcylinders," IEEE Proceedings of the 15th International Conference on Transparent Optical Networks–ICTON13, Cartagena, Spain (2013).

2. **A. Darafsheh**, N. I. Limberopoulos, J. S. Derov, D. E. Walker Jr., and V. N. Astratov, "Comparison between microsphere-assisted and confocal microscopies," IEEE Proceedings of the 15th International Conference on Transparent Optical Networks–ICTON13, Cartagena, Spain (2013).

3. **A. Darafsheh**, N. I. Limberopoulos, A. Lupu, and V. N. Astratov, "Filtering of radially polarized beams by microsphere-chain waveguides," Proceedings of SPIE, vol. 8627, 862713(7pp) (2013).

4. **A. Darafsheh**, N. I. Limberopoulos, J. S. Derov, D. E. Walker Jr., M. Durska, D. N. Krizhanovskii, D. M. Whittaker, and V. N. Astratov, "Optical microscopy with super-resolution by liquid-immersed high-index microspheres," Proceedings of SPIE, vol. 8594, 859411(7pp) (2013).

5. **A. Darafsheh**, T. C. Hutchens, A. Fardad, A. N. Antoszyk, H. S. Ying, N. M. Fried, and V. N. Astratov, "Contact focusing multimodal probes for potential use in ophthalmic surgery with the Erbium:YAG laser," Proceedings of SPIE, vol. 8567, 856780(10pp) (2013).

6. **A. Darafsheh**, M. A. Fiddy, and V.N. Astratov, "Super-Resolution Imaging by High-Index Microspheres Immersed in a Liquid," IEEE Proceedings of the 14th International Conference on Transparent Optical Networks–ICTON12, Coventry, England, paper Tu.A6.5(3pp) (2012).

7. **A. Darafsheh** and V.N. Astratov, "Radial polarization of periodically focused modes in chains of dielectric spheres," IEEE Proceedings of the 14th International Conference on Transparent Optical Networks –ICTON12, Coventry, England, paper Tu.P.27(4pp) (2012).

8. T. Hutchens, **A. Darafsheh**, A. Fardad, A. N. Antoszyk, H. S. Ying, V. N. Astratov, and N. M. Fried, "Novel Microsphere Chain Fiber Tips for use in Mid-IR Ophthalmic Laser Surgery," Proceedings of SPIE, vol. 8218, 821803(8pp) (2012).

9. K. W. Allen, **A. Darafsheh**, and V. N. Astratov, "Beam Tapering Effect in Microsphere Chains: From Geometrical to Physical Optics," Proceedings of SPIE, vol. 8236, paper 823622(7pp) (2012).

10. **A. Darafsheh**, A. Lupo, S. A. Burand, T. Hutchens, N. M. Fried, and V. N. Astratov, "Photonic Nanojet-Induced Modes: Fundamentals and Applications," Proceedings of SPIE, vol. 8264, 82640X(8pp) (2012).

11. K.W. Allen, **A. Darafsheh**, and V.N. Astratov, "Photonic nanojet-induces modes: from physics to applications," IEEE Proceedings of the 13th International Conference on Transparent Optical Networks–ICTON11, Stockholm, Sweden, paper Tu.C4.2(4pp) (2011).

12. **A. Darafsheh** and V. N. Astratov, "Chains of variable size spheres for focusing of multimodal beams in photonics applications," IEEE Proceedings of the 13th International Conference on Transparent Optical Networks–ICTON11, Stockholm, Sweden, paper We.P.2(4pp) (2011).

13. **A. Darafsheh**, A. Fardad, N. M. Fried, A. N. Antoszyk, H. S. Ying, and V. N. Astratov, "Contact Focusing Multimodal Microprobes for Ultraprecise Laser Tissue Surgery," in CLEO:2011-Laser Applications to Photonic Applications, OSA Technical Digest (CD) (Optical Society of America, 2011), paper AME3(2pp). Proc. of CLEO/QELS, Baltimore, MD, May 1-6 (2011).

14. **A. Darafsheh**, K. W. Allen, A. Fardad, N. M. Fried, A. N. Antoszyk, H. S. Ying, and V. N. Astratov, "Focusing capability of integrated chains of microspheres in the limit of geometrical optics," Proceedings of SPIE, vol. 7913, 79131A(7pp) (2011).

15. O. Svitelskiy, D. Sun, **A. Darafsheh**, M. Sumetsky, A. Lupu, M. Tchernycheva, and V. N. Astratov, "Characterization of high index microsphere resonators in fiber-integrated microfluidic platforms," Proceedings of SPIE, vol. 7913, 791314(7pp) (2011).

16. **A. Darafsheh**, O. V. Svitelskiy, and V. N. Astratov, "Light focusing microprobes for biomedical and photonics applications based on integrated microsphere arrays," IEEE Proceedings of the 12th International Conference on Transparent Optical Networks–ICTON10, Munich, Germany, paper Tu.C4.3(4pp) (2010).

17. V. N. Astratov, **A. Darafsheh**, M. D. Kerr, K. W. Allen, and N. M. Fried, "Focusing Microprobes Based on Integrated Chains of Microspheres," Progress in Electromagnetics Research Symposium Proceedings, Cambridge, USA, July 5-8, 419-423 (2010). PIERS Online, Vol. 6, No. 8, 793-797 (2010).

18. **A. Darafsheh**, M. D. Kerr, K. W. Allen, and V. N. Astratov, "Integrated Microsphere Arrays as Compact Focusing Tool for Biomedical and Photonics Applications," in Conference on Lasers and Electro-Optics, OSA Technical Digest (CD) (Optical Society of America, 2010), paper JWA63(2pp). Proc. of CLEO/QELS, San Jose, CA, May 16-21 (2010).

19. **A. Darafsheh**, M. D. Kerr, K. W. Allen, N. M. Fried, A. N. Antoszyk, H. S. Ying, and V. N. Astratov, "Integrated microsphere arrays: light focusing and propagation effects," Proceedings of SPIE, vol. 7605, 76050R(9pp) (2010).

APPENDIX B: SOME APPLICATIONS OF PHOTONIC NANOJETS

Photonic nanojets (PNJs), due to strong localization and high intensity, have applications in nanoparticle detection and size sorting [85, 86, 90, 138, 144, 145], high-density optical data-storage disks [146-148], enhanced Raman scattering [149, 150], enhanced optical absorption in photovoltaics [151], nanostructuring and dry laser cleaning [152-155, 159, 160], nanoparticle trapping [161], optical nanoantenna [162], and Fluorescence correlation spectroscopy (FCS) [163-167]. In this appendix, a brief review of some applications of PNJs is given.

B.1. Nanoparticle Detection and Size Sorting

Nanojet-enhancement backscattering of light, by nanoparticles positioned within a PNJ, was first reported for dielectric nanopatricles with side dimensions between 1.25-60 nm, located within a PNJ formed by a 6 μm diameter dielectric cylinder in Ref. [85] through 2-D high-resolution finite-difference time-domain (FDTD) computational solution of Maxwell's equations. Refractive index of the microcylinder, which was embedded in a medium with index n_2=1.33, was n_1=2.3275 (index contrast n_1/n_2=1.75), and the wavelength in the ambient medium was 300 nm. For each nanoparticle, enhancement of the effective backscattering cross section by several orders of magnitude was reported, for example by $\sim 10^4$ for a 5 nm particle.

By using the generalized multiparticle Mie (GMM) method, which provides rigorous analytical solution for light scattering by multiple spheres, the backscattering enhancement induced by 3-D PNJs was studied in Ref. [86]. Gold nanoparticles (n=1.47-j1.95) with diameters 2-60 nm were located within a PNJ, formed by a dielectric

microspheres (n=1.59) with 3.5 μm diameter illuminated by a plane wave with λ=400 nm. The distance between the center of the nanoparticle and proximal surface of the microsphere was assumed 240 nm for all nanoparticles sizes. It was found that the nanojet-enhanced backscattering phenomenon is extremely sensitive to the size and position of the nanoparticles, which can be used for nanoparticle detection and size sorting of nanoparticles [86].

Based on calculations using GMM theory, Ref. [90] tried to provide a physical explanation for the 7-11 orders of magnitude enhancement of backscattered light by dielectric particles, with sizes between 100-1 nm. It was found that the enhanced backscattering intensity of the nanoparticle is proportional to the third power of its size parameter; however, its physical origin remained unexplained. The following mechanism was proposed to explain the backscattering enhancement phenomenon: The nanoparticle is first excited by the PNJ, emerging from the microsphere, and its scattering intensity is raised by 2 orders of magnitude, determined by the intensity of the PNJ. The interaction of the reradiated fields by the PNJ-excited nanoparticle with the normal EM modes of the microsphere modifies the scattering properties of the nanoparticle, enhances its backscattered intensity by 4-9 additional orders of magnitude [90].

In Ref. [138], by using GMM theory calculations, it was shown that by using a dielectric microsphere illuminated at a Mie resonance, a gold nanosphere 100 times smaller than the sphere can be detected with $\sim\lambda/3$ resolution, where λ is wavelength in the background medium. Off-resonance spatial resolution of $\lambda/2$ was reported. This effect was interpreted due to the formation of narrower PNJs when the sphere is illuminated at WGM resonant wavelengths [138].

First experimental observation of the backscattering enhancement induced by photonic jets, already predicted in [85, 86], was carried out by using a polymethylmethacrylate (PMMA) sphere with 7.62 cm (7.62λ) diameter and n=1.60+j0.0016, at scaled-up microwave (30 GHz, λ_0=1 cm) region of the electromagnetic spectrum in Ref. [144]. Numerical FDTD calculation predicted the formation of a microwave jet with FWHM waist of $0.5\lambda_0$, and 130 times intensity enhancement. When metal particles with diameters 1-3 mm ($0.1\text{-}0.3\lambda_0$) were positioned in the jet region, enhanced position-dependant perturbation of the overall backscattered intensity was observed experimentally. Relatively good agreement between the experimental and simulation results was reported.

Backscattering enhancement induced by PNJs formed by dielectric microspheres was experimentally studied at visible wavelengths in Ref. [145]. Sample stage composed of multilayered pack of glass, solid polydimethylsiloxane (PDMS), and liquid PDMS (n=1.41) was considered to provide precise positioning of the gold nanoparticles (diameters 50-100 nm) within the PNJ formed by a 4.4 μm $BaTiO_3$ microsphere (n=2.1) embedded within the PDMS. It was observed that when the gold nanoparticle is optimally positioned within the nanojet, the backscattering of the microsphere increases significantly. The increased backscattering was found to be strongly dependant on the illumination wavelength and the NA of the imaging system. The measured data were found to be in agreement with the numerical calculations based on Mie-based theory and Fourier optics [145].

B.2. High-density Optical Data-storage Disks

Potential use of PNJs for detection of deeply sub-wavelength pits in an optical data storage disk was studied in Refs. [146-148]. Ref. [148] performed microwave (30 GHz, λ_0=10 mm) experiments, backed up by FDTD simulations, for dimensionally scaled-up pits and land in a simulated optical data-storage device, where data are encoded as nanoscale pits in a metal substrate. The pits-on-groove configuration used in Blu-ray© disks was imitated by machining a 1.25 mm (λ_0/8) by 2 mm (λ_0/5) hole (this dimension for data pit is much smaller than dimensions of data pits in conventional Blu-ray© disks) on an aluminum plate consisted of parallel stripes and grooves with 4 mm (λ_0/2.5) widths, as illustrated in Fig. B.1(a).

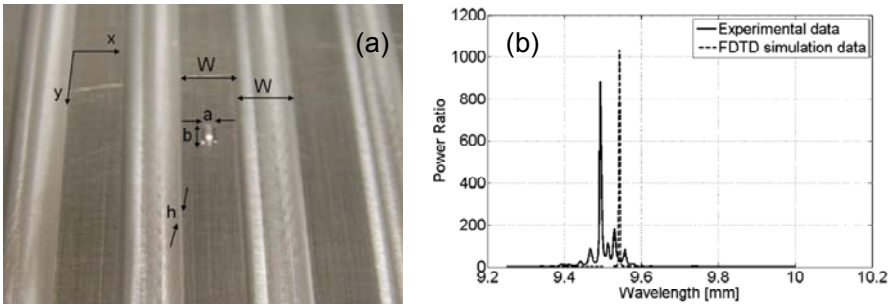

Figure B.1: (a) Photograph of a machined aluminum disk with a pit-on-groove structure. Dimensions are scaled up to 30 GHz (λ_0=10 mm): a=1.25 mm (λ_0/8), b=2 mm (λ_0/5), W=4 mm (λ_0/2.5), and h=1 mm (λ_0/10). (b) Comparison between experimental and simulation results for the no-pit-to-pit power ratio vs. wavelength [148]. Reprinted with permission. © 2008 American Institute of Physics.

The aluminum plate was covered with a Duroid layer with an optimized 11.75 mm (1.175 λ_0) thickness. A 50.8 mm (5.1 λ_0) diameter acrylic sphere (n=1.60) with 4 mm (λ_0/2.5) distance from the Duroid layer was used to create the “microwave jet”. 1 dB in

amplitude and 1% in wavelength agreement between the measurements and the FDTD model were reported, which indicate a no-pit-to-pit power ~700 times (28 dB) greater than the 1.2 value reported in Ref. [256] using a conventional lens for an octagonal pit of approximately the same lateral area in wavelength units. Furthermore, they showed that the peak no-pit-to-pit power ratio is sensitive to the pit depth as well, indicating that a pit-depth modulation can also be employed to increase the data capacity. Refs. [146, 147] conducted similar FDTD numerical modeling in optical wavelengths and concluded that the use of PNJs lead to development of optical data-storage disks, with much greater capacity and speed than those of the present state-of-the-art.

B.3. Enhanced Raman Scattering

Enhancement of Raman scattering was achieved by self-assembled silica microspheres [149] and by individual polystyrene microspheres [150]. In Ref. [149], silicon substrates covered with monolayers of self-assembled closely packed spherical silica particles, with different diameters in the range 0.33-5.08 μm, were employed to study particle-enhanced Raman scattering. A 50× microscope objective lens with NA=0.7 was used to focus the excitation argon laser beam (λ=514.5 nm) into a spot with ~2.5 μm FWHM waist. Same lens was used to collect the Raman scattering. The enhancement of Raman scattering was observed for all spheres' sizes; However, the enhancement was found to be size dependent. It was found that the strongest enhancement occurs when the particle diameter is equal to the spot size formed by the incident laser beam. By using numerical FDTD modeling using OPTIWAVE^{TM} (Optiwave Systems, Inc., Ottawa, Canada), it was shown that PNJs formed by 2.34 μm silica particles were confined to a sub-diffraction length of 100 nm, with waists of 120

nm. It was assumed that the presence of strongly localized electromagnetic fields within the nanojets leads to the enhancement of Raman scattering.

In Ref. [150], enhanced Raman scattering by individual polystyrene spheres was investigated (Fig. B.2) and was shown that the Raman scattering enhancement depends on both the microsphere size and the NA of the collection lens. In comparison with conventional surface-enhanced Raman scattering approaches, microsphere-enhanced Raman spectroscopy may be advantageous, due to the simplicity of sample preparation and precise control of the position and size of the microspheres.

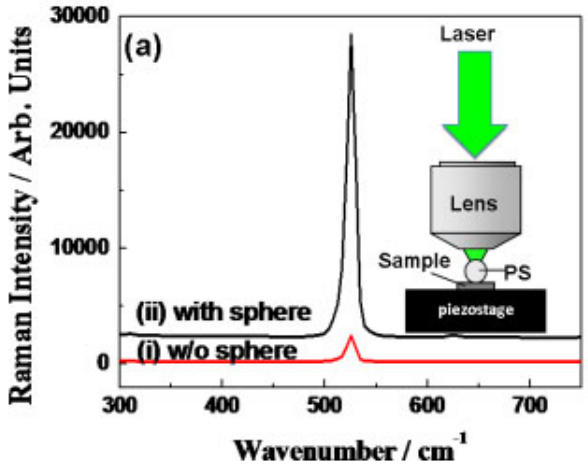

Figure B.2: Typical Raman spectra of bulk Si with collection objective lens 20×NA=0.40 without (i) and with (ii) a polystyrene microsphere. The inset shows the schematic diagram of the experimental setup [150]. Reprinted with permission. © 2010 John Wiley & Sons, Ltd.

B.4. Enhanced Optical Absorption in Photovoltaics

It has been shown that using dielectric mesoscopic particles (DMPs) as “mesoscopic lenses” in a solar cell leads to locally enhanced optical absorption and an overall increase in the power conversion efficiency [257]. Enhancing light interactions with the

photovoltaic material leads to using thinner and thus less expensive photo-active region, which is an improvement in the conditions for charge carrier collection and a raise in the efficiency by virtue of the concentrated energy density in the photovoltaic medium [258].

Ref. [151] studied the light focusing properties of wavelength-scale dielectric spheroidal particles, motivated by their implementation in photovoltaic devices. By using an analytical separation-of-variables method to determine the electromagnetic field distribution inside and in the near-field outside the particles, physical parameters of the spheroids were optimized to achieve maximum forward scattering in the near-field region. It was found that for spheres with mesoscopic sizes, the optimal refractive index to achieve maximum field enhancement just at the shadow-side surface of the sphere is $n \sim \sqrt{3}$.

B.5. Nanostructuring and Dry Laser Cleaning

Refs. [152-155] are among the first studies of employing local field enhancement effects of microspheres for surface nanostructuring and laser-assisted particle removal (dry laser cleaning). By applying short and ultra-short laser pulses on polystyrene spheres with D=0.32-1.7 μm, deposited on a silicon or glass surface, creation of nanoholes underneath the spheres was observed in Ref. [152]. It was concluded that the focusing effect of spheres, in combination with the near-field effects, contribute to the size and shape of the created holes. The mentioned studies were performed few years before the realization of the "photonic nanojets" effect.

In Ref. [160], a multiphysics numerical model was developed to simulate a micro-slot laser cleaning process. Using finite integral technique (FIT), performed with CST Microwave Studio (Computer Simulation Technology AG), single and multiple glass

(n=1.51) microspheres with diameters 1-2 μm, placed at the bottom of a micro-slot, were considered, as illustrated in Fig. B.3. UV laser radiation at λ=248 nm was considered to enhance the cleaning effect [259]. The influences of the slot width, microsphere's size, and the layout on the near-field distribution were studied. Field intensity enhancement of ~25%, influenced by the slot width and the number of spheres, was reported.

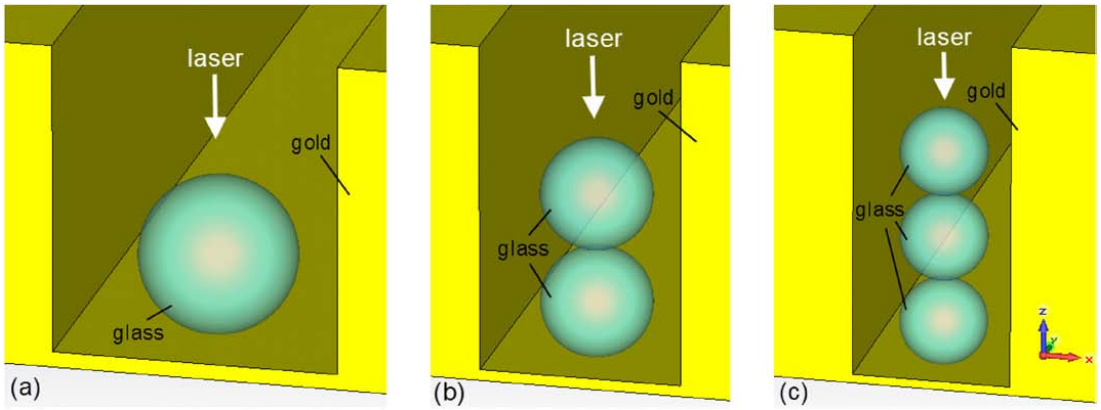

Figure B.3: Schematic of (a) one, (b) two, and (c) three glass (n=1.51) microspheres, with diameter 1 μm, placed in a micro-slot [160]. Reprinted with permission. © 2012 IOP Publishing Ltd.

Ref. [156] reported a low-cost and high-throughput fabrication process of 2-D arrays of sub-wavelength nanoholes or nanopillars, using silica or polystyrene microspheres. As illustrated in Fig. B.4, in this technique, a monolayer of self-assembled microspheres was deposited on top of the photoresist. A very short UV exposure interacted with the photoresist only in the locations of the nanojets formed by microspheres. After developing the photoresist, nanoholes or nanopillars were formed for positive or negative photoresists, respectively. By using 3-D FDTD computations, it was shown that the sizes of nanojets formed by silica spheres, with D=0.5-5 μm (λ=365 nm), weakly depend on

the spheres' diameters, i.e. variation of FWHMs is ~0.6 % of the change in *D*. Therefore, uniform pattern size can be achieved, even for relatively poor sphere size uniformity. The period of the holes and pillars, formed with this technique, can be controlled precisely by the size of the spheres.

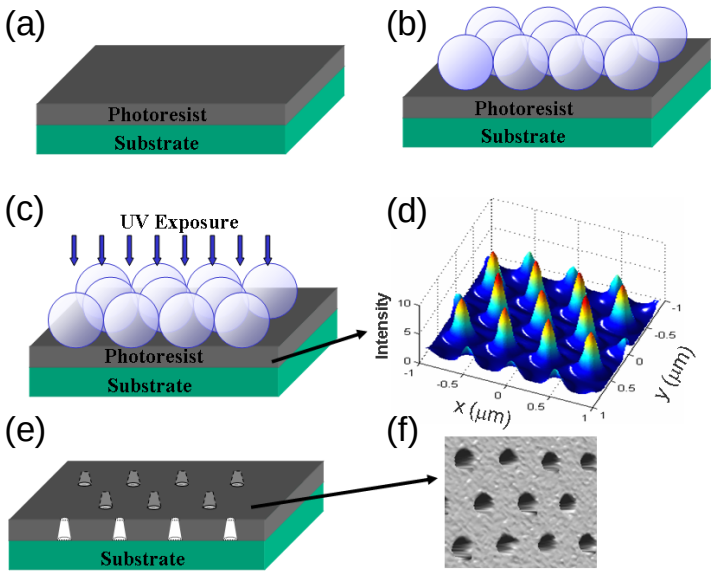

Figure B.4: A schematic illustration of the fabrication process of periodic nano-arrays: (a) spin-on deposition of a photoresist on a substrate. (b) A monolayer microspheres on top of the photoresist. (c) UV light (λ=400 nm) exposure of (b). (d) Calculated intensity profile in the photoresist plane. (e) Obtained sub-wavelength patterns. (f) An AFM image of a developed photoresist (hole sizes are ~250 nm) [156]. Reprinted with permission. © 2007 IOP Publishing Ltd.

Ref. [157] used an optically trapped microsphere, near the surface of a polyimide substrate, for direct-writing [260] of nanopatterns with minimum sizes of ~100 nm ($<\lambda/3$). The microsphere was used as an objective lens to focus the processing laser. The roles of the microsphere's size and material, substrate material, and pulsed laser energy were studied. The optimal experimental results were achieved by using a 0.76 μm

polystyrene sphere, which provided small spot size with good positioning accuracy and optical intensity enhancement.

B.6. Nanoparticle Trapping

Ref. [161], through numerical modeling, studied the optical forces acting on a metallic nanoparticle, when brought into a PNJ formed by a plane wave-illuminated microcylinder. It was found that WGMs are formed in the microcylinder, even at off-resonance wavelengths, if the scattering from the nanoparticle is strong enough. The optical force depends on the separation distance, size and dielectric permittivity of the particle, size and intensity of the PNJ, and wavelength of the light. Furthermore, resonant condition of either the mircocylinder or the nanoparticle leads to enhancement of the optical force and also the PNJ's attractive force can be changed to a repulsive force by varying the state of polarization of the incident beam. The reversal of the force was attributed to the particle's polarizability and localized surface plasmon excitation.

B.7. Optical Nanoantenna

By numerical modeling, Ref. [162] designed an optical antenna [261] consisted of a pair of silver nanospheres (D=60 nm separated by 8 nm) for large enhancements of both excitation strength and radiative decay rates, and a high refractive index TiO_2 dielectric microsphere (D=500 nm) to efficiently collect light without spoiling the emitter quantum efficiency. Simulations results showed 3 orders of magnitude potential enhancements of fluorescence rate over the entire optical frequency range.

B.8. Fluorescence Correlation Spectroscopy

Ref. [165, 166] considered using PNJ effect to enhance excitation and collection of single fluorescent molecules in the vicinity of the PNJ formed by dielectric microspheres. It was reported that by using latex microspheres (n=1.6) illuminated by a focused Gaussian beam, the detection volume reduction of one order of magnitude less than the diffraction limit is achieved. The excitation intensity sensed by the fluorescent molecule is increased by a factor of ~2.2 and the collection efficiency is increased ~60%. The net effect is that the collected fluorescence rate per molecule is increased by a factor of 5 in comparison with confocal microscopy.

It was proposed later, that by using latex microsphere placed at the end of an optical fiber, remote fluorescence correlation spectroscopy (FCS) with sensitivity at single molecule level can be performed due to the PNJ effect [164].

Ref. [167] considered using PNJ effect in two-photon FCS to increases the absorption cross section of Two-photon excitation fluorescence. It was reported that two-photon fluorescence rates per molecule are enhanced by ~1 order of magnitude and confocal analysis volume decreases by a factor of 8, which enables FCS for higher analyte concentrations.

In Ref. [168], an FCS system based on tailoring of the PNJs by using incident cylindrical vector beams [222] combined with stimulated emission depletion microscopy (STED) was proposed for creating attoliter (10^{-18} Lit = 0.001 μm^3) detection volume. The authors proposed using a microsphere illuminated by a radially polarized plane wave, which compresses the axial part of the PNJ, to excite two-photon fluorescence. The azimuthally polarized beam illuminates the same sphere to obtain depletion field, which

reduces the transverse range of the effective volume. Via numerical modeling using FDTD method based on vector electromagnetic wave theory, the excitation and depletion fields of photonic nanojets were simulated using FDTD Solution (Lumerical Solution, Inc., Vancouver, Canada). The result of the numerical modeling showed that the effective volume of the PNJ can reach 0.002 μm^3 (2 aL), which provides 2 orders of magnitude reduced effective volume compared with conventional confocal microscopy.

APPENDIX C: DERIVATION OF PFMS CONDITIONS

In this appendix, first, we derive the equations satisfying the periodically focused mode (PFM) conditions in a linear array of dielectric spheres. In order to satisfy the PFM conditions, the incident ray is considered to be parallel with the optical axis. To achieve $2D$ period of propagation of the incident ray, the ray is forced to go through the point where two spheres touch, as illustrated in Fig. C.1.

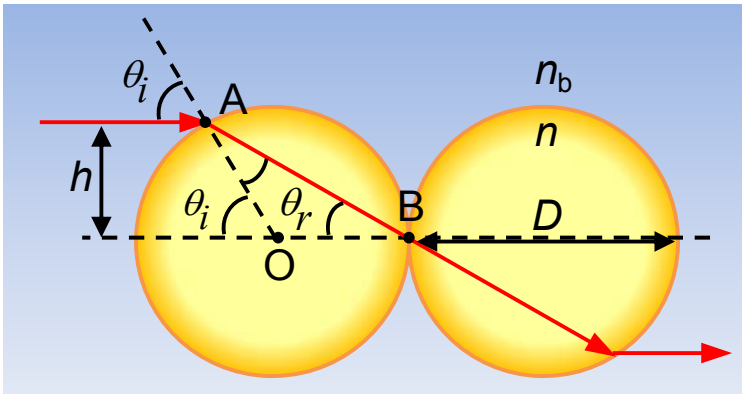

Figure C.1: Ray picture of a PFM in an array of spheres.

From the geometry of the triangle AOB in Fig. C.1, we have:

$$\theta_i = 2\theta_r. \tag{C-1}$$

Applying Snell's law of refraction at the surface of the sphere gives:

$$n_b \sin\theta_i = n \sin\theta_r. \tag{C-2}$$

Substituting Eq. (C-1) in (C-2) yields:

$$n_b \sin\theta_i = n \sin\left(\frac{\theta_i}{2}\right). \tag{C-3}$$

The following trigonometric identity is used to simplify Eq. (C-3):

$$\sin\theta_i \equiv 2 \sin\left(\frac{\theta_i}{2}\right) \cos\left(\frac{\theta_i}{2}\right). \tag{C-4}$$

The following equation is deduced from Eqs. (C-3) and (C-4):

$$\theta_i = 2\cos^{-1}\left(\frac{n}{2n_b}\right). \tag{C-5}$$

From the geometry of Fig. C.1, the following equation holds:

$$\sin\theta_i = 2\frac{h}{D}. \tag{C-6}$$

By substituting Eq. (C-5) in (C-6), the following equation is obtained for the axial offset of the rays satisfying PFM or quasi-PFM conditions:

$$\frac{h}{D} = \frac{1}{2}\sin\left(2\cos^{-1}\left(\frac{n}{2n_b}\right)\right). \tag{C-7}$$

In the following, it is shown that when any given ray travelling in a background medium (n_b) impinges upon a sphere with refractive index n at the Brewster's angle ($\theta_i = \tan^{-1}(n/n_b)$) between materials with n_b and n, it will consequently be incident on the exiting boundary at the corresponding Brewster's angle ($\theta_r = \tan^{-1}(n_b/n)$) between materials n and n_b.

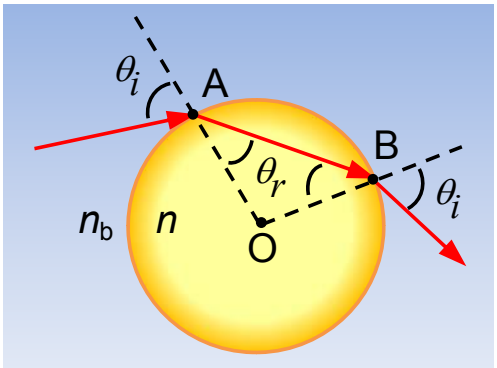

Figure C.2: An arbitrary ray incident at the Brewster's angle on a sphere.

For a given ray travelling in a background medium (n_b) impinges upon a sphere (n), as illustrated in Fig. C.2, the Brewster's angle between materials with n_b and n is:

$$\theta_i = \tan^{-1}(n/n_b). \tag{C-8}$$

For an incident ray at the Brewster's angle, always we have [212]:

$$\theta_i + \theta_r = \pi/2. \tag{C-9}$$

The following trigonometric identity is applied to Eq. (C-8):

$$\tan\theta \equiv [\tan(\tfrac{\pi}{2} - \theta)]^{-1}. \tag{C-10}$$

Applying Eqs. (C-9) and (C-10) to Eq. (C-8) yields:

$$\theta_r = \tan^{-1}(n_b/n), \tag{C-11}$$

which is the Brewster's angle for a ray hitting the boundary between n and n_b.

Finally, we calculate the optical path length (OPL) of periodically focused modes in arrays of dielectric spheres. We consider a 2-sphere chain as an optical resonator, as shown in Fig. C.3. The OPL in the 2-sphere resonator from point A to D is:

$$\mathrm{OPL} = n\,\overline{\mathrm{AB}} + n_b\overline{\mathrm{BC}} + n\,\overline{\mathrm{CD}}. \tag{C-12}$$

From the geometry of Fig. C.3, we have the following relations:

$$\overline{\mathrm{AB}} = \overline{\mathrm{AE}}(\cos\theta_r)^{-1}, \tag{C-13}$$

$$\overline{\mathrm{AE}} = r + r\cos 2\theta_r. \tag{C-14}$$

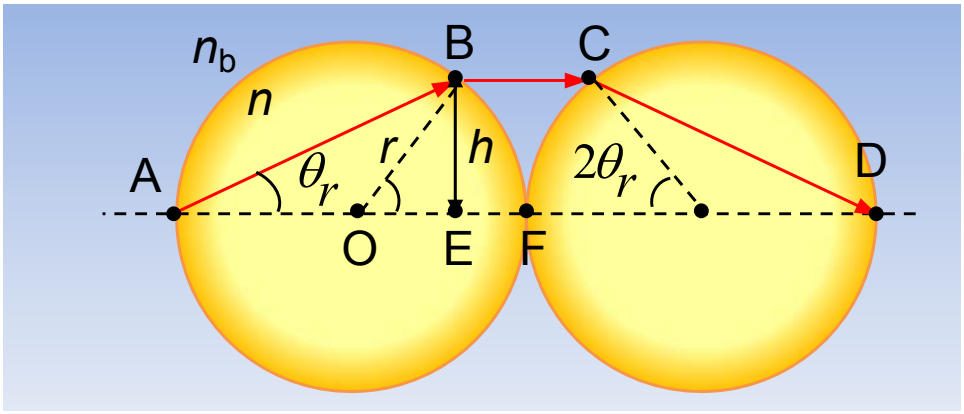

Figure C.3: Optical path length in a 2-sphere chain.

We use the following trigonometric identity to find the optical path length:

$$\cos 2\theta \equiv 2\cos^2 \theta - 1. \tag{C-15}$$

Substituting Eq. (C.14) in Eq. (C.13), and using Eqs. (C.1), (C.5), and (C.15) yields:

$$\overline{\mathrm{AB}} = r(1 + \cos 2\theta_r)(\cos \theta_r)^{-1} = rn/n_b. \tag{C-16}$$

From the geometry of Fig. C.3, we have the following relations:

$$\overline{\mathrm{BC}} = 2\overline{\mathrm{EF}} = 2r(1 - \cos 2\theta_r). \tag{C-17}$$

By using Eqs. (C.1), (C.5), and (C.15), we can show:

$$\overline{\mathrm{BC}} = 2r[2 - n^2/(2n_b^2)]. \tag{C-18}$$

Therefore, the optical path length is:

$$\mathrm{OPL} = 2rn^2/n_b + 2r\,[2n_b - n^2/(2n_b)]. \tag{C-19}$$

If we assume $n_b = 1$, then we have:

$$\mathrm{OPL} = r(n^2 + 4). \tag{C-20}$$

APPENDIX D: MATRIX OPTICS FOR SPHERE-CHAINS

In this appendix, we derive the ABCD matrix [262] for linear arrays of touching identical dielectric spheres, and show that there is an essential distinction between the focusing properties of paraxial rays and that of periodically focused modes (PFMs). First we find the ABCD matrix for a general spherical thick lens, with refractive index n and radii of curvature R_1 and R_2 separated by a distance d. It is assumed that we have n_1 and n_2 for the object and image spaces, respectively, i.e. the surface with radius $R_1(R_2)$ is surrounded by a medium with refractive index $n_1(n_2)$, as shown in Fig. D.1. When both sides of the lens are in air, we have n_1=n_2=n_b=1.

Several equivalent variations of matrices can be found in the literature to represent optical systems. Here, we mention briefly two of them. The following formats of matrices are adopted from [262] and [212], respectively.

$$\begin{bmatrix} r_{out} \\ \theta_{out} \end{bmatrix} = \begin{bmatrix} \mathrm{A} & \mathrm{B} \\ \mathrm{C} & \mathrm{D} \end{bmatrix} \begin{bmatrix} r_{in} \\ \theta_{in} \end{bmatrix}, \tag{D.1}$$

and

$$\begin{bmatrix} n_{t1}\alpha_{t1} \\ y_{t1} \end{bmatrix} = \begin{bmatrix} a_{11} & a_{12} \\ a_{21} & a_{22} \end{bmatrix} \begin{bmatrix} n_{i1}\alpha_{i1} \\ y_{i1} \end{bmatrix}, \tag{D.2}$$

where r (or y) is positive if the intercept of the ray with the reference plane is above the z-axis. The angle is positive if the direction of rotation from the z-axis to the positive ray direction is counterclockwise. Thus, a positive angle means that r increases as a function of z. The following relation holds between matrices of Eqs. (D.1) and (D.2):

$$\begin{bmatrix} \mathrm{A} & \mathrm{B} \\ \mathrm{C} & \mathrm{D} \end{bmatrix} = \begin{bmatrix} a_{22} & a_{21}n_1 \\ a_{12}/n_2 & a_{11}n_1/n_2 \end{bmatrix}. \tag{D.3}$$

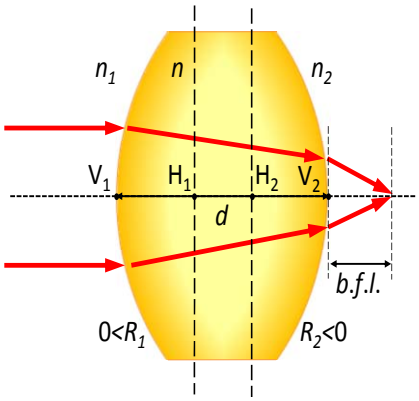

Figure D.1: A thick lens surrounded by two different media.

The cardinal points [212], which are properties of the lens, are deduced from the system matrix due to the fact that the latter is expressed in terms of physical lens parameters, such as radii of curvature, thickness, and indices of refraction.

Front focal length (f.f.l.) and object focus (f_o) are positive if they are to the left of the left vertex of the lens. Back focal length (b.f.l.) and image focus (f_i) are positive if they are to the right of the right vertex of the lens. Principal planes are located at distances h_1 and h_2 which are positive when the plane lies to the right of their respective vertex [212]. According to the mentioned sign convention, the following relations hold:

$$\text{f.f.l.} + h_1 = f_0, \tag{D.4}$$

$$\text{b.f.l.} - h_2 = f_i, \tag{D.5}$$

where the location of principal planes are obtained from the following relations [212]:

$$\overline{\mathrm{V_1H_1}} = h_1 = \frac{n_1(1-a_{11})}{-a_{12}} = \frac{n_1 - n_2\mathrm{D}}{-n_2\mathrm{C}}, \tag{D.6}$$

$$\overline{\mathrm{V_2H_2}} = h_2 = \frac{n_2(a_{22}-1)}{-a_{12}} = \frac{1-\mathrm{A}}{\mathrm{C}}. \tag{D.7}$$

The object and image foci are obtained from [212]:

$$a_{12} = n_2 C = -\frac{n_1}{f_o} = -\frac{n_2}{f_i}, \tag{D.8}$$

where f_o and f_i are measured with respect to their corresponding principal planes, i.e. H_1 and H_2, respectively.

The ratio –A/C from the ABCD matrix gives the effective back focal length (b.f.l.), measured from the right vertex of the lens [262], as shown in Fig. D.1.

For a spherical convex/concave refracting surface (Fig. D.2), the ABCD matrix is written as [262]:

$$\mathrm{M} = \begin{bmatrix} 1 & 0 \\ \frac{1}{R}\,\frac{n_L - n_R}{n_R} & \frac{n_L}{n_R} \end{bmatrix}. \tag{D.9}$$

According to the sign convention, radius of curvature is positive (R>0) for a convex surface and negative for a concave (R<0) surface [212].

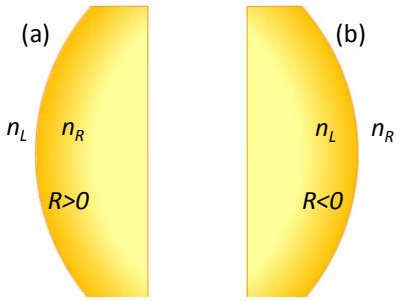

Figure D.2: (a) A spherical concave and (b) convex surface considered to find the ABCD matrix. n_L and n_R represent the refractive index of the left-hand and right-hand side of the surface, respectively.

In order to derive the ABCD matrix for the lens shown in Fig. D.1, we begin from the left surface of the lens as and write:

$$\mathrm{M_1} = \begin{bmatrix} 1 & 0 \\ \frac{n_1 - n}{R_1 n} & \frac{n_1}{n} \end{bmatrix}. \tag{D.10}$$

Ray propagation in a dielectric layer of thickness d is represented by the following matrix [262]:

$$\mathrm{M_d} = \begin{bmatrix} 1 & d \\ 0 & 1 \end{bmatrix}. \tag{D.11}$$

For the right surface of the lens we have:

$$\mathrm{M_r} = \begin{bmatrix} 1 & 0 \\ \frac{n-n_2}{R_2 n_2} & \frac{n}{n_2} \end{bmatrix}. \tag{D.12}$$

The ABCD matrix of the lens is obtained by the multiplication of these three matrices in reverse order [262]:

$$\mathrm{M} = \mathrm{M_r M_d M_l} = \begin{bmatrix} \frac{R_1 n + d(n_1 - n)}{R_1 n} & \frac{d n_1}{n} \\ \frac{n-n_2}{R_2 n_2} - \frac{n-n_1}{R_1 n_2} - \frac{d(n-n_1)(n-n_2)}{R_1 R_2 n n_2} & \frac{n_1}{n_2} + \frac{d(n-n_2)n_1}{R_2 n n_2} \end{bmatrix}. \tag{D.13}$$

And the effective back focal length is:

$$\mathrm{b.f.l.} = \frac{-\mathrm{A}}{\mathrm{C}} = \frac{\frac{d(n-n_1)-R_1 n}{R_1 n}}{\frac{n-n_2}{R_2 n_2} - \frac{n-n_1}{R_1 n_2} - \frac{d(n-n_1)(n-n_2)}{R_1 R_2 n n_2}}. \tag{D.14}$$

If both surfaces of the lens are placed in the same medium, i.e. $n_1=n_2=n_b$, then [262]:

$$\mathrm{M} = \begin{bmatrix} \frac{R_1 n + d(n_b - n)}{R_1 n} & \frac{d n_b}{n} \\ \frac{n-n_b}{n_b}\left(\frac{1}{R_2} - \frac{1}{R_1}\right) - \frac{d(n-n_b)^2}{R_1 R_2 n n_b} & \frac{R_2 n + d(n-n_b)}{R_2 n} \end{bmatrix}. \tag{D.15}$$

And

$$\mathrm{b.f.l.} = \frac{\frac{d(n-n_b)-R_1 n}{R_1 n}}{\frac{n-n_b}{n_b}\left(\frac{1}{R_2} - \frac{1}{R_1}\right) - \frac{d(n-n_b)^2}{R_1 R_2 n n_b}}. \tag{D.16}$$

For the case of $n_1=n_2=1$, where it is assumed that the lens is in air, we have:

$$\mathrm{M} = \begin{bmatrix} \frac{R_1 n + d(1-n)}{R_1 n} & \frac{d}{n} \\ (n-1)\left(\frac{1}{R_2} - \frac{1}{R_1}\right) - \frac{d(n-1)^2}{R_1 R_2 n} & \frac{R_2 n + d(n-1)}{R_2 n} \end{bmatrix}. \tag{D.17}$$

And

$$\mathrm{b.f.l.} = \frac{\frac{d(n-1)-R_1 n}{R_1 n}}{(n-1)\left(\frac{1}{R_2} - \frac{1}{R_1}\right) - \frac{d(n-1)^2}{R_1 R_2 n}}. \tag{D.18}$$

For the special case of a sphere with radius R, we have $|R_1|=|R_2|=R$ and $d=2R$. According to the sign convention, we have $R_1>0$ and $R_2<0$. Therefore:

$$\mathrm{M}=\begin{bmatrix} \frac{2n_1-n}{n} & \frac{2Rn_1}{n} \\ \frac{2n_1n_2-n(n_1+n_2)}{Rnn_2} & \frac{2n_1n_2-nn_1}{nn_2} \end{bmatrix}. \tag{D.19}$$

And

$$\mathrm{b.f.l.}=\frac{Rn_2(2n_1-n)}{n(n_1+n_2)-2n_1n_2}. \tag{D.20}$$

If we assume $n_1=1$, for $n=2$ we have b.f.l.=0 for all R, which means that in paraxial regime, rays are focused at the back surface (concave surface) of the spheres and b.f.l. is not affected by n_2.

For the case of $n_1=n_2=n_b$, we have:

$$\mathrm{M}=\begin{bmatrix} \frac{2n_b-n}{n} & \frac{2Rn_b}{n} \\ \frac{2(n_b-n)}{Rn} & \frac{2n_b-n}{n} \end{bmatrix}. \tag{D.21}$$

And

$$\mathrm{b.f.l.}=\frac{R(2n_b-n)}{2(n-n_b)}. \tag{D.22}$$

In this case, according to Eq. (D.22), the condition $n=2$ does not provide focusing at the back surface of the sphere, in contrast with previous case, where we had $n_1=1$. Here, we need $n=2n_b$ to provide the focusing at the back surface of the sphere.

Finally, if it assumed that $n_1=n_2=1$, then:

$$\mathrm{M}=\begin{bmatrix} \frac{2-n}{n} & \frac{2R}{n} \\ \frac{2(1-n)}{Rn} & \frac{2-n}{n} \end{bmatrix}. \tag{D.23}$$

And

$$\mathrm{b.f.l.}=\frac{R(2-n)}{2(n-1)}. \tag{D.24}$$

In this case, for n=2, we have b.f.l.=0 for all R, which means that in paraxial regime rays are focused at the back surface (concave surface) of the spheres. It can be seen that for $1<n<2$ we have b.f.l.>0, which means that the focusing happens outside the spheres. For $n>2$, we have b.f.l.<0, which means focusing happens inside the sphere.

Now, we consider a linear chain of three identical spheres surrounded by air from all sides, as shown in Fig. D.3.

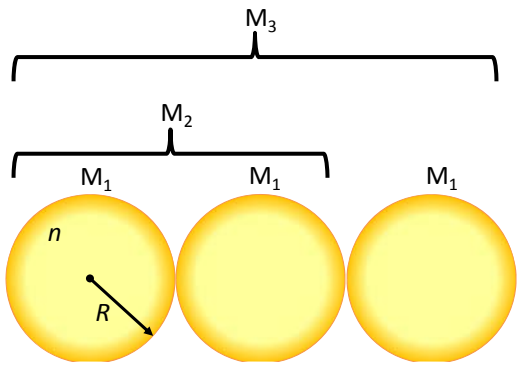

Figure D.3: A linear chain of N=3 identical touching dielectric spheres.

The ABCD matrix for a 2-sphere system is calculated as:

$$\mathrm{M}_2 = \mathrm{M}_1\mathrm{M}_1 = \mathrm{M}_1^2 = \begin{bmatrix} \frac{(2-n)^2+4(1-n)}{n^2} & \frac{4R(2-n)}{n^2} \\ \frac{4(1-n)(2-n)}{Rn^2} & \frac{(2-n)^2+4(1-n)}{n^2} \end{bmatrix}, \tag{D.25}$$

where M_1 is the ABCD matrix for a single sphere. Effective back focal length of a chain of N=2 spheres is:

$$\mathrm{b.f.l.} = \frac{-R\left((2-n)^2+4(1-n)\right)}{4(1-n)(2-n)}. \tag{D.26}$$

At n=2, we have b.f.l.=∞ for all R, which indicates collimated output rays in the paraxial regime.

By considering b.f.l.=0 and solving Eq. (D.26) for n for a given R, we can find the refractive index needed to provide focusing at the concave surface of the second sphere. For example, R=0.125 mm and n=1.5 gives b.f.l.=0, but for R=0.150 mm the above equation has no solution for b.f.l.=0.

For a chain of N=3 spheres, we have:

$$\mathrm{M}_3 = \mathrm{M}_1\mathrm{M}_2 = \mathrm{M}_1^3 = \begin{bmatrix} \frac{(2-n)^3+12(2-n)(1-n)}{n^3} & \frac{6R(2-n)^2+8R(1-n)}{n^3} \\ \frac{6(2-n)^2(1-n)+8(1-n)^2}{Rn^3} & \frac{(2-n)^3+12(2-n)(1-n)}{n^3} \end{bmatrix}. \tag{D.27}$$

And:

$$\mathrm{b.f.l.} = \frac{-R\left((2-n)^3+12(2-n)(1-n)\right)}{6(2-n)^2(1-n)+8(1-n)^2}. \tag{D.28}$$

Again, it can be seen that at n=2, we have b.f.l.=0 for all R.

For N=4 we have:

$$\mathrm{M}_4 = \begin{bmatrix} \frac{(2-n)^4+24(2-n)^2(1-n)+16(1-n)^2}{n^4} & \frac{8R(2-n)^3+32R(2-n)(1-n)}{n^4} \\ \frac{8(2-n)^3(1-n)+32(2-n)(1-n)^2}{Rn^4} & \frac{(2-n)^4+24(2-n)^2(1-n)+16(1-n)^2}{n^4} \end{bmatrix}. \tag{D.29}$$

$$\mathrm{b.f.l.} = \frac{-R\left((2-n)^4+24(2-n)^2(1-n)+16(1-n)^2\right)}{8(2-n)^3(1-n)+32(2-n)(1-n)^2}. \tag{D.30}$$

For N=5 we have:

$$\mathrm{M}_5 = \tag{D.31}$$

$$\begin{bmatrix} \frac{(2-n)^5+40(2-n)^3(1-n)+80(2-n)(1-n)^2}{n^5} & \frac{10R(2-n)^4+80R(2-n)^2(1-n)+32R}{n^5} \\ \frac{10(2-n)^4(1-n)+80(2-n)^2(1-n)^2+32(1-n)^3}{Rn^5} & \frac{(2-n)^5+40(2-n)^3(1-n)+80(2-n)(1-n)^2}{n^5} \end{bmatrix}.$$

$$\mathrm{b.f.l.} = \frac{-R\left((2-n)^5+40(2-n)^3(1-n)+80(2-n)(1-n)^2\right)}{10(2-n)^4(1-n)+80(2-n)^2(1-n)^2+32(1-n)^3}. \tag{D.32}$$

Using the same procedure for a chain of N spheres, we have:

$$\mathrm{M}_\mathrm{N} = \mathrm{M}_1^\mathrm{N}. \tag{D.33}$$

In Fig. D.4, we show the b.f.l. as a function of n for chains of N=1-5 identical spheres with D=300 μm, by using Eqs. (D.24), (D.26), (D.28), (D.30), and (D.32), which shows that by adding more spheres to the chain, generally, the paraxial b.f.l. moves away from the back surface of the end-sphere. For example, for sapphire spheres considered in Section 4.2.2.3 of Chapter 4, with n=1.71, the paraxial b.f.l. for 1, 3, and 5 spheres is 31, 100, and 203 μm, respectively. However, as we showed in Section 4.2.2.3, due to the dominant contribution of PFMs (which experience much smaller loss compared with paraxial rays) in the output beams, the focusing (maximum irradiance) is provided just at the back surface of the end-sphere for chains considered in Section 4.2.2.3. This point indicates that an essential distinction exists between the focusing properties of paraxial rays and that of the PFMs.

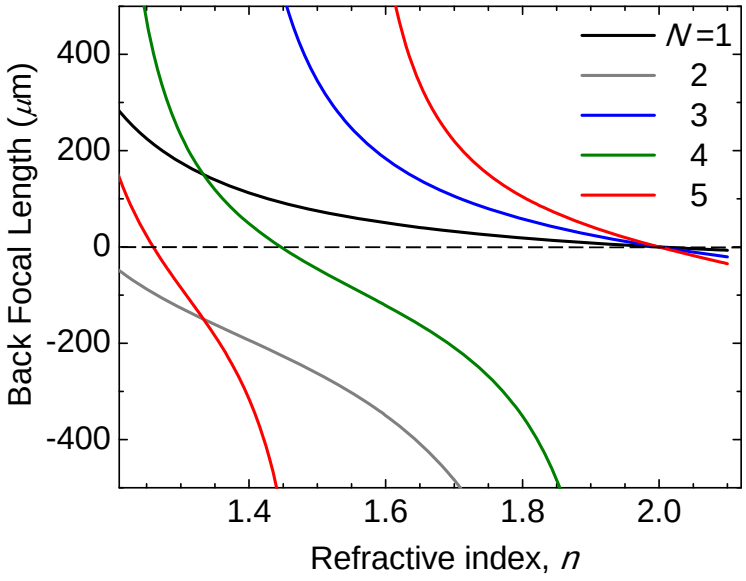

Figure D.4: Paraxial back focal length as a function of refractive index for linear arrays of touching spheres with D=300 μm.

APPENDIX E: SPHERES SIZES IN A CONICAL DESIGN

In this appendix, we find the relation among radii of the spheres in a conical structure. From the geometry of Fig. E.1, we can write the following equalities:

$$(r_1 - r_2)^2 + x_1^2 = (r_1 + r_2)^2 \rightarrow x_1 = 2\sqrt{r_1 r_2}, \tag{E.1}$$

$$(r_2 - r_3)^2 + x_2^2 = (r_2 + r_3)^2 \rightarrow x_2 = 2\sqrt{r_2 r_3}, \tag{E.2}$$

$$\frac{x_3}{x_2 + x_3} = \frac{r_3}{r_2} \rightarrow x_3 = \frac{r_3 x_2}{r_2 - r_3} = \frac{2r_3\sqrt{r_2 r_3}}{r_2 - r_3}, \tag{E.3}$$

$$\frac{x_4 + r_3}{x_4 + 2r_3 + r_2} = \frac{r_3}{r_2} \rightarrow x_4 = \frac{2r_3^2}{r_2 - r_3}, \tag{E.4}$$

$$r_1^2 + (x_1 + x_2 + x_3)^2 = (r_1 + 2r_2 + 2r_3 + x_4)^2, \tag{E.5}$$

Substituting values of x_1 to x_4 from Eqs. (E.1-E.4) in Eq. (E.5), yields:

$$r_1^2 + \left(2\sqrt{r_1 r_2} + 2\sqrt{r_2 r_3} + \frac{2r_3\sqrt{r_2 r_3}}{r_2 - r_3}\right)^2 = \left(r_1 + 2r_2 + 2r_3 + \frac{2r_3^2}{r_2 - r_3}\right)^2. \tag{E.6}$$

By selecting the values for r_1 (175 μm) and r_3 (25 or 50 μm), the value for r_2 for each case is calculated from Eq. (E.6).

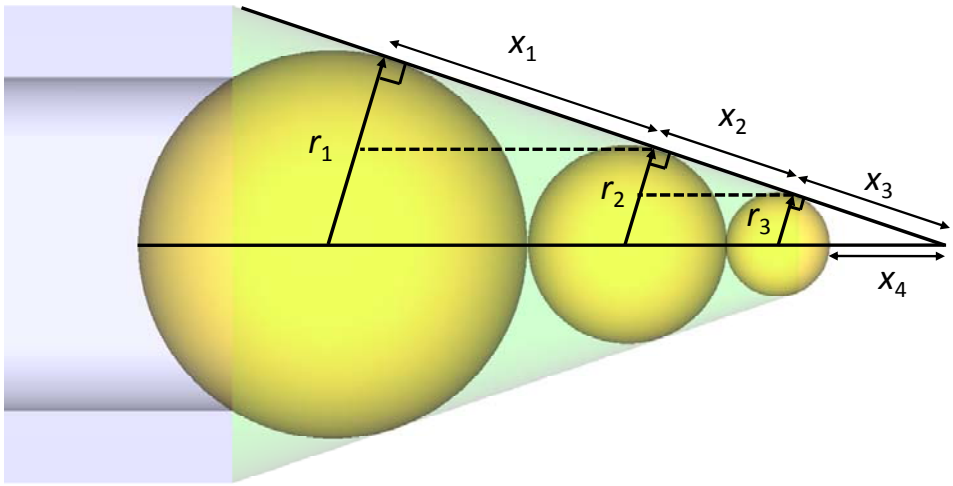

Figure E.1: Schematic of a conical design with three spheres.